UNIVERSITY OF SOUTHAMPTON
FACULTY OF ENGINEERING AND THE ENVIRONMENT
Institute of Sound and Vibration Research

Random-Vortex-Particle Methods Applied to Broadband Fan Interaction Noise

by

Martina Dieste

Thesis for the degree of Doctor of Philosophy

June 2011

UNIVERSITY OF SOUTHAMPTON

ABSTRACT

FACULTY OF ENGINEERING AND THE ENVIRONMENT
INSTITUTE OF SOUND AND VIBRATION RESEARCH

Doctor of Philosophy

RANDOM-VORTEX-PARTICLE METHODS APPLIED TO BROADBAND FAN INTERACTION NOISE

by Martina Dieste

The general aim of this thesis is to investigate the suitability of a stochastic method for computational aeroacoustics, the specific objective being to devise a stochastic method to generate synthetic turbulence and combine it with the linearised Euler equations to predict broadband fan interaction noise. In modern turbofan designs broadband fan noise is a dominant source of aircraft noise, the most efficient source being the interaction between upstream turbulence and the stator vanes.

The stochastic method developed to generate synthetic turbulence reproduces two-dimensional isotropic turbulent flows by filtering a random field. The filter is expressed in terms of the energy spectrum and controls the spatial properties of the synthetic turbulence. In contrast with previous work, non-Gaussian filters are developed to model more realistic energy spectra such as Liepmann and von Kármán spectra. The temporal decorrelation present in turbulent flows is modelled using Langevin Equations. A standard Langevin equation and a second-order Langevin model are derived in details and validated for fan interaction noise. In contrast with classical methods to generate synthetic turbulence, random-vortex-particle methods can be extended to cope with inhomogeneous non-stationary turbulence with little modification from the formulation for homogeneous turbulence.

The stochastic method is applied for first time to broadband fan interaction noise. The method is firstly validated for frozen turbulence interacting with an airfoil. The temporal decorrelation is then included in the method to assess the influence of the integral time scale on the radiated acoustic sound field. The method is also combined with an existing wake model to represent the inhomogeneous non-stationary turbulent flow found downstream of a fan. Finally, comparison with existing experimental data for an isolated airfoil in a turbulent jet demonstrates the benefits of using more realistic energy spectra.

DECLARATION OF AUTHORSHIP

I, MARTINA DIESTE, declare that the thesis entitled

RANDOM-VORTEX-PARTICLE METHODS
APPLIED TO BROADBAND FAN INTERACTION NOISE

and the work presented in the thesis are both my own, and have been generated by me as the result of my own original research. I confirm that:

- this work was done wholly or mainly while in candidature for a research degree at this University;
- where any part of this thesis has previously been submitted for a degree or any other qualification at this University or any other institution, this has been clearly stated;
- where I have consulted the published work of others, this is always clearly attributed;
- where I have quoted from the work of others, the source is always given. With the exception of such quotations, this thesis is entirely my own work;
- I have acknowledged all main sources of help;
- where the thesis is based on work done by myself jointly with others, I have made clear exactly what was done by others and what I have contributed myself;
- parts of this work have been published as:

  Dieste, M. and Gabard, G., "Broadband Fan Interaction Noise using Synthetic Inhomogeneous Non-stationary Turbulence," 17$^{\text{th}}$ *AIAA/CEAS Aeroacoustics Conference*, No. 2708, Portland, Oregon, June 2011.

  Dieste, M. and Gabard, G., "Predicting Broadband Fan Interaction Noise using a Random-Vortex-Particle Method," 20$^{\text{th}}$ *International Congress on Acoustics*, No. 615, Sydney, Australia, August 2010.

  Dieste, M. and Gabard, G., "Investigations of Broadband Fan Interaction Noise using Synthetic Turbulence," 17$^{\text{th}}$ *International Conference in Sound and Vibration*, No. 738, Cairo, Egypt, July 2010.

Dieste, M. and Gabard, G., "Random-Vortex-Particle Methods for Broadband Fan Interaction Noise," 16$^{\text{th}}$ *AIAA/CEAS Aeroacoustics Conference*, No. 3885, Stockholm, Sweden, June 2010.

Dieste, M. and Gabard, G., "Broadband Interaction Noise Simulations using Synthetic Turbulence," 16$^{\text{th}}$ *International Conference in Sound and Vibration*, No. 451, Krakow, Poland, July 2009.

Dieste, M. and Gabard, G., "Synthetic Turbulence Applied to Broadband Interaction Noise," 15$^{\text{th}}$ *AIAA/CEAS Aeroacoustics Conference*, No. 3267, Miami, Florida, May 2009.

Dieste, M., "Generation of Synthetic Turbulent Velocity Fields using Filter Kernels," MSc. thesis, Facultade de Matemáticas - Universidade de Santiago de Compostela, Santiago de Compostela, Spain, July 2008.

Signed:

Date:

Contents

List of Figures

List of Tables

Nomenclature

Abbreviations

AIAA	American Institute of Aeroacoustics
CAA	Computational Aero-Acoustics
CEAS	Confederation of European Aerospace Societies
CFD	Computational Fluid Dynamics
CFL	Courant-Friedrichs-Lewy number
DNS	Direct Numerical Simulations
DRP	Dispersion-Relation-Preserving finite-difference scheme
FWH	Ffowcs-Williams Hawking
ISVR	Institute of Sound and Vibration Research
LEE	Linearised Euler Equations
LES	Large Eddy Simulations
MPI	Message Passing Interface
OGVs	Outlet Guide Vanes
PSD	Power Spectral Density
PWL	Sound Power Levels
RANS	Reynolds Averaged Navier-Stokes
RPM	Random-Particle-Mesh
SNGR	Stochastic Noise Generation and Radiation
SPL	Sound Pressure Levels

Greek Letters

Δt	Time step
δ	Dirac function
κ	Wavenumber
κ_c	Characteristic wavenumber used in methods based on Fourier modes
λ	Integral length scale
∇	Del operator
ω	Angular frequency
ω_c	Characteristic frequency in Kraichnan's model
ψ_n	Phase of the n^{th} Fourier mode
σ_n	Direction of the n^{th} Fourier mode
τ	Integral time scale of the turbulence

$\Delta\kappa_l$ Logarithmic step used by Bechara *et al.* to discretise the wavenumber space
Δ Distance between vortices
Δ_s Sampling rate
δ_{ij} Kronecher symbol
ϵ Intensity of noise
Γ Gamma function
γ Ratio for specific heats
κ_0 Free-field acoustic wavenumber
κ_l Characteristic wavenumber of the largest eddy
κ_x Chordwise hydrodynamic wavenumber
κ_{kol} Kolmogorov wavenumber
$\mathbf{\Lambda}$ Phase speed of the characteristics
π Modified acoustic pressure
$\mathcal{L}$ Lift function generated by the airfoil's response function
g Airfoil response function
ν Kinematic viscosity
ρ Density
τ_d Characteristic time scale of the diffusion process
Θ_c Corrected microphone location, angle
Θ_m Microphone location, angle
ε Dissipation rate
ε_{ijk} Alternating symbol

Roman Letters

b Airfoil half chord
c Airfoil chord
D Dirac comb function
E Energy spectrum of the turbulence
K Kinetic energy
u_{rms} Root-mean-square velocity measured in any direction
v_n Amplitude of the n^{th} Fourier mode
w_A Window function with width A
$\mathcal{C}_0$ Kolmogorov universal constant
$\mathcal{G}$ Green's function
$\overline{w_b^2}$ Mean square velocity of the background turbulence
$\overline{w_w^2}$ Mean square velocity of the wake turbulence
${}_1\mathrm{F}_2$ Generalised hypergeometric function with parameters $p = 1$ and $q = 2$
j_i Spherical Bessel function of i^{th} order
J_i Bessel function of i^{th} order
A_c Corrected amplitude
c_0 Speed of sound
f Lateral autocorrelation function

g	Longitudinal autocorrelation function
J	Jacobian
L	Span of the airfoil
l	Characteristic scale of the largest eddy
L_w	Half width of the rotor wakes
l_z	Integral length scale in the spanwise direction
M	Mach number
N_f	Total number of time steps
N_s	Number of samples
p	Acoustic pressure
p_∞	Variable introduced to formulate Lilley's equation
q_a^+	Amplitude of the characteristic acoustic wave travelling out of the computational domain
q_a^-	Amplitude of the characteristic acoustic wave travelling into the computational domain
q_e	Amplitude of the characteristic entropy wave
q_v	Amplitude of the characteristics vorticity wave
r_{max}	Maximum distance at which a vortex is yet contributing to the velocity field
S_{pp}	Analytical power spectral density
St	Strouhal number
T	Period between adjacent rotor wakes
t_A	Airfoil thickness
TI	Turbulence intensity

Symbols

$\langle\rangle$	Ensemble average
$*$	Convolution operator
$\hat{\cdot}$	Fourier transform of $\cdot$

Subscripts and Superscripts

n	Referred to the n^{th} Fourier mode
T	Transpose of a vector
$'$	Fluctuating component
0	Mean component
$*$	Complex conjugate
$\cdot_{,j}$	Partial derivative of $\cdot$ with respect to the j^{th} component
g	Referred to the Gaussian spectrum
k	Referred to the von Kármán spectrum
l	Referred to the Liepmann spectrum

Vectors and Matrices

$\boldsymbol{\kappa}$	Wave vector
$\boldsymbol{\xi}$	Stochastic vector
$\boldsymbol{\zeta}$	Stochastic vector

R_{ij}	Correlation tensor of the turbulent velocity field
ϕ_{ij}	Velocity spectrum
$\boldsymbol{u}$	Total velocity field
$\boldsymbol{u}'_i$	Incident component of $\boldsymbol{u}'$
$\boldsymbol{u}'_s$	Scattered component of $\boldsymbol{u}'$
$\boldsymbol{u}_0$	Mean flow velocity
$\boldsymbol{u}_c$	Convection velocity
$\boldsymbol{w}$	Vorticity field
$\tilde{\mathbf{q}}$	Amplitudes of the characteristics
E_{ij}	One-dimensional energy spectrum matrix

Acknowledgements

I would like to thank my supervisor Gwénaël Gabard for his invaluable contribution to this thesis. Thank you for giving me the opportunity to work in the ISVR and for your advise, guidance, enlightening discussions and patience during these years.

This work was supported by the Engineering and Physical Science Research Council (UK) and by Rolls-Royce plc through the Rolls-Royce University Technology Centre in Gas Turbine Noise at the University of Southampton. Additional funding was provided by the Royal Academy of Engineering and the ISVR.

I would like to acknowledge Jeremy Astley, Phil Joseph and Anurag Agarwal for their valuable inputs as examiners in the annual reviews of my PhD studies. I would also like to thank Andrew Kempton for the time invested in appraising my work. Many thanks to Vincent Blandeau for his help with the modification of Amiet's model, to Matthieu Grubber for providing the experimental data used in this thesis and to Prathibal Sureshkumar and George Perakis for taking the time to assist me in proof-reading this thesis.

I am grateful to José Luis Ferrín González, Pablo Gamallo Ponte, Óscar López Pouso and Elena Vázquez Cendón for their support on my research studies.

I would like to thank all the ISVR personnel as I very much enjoyed my time there. Thanks to Susan Brindle for her diligence and patience while taking care of all the administrative issues. Also, thank you to the PhD students and postdocs with whom I shared office, coffee breaks and laughs. Thanks to those of you who made the lunch break one of the best parts of the day. I am going to miss such a weird mixture of deep, trivial and sometimes quite scaring conversational topics. Special thanks to Adriana Salgado who along the years became a very good friend.

I would also like to thank my friends and family for their support during my PhD studies. In particular, thanks to Natalia and Rocío for their ability to turn my bad days into great ones.

Finally, special mention to Fernando González who has been kind enough to make all the necessary changes in his life to make mine much happier. For your generosity, patience, understanding and love I am immensely grateful. Thanks for swimming against the current by my side.

Chapter 1

Introduction

1.1 Background

Nowadays, additional noise pollution is not tolerated by the general public. As a consequence, noise regulations are being progressively strengthened. The growth in air traffic (predicted to nearly triple between 2009 and 2028 [1]) must therefore be compensated by the design of quieter aircraft. This will require important advances in low-noise technologies. Significant efforts are being made by industries and research institutes in order to understand, predict and ultimately reduce noise emission from aircraft.

The major sources of aircraft noise include jet mixing noise, fan noise, turbine noise, combustor noise, compressor noise and airframe noise [2]. Since the appearance of noise regulations in the 1960s and the subsequent development of noise reduction technologies, the relative importance of aircraft noise sources and the total sound power radiated have evolved. The individual contributions of various engine noise sources corresponding to an early commercial turbojet and a modern high bypass-ratio turbofan engine are shown in Figure 1.1. A dramatic reduction in jet noise has been achieved thanks to engine designs with increasingly higher bypass-ratio; and fan noise has become a dominant source of noise on modern aircraft. A breakdown of the relative contribution of noise sources on modern aircraft at take-off and approach are shown in Figure 1.2. At take-off, jet and fan noise are the most significant sources contributing to overall sound power. At approach, fan noise is the dominant source, followed by airframe noise. Therefore, reducing fan noise in modern aircraft is a major priority in order to balance the expected growth in air traffic with noise restrictions near airports.

Fan noise is composed of both tonal noise and broadband noise. Tonal noise can be efficiently attenuated by optimising the properties of the acoustic liners to target the blade passing frequency and its harmonics. Broadband fan noise remains more difficult to predict and reduce due to its random nature, wide frequency content and numerous source mechanisms.

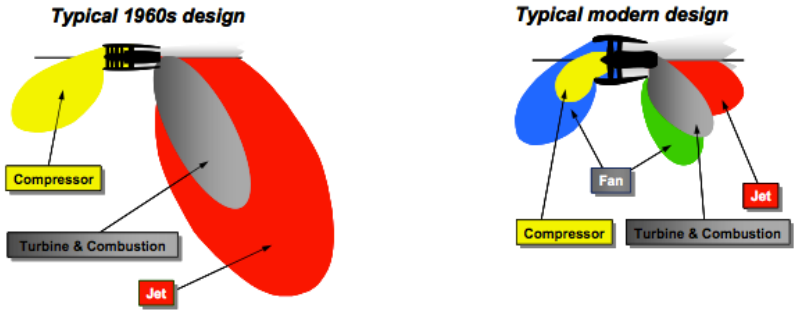

FIGURE 1.1: Amplitude and directivity of engine noise sources from an early turbojet and a modern turbofan. (Reproduced with permission from Astley *et al.* [2].)

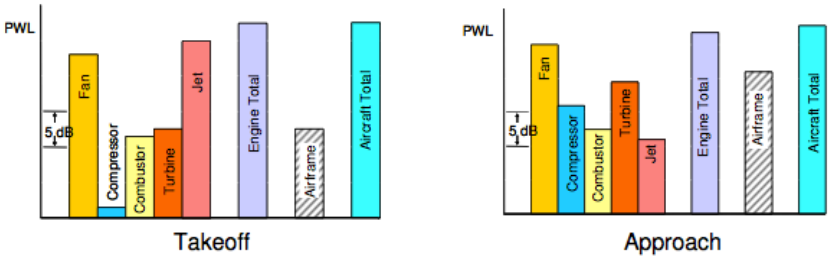

FIGURE 1.2: Relative power levels of noise sources in modern aircraft at take-off and approach. (Reproduced with permission from Astley *et al.* [2].)

In modern turbofan engines broadband fan noise is generated at the fan rotor blades and the fan outlet guide vanes. Broadband fan noise is efficiently generated by the interaction between upstream turbulence and the rotor blades or stator vanes (interaction noise). Even if the upstream flow is clean of turbulence, broadband fan noise is generated by the scattering of surface pressure at the trailing edge caused by the boundary layers that develop along the fan blades and stator vanes (self-noise). Tip-vortex noise is also generated in the annular gap between the blade tips and the fan casing. The most efficient source of broadband fan noise in modern aircraft engines is thought to be the interaction of the rotor turbulent wakes with the downstream stator vanes [3].

1.2 Techniques for predicting broadband fan noise

A possible avenue to predict broadband fan noise is the use of Direct Numerical Simulations (DNS) where the complete Navier-Stokes of fluid dynamics are solved without simplification. Another possibility is Large Eddy Simulation (LES) where small-scale turbulence is modelled but large-scale turbulence is fully resolved. Due to the large range of spatial and time scales present in turbulent flows, these methods can be very demanding in time and computational resources, and they are restricted to relatively low

Reynolds numbers. Even though computational resources available have drastically increased over the past few years, DNS and LES remain too expensive to be used routinely within an industrial context.

An alternative approach to DNS and LES is to split the problem in two parts. Based on the observation that the acoustic field is a small by-product of the overall fluid dynamics, the acoustic source region, generally governed by non-linear effects, is solved using standard Computational Fluid Dynamics (CFD) tools, and then the acoustic field is predicted using source and propagation models such as Lighthill's analogy. Although these methods are cheaper than a complete CFD analysis, the CFD simulation of the source region still remains expensive for industrial applications [4].

The computational cost of these so-called hybrid methods can be reduced by replacing the unsteady CFD stage by synthetic turbulence. Stochastic methods can be used to generate synthetic random turbulent fields that are not exact solutions of the fluid dynamics but that capture several key features of the sound sources, such as the correlation length and time scales, spectrum, etc. Input parameters are obtained from Reynolds Averaged Navier-Stokes (RANS) equations which are significantly less costly than complete unsteady simulations like LES. The resulting synthetic field can be combined with an aeroacoustic model describing both the sources and the propagation of sound. This approach results in accurate predictions of the generation and propagation of acoustic perturbations [5]. The rationale is that this approach is cheaper than DNS and LES from a computational point of view, and therefore working with higher Reynolds numbers is more affordable.

Stochastic methods to generate synthetic turbulent flows have been originally developed to simulate scalar diffusion and also to obtain inflow turbulence for DNS or LES. Early attempts relied on expressing the turbulent velocity field as a finite sum of Fourier modes where parameters such as amplitudes, wavenumbers and phases are chosen randomly following certain distributions. This approach was first introduced by Kraichnan [6] in 1970 and different revisions of this method for computational aeroacoustic purposes have been presented [7, 8, 5]. These revisions include the use of more realistic models to describe the turbulence energy spectrum and more sophisticated treatment of the temporal properties of the turbulence. Fourier-mode methods, also known as SNGR methods, present a good level of accuracy, however they can be computationally demanding and have difficulties representing inhomogeneous turbulence [4].

In order to develop cheaper computational methods, techniques based on filtering random data have been developed [9, 10, 11]. The main idea behind these methods is to obtain the turbulent field by filtering stochastic fields. The filter is used to control the statistical properties of the generated field in such a way that they match the properties of the turbulent flow. An important effort to develop filter-based methods for computational aeroacoustics has been lead by Ewert [12].

1.3 Aims and contributions of this thesis

The general aim of this thesis is to investigate the suitability of stochastic methods for computational aeroacoustic purposes, the specific aim being to devise a stochastic method to generate synthetic turbulence and combine it with the linearised Euler equations to predict broadband fan interaction noise. Therefore, the work done in this thesis can be split in two areas, the computational method (develop and validate and stochastic method to generate synthetic turbulence) and the application (use the stochastic method to study broadband fan interaction noise).

Based on this distinction between method and application, different methods to generate synthetic turbulent flows are reviewed in chapter 2 and then an overview of different techniques used to investigate broadband fan noise with an emphasis on stochastic methods is provided in chapter 3.

1.3.1 Synthetic turbulence

The stochastic method used in this thesis is a filter-based method that stems from the works of Careta *et al.* [9] and Ewert *et al.* [10]. It generates synthetic two-dimensional isotropic turbulent flows and requires as inputs some statistical properties of the turbulent flow such as energy spectrum, integral length and time scales and kinetic energy. These properties can be either modelled using empirical laws, measured or predicted from RANS simulations.

The spatial statistical properties of the synthetic turbulence are controlled by a filter which is fully determined by the turbulence energy spectrum. In contrast with Ewert and coworkers who focus on the use of Gaussian filters, in this work different energy spectra are considered by selecting different filters. In particular, Gaussian, Liepmann and von Kármán spectra are considered. Whilst the Gaussian spectrum has certain advantages from a computational point of view, Liepmann and von Kármán spectra are more commonly used in turbulence modelling for broadband fan noise applications [13]. Advantages and disadvantages of selecting different filters will be discussed in terms of computational performance and accuracy.

The temporal properties of the turbulence are included in the method via the stochastic field upon which the filter acts. Two cases are considered. The first case is frozen turbulence where only convection effects are included. The second case is evolving turbulence where the time correlation of the turbulence is modelled through Langevin equations. Standard Langevin equations are stochastic differential equations widely used to model the fluid dynamics involved in turbulent diffusion at large Reynolds numbers [14]. However, it will be shown that a standard Langevin equation is not suitable for coupling with

the linearised Euler equation solver used here due to the lack of differentiability of the resulting synthetic velocity field. A second-order Langevin model is proposed to overcome numerical issues related to the standard Langevin equation. A second-order Langevin model has also been used by Siefert and Ewert [15] to model temporal correlations for aeroacoustics but a different formulation is proposed here.

The stochastic method is implemented in a purely Lagrangian approach. In a purely Lagrangian approach the locations of the vortices are not restricted to the grid points and move freely due to the convection effects. In addition, in contrast with Ewert *et al.*'s work, vorticity is not interpolated onto an auxiliary grid to compute the synthetic velocity field.

Note that a grid-based discretisation of the method is also briefly presented in this work. This implementation is used as a preliminary validation of the stochastic method[1].

Different implementations of the stochastic method to generate synthetic inhomogeneous non-stationary turbulence are proposed and validated. In contrast with Fourier-mode methods, which have difficulties representing inhomogeneous turbulence, it will be shown that the stochastic method used here can produce synthetic inhomogeneous non-stationary turbulence accurately with only little modification.

1.3.2 Application to broadband fan noise

In this thesis synthetic turbulence is combined with the linearised Euler equations to predict broadband fan interaction noise. This application of filter-based methods in computational aeroacoustics has not been considered before.

The linearised Euler equations are solved in the time domain using a general in-house finite-difference code with the synthetic turbulence implemented as a boundary condition along the airfoil. The test case considered is a flat plate interacting with a two-dimensional turbulent stream. This test case is particularly suitable for this work because analytical solutions are available.

The LEE solver is initially validated for incident frozen gusts at different frequencies covering the typical range of interest of broadband noise. The accuracy of the solver is assessed by comparing the response function of the airfoil against the analytical solution proposed by Amiet [17] modified for a fully two-dimensional acoustic field.

The linearised Euler equations are then combined with the stochastic method to generate synthetic turbulence previously devised in this thesis. Firstly, the interaction between frozen turbulence and an isolated flat plate is considered. This serves as a validation

[1]The preliminary validation of the stochastic method has been submitted by the author for partial fulfilment of a MSc at Universidad de Santiago de Compostela, Spain. See Ref. [16].

of the stochastic method and also as a validation of the full method to predict broadband fan noise. The synthetic turbulence is validated by computing correlations and one-dimensional energy spectra along the airfoil. In order to improve the quality of the synthetic velocity field, a parametric study is conducted to select the optimal numerical parameters for the method. The far-field acoustic pressure is validated against Amiet's analytical solution. Trade-offs between computational costs and accuracy are also discussed.

Secondly, broadband fan interaction noise generated by evolving turbulence is examined. The temporal decorrelation of the turbulence is first modelled with a standard Langevin equation. Even though it provides accurate statistics of the turbulence along the flat plate, significant spurious sound sources are introduced at high frequencies. In contrast, the proposed second-order Langevin model not only provides accurate statistics of the turbulence but also reliable far-field noise predictions. This test case validates the stochastic method to generate synthetic evolving turbulence and also allows to assess the sensitivity of the predicted acoustic field to the integral time scale of the turbulence.

Thirdly, the stochastic method is modified to provide a more realistic description of rotor-stator interaction noise. Broadband noise is produced when the turbulent wakes generated by the rotor blades impinge on the stator vanes. To model the inhomogenous non-stationary turbulence typically found upstream of the stator vanes, the stochastic method is combined with the wake model proposed by Jurdic [18]. This wake model allows for strong variations of the turbulent kinetic energy.

Finally, numerical results are compared against existing experimental data of an airfoil interacting with a turbulent stream. While experiments are carried out with an airfoil with realistic geometry, a flat plate is used in the numerical simulations which in addition are fully two-dimensional. This comparison provides another opportunity to validate the numerical method and it also demonstrates the benefits of using the von Kármán spectrum instead of a Gaussian spectrum to describe the turbulence energy spectrum.

1.3.3 Contributions of this thesis

The contributions of this thesis are:

- New non-Gaussian filters are developed to represent non-Gaussian spectra instead of using a series of Gaussian filters.
- A detailed description and validation of a second-order Langevin model to describe the temporal correlation of turbulent flows is provided.
- A wake model is combined with a filter-based method to generate synthetic the inhomogeneous non-stationary turbulence found downstream of a fan.

- The stochastic method is implemented in a purely Lagrangian approach.
- The filter-based method is applied to predict broadband fan interaction noise. The effects of temporal decorrelation and inhomogeneity are carefully assessed. In addition, numerical results are compared against experimental data.

Results obtained during this project have been presented at the 15^{th}, 16^{st} and 17^{nd} AIAA/CEAS Aeroacoustic Conference [19, 20, 21], 16^{th} and 17^{th} International Conference in Sound and Vibration [22, 23] and at the 20^{th} International Congress on Acoustics [24].

1.4 Outline of contents

This thesis is structured as follows. In the next chapter the generation of synthetic turbulence is discussed. After an overview of the subject, the more relevant methods and issues of generating synthetic turbulence are presented, the method used in this work is then derived. The numerical implementation of the method is also described. The formulation of the method for Gaussian, Liepmann and von Kármán energy spectra is then discussed. Finally, results of a preliminary validation of the stochastic method for the Gaussian spectrum are shown.

In chapter 3 the synthetic turbulence is combined with the linearised Euler equations to predict broadband fan interaction noise. After reviewing different techniques to predict broadband fan interaction noise, the physical model under consideration is explained. The implementation of the LEE solver is described and validated for the case of incident frozen gusts interacting with a flat plate.

In chapter 4 broadband fan interaction noise is predicted by combining the LEE solver presented in the previous chapter with the stochastic method to generate synthetic turbulence introduced in chapter 2. The test case considered is that of an isolated flat plate interacting with frozen homogeneous isotropic turbulence. The stochastic method is validated for Gaussian, Liepmann and von Kármán spectra by assessing the statistics of the turbulence and comparing far-field noise levels against a modified version of Amiet's analytical solution [17]. The computational performance of the method is discussed for each of the three spectra considered in this work.

In chapter 5 the method is extended to include the temporal decorrelation of the turbulence by considering first- and second-order Langevin models. Both models are derived in details and validated for the test case previously considered in chapter 4. Finally, the sensitivity of the far-field noise levels to the integral time scale of the turbulence is evaluated.

In chapter 6 different implementations of the stochastic method to generate synthetic inhomogeneous non-stationary turbulence are examined and then combined with a wake model to represent trains of turbulent rotor wakes. The statistical behaviour of the synthetic turbulence along the flat plate and noise levels in the far field are assessed for different wake configurations.

In chapter 7, numerical results are compared against existing experimental data for an isolated airfoil in a turbulent stream. First, the experimental set up is described and the aerodynamic and acoustic measurements are analysed to extract the input data for the stochastic method. Numerical simulations of the experiment are then performed using Gaussian and von Kármán filters and numerical results are compared against aerodynamic and acoustic measurements.

Finally, chapter 8 discusses the main conclusions and future areas of research.

Chapter 2

Synthetic Turbulence

In this chapter methods to generate synthetic turbulent flows are discussed. Firstly, an overview of existing techniques to generate synthetic turbulence is presented. Special attention is given to the procedures to obtain the velocity field, the choice of target statistical parameters and features such as time-decorrelation, inhomogeneity and anisotropy. Advantages and limitations of the methods are discussed. Secondly, the stochastic method that forms the basis for the work presented in this thesis is described in details. It accounts for two-dimensional, evolving, homogeneous, isotropic turbulence. The method consists of filtering a random field where the filter is defined such that target statistical properties of the turbulence are recovered. The numerical implementation is then discussed using a Lagrangian formulation and also with a grid-based approach for the specific case of separable filters. Thirdly, the stochastic method is illustrated by considering the filters corresponding to Gaussian, Liepmann and von Kármán turbulence spectra. Finally, a preliminary validation of the method to generate synthetic turbulence is performed for the Gaussian spectrum.

2.1 Overview of methods to generate synthetic turbulence

The aim of stochastic methods is to generate synthetic turbulent velocity fields that capture the key features of turbulence, such as integral length and time scales and target values of kinetic energy, but that are not necessarily exact solutions of fluid dynamics equations. The idea is that such an approach is cheap and yet provides accurate solutions.

While this work concentrates on using synthetic turbulence as a source of sound for Computational Aero-Acoustics (CAA), synthetic turbulence has been used for a wide range of applications. For instance, synthetic turbulence has also been used to model scalar diffusion and to generate unsteady inflow forcing for CFD simulations.

Early attempts to stochastically generate velocity fields relied on expressing them as a finite sum of Fourier modes with random amplitudes. More recently, methods based on digital filtering of random data have also been devised in order to develop cheaper and more flexible computational codes.

This section intends to provide an overview of the methods (rather than the applications) and to highlight their advantages and disadvantages. The main aspects covered are how the synthetic velocity field is defined and how it copes with temporal correlation and inhomogeneity. After reviewing different methods, techniques to include the effects of anisotropy are discussed.

2.1.1 Methods based on Fourier modes

2.1.1.1 Kraichnan's method

The generation of stochastic velocity fields based on random Fourier modes was initially introduced by Kraichnan [6] in 1970, the objective being to reproduce the diffusion of fluid particles by the random velocity field of a turbulent incompressible flow. Kraichnan's method is the precursor of the family of methods known as Stochastic Noise Generation and Radiation (SNGR). It generates an artificial velocity field with prescribed energy spectra in two or three dimensions. The field obtained is divergence-free, statistically stationary, homogeneous and isotropic.

Kraichnan's method expresses the velocity field as a superposition of time-harmonic plane waves as follows:

$$\boldsymbol{u}(\boldsymbol{x},t) = \sum_{n=1}^{N} \left[\boldsymbol{v}(\boldsymbol{\kappa}_n)\cos(\boldsymbol{\kappa}_n \cdot \boldsymbol{x} + \omega_n t) + \boldsymbol{w}(\boldsymbol{\kappa}_n)\sin(\boldsymbol{\kappa}_n \cdot \boldsymbol{x} + \omega_n t)\right], \tag{2.1}$$

where $\boldsymbol{\kappa}_n$ is the wave vector and ω_n the angular frequency of each mode. In order to ensure that the velocity field is incompressible ($\nabla \cdot \boldsymbol{u} = 0$), the amplitudes $\boldsymbol{v}$ and $\boldsymbol{w}$ are defined in terms of the wave vector using

$$\boldsymbol{v}(\boldsymbol{\kappa}_n) = \boldsymbol{\zeta}_n \times \boldsymbol{\kappa}_n, \quad \boldsymbol{w}(\boldsymbol{\kappa}_n) = \boldsymbol{\xi}_n \times \boldsymbol{\kappa}_n, \tag{2.2}$$

where $\boldsymbol{\zeta}_n$ and $\boldsymbol{\xi}_n$ are random unit vectors and their distributions are defined so as to obtain a solution of $\boldsymbol{u}$ which is statistically isotropic and with the prescribed energy spectrum. The frequencies ω_n are independent Gaussian variables with zero mean and standard deviation ω_c^{-1} such that the time correlation is given by

$$R(t) = \langle \boldsymbol{u}(\boldsymbol{x},t_1)\ \boldsymbol{u}(\boldsymbol{x},t_2)\rangle = \exp\left(-\frac{\omega_c^2 t^2}{2}\right), \tag{2.3}$$

where $t = |t_2 - t_1|$ and $\langle\ \rangle$ stands for the ensemble average. The corresponding integral time scale is $\tau = \sqrt{\pi/2}\omega_c^{-1}$. Frozen turbulence can be considered by setting $\omega_c = 0$.

Kraichnan considered two different energy spectra: a Gaussian spectrum centred at a given wavenumber κ_c; or a single wavenumber component using a Dirac delta function. In 3D these spectra are

$$E_1(\kappa) = \frac{16\sqrt{2\pi}}{\pi} u_{rms}^2 \kappa^4 \kappa_c^{-5} \exp\left(-\frac{2\kappa^2}{\kappa_c^2}\right), \quad E_2(\kappa) = \frac{3}{2} u_{rms}^2 \delta(\kappa - \kappa_c), \tag{2.4}$$

and in 2D,

$$E_3(\kappa) = \frac{9}{2} u_{rms}^2 \kappa^3 \kappa_c^{-4} \exp\left(-\frac{3\kappa^2}{2\kappa_c^2}\right), \quad E_4(\kappa) = u_{rms}^2 \delta(\kappa - \kappa_c), \tag{2.5}$$

where u_{rms} is the root-mean-square velocity measured in any direction and δ stands for the Dirac function. The wavenumber κ_c at which the spectrum peaks can be related to the integral length scale of the turbulence λ using that (see Ref. [14])

$$\lambda = \frac{\pi}{2u_{rms}^2} \int_0^\infty \frac{E(\kappa)}{\kappa} \mathrm{d}\kappa, \qquad \text{(3D)} \tag{2.6}$$

$$\lambda = \frac{2}{u_{rms}^2} \int_0^\infty \frac{E(\kappa)}{\kappa} \mathrm{d}\kappa. \qquad \text{(2D)} \tag{2.7}$$

It follows that the integral length scales corresponding to the energy spectra in Eqs. (2.4) and (2.5) are:

$$\lambda_1 = \sqrt{2\pi}\kappa_c^{-1}, \quad \lambda_2 = \frac{3}{4}\pi\kappa_c^{-1}, \quad \lambda_3 = \sqrt{\frac{3\pi}{2}}\kappa_c^{-1}, \quad \lambda_4 = 2\kappa_c^{-1}. \tag{2.8}$$

The wavenumber space is stochastically discretised by picking the wave numbers $\boldsymbol{\kappa}_n$ from statistically isotropic distributions so that in the limit $N \to \infty$ the desired energy spectrum is realised.

Note that Kraichnan's method requires a large number of modes N to properly capture the statistical behaviour of the turbulence. Note also that in order to compute statistical quantities, such as correlations, a number of realisations of the velocity field in Eq. (2.1) has to be computed.

2.1.1.2 Bechara *et al.*'s method

Kraichnan's [6] method has been modified by Bechara *et al.* [8] to study aerodynamic noise from free turbulent flows, with the objective to use more realistic energy spectrum models than those considered by Kraichnan.

Bechara *et al.* proposed to obtained the synthetic velocity field as a finite sum of only cosine waves but with random phase

$$\boldsymbol{u}(\boldsymbol{x}) = 2\sum_{n=1}^{N} v_n \cos(\boldsymbol{\kappa}_n \cdot \boldsymbol{x} + \psi_n)\boldsymbol{\sigma}_n, \tag{2.9}$$

where v_n, ψ_n, and $\boldsymbol{\sigma}_n$ are the amplitude, phase, and direction of the n^{th} mode associated with the wave vector $\boldsymbol{\kappa}_n$. Flow incompressibility is achieved by ensuring that $\boldsymbol{\kappa}_n \cdot \boldsymbol{\sigma}_n = 0$.

A key difference with Kraichnan's method is that, instead of representing the range of wavenumbers by a random distribution along the κ-axis, Bechara *et al.* suggested to used a fixed discretisation of the wavenumbers so that the resolution can be optimised at different ranges of the energy spectrum. Bechara *et al.* proposed to use a logarithmic distribution of N wavenumbers between $\kappa_l = 2\pi/l$, which corresponds to the largest eddy with l being the characteristic length scale of the largest eddy, and the Kolmogorov wavenumber $\kappa_{kol} = \left(\varepsilon/\nu^3\right)^{1/4}$ where ε stands for the dissipation rate and ν for the kinematic viscosity. The logarithmic step is given by

$$\Delta\kappa_l = \frac{1}{N-1}\log\left(\frac{\kappa_{kol}}{\kappa_l}\right), \tag{2.10}$$

and the list of wavenumbers is given by $\kappa_n = (\Delta\kappa_l)^{n-1}\kappa_l$. This distribution provides a better resolution of the smaller wavenumbers than the inertial subrange, therefore one can argue that the discretisation is improved in the regime where most of the energy is contained.

Then, the amplitude of each Fourier mode, v_n, is determined through the definition of the kinetic energy, K, in terms of the energy spectrum

$$K = \int_0^\infty E(\kappa)\mathrm{d}\kappa, \tag{2.11}$$

and the velocity field

$$K = \frac{1}{2}\langle \boldsymbol{u}_i(\boldsymbol{x},t)\ \boldsymbol{u}_i(\boldsymbol{x},t)\rangle = \sum_{n=1}^{N} v_n^2. \tag{2.12}$$

The amplitude of each wavenumber component can therefore be directly related to the energy spectrum by using:

$$v_n = \sqrt{E(\kappa_n)\Delta\kappa_n}, \tag{2.13}$$

where $\Delta\kappa_n$ is the small interval in the spectrum centred at κ_n. Note that in contrast with Kraichnan's method, the amplitude of each mode is not a random variable with a given distribution but deterministically prescribed by the energy spectrum of the turbulence.

Bechara *et al.* [8] selected the modified von Kármán spectrum

$$E(\kappa) = A\frac{K}{\kappa_c}\frac{(\kappa/\kappa_c)^4}{[1+(\kappa/\kappa_c)^2]^{17/6}}\exp\left(\frac{-2\kappa^2}{\kappa_{kol}^2}\right) \tag{2.14}$$

to simulate the energy spectrum. A is an amplitude parameter such that Eq. (2.11) is verified. This spectrum is a more accurate description of the turbulence energy spectrum than the Gaussian spectrum proposed by Kraichnan. It is able to represent not only the energy containing range but also the inertial subrange capturing the 5/3 Kolmogorov's law and the exponential decay characteristic of the dissipation range.

Note that from a computational point of view, Eq. (2.9) is cheaper than Eq. (2.1) since it requires the generation of less random numbers, but the resulting velocity field is independent of time. In order to obtain temporal decorrelations, Bechara *et al.* proposed to form a time series by using a succession of independent realisations of the velocity field and then filtering these to obtain the desired loss of correlation in time.

2.1.1.3 Bailly *et al.*'s method

The velocity field, $\boldsymbol{u}$, generated with the method proposed by Bechara *et al.* in Eq. (2.9) does not include convection effects. This limitation has been addressed by Bailly *et al.* in Ref. [7] where the method proposed by Bechara *et al.* [8] has been modified by explicitly including time dependence and convection effects. Eq. (2.9) is modified to read

$$\boldsymbol{u}(\boldsymbol{x},t) = 2\sum_{n=1}^{N} v_n \cos[\boldsymbol{\kappa}_n\cdot(\boldsymbol{x}-t\boldsymbol{u}_c)+\psi_n+\omega_n t]\boldsymbol{\sigma}_n, \tag{2.15}$$

where $\boldsymbol{u}_c$ is the convection velocity and the random variable ω_n is the angular frequency of the n^{th} mode and is given by $\omega_n = \sqrt{2K/3}\kappa_n$. Convection effects are introduced by essentially considering a change of frame of reference.

In contrast with Bechara *et al.*, Bailly *et al.* chose to discretise the wavenumber range with the non-linear distribution

$$\kappa_n = \kappa_l + (\Delta\kappa_l)^{n-1}, \quad \text{for } n = 1,2,\ldots,N \text{ where } \Delta\kappa_l = \tfrac{\kappa_{kol}-\kappa_l}{N-1}, \tag{2.16}$$

A comparison of Bechara *et al.*'s and Bailly *et al.*'s methods performed by Billson *et al.* [5] shows that the distribution given by Eq. (2.16) is more appropriate than the logarithmic distribution proposed by Bechara *et al.*. As argued by Bechara *et al.*, a logarithmic distribution of the wavenumbers offers a better resolution of the spectrum for small wavenumbers corresponding to the most energy containing eddies. However, the error on the largest wavenumbers, which are poorly resolved, is amplified by the increasing $\Delta\kappa_n$ for larger wavenumbers in Eq. (2.13).

From a computational point of view Bailly *et al.*'s method is more efficient than Bechara *et al.*'s because in the former one velocity field needs to be computed for each time. However, Bechara *et al.*'s method requires the computation, storage and then filtering series of independent realisations of the velocity field for each time step.

A drawback of Bailly *et al.*'s method is that an extension to inhomogeneous turbulence is not straightforward, as argued by Omais *et al.* [4]. If $\boldsymbol{r}$ is a spatial separation and T is the time over which the averaging is performed, the spatial correlation tensor for the velocity field in the directions i and j and for a single mode n, R_{ijn}, can be written as

$$R_{ijn}(\boldsymbol{r}) = \frac{F}{T}\left\{1 - \left[\frac{\omega_n(\boldsymbol{x}) + \boldsymbol{\kappa}_n \cdot \boldsymbol{u}_c(\boldsymbol{x})}{\omega_n(\boldsymbol{x}+\boldsymbol{r}) + \boldsymbol{\kappa}_n \cdot \boldsymbol{u}_c(\boldsymbol{x}+\boldsymbol{r})}\right]^2\right\}^{-1}, \tag{2.17}$$

where F is a finite non-zero quantity. For an inhomogeneous turbulence the term in square brackets is different from one and therefore the spatial correlation tensor tends to zero as time increases, which is not physical.

2.1.1.4 Billson *et al.*'s method

Billson *et al.* [25] proposed a modification of the SNGR methods to model the time correlation of the turbulence. First, at each time step an auxiliary synthetic velocity field, $\boldsymbol{v}$, is defined using Bechara *et al.*'s [8] method but considering the wavenumber discretisation proposed by Bailly *et al.* [7]. Then, the time-dependent velocity field, $\boldsymbol{u}$, is obtained by solving the stochastic equation

$$\boldsymbol{u}(\boldsymbol{x}, t) = \alpha \boldsymbol{u}(\boldsymbol{x}, t - \Delta t) + \beta[\boldsymbol{v}(\boldsymbol{x}, t) + \boldsymbol{v}(\boldsymbol{x}, t - \Delta t)], \tag{2.18}$$

where $\alpha = \exp(-\Delta t/\tau)$, $\beta = A\sqrt{(1-\alpha^2)/2}$, Δt is the time step, τ is the integral time scale and A is an amplitude parameter that enables the control of the kinetic energy of the turbulence. Note that Eq. (2.18) models the time correlation of $\boldsymbol{u}$ as $\exp(-t/\tau)$.

Convection effects are introduced in Billson *et al.*'s method by solving the convection equation $\frac{\partial}{\partial t}\boldsymbol{u} + \frac{\partial}{\partial x_j}\left[(\boldsymbol{u}_c)_j \boldsymbol{u}\right] = \boldsymbol{0}$ for $\boldsymbol{u}(\boldsymbol{x}, t - \Delta t)$ prior to its use in Eq. (2.18).

In comparison with Bailly *et al.*'s method, this approach requires fewer Fourier modes to achieve a similar accuracy for the statistics since at each time step the velocity field $\boldsymbol{u}$ is the weighted sum of previous independent velocity fields $\boldsymbol{v}$. However, in contrast with Bailly *et al.*'s method, Billson *et al.*'s method requires the storage the auxiliary velocity field, $\boldsymbol{v}$, and the time-dependent velocity field, $\boldsymbol{u}$, from the previous time step.

2.1.2 Methods based on digital filters

Fourier-mode methods can be computationally demanding as they require a large number of modes and for each mode various random variables must be provided. In addition, they have problems representing inhomogeneous turbulence. In an attempt to improve computational efficiency, methods based on digital filters have been devised. The basic idea behind these methods is to filter white noise in order to obtain the velocity field of a turbulent flow with the desired properties. Therefore, the key with these methods is to define the appropriate filter.

2.1.2.1 Klein *et al.*'s method

Klein *et al.* [11] proposed a new approach to generate artificial inflow data reproducing first and second order one-point statistics as well as two-point correlations. This approach is based on filtering white noise and it is directly formulated in the discrete setting. The one-dimensional discrete filter-based method reads

$$v(x_m) = \sum_{n=-N}^{N} b_n r_{m+n}, \tag{2.19}$$

where r_m is a random series of white noise with zero mean and $\langle r_n \; r_m \rangle = \delta_{nm}$. b_n are the filter coefficients and N is the support of the filter. Eq. (2.19) is similar to finite difference stencil applied to a random field weighted by the filter coefficients.

From the definition of the velocity field in Eq. (2.19), a relation between the filter and the normalised autocorrelation of v can easily be derived,

$$R_{vv}(|x_{m+k} - x_m|) = \frac{\langle v(x_m) \; v(x_{m+k}) \rangle}{\langle v(x_m) \; v(x_m) \rangle} = \frac{\sum_{j=-N+k}^{N} b_j b_{j-k}}{\sum_{j=-N}^{N} b_j^2}. \tag{2.20}$$

Hence, the coefficients b_n of the filter have to be defined such that the velocity field has the desired autocorrelation. It is important to note that this equation is implicitly assuming filter coefficients that are independent of spatial position, and hence assuming homogeneity.

The simplest way to calculate the filter coefficients is by assuming a Gaussian shape for the autocorrelation

$$R_{vv}(r) = \exp\left(-\frac{\pi r^2}{4\lambda^2}\right), \tag{2.21}$$

where λ is the integral length scale. Without this simplification finding the filters is not trivial and for instance in semi-infinite domains the filters are not uniquely defined. A detailed description of the process to obtained the filter coefficients is presented in Ref. [26].

An extension to three dimensions is achieved by generating three independent one-dimensional velocity fields using Eq. (2.19). Different sets of filter coefficients may be considered in each direction so that the desired integral length scales are recovered.

A significant drawback of Klein *et al.*'s method is that it is based solely on the reproduction of statistical data and does not incorporate any information about the physics, apart from the two-point correlation. For instance, the velocity field is not even divergence-free as one would expect from an incompressible flow.

2.1.2.2 Careta *et al.*'s method

Careta *et al.* [9] presented a method that uses a random scalar field in order to obtain a two-dimensional, isotropic, stationary, and homogeneous stochastic velocity field. In contrast with Klein *et al.*'s method, the turbulent velocity field obtained with Careta *et al.*'s method is guaranteed to be divergence free. This is achieved by working in terms of the stream function, η, such that

$$\boldsymbol{u}(\boldsymbol{x},t) = \left(-\frac{\partial \eta}{\partial y}(\boldsymbol{x},t), \frac{\partial \eta}{\partial x}(\boldsymbol{x},t)\right)^{\mathrm{T}}. \tag{2.22}$$

The central point of this method is to define η in such a way that the synthetic velocity field has the required statistical properties. Careta *et al.* proposed to describe the temporal correlation by means of a stochastic differential equation known as Langevin equation [14]

$$\frac{\partial}{\partial t}\eta(\boldsymbol{x},t) = -\frac{1}{\tau}\eta(\boldsymbol{x},t) + \frac{Q[\lambda^2\nabla^2]}{\tau}\zeta(\boldsymbol{x},t), \tag{2.23}$$

where λ and τ are the spatial and temporal length scales respectively.

The first term in Eq. (2.23) is a linear drift coefficient that causes the velocity of η to relax toward zero on the time scale τ. The second term introduces a zero-mean random source whose standard deviation is controlled by the linear differential operator Q and $\zeta(\boldsymbol{r},t)$ is a Gaussian white noise with zero mean and correlation

$$\langle \zeta(\boldsymbol{x}_1,t_1)\ \zeta(\boldsymbol{x}_2,t_2)\rangle = 2\epsilon\delta(\boldsymbol{x}_1-\boldsymbol{x}_2)\delta(t_1-t_2), \tag{2.24}$$

with ϵ the intensity of the noise. The operator Q, which is written in terms of the Laplacian ∇^2, acts as a filter that controls the statistics of the turbulence, such as the correlation length. Eq. (2.23) also determines that the time correlation of the synthetic velocity field is exponential, $\exp(-t/\tau)$.

To identify the differential operator Q, it is convenient to work in the wavenumber space. In particular, by expressing the two-point two-time correlation of the velocity field $\boldsymbol{u}$ in terms the two-point two-time correlation of the stream function η, it is possible to relate

the operator Q with the energy spectrum of the turbulence yielding

$$E(\kappa) = \frac{\epsilon}{4\pi\tau}\kappa^3 Q^2[-\lambda^2\kappa^2]. \tag{2.25}$$

Therefore, Careta *et al.*'s method relies on finding an operator Q that yields the desired velocity field assuming that the intensity of the noise, the spatial and temporal correlation lengths, and the energy spectrum are prescribed.

The method by Careta *et al.* has the advantage of not being restricted to a specific energy spectrum, and more realistic expressions for the energy spectrum can be used instead of Gaussian spectrum. In addition, in contrast with Klein *et al.*'s method, the synthetic velocity field is divergence free but it does not include convection effects.

2.1.2.3 Ewert's method

A filter-based method able to reproduce the convection effects has been developed by Ewert [10] and is known as Random-Particle-Mesh (RPM) or Fast-Random-Particle-Mesh (FRPM) depending on the numerical implementation.

Ewert presented a new method to generate synthetic turbulence specifically for aeroacoustic applications with the aim of developing a fast and cheap stochastic approach to model unsteady turbulent sound sources [10]. The method has already been applied to a wide range of aeroacoustic problems in jet noise and broadband fan noise, see Ref. [27, 28, 29, 30].

The RPM method borrows ideas from Careta *et al.* [9] and Klein *et al.* [11]. From the former, the method expresses the velocity field in terms of a stream function and models the time correlation by solving a Langevin equation. From the latter, it uses the idea of filtering random data to obtain the stream function. Note that, in contrast with Careta *et al.*'s method, the filter is expressed in terms of a convolution product rather than as a differential operator. The result is a divergence-free velocity field able to reproduce the two-point two-time correlation tensor of locally homogeneous isotropic turbulence.

The RPM method generates a three-dimensional synthetic velocity field, $\boldsymbol{u}$, by expressing it in terms of a 3D stream function $\boldsymbol{\eta}$ such that each of its components is defined as

$$\eta_i(\boldsymbol{x}, t) = \int_{\mathbb{R}^3} G(|\boldsymbol{x} - \boldsymbol{x'}|) U_i(\boldsymbol{x'}, t) \mathrm{d}\boldsymbol{x'}, \tag{2.26}$$

with $i = 1, 2, 3$ and U_i are three independent white noise fields with zero mean. The filter G controls the spatial properties of the synthetic turbulence. Once it is discretised, the RPM method can by interpreted as a collection of random vortex particles. Each of these particles induces a velocity field and $\boldsymbol{u}$ is given by summing up their contributions.

In contrast with Careta *et al.*'s method, which is not restricted to a specific energy spectrum, the original RPM method is based on the assumption that the spatial correlation function of each η_i is Gaussian and therefore the corresponding energy spectrum is Gaussian. This assumption yields a filter of the form:

$$G(x) = A \exp\left(-\frac{\pi x^2}{2\lambda^2}\right), \tag{2.27}$$

where A is related with the kinetic energy of the turbulence and λ is the integral length scale of the turbulence.

The limitation of the original method to model only Gaussian energy spectra has been addressed by Siefert and Ewert in Ref. [15] where they proposed an extension of RPM to deal with non-Gaussian spectra by using a hierarchy of Gaussian filters. The extended method consists in superposing N independent velocity fields by defining the stream function as

$$\eta_i(\boldsymbol{x}, t) = \sum_{n=1}^{N} \int_{\mathbb{R}^3} G^{(n)}(|\boldsymbol{x} - \boldsymbol{x'}|) U_i^{(n)}(\boldsymbol{x'}, t) \mathrm{d}\boldsymbol{x'}, \tag{2.28}$$

where each filter $G^{(n)}$ is defined by Eq. (2.27) with amplitude factor A and the integral length scale λ chosen to describe a specific wavenumber range of the non-Gaussian energy spectrum. In order to include the different integral length scales to recreate non-Gaussian spectra, the number of vortices considered must therefore increase compared to the Gaussian spectrum.

Convection effects can be taken into account by stating that each stochastic field U_i follows a transport equation

$$\frac{\mathrm{D}_0}{\mathrm{D}t} U_i = 0, \tag{2.29}$$

where $\mathrm{D}_0/\mathrm{D}t = \partial/\partial t + \boldsymbol{u}_c \cdot \nabla$ is the material derivative and $\boldsymbol{u}_c$ is a given convection velocity. Assuming a constant convection velocity and Taylor's frozen turbulence hypothesis, for small spatial and temporal separation, $\boldsymbol{r} = \boldsymbol{x}_2 - \boldsymbol{x}_1$ and $t = |t_2 - t_1|$,

$$\langle U_i(\boldsymbol{x}_1, t_1) U_j(\boldsymbol{x}_2, t_2) \rangle = \delta(\boldsymbol{r} - \boldsymbol{u}_c t) \delta_{ij}. \tag{2.30}$$

In order to include the effects of time correlation, a similar method to that of Careta [9] is used. Each random field U_i is generated by solving a Langevin equation (see Ref. [28])

$$\frac{D_0}{Dt} U_i = \frac{1}{\tau} U_i + \sqrt{\frac{2}{\tau}} \zeta_i, \tag{2.31}$$

where τ is a Lagrangian integral time scale and ζ_i is a white noise field such that

$$\langle \zeta_i(\boldsymbol{x}, t) \rangle = 0, \quad \langle \zeta_i(\boldsymbol{x}_1, t_1)\ \zeta_j(\boldsymbol{x}_2, t_2) \rangle = \delta(\boldsymbol{r}) \delta(t) \delta_{ij}. \tag{2.32}$$

For small spatial separations $\boldsymbol{r}$ and temporal separations t, for which Taylor's hypothesis holds, each random field U_i has the properties

$$\langle U_i(\boldsymbol{x},t)\rangle = 0, \quad \langle U_i(\boldsymbol{x}_1,t_1)U_j(\boldsymbol{x}_2,t_2)\rangle = \delta(\boldsymbol{r}-\boldsymbol{u}_c t)\exp(-t/\tau)\delta_{ij}. \tag{2.33}$$

Note that the RPM method assumes an exponential correlation in time. This choice is supported by the measurements of Davis *et al.* [27]. Note also that if we assume $\tau \to \infty$, Eqs. (2.29) - (2.30) for frozen turbulence are recovered.

From a computational point of view, Ewert's method has some advantages. Gaussian filters are separable functions of each component of $\boldsymbol{x}$, and hence the velocity field can be computed by applying a one-dimensional filtering operation in each direction. In addition, only one set of random values needs to be generated for each realisation of the synthetic velocity field. This is in contrast with random Fourier-mode methods where various random variables have to be generated.

2.1.3 Methods to generate synthetic anisotropic turbulence

Methods to generate synthetic anisotropic turbulence are now reviewed. They follow a common scheme:

1. Obtain the desired statistical properties of the turbulence such as integral length and time scales and Reynolds stress $R_{ij} = \langle u_i\ u_j\rangle$.
2. Generate an auxiliary isotropic synthetic velocity field.
3. Apply a set of transformations to the auxiliary velocity field so that the resulting velocity field is anisotropic and recreates the required statistical properties.

The mean flow components, integral length and time scales and the Reynolds stresses can be either measured or predicted from RANS simulations. Reynolds stresses specified locally at any point can be estimated from the local turbulent kinetic energy and dissipation rates. A model commonly used for that purpose is a linear approach, however it has been shown by Omais *et al.* [4] that the use of a non-linear Reynolds stress tensor model can significantly improve the quality of the anisotropic synthetic turbulent field.

Lund *et al.* [31] presented a method to generate synthetic anisotropic turbulence to provide inflow conditions for LES. The proposed method generates three independent sequences of random numbers, v_i, $i = 1, 2, 3$ each with zero mean and unit variance and then applies the transformation $u_i = A_{ij}v_j$, where

$$\boldsymbol{A} = \begin{pmatrix} (R_{11})^{1/2} & 0 & 0 \\ R_{21}/A_{11} & (R_{22}-A_{21}^2)^{1/2} & 0 \\ R_{31}/A_{11} & (R_{32}-A_{21}A_{31})/A_{22} & \left(R_{32}-A_{31}^2-A_{32}^2\right)^{1/2} \end{pmatrix}, \tag{2.34}$$

to obtained the anisotropic velocity field $\boldsymbol{u}$. This basic procedure to recover Reynolds stresses does not however provide information on two-point correlations. A way of overcoming this problem is by generating random numbers which are correlated in space. For instance, the filter-based method by Klein *et al.*'s [11] can be used to generate the random numbers, and the resulting velocity field would have the desired integral length scale, Reynolds stresses and a Gaussian two-point correlation tensor.

A more sophisticated method to generate synthetic anisotropic turbulent flows has been presented by Smirnov *et al.* [32]. This method was used to generate anisotropic turbulence for initial and inlet boundary conditions for LES. Smirnov *et al.*'s method uses scaling and orthogonal transformation operations applied to isotropic turbulence, and takes as input the integral length and time scales of the turbulence, and the Reynolds stresses. The three-dimensional anisotropic turbulence is generated by Smirnov *et al.*'s method in three steps:

- Firstly the anisotropic correlation tensor $\boldsymbol{R}$ is diagonalised by writing $\boldsymbol{R} = \boldsymbol{A}^T\boldsymbol{C}\boldsymbol{A}$ with $\boldsymbol{C}$ the diagonal matrix of the eigenvalues. $\boldsymbol{R}$ being symmetric, the tensor $\boldsymbol{A}$ defines an orthogonal transformation associated with the principal directions of the correlation tensor.
- Secondly, a transient flow field $\boldsymbol{v}$ is generated. In their paper Smirnov *et al.* used a Fourier-mode technique similar to Kraichnan's [6] to generate the isotropic velocity field $\boldsymbol{v}$. However, this method to achieve anisotropic turbulence is not restricted to velocity fields obtained through random Fourier modes. One might prefer instead to generate the isotropic velocity field using a method based on digital filters.
- Finally, the anisotropic velocity field $\boldsymbol{u}$ is obtained through the relation: $\boldsymbol{u} = \boldsymbol{A}\boldsymbol{C}\boldsymbol{v}$.

Smirnov *et al.*'s is not only able to obtain an anisotropic turbulent velocity field, but it also preserves the incompressibility condition for locally homogeneous turbulence. Note that the derivatives of $\boldsymbol{C}$ can be neglected in the case of weakly inhomogeneous flows since they are slowly varying functions of position. The resulting anisotropic velocity field has the desired Reynolds stresses and integral length and time scales.

Billson *et al.*'s [33] used a method similar to Smirnov *et al.*'s to generate synthetic anisotropic turbulence for aeroacoustic purposes. In this case, an auxiliary isotropic velocity field is first generated using Bechara *et al.*'s [8] method. Then a series of transformations similar to those proposed by Smirnov *et al.* are applied to recover Reynolds stresses and length scales. Finally the filtering in time described in section 2.1.1.4 is performed to obtain a time-dependent, anisotropic velocity field.

2.2 Random-Vortex-Particle method

We now present the random-vortex-particle method used in this work to generate synthetic turbulent flows. It generates synthetic two-dimensional, isotropic, locally homogenous turbulent flows[1]. It requires as inputs some statistical properties of the turbulent flow such as energy spectrum, correlation, integral length scale and kinetic energy. These properties can be either modelled using empirical laws, measured or predicted from RANS simulations.

The method developed in this work is a filter-based method that builds upon the work of Careta *et al.* [9] and Ewert *et al.* [27, 28]. In both methods, the velocity field is defined in terms of a stream function that is obtained by filtering random data. In addition, both methods use a Langevin equation to model the temporal decorrelation of the velocity field. The main difference between them is the definition of the stream function; and in particular the filter that determines the stream function. Ewert's method enforces a Gaussian correlation, but the filter in Careta *et al.* is defined in terms of the energy spectrum.

The idea here is to combine both methods in the sense of being able to obtain a turbulent velocity field by providing either the correlation or the energy spectrum. Therefore, the resulting method is not restricted to any specific correlation or energy spectrum and convection effects and temporal correlations are captured. Special care will be made in the mathematical derivation of the equations involved.

We are interested in the generation of the velocity field, denoted by $\boldsymbol{u}'(\boldsymbol{x},t)$ with components $u'_x(\boldsymbol{x},t)$ and $u'_y(\boldsymbol{x},t)$, of an isotropic two-dimensional turbulent flow.

Assuming an incompressible flow, mass conservation is equivalent to a divergence-free condition. From Helmholtz decomposition (see Ref. [34]) we know that there exists a stream function, $\boldsymbol{\eta} = (0,0,\eta)$, such that

$$\boldsymbol{u}'(\boldsymbol{x},t) = \left(\frac{\partial \eta}{\partial y}(\boldsymbol{x},t), -\frac{\partial \eta}{\partial x}(\boldsymbol{x},t)\right)^{\mathrm{T}}. \tag{2.35}$$

This simplifies our problem by reducing the formulation to a scalar field.

Since the turbulent velocity field is written in terms of the stream function, our problem can be split into two parts: establishing the relationship between the statistics of the flow itself $\boldsymbol{u}'$ and those of the stream function η, and providing an appropriate method to describe the stream function.

[1] In chapter 6 the stochastic method is extended to deal with non-stationary inhomogeneous turbulent flows. The extension for three-dimensional anisotropic turbulence is discussed in Appendix A.

2.2.1 Spatial statistics of the stream function

In this section, the turbulence is assumed statistically stationary and locally homogeneous. Therefore the statistics of the turbulence are invariant under a shift in time and slow varying functions of position. In addition, we are only interested in the fluctuations so we look at the correlations independently of the mean flow.

The stationary spatial two-point correlation tensor of the velocity field $\boldsymbol{u}'$,

$$R_{ij}(\boldsymbol{r}) = \langle u_i'(\boldsymbol{x}_1, t)\ u_j'(\boldsymbol{x}_2, t)\rangle, \tag{2.36}$$

where $\boldsymbol{r} = \boldsymbol{x}_2 - \boldsymbol{x}_1$, is related to the stationary two-point correlation of the stream function η,

$$C(\boldsymbol{r}) = \langle \eta(\boldsymbol{x}_1, t)\ \eta(\boldsymbol{x}_2, t)\rangle. \tag{2.37}$$

Their relationship will provide the definition of the filter from which the model to generate synthetic turbulence used in this work is built.

For convenience, instead of working directly with the two-point correlation tensor, the trace of the correlation tensor R_{ij} is considered (see Ref. [9])

$$R(\boldsymbol{r}) = \frac{1}{2} R_{ii}(\boldsymbol{r}). \tag{2.38}$$

Inserting the definition of the turbulent velocity field in Eq. (2.35) into Eq. (2.36) and combining with Eq. (2.38) yields (see Appendix B.1)

$$R(\boldsymbol{r}) = -\frac{1}{2}\left[\frac{1}{r}\frac{\mathrm{d}C}{\mathrm{d}r}(r) + \frac{\mathrm{d}^2 C}{\mathrm{d}r^2}(r)\right]. \tag{2.39}$$

In isotropic turbulence, the statistics of the flow do not depend on direction but only on distance. As a consequence, the Fourier transform of the statistics into wavenumber space can be expressed in terms of the Bessel function of zeroth order J_0, (see Appendix B.2). In particular, the stationary two-point correlation of the stream function η can be written

$$C(r) = \frac{1}{4\pi^2}\int_{\mathbb{R}^2} \hat{C}(\boldsymbol{\kappa}) \exp(i\boldsymbol{\kappa}\cdot\boldsymbol{r})\mathrm{d}\boldsymbol{\kappa} = \frac{1}{2\pi}\int_0^\infty \kappa \hat{C}(\boldsymbol{\kappa})\mathrm{J}_0(\kappa r)\mathrm{d}\kappa, \tag{2.40}$$

where κ is the wavenumber associated with the wave vector $\boldsymbol{\kappa}$ and $\hat{C}$ stands for the Fourier transform of C in wavenumber space. Hence, using Eq. (2.40) it is possible to simplify the expression for $R(r)$:

$$R(r) = \frac{1}{8\pi}\int_0^\infty \kappa^3 \hat{C}(\boldsymbol{\kappa})\left[\frac{2}{\kappa r}\mathrm{J}_1(\kappa r) + \mathrm{J}_0(\kappa r) - \mathrm{J}_2(\kappa r)\right]\mathrm{d}\kappa. \tag{2.41}$$

Using the relation $\mathrm{J}_1(\kappa r) = \kappa r \left[\mathrm{J}_0(\kappa r) + \mathrm{J}_2(\kappa r)\right]/2$ yields

$$R(r) = \frac{1}{4\pi} \int_0^\infty \kappa^3 \hat{C}(\boldsymbol{\kappa}) \mathrm{J}_0(\kappa r) \mathrm{d}\kappa. \tag{2.42}$$

Due to the relation between the Fourier transform and Bessel functions in isotropy and comparing with Eq. (2.40) we get:

$$\hat{R}(\boldsymbol{\kappa}) = \frac{1}{2}\kappa^2 \hat{C}(\boldsymbol{\kappa}), \tag{2.43}$$

which represents the relation between the correlation of the turbulent velocity field and the correlation of the stream function η in wavenumber space.

By assuming isotropic homogeneity, the stationary spatial two-point correlation tensor of the velocity field $\boldsymbol{u}'$, R_{ij}, can be written in terms of the lateral, $f(r)$, and longitudinal, $g(r)$, autocorrelation functions as

$$R_{ij}(\boldsymbol{r}) = \left[f(r) - g(r)\right] n_i n_j + g(r)\delta_{ij}, \tag{2.44}$$

where $r = |\boldsymbol{r}|$, the vector components n_i stand for the unit vector in the $\boldsymbol{r}_2 - \boldsymbol{r}_1$ direction and δ_{ij} is the Kronecker symbol. Note that

$$R_{11}(r\boldsymbol{e}_1) = f(r), \quad R_{22}(r\boldsymbol{e}_1) = g(r), \tag{2.45}$$

where $\boldsymbol{e}_1 = (1, 0)$. Using continuity in 2D we can relate f and g via

$$g(r) = f(r) + r\frac{\mathrm{d}f}{\mathrm{d}r}(r). \tag{2.46}$$

By relating Eq. (2.36) with Eqs. (2.45) and (2.46) (see Appendix B.3), we can give explicit expressions for f and g in terms of the stationary two-point correlation C of the stream function η:

$$f(r) = -\frac{1}{r}\frac{\mathrm{d}C}{\mathrm{d}r}(r), \quad g(r) = -\frac{\mathrm{d}^2 C}{\mathrm{d}r^2}(r). \tag{2.47}$$

It will also be useful to derive the relation between the energy spectrum, denoted as $E(\kappa)$, and the correlation of the stream function. To do so, R will be related to $E(\kappa)$ through the velocity spectrum, $\phi_{ij}(\boldsymbol{\kappa})$.

On the one hand, the velocity spectrum is defined in homogeneous turbulence as the Fourier transform of the correlation $R_{ij}(\boldsymbol{r})$ [14]:

$$\phi_{ij}(\boldsymbol{\kappa}) = \int_{\mathbb{R}^2} R_{ij}(\boldsymbol{r}) \exp(-i\boldsymbol{\kappa} \cdot \boldsymbol{r}) \mathrm{d}\boldsymbol{r}. \tag{2.48}$$

Hence, the Fourier transform of Eq. (2.38) is $\hat{R}(\boldsymbol{\kappa}) = \phi_{ii}(\boldsymbol{\kappa})/2$, which yields when comparing with Eq. (2.43)

$$\phi_{ii}(\boldsymbol{\kappa}) = \kappa^2 \hat{C}(\boldsymbol{\kappa}). \tag{2.49}$$

On the other hand, the energy spectrum is defined in terms of the velocity spectrum as [14]

$$E(\kappa) = \frac{1}{4\pi^2} \oint \frac{1}{2} \phi_{ii}(\boldsymbol{\kappa}) \mathrm{d}S(\kappa), \tag{2.50}$$

where $S(\kappa)$ denotes the circle in the wavenumber space of radius κ centred at the origin. Hence

$$E(\kappa) = \frac{1}{4\pi} \kappa \phi_{ii}(\boldsymbol{\kappa}). \tag{2.51}$$

Inserting Eq. (2.49) into Eq. (2.51) we finally get the relation between the correlation of the stream function and the energy spectrum

$$E(\kappa) = \frac{1}{4\pi} \kappa^3 \hat{C}(\boldsymbol{\kappa}). \tag{2.52}$$

2.2.2 Stochastic model

Now that the statistics of the turbulent velocity field have been defined in terms of those of the stream function, an appropriate method to define the stream function needs to be provided.

Following Ewert's *et al.* [28] approach, a two-dimensional turbulent flow can be obtained when the stream function η is generated by filtering a random field. This can be written as

$$\eta(\boldsymbol{x}, t) = \int_{\mathbb{R}^2} G(|\boldsymbol{x} - \boldsymbol{x}'|, t) U(\boldsymbol{x}', t) \mathrm{d}\boldsymbol{x}', \tag{2.53}$$

where G is the filter and U is a random field that controls the temporal properties of the turbulence.

The stochastic field U is defined as zero-mean white noise field in space:

$$\langle U(\boldsymbol{x}, t) \rangle = 0, \quad \langle U(\boldsymbol{x}_1, t)\, U(\boldsymbol{x}_2, t) \rangle = \delta(\boldsymbol{x}_2 - \boldsymbol{x}_1). \tag{2.54}$$

$R_U(t) = \langle U(\boldsymbol{x}, t_1)\, U(\boldsymbol{x}, t_2) \rangle$ denotes the time correlation of U with $t = |t_2 - t_1|$. For small spatial and temporal separation, for which Taylor's frozen turbulence hypothesis holds (the scale for the turbulence dynamics is large compared to the passage time) U satisfies the following properties:

$$\langle U(\boldsymbol{x}, t) \rangle = 0, \quad \langle U(\boldsymbol{x}_1, t_1)\, U(\boldsymbol{x}_2, t_2) \rangle = \delta(\boldsymbol{r} - t\boldsymbol{u}_c) R_U(t), \tag{2.55}$$

If the turbulence is assumed to be frozen (the integral time scale of the turbulence tends to infinity), then the time correlation of U is independent of the temporal separation and only convection effects are included in the model. Therefore

$$\frac{\mathrm{D}_0}{\mathrm{D}t}U = 0, \tag{2.56}$$

where $\mathrm{D}_0/\mathrm{D}t = \partial/\partial t + \boldsymbol{u}_c \cdot \nabla$ with $\boldsymbol{u}_c$ the convection velocity. This yields $R_U(t) = 1$. The convection velocity of the flow, $\boldsymbol{u}_c$, is an input parameter of the stochastic method. This parameter can be provided by RANS or LES simulations or by measurements.

However, in addition to convection effects, there is a loss of correlation in time due to the turbulent mixing. Effects of time decorrelation in turbulent flows can be introduced in the method by assuming $\mathrm{D}_0U/\mathrm{D}t \neq 0$. This yields a correlation for U which is a function of temporal separation. A common way to model the time-dependence present in turbulent flows is to use Langevin models [14]. A detailed discussion on how to include the effects of loss of correlation in time in the method proposed in this work to generate synthetic turbulence can be found in chapter 5.

The expression of the synthetic velocity field, $\boldsymbol{u'}$, can be recovered when rewriting the correlation of η in terms of the filter G. This is done by combining Eq. (2.53) and Eq. (2.55) (see Appendix B.4) to get

$$C(r,t) = (G * G)(|\boldsymbol{r} - t\boldsymbol{u}_c|, t)R_U(t), \tag{2.57}$$

where $*$ represents the convolution operator in space. R_U models the loss of correlation in time. The term $\boldsymbol{r} - t\boldsymbol{u}_c$ introduces the convection effects in the correlation. Since the effect of a uniform flow is equivalent to that of a change of frame of reference, considering a frame of reference associated with the mean flow we have

$$C(r,t) = (G * G)(r,t)R_U(t), \quad \hat{C}(\kappa,t) = \hat{G}(\kappa,t)^2 R_U(t). \tag{2.58}$$

Note that the analysis in the previous section was carried out in a frame of reference moving with the mean flow. Time evolution of $\boldsymbol{u'}$ is fully specified by $R_U(t)$ and spatial statistics are characterised by the filter.

The expression of the filter in the wavenumber space is found when inserting Eq. (2.58) into Eq. (2.43) or into Eq. (2.52) yielding

$$\hat{R}(\kappa) = \frac{1}{2}\kappa^2\hat{G}(\kappa)^2, \quad E(\kappa) = \frac{1}{4\pi}\kappa^3\hat{G}(\kappa)^2. \tag{2.59}$$

The filter in physical space can be obtained by applying the inverse Fourier transform to Eq. (2.59) to get

$$G(r) = \frac{1}{\sqrt{2}\pi} \int_0^\infty \hat{R}(\kappa)^{1/2} \mathrm{J}_0(\kappa r) \mathrm{d}\kappa, \quad G(r) = \frac{1}{\sqrt{\pi}} \int_0^\infty \left(\frac{E(\kappa)}{\kappa} \right)^{1/2} \mathrm{J}_0(\kappa r) \mathrm{d}\kappa. \tag{2.60}$$

To summarise, the synthetic velocity field $\boldsymbol{u}'$ can be defined in terms of a prescribed energy spectrum or a prescribed correlation function by

$$u'_x(\boldsymbol{x}, t) = \frac{\partial}{\partial y} \int_{\mathbb{R}^2} G(|\boldsymbol{x} - \boldsymbol{x}'|) U(\boldsymbol{x}', t) \mathrm{d}\boldsymbol{x}', \tag{2.61a}$$

$$u'_y(\boldsymbol{x}, t) = -\frac{\partial}{\partial x} \int_{\mathbb{R}^2} G(|\boldsymbol{x} - \boldsymbol{x}'|) U(\boldsymbol{x}', t) \mathrm{d}\boldsymbol{x}', \tag{2.61b}$$

where G is a function satisfying either of the expressions in Eq. (2.60) and the random field U is completely specified by Eq. (2.56) if the turbulence is assumed frozen. A more general expression of U that accounts for the influence of the integral time scale of the flow is provided in chapter 5.

2.3 Numerical implementation

In this section, numerical discretisation of the equations following a grid-based scheme and a Lagrangian approach are discussed. So far the method has been derived in a continuous frame, but once it is discretised the synthetic turbulence can be interpreted as a cloud of vortices with random strengths as it will be shown in section 2.3.1.

With a grid-based discretisation vortices are only located at grid points. In contrast, in a Lagrangian discretisation vortices are convected with the base flow independently of the grid points and two implementations can be considered to compute the induced velocity field. In the first implementation the vorticity is interpolated onto an auxiliary grid, which is then used to compute the velocity field. This approach is followed by Ewert [30]. In the second implementation, the velocity field is computed using directly the vortices locations. We refer to this implementation as a purely Lagrangian approach. From a computational point of view, for the particular application considered here, one could argue that a purely Lagrangian discretisation yields a cheaper and faster simulation. Vorticity does not need to be interpolated onto an auxiliary grid and although the computation of the velocity field could be optimised by having the vorticity located at specific grid points, in this case it is not relevant since the velocity field is just computed at a few grid points that are nearby. The benefits of a purely Lagrangian approach could drastically increase when using more complex geometries (and therefore more complex grids) and non-uniform mean flows.

We briefly use a grid-based discretisation for validating the random-vortex-particle method, but for the application of the method we move to a Lagrangian approach.

2.3.1 Lagrangian discretisation

A novelty of the method to generate synthetic turbulence used in this work is that it is discretised in a purely Lagrangian approach. This discretisation will be used to combine the linearised Euler equations and the synthetic turbulence. Therefore, the synthetic velocity field will be computed independently of the grid used to discretise the simulation domain.

The following notation is introduced in order to rewrite Eq. (2.61) in a Lagrangian formulation. Each fluid element in the region $\mathbb{S}_0$ at an initial time t_0 follows a trajectory given by $\boldsymbol{x}'(\boldsymbol{x}_0, t)$, where $\boldsymbol{x}_0(\boldsymbol{x}', t)$ is its starting point and $J = |\mathrm{d}\boldsymbol{x}'/\mathrm{d}\boldsymbol{x}_0|$ the corresponding Jacobian (note that for incompressible flows $J = 1$).

The fluctuating component of the turbulent velocity field for a fixed frame of reference is obtained using the method to generate synthetic turbulence by the expression

$$\boldsymbol{u}'(\boldsymbol{x}, t) = \int_{\mathbb{R}^2} \boldsymbol{G}(|\boldsymbol{x} - \boldsymbol{x}'|) U(\boldsymbol{x}', t) \mathrm{d}\boldsymbol{x}', \tag{2.62}$$

where $\boldsymbol{G} = (\partial G/\partial y, -\partial G/\partial x)^{\mathrm{T}}$. Using the above notation, it can be rewritten in a Lagrangian formulation yielding

$$\boldsymbol{u}'(\boldsymbol{x}, t) = \int_{\mathbb{S}_0} \boldsymbol{G}(|\boldsymbol{x} - \boldsymbol{x}'(\boldsymbol{x}_0, t)|, K(\boldsymbol{x}'), \lambda(\boldsymbol{x}')) U(\boldsymbol{x}_0, t) J \mathrm{d}\boldsymbol{x}_0. \tag{2.63}$$

Note that here we are making explicit the dependence of the filter on the kinetic energy, K, and the integral length scale, λ, of the fluid. In addition, both quantities are said to depend on the position $\boldsymbol{x}'$ and not on $\boldsymbol{x}$. While this is not necessary for homogeneous turbulent flows (statistics are not dependent on position), it is crucial for inhomogeneous turbulent flows. This will be addressed in chapter 6 where inhomogeneous, non-stationary turbulence is considered.

By describing the volume $\mathbb{S}_0$ using elements $\{\mathbb{S}_{0n}\}_{n=1}^{N}$, Eq. (2.63) can be written

$$\boldsymbol{u}'(\boldsymbol{x}, t) = \sum_{n=1}^{N} \int_{\mathbb{S}_{0n}} \boldsymbol{G}(|\boldsymbol{x} - \boldsymbol{x}'(\boldsymbol{x}_0, t)|, K(\boldsymbol{x}'), \lambda(\boldsymbol{x}')) U(\boldsymbol{x}_0, t) J \mathrm{d}\boldsymbol{x}_0. \tag{2.64}$$

Each element $\mathbb{S}_{0n}$ can be understood as a small fluid element whose trajectory is given by $\boldsymbol{x}'(\boldsymbol{x}_0, t)$.

If the fluid elements $\mathbb{S}_{0n}$ are small compared to the integral length scale $\lambda(\boldsymbol{x}_n)$, it is possible to consider that $\boldsymbol{G}$ is almost constant over each $\mathbb{S}_{0n}$, yielding the following

approximation

$$\boldsymbol{u}'(\boldsymbol{x},t) = \sum_{n=1}^{N} \boldsymbol{G}(|\boldsymbol{x} - \boldsymbol{x}_n(t)|, K(\boldsymbol{x}_n), \lambda(\boldsymbol{x}_n)) \int_{\mathbb{S}_{0n}} U(\boldsymbol{x}_0,t) J \mathrm{d}\boldsymbol{x}_0, \tag{2.65}$$

where $\boldsymbol{x}_n$ is the position of $\mathbb{S}_{0n}$ as it moves across the domain. $\boldsymbol{x}_n$ can be defined as the barycenter of $\mathbb{S}_{0n}$

$$\boldsymbol{x}_n = \int_{\mathbb{S}_{0n}} \boldsymbol{x}'(\boldsymbol{x}_0,t) J \mathrm{d}\boldsymbol{x}_0. \tag{2.66}$$

Finally, Eq. (2.65) can be rewritten as

$$\boldsymbol{u}'(\boldsymbol{x},t) = \sum_{n=1}^{N} \boldsymbol{G}(|\boldsymbol{x} - \boldsymbol{x}_n(t)|, K(\boldsymbol{x}_n), \lambda(\boldsymbol{x}_n)) U_n(t), \tag{2.67}$$

by defining U_n as the weighted average of U over the fluid element $\mathbb{S}_{0n}$

$$U_n(t) = \int_{\mathbb{S}_{0n}} U(\boldsymbol{x}_0,t) J \mathrm{d}\boldsymbol{x}_0. \tag{2.68}$$

Therefore, the synthetic turbulent velocity field at $\boldsymbol{x}$ can be interpreted as the sum of N vortices such that the n^{th} vortex is located at $\boldsymbol{x}_n$. The velocity distribution induced by each vortex depends on the distance between the vortex and the observer and the integral length scale of the flow λ, and has strength U_n.

For the case of frozen turbulence, for an observer moving with the base flow the value of $U(\boldsymbol{x}_0,t)$ is constant with respect to time yielding a constant expression for the strength of the vortices. By frozen turbulence we are then not just stating that the statistics of the turbulence are frozen, but also the turbulent velocity field is frozen with respect to an observer moving with the base flow.

If including the effects of time correlation in the random-vortex-particle method, the expression of $U(\boldsymbol{x}_0,t)$ is time dependent. The time variation of U_n controls the temporal decorrelation of the turbulence and it is usually modelled by a Langevin equation [14]. See chapter 5 for further details on the implementation of evolving turbulence.

In this thesis we consider uniform mean flows in which case the Jacobian is unit simplifying Eqs. (2.66) and (2.68). In addition, the volume $\mathbb{S}_0$ can be described using N fluid elements $\mathbb{S}_{0n}$ of equal size meaning that the the initial strength of the vortex particles can be picked from the same distribution.

More general cases can also be considered. For incompressible non-uniform mean flows, more care is required to establish the size of each fluid element $\mathbb{S}_{0n}$. In addition, the mean flow has to be interpolated onto the CAA grid which can then be used to get the mean flow at each vortex location. For compressible flows, the Jacobian is not expected to strongly vary over each fluid element and hence the vortex locations $\boldsymbol{x}_n$ defined in

Eq. (2.66) and their strength U_n in Eq. (2.68) can be obtained by:

$$\boldsymbol{x}_n(t) = \bar{J}_n(t) \int_{\mathbb{S}_{0n}} \boldsymbol{x}'(\boldsymbol{x}_0, t) \mathrm{d}\boldsymbol{x}_0, \quad U_n(t) = \bar{J}_n(t) \int_{\mathbb{S}_{0n}} U(\boldsymbol{x}_0, t) \mathrm{d}\boldsymbol{x}_0, \tag{2.69}$$

where $\bar{J}_n(t)$ is the average of the Jacobian over the fluid element $\mathbb{S}_{0n}$ at time t. This implies that for each vortex particle its initial strength is stochastically generated and then at each time its strength and current location is deterministically modified to accommodate for the change in volume of the fluid element.

2.3.2 Grid-based discretisation

A grid-based discretisation is used in this work for a preliminary validation of the numerical method which serves as a proof of concept, see section 2.5. The random-vortex-particle method in Eq. (2.61) is discretised here assuming filters separable in space and neglecting convection effects. A parametric study to assess the error introduced when approximating the continuous method with the grid-based discrete method is also included in this section.

2.3.2.1 Discretisation

The grid-based discrete version of Eq. (2.61) is now derived under the assumption that the filter is a separable function of x and y, $G(x, y) = G_x(x)G_y(y)$.

The continuous model in Eq. (2.61) can then be rewritten as

$$u'_x(x, y) = \int_{-\infty}^{\infty} F_x(x - x') \left[\int_{-\infty}^{\infty} F_y(y - y') U(x', y') \mathrm{d}y' \right] \mathrm{d}x', \tag{2.70a}$$

$$u'_y(x, y) = \int_{-\infty}^{\infty} H_x(x - x') \left[\int_{-\infty}^{\infty} H_y(y - y') U(x', y') \mathrm{d}y' \right] \mathrm{d}x', \tag{2.70b}$$

where

$$F_x(x) = G_x(x), \quad F_y(y) = \frac{\partial G_y}{\partial y}(y), \quad H_x(x) = -\frac{\partial G_x}{\partial x}(x), \quad H_y(y) = G_y(y). \tag{2.71}$$

Considering non-uniform Cartesian grids $\{x_p\}_{p=-\infty}^{\infty}$ and $\{y_q\}_{q=-\infty}^{\infty}$ in the x and y-directions respectively, and assuming fine grids compared to the variation of F_x, F_y, H_x and H_y, Eq. (2.70) can be approximated at the grid point (x_n, y_m) by

$$u'_x(x_n, y_m) = \sum_{q=-M_1}^{M_1} \sum_{p=-N_1}^{N_1} F_y(y_n - y_q) F_x(x_n - x_p) r(x_p, y_q), \tag{2.72a}$$

$$u'_y(x_n, y_m) = \sum_{q=-M_2}^{M_2} \sum_{p=-N_2}^{N_2} H_y(y_n - y_q) H_x(x_n - x_p) r(x_p, y_q). \tag{2.72b}$$

The quantity $r(x_p, y_q)$ is a random value obtained by averaging the stochastic field U over the grid spacing

$$r(x_p, y_q) = \int_{-\frac{\triangle_{q-1}}{2}}^{\frac{\triangle_q}{2}} \int_{-\frac{\triangle_{p-1}}{2}}^{\frac{\triangle_p}{2}} U(\tilde{x}, \tilde{y}) \mathrm{d}\tilde{x} \mathrm{d}\tilde{y}, \tag{2.73}$$

where $\triangle_p$ stands for the distance between the grid points x_p and x_{p+1} and $\triangle_q$ for the distance between y_q and y_{q+1}. Straightforward algebra using the properties of U yields

$$\langle r(x_p, y_q) \rangle = 0, \quad \langle r(x_p, y_q)\ r(x_{p'}, y_{q'}) \rangle = \frac{(\triangle_p + \triangle_{p-1})(\triangle_q + \triangle_{q-1})}{4} \delta_{pp'} \delta_{qq'}. \tag{2.74}$$

Note that in principle the summations in Eq. (2.72) should be infinity but in practice they are approximated by the finite quantities M_1, M_2, N_1 and N_2.

The set of equations in Eq. (2.72) can be seen as a finite difference stencil applied to the random field r where F_x, F_y, H_x, and H_y act as weights.

2.3.2.2 Analysis of the numerical error

In this section, the level of error incurred by approximating the continuous equations defining $\boldsymbol{u}'$ in Eq. (2.61) by their discrete version in Eq. (2.72) is assessed.

An analysis of the effect of truncation and discretisation over the correlation and energy spectrum is carried out to determine the error. Since the filter is assumed to be a separable function following the same behaviour in x and y directions, this analysis is performed in one dimension. In this case, the analytical expression of the stream function is

$$\eta(x) = \int_{-\infty}^{\infty} G(x - x') U(x') dx', \tag{2.75}$$

and the expressions of the correlation and the energy spectrum in wavenumber space are respectively

$$\hat{C}(\kappa) = \hat{G}(\kappa)^2, \quad E(\kappa) = \frac{1}{4\pi} \kappa^3 \hat{G}(\kappa)^2, \tag{2.76}$$

where $\hat{G}$ stands for the one-dimensional filter in wavenumber space.

The effects of truncation can be represented by a 'window' function with width A

$$w_A(x) = \begin{cases} 1 & \text{if } -A < x < A \\ 0 & \text{otherwise} \end{cases} \tag{2.77}$$

that when applied to the filter makes its support finite. Therefore, Eq. (2.75) can be approximated by

$$\eta(x) \approx \int_{-\infty}^{\infty} w_A(x')G(x')U(x+x')\mathrm{d}x'. \tag{2.78}$$

It this case, the correlation and the energy spectrum are given by the convolution of the filter and the window function as

$$\hat{C}(\kappa) \approx (\hat{G} * \hat{w}_A)(\kappa)^2, \quad E(\kappa) \approx \frac{1}{4\pi}\kappa^3(\hat{G} * \hat{w}_A)(\kappa)^2. \tag{2.79}$$

The error derived from the discretisation of the problem can also be taken into account by introducing the Dirac comb function weighted by the grid spacing

$$D(x) = \sum_{n=-\infty}^{\infty} \frac{\triangle_{n-1} + \triangle_n}{2}\, \delta(x - x_n). \tag{2.80}$$

Substituting the filter G in Eq. (2.75) by DG, the stream function reads

$$\eta(x) \approx \sum_{n=-\infty}^{\infty} \frac{\triangle_{n-1} + \triangle_n}{2}\, G(x_n)U(x+x_n). \tag{2.81}$$

Consequently, the correlation and the energy spectrum are recovered through

$$\hat{C}(\kappa) \approx (\hat{G} * \hat{D})(\kappa)^2, \quad E(\kappa) \approx \frac{1}{4\pi}\kappa^3(\hat{G} * \hat{D})(\kappa)^2. \tag{2.82}$$

In order to evaluate both effects at a time, the infinite sum in Eq. (2.80) is truncated

$$D(x) = \sum_{n=-M}^{M} \frac{\triangle_{n-1} + \triangle_n}{2}\, \delta(x - x_n), \quad \text{where} \quad A = \frac{1}{2}\sum_{i=-M}^{M-1} \triangle_i. \tag{2.83}$$

This can be understood as applying the window function w_A to the Dirac comb function D instead of directly to the filter. By comparing Eq. (2.82) against the corresponding theoretical expressions in Eq. (2.76), it is possible to perform a parametric study that enables us to measure the level of error introduced by the discretisation of the method. This analysis will be performed in section 2.5.3.

2.4 Extension to non-Gaussian energy spectra

The random-vortex-particle method described in section 2.2 requires as input either the correlation tensor or the energy spectrum of the turbulence. For each choice of these functions a different filter will be obtained, see Eq. (2.60). In this section, we focus on the advantages and disadvantages of selecting different energy spectra, and hence different filters, for two-dimensional turbulent flows.

So far, most methods using filtered random data have been based on Gaussian filters, yielding Gaussian correlation and Gaussian spectra. For turbulence modelling, and especially for broadband fan noise considered in this work, it is more common to use Liepmann and von Kármán spectra.

The use of Gaussian filters does not restrict the synthetic velocity field to Gaussian energy spectrum as shown by Siefert and Ewert in Ref. [15]. By superimposing a collection of Gaussian filters with different length scales non-Gaussian energy spectra are recovered. Such a procedure has a higher computational cost when reproducing non-Gaussian spectra instead of Gaussian spectrum since a much larger number of vortices is required.

A different approach from that of Siefert and Ewert is considered in this work. Instead of superimposing Gaussian filters to obtain non-Gaussian spectra, non-Gaussian filters are directly used. Expressions for the filter required by the method to generate synthetic turbulence used in this work corresponding to the Gaussian, Liepmann and von Kármán spectra are now derived and the main differences are then discussed.

2.4.1 Gaussian spectrum

Kraichnan proposed to simulate a 2D energy spectrum in Ref. [6] with a Gaussian shape function given by

$$E_g(\kappa) = \frac{2}{\pi^2} K \lambda^4 \kappa^3 \exp\left(-\frac{\lambda^2 \kappa^2}{\pi}\right), \tag{2.84}$$

where K is the kinetic energy and λ the integral length scale.

Comparing the latter expression in Eq. (2.59) and Eq. (2.84), the filter in wavenumber space is found to be

$$\hat{G}_g(\kappa) = 2\lambda^2 \sqrt{\frac{2K}{\pi}} \exp\left(-\frac{\lambda^2 \kappa^2}{2\pi}\right). \tag{2.85}$$

Using the relation Eq. (2.40) between the Fourier transform and the Bessel function for two-dimensional isotropic flows, the filter in physical space reads

$$G_g(r) = \sqrt{\frac{2K}{\pi}} \exp\left(-\frac{\pi r^2}{2\lambda^2}\right). \tag{2.86}$$

From a computational point of view, the filter given by Eq. (2.86) provides a good computational performance. Gaussian filters are separable functions of x and y. Hence the filtering procedure can be successively applied in each direction. This yields a more efficient method.

2.4.2 Liepmann spectrum

Liepmann proposed to represent the energy spectrum of a turbulent flow in wavenumber space by

$$E_l(\kappa) = \frac{16}{3\pi} K\lambda^5 \frac{\kappa^4}{\left(1+\lambda^2\kappa^2\right)^3}. \tag{2.87}$$

The Liepmann spectrum provides a better representation of the energy-containing range than the Gaussian energy spectrum.

The filter corresponding to the Liepmann spectrum is obtained by inserting Eq. (2.87) into the latter expression in Eq. (2.59), which yields in the wavenumber space

$$\hat{G}_l(\kappa) = 8\lambda^2 \sqrt{\frac{K\lambda}{3}} \frac{\kappa^{1/2}}{\left(1+\lambda^2\kappa^2\right)^{3/2}}. \tag{2.88}$$

Using Eq. (2.60), the filter in physical space reads

$$G_l(r) = \frac{4}{\pi}\sqrt{\frac{K}{3}}\left[\frac{\Gamma(1/4)\Gamma(5/4)}{\sqrt{\pi}}\ {}_1\mathrm{F}_2\left(\frac{5}{4};\frac{3}{4},1;\frac{r^2}{4\lambda^2}\right) - \frac{\Gamma(3/4)}{\Gamma(5/4)}\sqrt{\frac{2r}{\lambda}}\ {}_1\mathrm{F}_2\left(\frac{3}{2};\frac{5}{4},\frac{5}{4};\frac{r^2}{4\lambda^2}\right)\right], \tag{2.89}$$

where Γ is the gamma function and ${}_1\mathrm{F}_2$ stands for the generalised hypergeometric function with parameters $p = 1$ and $q = 2$ (see Ref. [35]).

2.4.3 Von Kármán spectrum

The von Kármán spectrum is recognised as giving a better fit to measured turbulence spectra than Liepmann and Gaussian models. It is able to recreate the energy containing range and the inertial subrange capturing the $-5/3$ Kolmogorov's law. Its expression is given by

$$E_k(\kappa) = \frac{110}{27\pi} K\lambda\varsigma^4 \frac{\kappa^4}{\left(1+\varsigma^2\kappa^2\right)^{17/6}}, \tag{2.90}$$

where $\varsigma = \dfrac{\Gamma(1/3)}{\sqrt{\pi}\Gamma(5/6)}\lambda$. Comparing the latter expression in Eq. (2.59) and Eq. (2.90), the filter in wavenumber space is

$$\hat{G}_k(\kappa) = \frac{2}{3}\sqrt{\frac{110K\lambda}{3}}\varsigma^2 \frac{\kappa^{1/2}}{\left(1+\varsigma^2\kappa^2\right)^{17/12}}. \tag{2.91}$$

Inserting Eq. (2.90) into the latter expression in Eq. (2.60) the filter reads in physical space

$$G_k(r) = \frac{1}{\pi}\sqrt{\frac{110K\lambda}{3\varsigma}}\left[\frac{\Gamma(7/6)\Gamma(5/4)}{\Gamma(17/12)}\ {}_1\mathrm{F}_2\left(\frac{5}{4};\frac{5}{6},1;r_*^2\right) - \frac{\Gamma(5/6)}{\Gamma(7/6)} r_*^{1/3}\ {}_1\mathrm{F}_2\left(\frac{17}{12};\frac{7}{6},\frac{7}{6};r_*^2\right)\right], \tag{2.92}$$

where $r_* = r/(2\varsigma)$.

2.4.4 Discussion

So far most of the methods to generate synthetic turbulence based on filtering random data have considered only Gaussian filters, so it is worth discussing the differences with von Kármán and Liepmann filters. The three energy spectra considered in this work are depicted in Figure 2.1 for the same kinetic energy, K, and integral length sale, λ.

The von Kármán spectrum provides the best fit to measured turbulence spectra of the three models considered here decaying with a slope of $-5/3$ in the inertial subrange. The Liepmann spectrum represents a good fit to real energy spectra but does not account for the $-5/3$ Kolmogorov's law in the inertial subrange. Gaussian spectrum is not able to approximate the inertial subrange due to the fast decay of the exponential function. The loss of energy captured by the Gaussian energy spectrum at the universal subrange is compensated by a higher peak, so that they all achieve the same target value of kinetic energy.

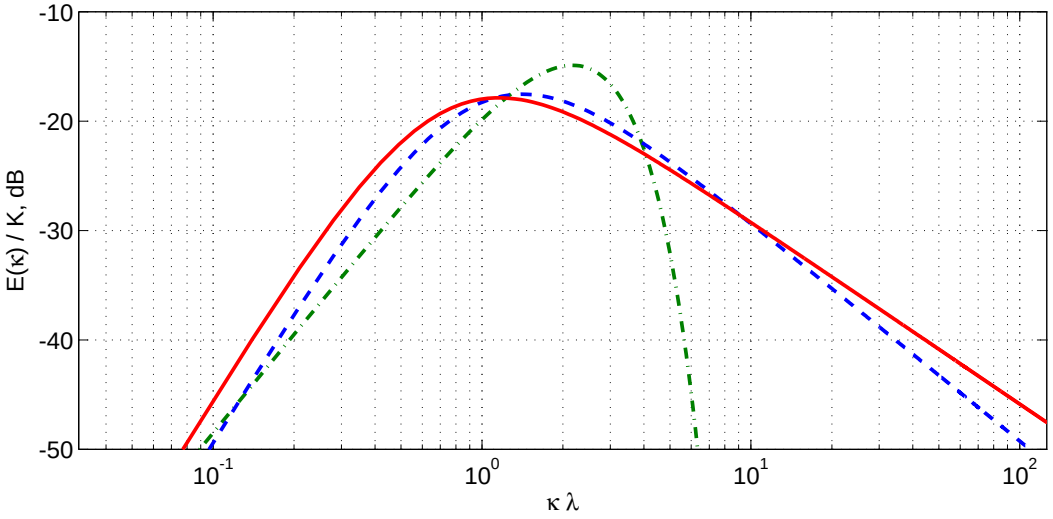

FIGURE 2.1: Comparison of energy spectra models. (– · –) Gaussian spectrum, (– –) Liepmann spectrum and (——) von Kármán spectrum.

The different behaviour of the energy spectra shown in Figure 2.1 is reflected in the behaviour of the filters, as shown in Figure 2.2. Of particular importance is the behaviour of the filter near the origin. Using an asymptotic expansion for small r, the Gaussian filter has a regular behaviour $G_g(r) \approx G_0 + G_1 r^2$ when $r \to 0$. In contrast Liepmann and von Kármán filters behave as $G_l(r) \approx L_0 + L_1 r^{1/2}$ and $G_k(r) \approx K_0 + K_1 r^{1/3}$, respectively (the coefficients G_0, L_0, L_1, K_0 and K_1 are functions of the integral length scale and kinetic energy alone). The fact that Liepmann and von Kármán filters are not as regular as the Gaussian filter can also be seen in Figure 2.2. This is a direct consequence of the

fact that the Liepmann and von Kármán filters present a slow algebraic decay in the wavenumber space as $\kappa \to \infty$ (see Eqs. (2.88) and (2.91)) in contrast to an exponential decay for the Gaussian filter. The Liepmann filter decays in the wave number space as $\kappa^{-5/2}$ and von Kármán filter as $\kappa^{-7/3}$. Smoothness and compactness properties of Fourier transforms indicate that the smoother a function is, the faster its transform decays for large wavenumber [36]. Therefore, in both cases –Liepmann and von Kármán– the filter itself is a continuous function within the physical space but their first and second derivatives do not exist at zero, otherwise the decay in the wavenumber space would be at least as fast as κ^{-3}. This lack of regularity has consequences for the numerical implementation described in section 3.3.2.

Regarding the behaviour of the filters for large distances ($r \to \infty$) the Liepmann and von Kármán filters decrease at much lower rates than the Gaussian filter. This implies that the region of influence of each vortex will be larger for Liepmann and von Kármán filters than for the Gaussian filter. In turn, this implies that the numerical method will be more demanding for the von Kármán filter, followed by the Liepmann filter and finally the Gaussian filter, see section 4.3.1.

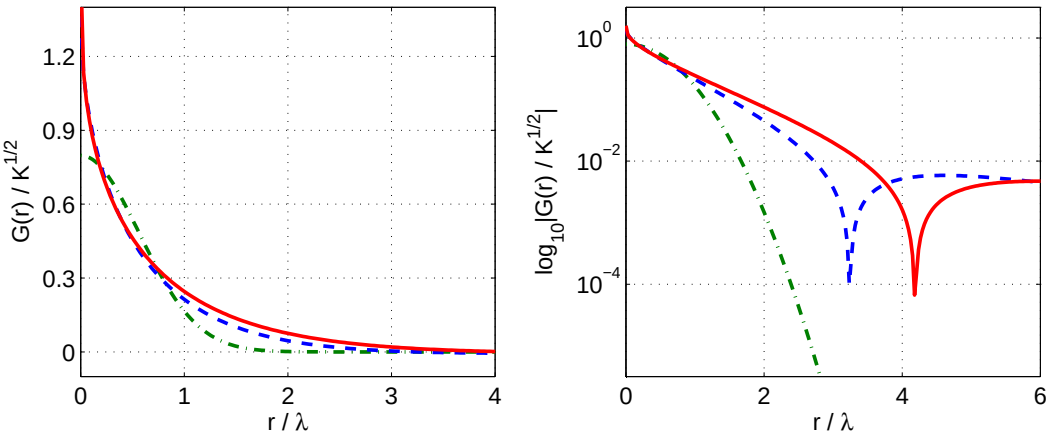

FIGURE 2.2: Filters corresponding to Gaussian (– · –), Liepmann (– –) and von Kármán (——) spectra versus distance in linear scale (left) and logarithmic scale (right).

2.4.5 Interpolation of the filters

The computational performance of the random-vortex-particle method in Eq. (2.62) is directly related with the mathematical expression that defines the filter. The filters derived from Gaussian, Liepmann and von Kármán energy spectra involve the calculations of exponentials and hypergeometric functions which can be very costly, see Eqs. (2.86), (2.89) and (2.92). In addition, for a typical simulation one needs to evaluate these filters several million times. An attempt was therefore made in this work to use interpolated filters which are much faster than the exact expressions.

In order to compute the synthetic velocity field, the random-vortex-particle method uses the filter derivatives, see Eq. (2.62), which further complicates the analytical expressions. Therefore, it is the derivatives of the filters that are interpolated.

The Gaussian filter decays exponentially in physical space, Eq. (2.86), and it is an infinitely continuous and differentiable function. Thus an accurate interpolation of the derivative of the Gaussian filter is achieved relatively easily. Obtaining accurate interpolations for Liepmann and von Kármán spectra requires more care. As discussed in section 2.4.4, larger radius than that for the Gaussian spectrum have to be considered in order not to introduce significant truncation error. In addition, the derivatives of Liepmann and von Kármán filters have a singularity at $r = 0$. The interpolations used in this work have been obtained with Matlab using rational function approximations.

2.5 Validation

Filter-based methods to generate synthetic turbulence have so far being mainly restricted to Gaussian filters. Therefore, the method used in this work is firstly validated for these filters. Since Gaussian filters are separable in space, a grid-based discretisation is simple to derive and implement as the filter can be applied separately in each direction, see section 2.3.2. Convection effects and temporal decorrelation are not included in this preliminary validation which is intended as a proof of concept only and a full validation of the random-vortex-particle method in Eq. (2.61) will be presented when applying the method to broadband fan noise.

As a first step, the parametric study introduced in section 2.3.2 is performed to determine the values of the grid spacing and stencil width in Eq. (2.72). In a second step, simulation results are presented. The statistical properties of the turbulence are compared against theoretical results in order to assess the accuracy of the numerical method.

2.5.1 Problem definition and computational setup

The problem is made non-dimensional using the integral length scale λ and the kinetic energy K.

The computational domain is a square grid of size 6λ with grid spacing $\triangle$ in both directions. The number of nodes in the domain is $N \times N$. Since the velocity field at each grid point depends on points in a lattice centred at this grid point (see Eq. (2.72)), an extended grid has to be considered. This grid has $N + 2M$ points in each direction when choosing $M_1 = M_2 = N_1 = N_2 = M$ in Eq. (2.72). As an example both grids are plotted in Figure 2.5(a) for the values $N = 37$ and $M = 12$.

2.5.2 Method

The discrete version of the random-vortex-particle method in Eq. (2.72) for the Gaussian filter in Eq. (2.86) reads

$$u'_x(x_n, y_m) = -\frac{\sqrt{2\pi K}}{\lambda^2} \sum_{q=-M}^{M} \sum_{p=-M}^{M} (y_n - y_q) \exp\left\{-\frac{\pi[(x_n - x_p)^2 + (y_n - y_q)^2]}{2\lambda^2}\right\} r(x_p, y_q), \tag{2.93a}$$

$$u'_y(x_n, y_m) = \frac{\sqrt{2\pi K}}{\lambda^2} \sum_{q=-M}^{M} \sum_{p=-M}^{M} (x_n - x_p) \exp\left\{-\frac{\pi[(x_n - x_p)^2 + (y_n - y_q)^2]}{2\lambda^2}\right\} r(x_p, y_q). \tag{2.93b}$$

According to Eq. (2.74), $r(x_p, y_q)$ follows a normal distribution with zero mean and standard deviation $\triangle$. They are independently generated for each realisation.

Another way to assess the method is to consider the stream function and the vorticity field. For the stream function we have:

$$\eta(x_n, y_m) = \sqrt{\frac{2K}{\pi}} \sum_{q=-M}^{M} \sum_{p=-M}^{M} \exp\left\{-\frac{\pi[(x_n - x_p)^2 + (y_n - y_q)^2]}{2\lambda^2}\right\} r(x_p, y_q). \tag{2.94}$$

For the vorticity field $\boldsymbol{w} = \nabla \times \boldsymbol{u}'$, we have $w_3 = -\partial^2\eta/\partial x^2 - \partial^2\eta/\partial y^2$. In the case of the Gaussian spectrum, this yields

$$\begin{aligned} w_3(x_n, y_m) = & \frac{\sqrt{2\pi K}}{\lambda^2} \sum_{q=-M}^{M} \sum_{p=-M}^{M} \exp\left\{-\frac{\pi[(x_n - x_p)^2 + (y_n - y_q)^2]}{2\lambda^2}\right\} \\ & \left(2 - \frac{\pi}{\lambda^2}[(x_n - x_p)^2 + (y_n - y_q)^2]\right) r(x_p, y_q). \end{aligned} \tag{2.95}$$

2.5.3 Effect of truncation and discretisation

As shown in section 2.3.2, the error derived from the numerical discretisation of the continuous method in Eq. (2.61) can be controlled by choosing appropriate values for grid spacing $\triangle$ and the stencil width M. These values can be chosen by comparing the numerical correlation and the energy spectrum in Eq. (2.82) against the corresponding theoretical expressions in Eq. (2.76).

Figure 2.3 shows the correlation and the energy spectrum in wavenumber space for values of grid spacing $\triangle = \lambda/4$, $\lambda/6$, $\lambda/8$ and $\lambda/10$ and a large value for $M = 24$ such that the truncation error is negligible. There is a very good agreement between analytical and numerical results up to wavenumbers corresponding to wavelengths resolved by four grid points. The effect of truncation is assessed in Figure 2.4 where the correlation and energy spectrum in wavenumber space are shown for a fixed value of $\triangle = \lambda/6$ and

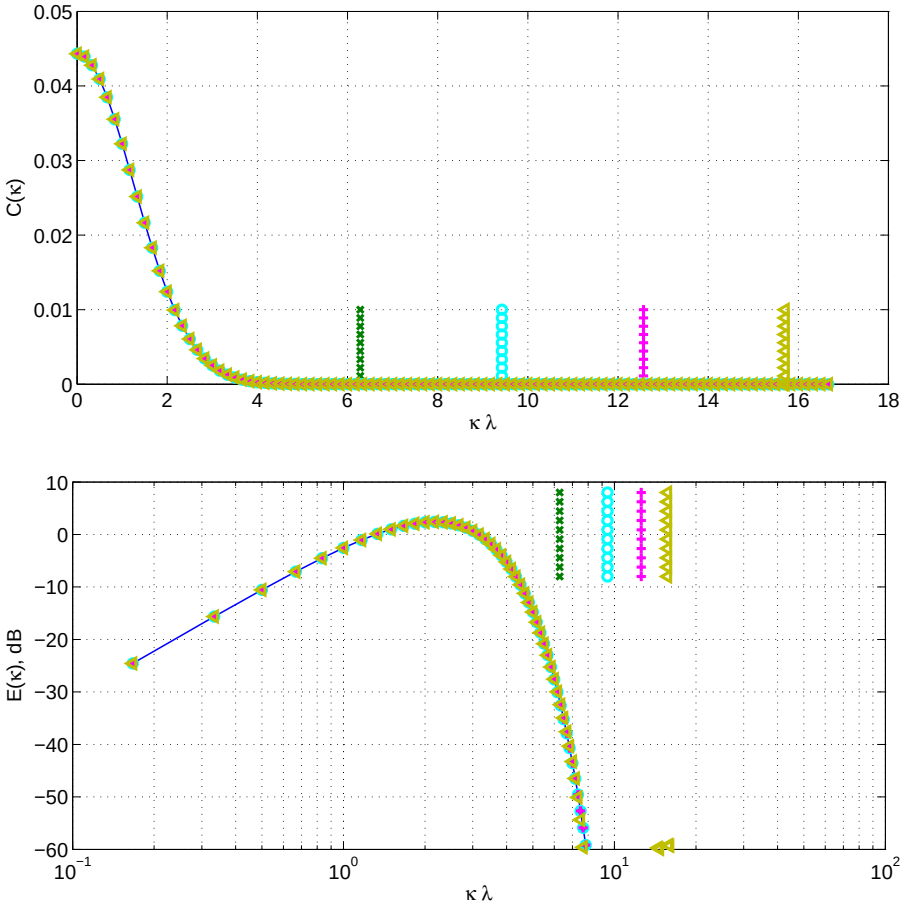

FIGURE 2.3: Correlation and energy spectrum versus $\kappa\lambda$ in linear and logarithmic scales, respectively. Solid line corresponds to analytical expressions and symbols to numerical results obtained for $M = 24$, and $\triangle = \lambda/4$ ($\times$), $\triangle = \lambda/6$ ($\circ$), $\triangle = \lambda/8$ ($+$) and $\triangle = \lambda/10$ ($\triangleleft$). Vertical lines represent where four points per wavelength are achieved.

allowing M to vary from 10 to 16. Little differences are observed in the correlation by increasing the width of the stencil, see Figure 2.4(a). However, if we look at the energy spectrum in Figure 2.4(b) we see that including contributions from grid points that are further away improves the accuracy of the method for large wavenumbers. For values of M larger than 12, numerical results provide a good fit to the theoretical spectrum for wavenumbers corresponding to amplitudes more than 40 dB lower than the peak of the Gaussian. In conclusion, with $\triangle = \lambda/6$ and $M = 12$ the statistics of the turbulence are considered to be accurately reproduced.

2.5.4 Validation and illustration of the synthetic field

Now that the parameter values in Eq. (2.93) have been selected to control the numerical error, we focus on the preliminary validation of the random-vortex-particle method for Gaussian filters.

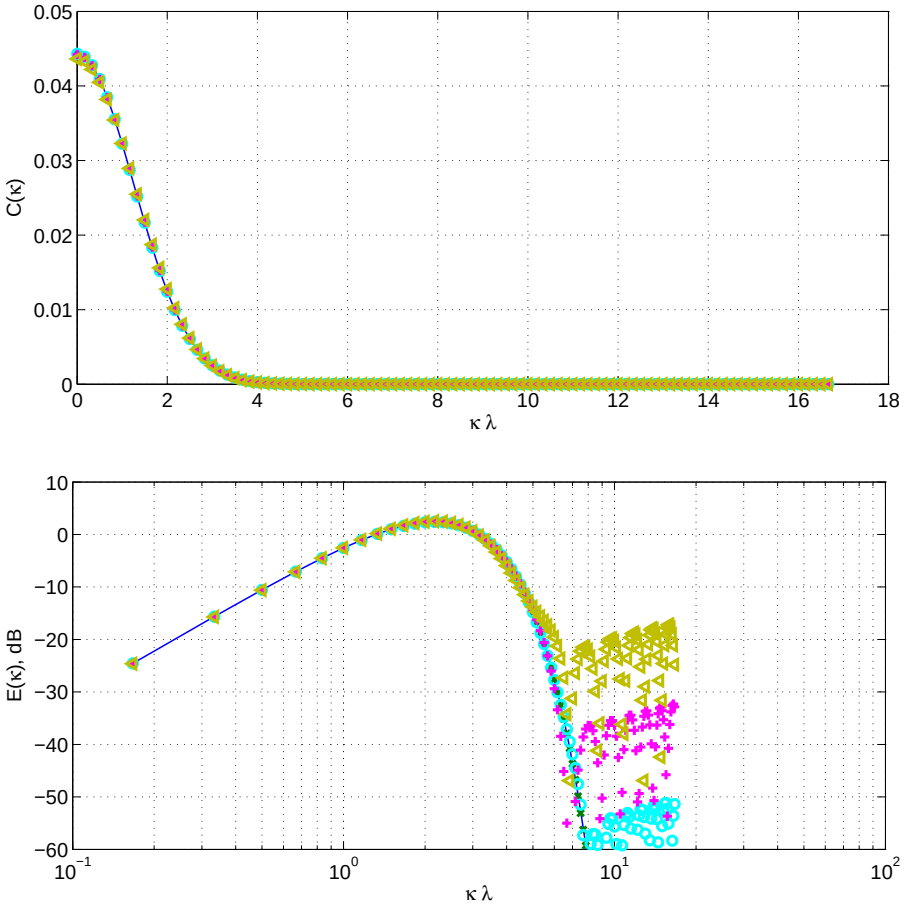

FIGURE 2.4: Correlation and energy spectrum versus $\kappa\lambda$ in linear and logarithmic scales, respectively. Solid line corresponds to analytical expressions and symbols to numerical results obtained for $\triangle = \lambda/6$, and $M = 10(\triangleleft)$, $M = 12$ $(+)$, $M = 14$ $(\circ)$, and $M = 16$ $(\times)$.

The computational domain corresponding to the parameter values selected is given by a grid with $N = 37$ nodes in each direction using a extended grid of $L = 61$ nodes in each direction as illustrated in Figure 2.5(a).

Figure 2.5(b) shows a given realisation of the fluctuating velocity field $\boldsymbol{u}'$ and Figure 2.6 snapshots of the corresponding the stream function η and the vorticity. It can be observed that the typical size of the vortices is consistent with the expected integral length scale of the turbulence.

With the aim of analysing of the statistical properties of the synthetic turbulent velocity field, analytical and numerical correlations computed with respect to the central point of the grid are studied. Analytical and stochastically generated two-point correlations R_{11}, R_{22} and R_{12} are shown in Figure 2.7. It shows that the numerical method captures the features present in the analytical two-point correlations over the whole domain. In order to get an estimate of the numerical error, the difference between analytical and numerical two-point correlations is shown in Figure 2.8. Very good agreement is obtained in all

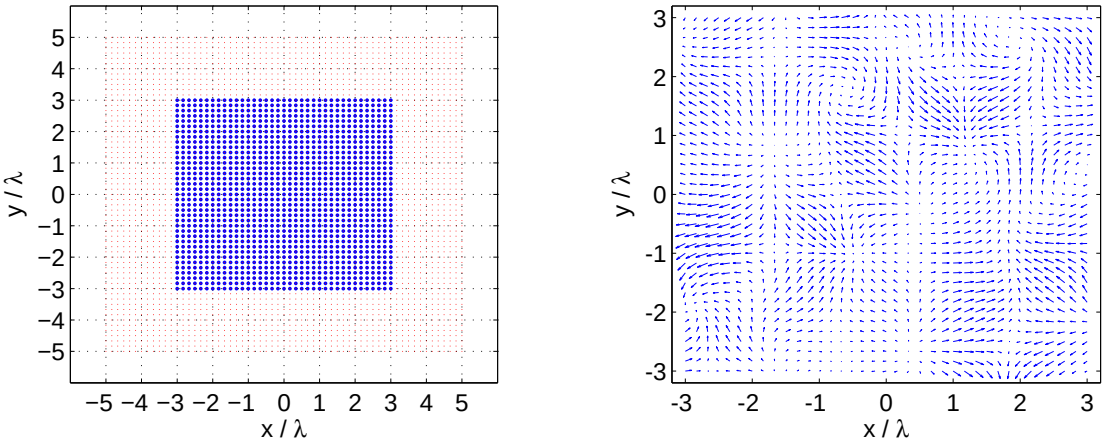

FIGURE 2.5: Left: Grid used in the simulation. Computational domain grid with 37×37 nodes ($\cdot$). Extended grid with 61×61 nodes ($\cdot$). Right: Snapshot of the synthetic velocity field $\boldsymbol{u}'$.

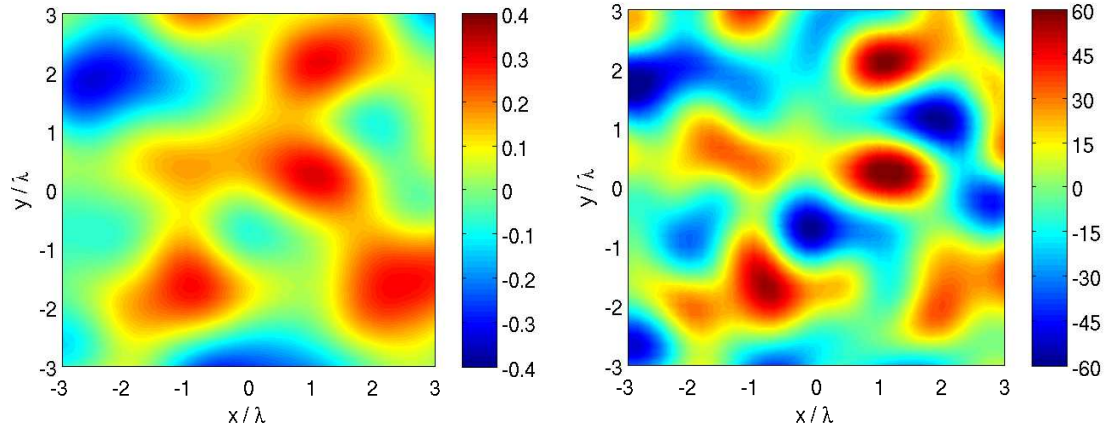

FIGURE 2.6: Snapshot of the stream function (left) used to generate the stochastic velocity field $\boldsymbol{u}'$ and the corresponding vorticity field (right).

cases with a maximum relative error of about 6%. To illustrate this error further, analytical and numerical two-point correlations are compared along a segment chosen such that the larger values of the correlation are captured. Figure 2.8(b) shows the two-point correlation R_{11} along the segment $\{(x, y)/x = 0; y \in [0, 0.5]\}$. Figure 2.8(d) shows the two-point correlation R_{22} along the segment $\{(x, y)/x \in [0, 0.5]\,; y = 0\}$. Figure 2.8(f) shows the two-point correlation R_{12} along the segment $\{(x, y)/x \in [0, 0.5]\,; y = x\}$. It can be observed that numerical results provide a very good fit to theoretical correlations.

In conclusion, the preliminary validation of the random-vortex-particle method performed in this section for Gaussian filters shows that the method is capable of reproducing the two-point correlation tensor and achieve a target value of kinetic energy. Therefore, we now focus on its application to predict broadband fan noise.

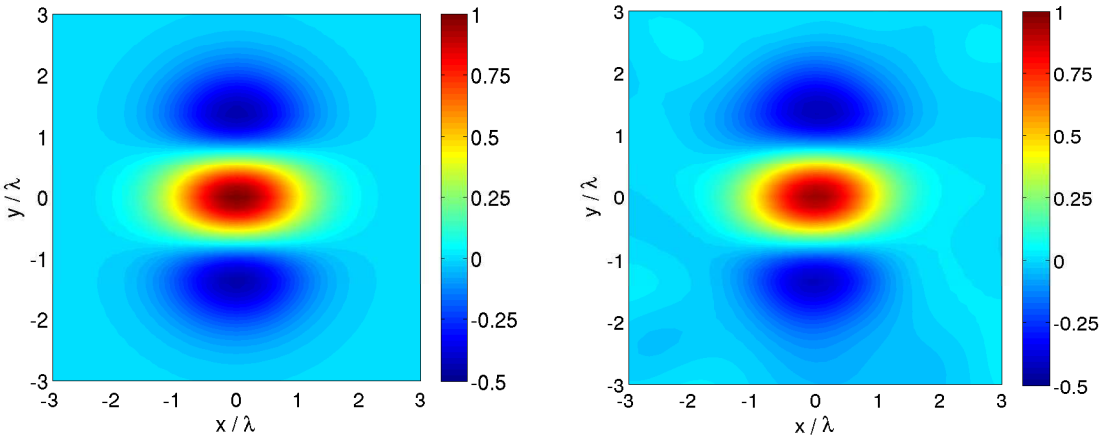

(a) Analytical two-point correlation R_{11}

(b) Numerical two-point correlation R_{11}

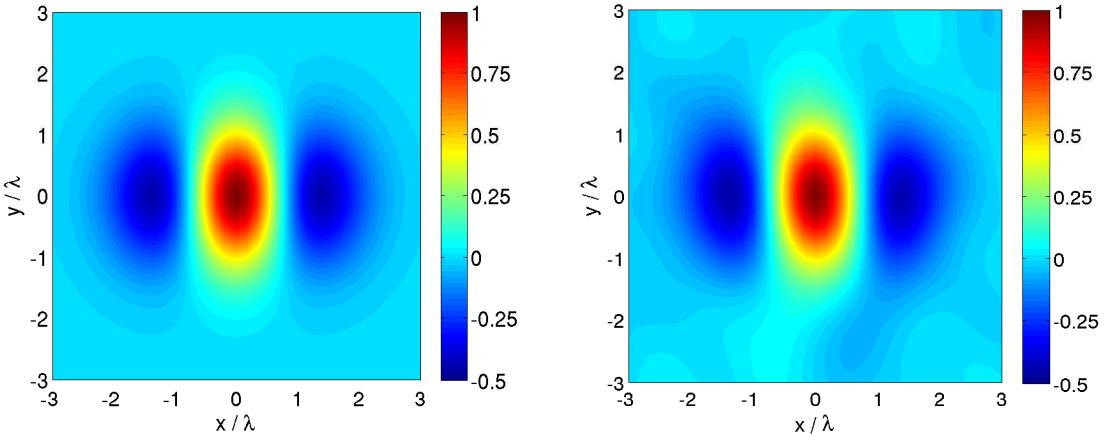

(c) Analytical two-point correlation R_{22}

(d) Numerical two-point correlation R_{22}

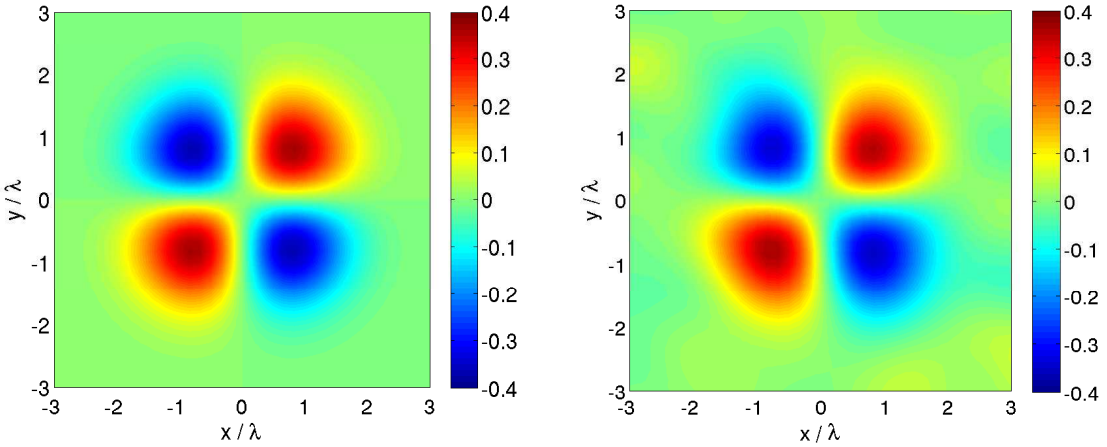

(e) Analytical two-point correlation R_{12}

(f) Numerical two-point correlation R_{12}

FIGURE 2.7: Contour plots of correlations R_{ij}. Averages taken over 2,000 realisations.

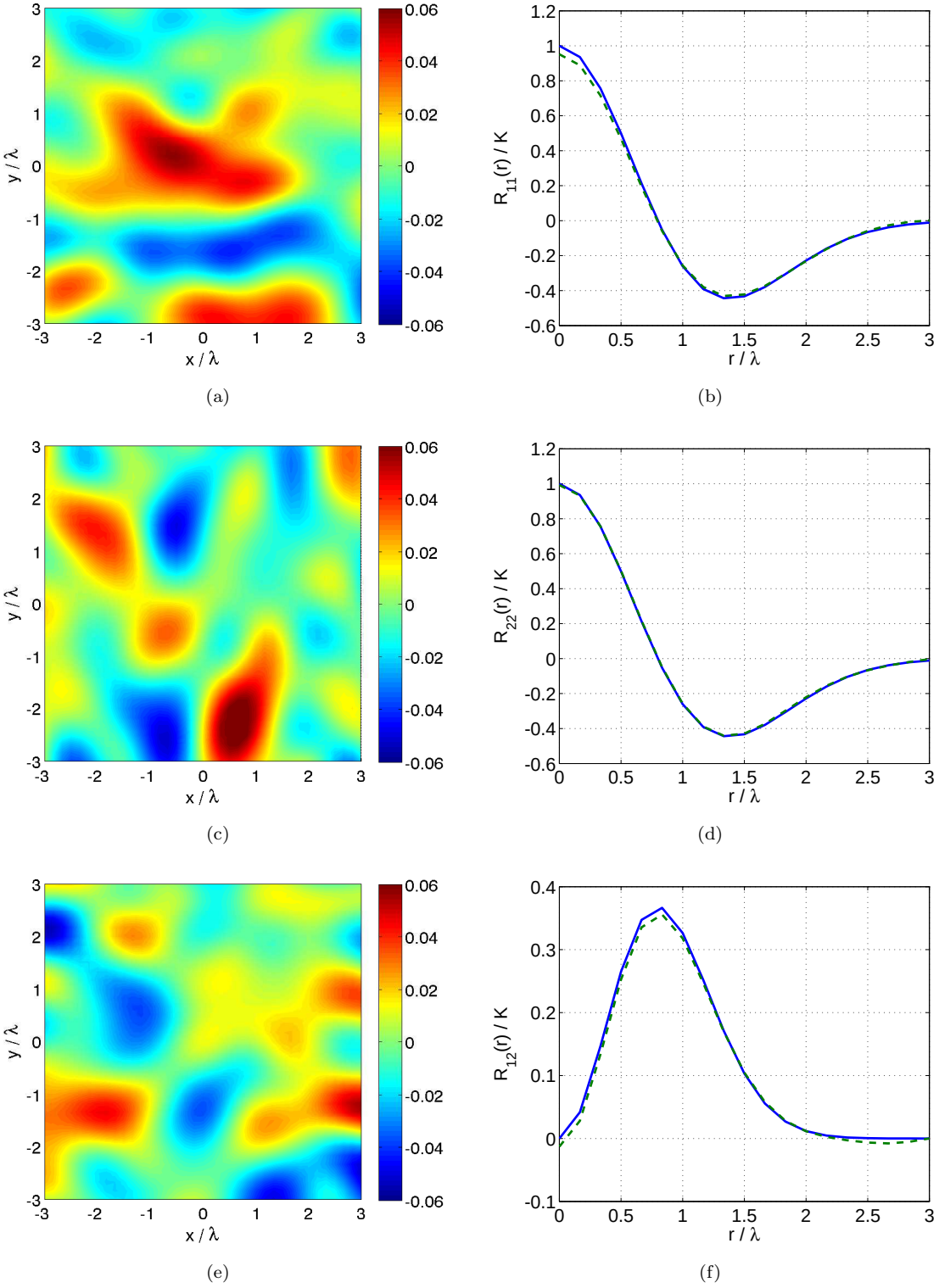

FIGURE 2.8: Left: Contour plots of the difference between analytical and numerical two-point correlations R_{11} (a), R_{22} (c) and R_{12} (e). Right: Analytical (—) and numerical (– –) two-point correlation R_{11} for distances r along the sengment $\{(x,y)/x = 0; y \in [0, 0.5]\}$ (b), R_{22} along $\{(x,y)/x \in [0, 0.5]\,; y = 0\}$ (d), and R_{12} along $\{(x,y)/x \in [0, 0.5]\,; y = x\}$ (f). Averages taken over 2,000 realisations.

Chapter 3

Broadband Fan Interaction Noise

The aim of this project is to predict broadband fan interaction noise by combining the linearised Euler equations (LEE) with the stochastic method to generate synthetic turbulence presented in the previous chapter.

Aerodynamic noise can be efficiently generated by unsteady flows interacting with rigid surfaces. When the flow around the surface is unsteady, it generates unsteady forces on the surface which conversely generate pressure fluctuations on the fluid, that then propagate as sound. The incoming unsteady velocity disturbances can already exist as atmospheric turbulence or be generated by flow interaction with other objects, for instance the turbulent wake of a rotor blade.

Analytical methods to predict broadband fan interaction noise are restricted to idealised geometries and mean flows. High fidelity numerical methods such as Direct Numerical Simulations (DNS) of the Navier-Stokes equations of fluid dynamics or Large Eddy Simulations (LES) are still too expensive to be used routinely in the design process. An objective of this work is to contribute in showing that a hybrid method where the Computational Fluid Dynamics (CFD) stage is replaced by stochastically generated turbulence is cheaper and provides accurate noise predictions.

We restrict ourselves to two-dimensional problems and we neglect the effects of the airfoil geometry. This is not a restriction of the method itself but a simplification made for validation purposes. Therefore, extending the numerical method to deal with three-dimensional non-uniform flows interacting with real airfoils is feasible but goes beyond the scope of the current research study which concentrates in formulating and validating the method.

This chapter begins with an overview of different techniques used to predict broadband fan noise with an emphasis on stochastic methods. Note that we focus on methods used in previous work rather than details of the applications. Then, the hybrid method proposed in this work to predict broadband fan interaction noise is presented. Also

included in this chapter is a description of the LEE-solver and its validation for a flat plate interacting with a single gust.

3.1 Overview of broadband interaction noise models

Important reductions in jet noise have been achieved since the 1960's by designing engines with increasingly higher bypass-ratio. Consequently, fan noise has become a major source of noise in modern aircraft [37]. While tonal noise can be efficiently reduced by tuning the liner properties to target the blade passing frequency and its harmonics, broadband fan noise remains more difficult to predict and to reduce due to its random nature, high frequency content and numerous source mechanisms.

Various noise sources mechanisms contribute to the overall broadband fan noise. Even if the inlet flow is steady and uniform, turbulent boundary layers develop along the blade surface and acoustic waves are scattered at the trailing edge. This is known as trailing-edge noise (or self-noise) and defines the minimum amount of noise from a fan in the absence of installation effects [38][1]. In ducted fans, tip vortex noise is generated in the annular gap between the blade tips and the fan casing. Its amplitude increases with the size of the gap and can affect the self-noise of the blade [3]. Leading-edge noise (or interaction noise) is generated by incoming turbulent flows impinging on the fan blades or stator vanes. Interaction is considered one of the main mechanisms of broadband noise on isolated airfoils in the presence of incoming turbulence [39]. In a rotor-stator configuration, rotor noise is likely to be less efficient than the interaction between the turbulent wakes shed from the rotor and the stator vanes [3].

Broadband fan noise has been studied extensively for the last seventy years and a large body of theoretical, experimental and numerical methods can be found in the literature. We first describe the difficulties that arise when deriving analytical models. Then, we focus on numerical techniques which are based on stochastic methods.

3.1.1 Analytical models

Von Kármán and Sears were the first to develop an analytical solution for broadband fan interaction noise in 1938 [40]. They considered the incompressible response of a zero-thickness isolated fixed flat plate undergoing a two-dimensional sinusoidal gust convected by the free stream. This theory was then generalised by Adamczyk [41] to capture the effects of three-dimensional oblique sinusoidal gusts in a compressible fluid. Effects of

[1] An additional source mechanism is vortex shedding noise which is associated with the laminar boundary layer along the blade surface and it is produced by vortices created in the wake of the trailing edge. Its effects increase with the thickness of the trailing edge but for the case of broadband fan noise its contribution to the total sound power radiated is not of practical importance [39].

compressibility are especially significant at high frequencies [39]. Adamczyk's analytical solution is based on Landahl's iteration procedure where leading and trailing edge boundary conditions are alternately applied. This allows the leading-edge solution to be calculated for a semi infinite flat plate, and similarly to calculate a trailing-edge correction that can be incorporated into the leading-edge solution [42].

Also using Landahl's iteration procedure, Amiet [17] proposed an analytical solution for the pressure jump along the flat plate and far-field noise levels generated by the interaction of frozen gusts with a two-dimensional flat plate. Different solutions were proposed for the low and high frequency ranges. While the airfoil response function at high frequencies is based on Landahl's iteration procedure, at the lower frequency range it is explicitly provided. This yields a more efficient method; due to the strong communication between the leading and the trailing edge at low frequencies, many iterations are required to give a good approximation of the response function [43]. In the high frequency range, Amiet proposed to used the first two iterations to obtain response function along the flat plate. Amiet's analytical solution was subsequently applied to the case of the rotational motion of a flat plate [44].

For turbomachinery, blade rows with large number of blades and large thickness, where interactions between nearby blades are important, analytical models representing cascades of airfoils are more suited [45]. For instance, Glegg [46] proposed an analytical solution for three-dimensional rectilinear cascade of flat plates with finite chord excited by three-dimensional gusts.

Efforts have also been focused on developing analytical solutions for more realistic geometries. Evers and Peake [47] proposed an analytical solution for gusts interacting with a cascade of blades in a non-uniform mean flow at non-zero angle of attack including the effects of small but non-zero camber and airfoil thickness. Roger [48] extended Amiet's analytical solution to include more realistic shapes such as parallelogram for segments of sweep blades and polygons accounting for chord length variations along the span and using strip theory to reconstruct a three-dimensional blade.

Current analytical solutions for broadband fan interaction noise are only approximate solutions and they are restricted to idealised geometries and mean flows. However, provided that careful assessment of the assumptions is made not to lead to substantial errors, analytical solutions are a powerful technique to obtain fast and cheap predictions. For instance, they are particularly useful for preliminary designs or for validating more realistic numerical techniques. In fact, numerical results obtained in this thesis are validated against Amiet's analytical model.

We will consider here an isolated fixed flat plate interacting with two-dimensional isotropic turbulence. Therefore, Amiet's analytical solution [17] is a well suited analytical model

once it is modified to account for a fully two-dimensional acoustic far field. More information on the modified analytical solution can be found in Appendix C.1 and it is summarised here for the sake of clarity.

The random sound field radiated by the airfoil is characterised in the far field by the Power Spectral Density (PSD) of the acoustic pressure. The corresponding expression for the analytical PSD in 2D is of the form

$$S_{pp}(x, y, \omega) = \frac{\rho_0^2 u_0 \kappa_0 y^2 \pi}{2\sigma^3} \phi_{vv}(\kappa_x) |\mathcal{L}(x, \kappa_x)|^2, \tag{3.1}$$

where ω is the angular frequency, $\kappa_0 = \omega/c_0$ is the free-field acoustic wavenumber, $\kappa_x = \omega/u_0$ is the chordwise hydrodynamic wavenumber, M the Mach number and $\sigma = \sqrt{x^2 + \beta^2 y^2}$ with $\beta^2 = 1 - M^2$. ϕ_{vv} is the velocity spectrum and is determined by the streamwise correlation of the turbulent velocity field normal to the airfoil

$$v(x,t) = \int_{\mathbb{R}} \hat{v}(\kappa_x) \exp[i\kappa_x(x - u_0 t)] \mathrm{d}\kappa_x, \quad \hat{v}(\kappa_x) = \frac{1}{2\pi} \int_{\mathbb{R}} v(\tilde{x}) \exp(-i\kappa_x \tilde{x}) \mathrm{d}\tilde{x}. \tag{3.2}$$

$\mathcal{L}$ is the lift function that relates to the net pressure jump $\Delta\hat{P}$ along the airfoil. For a single wavenumber component, the pressure jump is determined by the response function g and the turbulent velocity field v as:

$$\Delta\hat{P}(x, \omega) \quad = \quad 2\pi\rho_0 \hat{v}(\kappa_x) \mathsf{g}(x, \kappa_x). \tag{3.3}$$

Expressions for the response functions and lift of the airfoil can be found in [17].

3.1.2 Numerical methods

The most accurate approach to investigate broadband fan interaction noise is to fully resolved the Navier-Stokes equations via Direct Numerical Simulations. These simulations are extremely demanding from a computational point of view, because they require large computational domains to cover a few acoustic wavelengths, while the small scales present in turbulence have also to be resolved. Despite the rapid increase in computational resources, DNS are still restricted to low Reynolds numbers [49].

An alternative to DNS is Large Eddy Simulation which resolves only turbulent scales larger than the cell size of the mesh while the smaller scales are modelled. LES are considerably cheaper than DNS, but they remain too costly as well to be used routinely in an industrial context [45].

A third approach is to split the problem in two parts, the acoustic source region where nonlinear effects dominates is resolved using computational fluid dynamics tools, and then the acoustic field is predicted using source and propagation methods such as

Lighthill analogy [50]. Although these methods are cheaper than complete flow simulations, the DNS or LES stage still remains expensive within an industrial context [4].

An alternative to solving the complete Navier-Stokes equations in the source region is to generate a synthetic velocity field that captures the main features of the turbulence and then couple it with a sound propagation method. This approach is based on the stochastic generation of turbulent flows which can then be used to compute sound sources in the linearised Euler equations or Lighthill's analogy. Such a hybrid method can provide accurate predictions of the generation and propagation of acoustic perturbations [5]. The rationale is that this approach is cheaper than DNS and LES from a computational point of view, still capture relevant features of the sound sources and therefore provide a way to consider higher Reynolds numbers. We now review different techniques that rely on the use of stochastic methods to predict broadband fan noise.

Atassi *et al.* [51] studied the effects of three-dimensional gusts convected with a uniform mean flow on a cascade of flat plates. Sound generation and propagation are modelled by the linearised Euler equations and solved in the frequency domain for the incident and scattered fields. The perturbations are decomposed into an acoustical part and a vortical part. The incident velocity field is assumed to be purely vortical and it is specified as a sum of Fourier modes. The noise spectrum is calculated as the weighted sum of the acoustic response to a large number of upstream Fourier components. The method has later been extended to include non-uniform base flows [52] and different energy spectra [13]. In contrast with the method by Atassi and coworkers, the stochastic method proposed here solves the LEE in the time domain only for the scattered field. With a time-domain formulation the wide range of frequencies required to investigate broadband noise can be resolved simultaneously.

Casper and Farassat [53] developed a formulation for broadband fan noise predictions where the turbulent wall pressure along the airfoil is modelled by Fourier modes whose parameters are stochastically generated. A time-domain formulation of the Ffowcs-Williams Hawkings equation with loading term is used to predict the acoustic far field. This method has been applied to interaction noise of flat plate with homogeneous isotropic turbulence. To represent the incident turbulence, leading and trailing-edge response functions proposed by Adamczyk [41] were considered and combined with gust amplitudes derived from von Kármán energy spectrum. The method has also been applied to trailing-edge noise by considering only the trailing-edge response function [54].

Ewert *et al.* [55] studied the effects of trailing edge noise from a two-dimensional airfoil moving through evolving, homogeneous, isotropic turbulence. The method combines synthetic turbulence with an acoustic analogy. Following Atassi *et al.*'s approach, the flow perturbations are decomposed in an acoustical and a vortical part and sound propagation is solved for the incident and scattered fields. In contrast with Atassi and

Farassat, the stochastic method does not rely on Fourier modes, but it is a filter-based method. In particular, the RPM method described in section 2.1.2.3 is used to specify the vortical component of the velocity field. The synthetic turbulence is then used to compute the sound sources on acoustic analogy which are given by the fluctuating component of the Lamb vector ($\boldsymbol{w} \times \boldsymbol{u}$ where $\boldsymbol{w}$ is the vorticity). In order to reduce the computational cost, the synthetic velocity field is implemented only above the airfoil in a grid-based discretisation. The acoustic analogy is solved in the time domain and the predicted sound levels are rescaled to account for the noise sources on both sides of the airfoil and to adapt the simulation to the problem of sound radiation from a three-dimensional airfoil.

3.2 Physical Model

We propose to model broadband fan interaction noise by using an hybrid method that combines the linearised Euler equations with synthetic turbulence. The linearised Euler equations are solved in the time domain for the scattered field only. The sources of noise along the airfoil are computed using the method to generate synthetic turbulent velocity fields presented in the previous chapter and imposed as a boundary condition along the solid surfaces.

3.2.1 Governing equations

Sound propagation is separated from noise generation and modelled by the linearised Euler equations assuming that the fluid is an ideal gas, inviscid, and isentropic. The linearised Euler equations are solved in the time domain, so that a wide range of frequencies can be investigated with a single simulation. (Note that by choosing a conservative form, one avoids storing gradients of the mean flow.)

Assuming that the fluctuations are small compared to the mean flow, the flow variables are given by

$$\boldsymbol{u} = \boldsymbol{u}_0 + \boldsymbol{u}', \quad p = p_0 + p', \quad \rho = \rho_0 + \rho', \tag{3.4}$$

where $\boldsymbol{u} = (u, v)$ is the velocity field, p for acoustic pressure, ρ for density, subscript $_0$ for mean components and superscript $'$ for fluctuating components.

The governing equations for the linearised two-dimensional Euler equations in conservative form are written

$$\frac{\partial \mathbf{q}}{\partial t} + \frac{\partial \mathbf{A}\mathbf{q}}{\partial x} + \frac{\partial \mathbf{B}\mathbf{q}}{\partial y} = \mathbf{s}. \tag{3.5}$$

To obtain a conservative formulation of the LEE, the variable for pressure has been substituted by $\pi = (p/p_\infty)^{(1/\gamma)}$ with p_∞ constant, which is the variable introduced to

formulate Lilley's equation [56]. γ stands for the ratio of specific heats. The vector of unknowns is $\mathbf{q} = (\rho', (\rho u)', (\rho v)', \pi')^T$ with $\pi' = \pi_0 p'/(\gamma p_0)$, the coefficient matrices are

$$\mathbf{A} = \begin{bmatrix} 0 & 1 & 0 & 0 \\ -u_0^2 & 2u_0 & 0 & \rho_0 c_0^2/\pi_0 \\ -u_0 v_0 & v_0 & u_0 & 0 \\ -u_0\pi_0/\rho_0 & \pi_0/\rho_0 & 0 & u_0 \end{bmatrix}, \quad \mathbf{B} = \begin{bmatrix} 0 & 0 & 1 & 0 \\ -u_0 v_0 & v_0 & u_0 & 0 \\ -v_0^2 & 0 & 2v_0 & \rho_0 c_0^2/\pi_0 \\ -v_0\pi_0/\rho_0 & 0 & \pi_0/\rho_0 & v_0 \end{bmatrix},$$

where c_0 stands for the sound speed and $\mathbf{s}$ is the source term. The mean flow can be obtained either from measurements or using CFD tools. The equations in the system Eq. (3.5) correspond to mass conservation, momentum and modified pressure.

3.2.2 Boundary condition along the airfoil

Because we solve the linearised Euler equations for the scattered field only, sources of noise along the airfoil are introduced in the linearised Euler equations as a hard-wall boundary condition. If we note $\boldsymbol{n}$ the unit normal vector pointing towards the airfoil, a hard-wall boundary condition along the airfoil implies that $\boldsymbol{u}_0 \cdot \boldsymbol{n} = 0$ and $\boldsymbol{u}' \cdot \boldsymbol{n} = 0$.

The turbulent velocity field can be decomposed into a scattered field, $\boldsymbol{u}'_s$, (which is mostly acoustic although, due to the vortex shedding, also has a vortical part) and an incident turbulent field, $\boldsymbol{u}'_i$, yielding: $\boldsymbol{u}' = \boldsymbol{u}'_s + \boldsymbol{u}'_i$. Therefore, by imposing the hard-wall boundary condition, the normal component of the scattered field along the airfoil is fully specified in terms of the incident velocity filed as $\boldsymbol{u}'_s \cdot \boldsymbol{n} = -\boldsymbol{u}'_i \cdot \boldsymbol{n}$. The incident velocity field, $\boldsymbol{u}'_i$, is computed along the airfoil using the random-vortex-particle method as if there were no flat plate.

Therefore, the acoustic field can be computed by solving the linearised Euler equations for the scattered field only. Note that the model in Eq. (3.5) is still valid when replacing $\boldsymbol{u}'$ by $\boldsymbol{u}'_s$.

3.3 Linearised Euler equations code

The numerical implementation of the physical model described in the previous section is now presented. The linearised Euler equations are solved using a general in-house finite-difference solver developed at the ISVR.

Spatial derivatives are approximated using seven-point fourth-order Dispersion-Relation-Preserving (DRP) [57] schemes, which are optimised to minimise the dispersion error. A six-stage optimised explicit Runge-Kutta scheme [58] is implemented to perform the time integration. The time step of the method is an input parameter that can be provided directly or through the Courant-Friedrichs-Lewy (CFL) number. The simulation domain

is divided into overlapping blocks which are synchronised between the stages of the Runge-Kutta scheme using Message Passing Interface (MPI). The order of the tasks performed by the solver at each stage of the Runge-Kutta scheme is as follows:

1. Update the flux vectors **Aq** and **Bq**.
2. Compute the divergence of the flux vectors to obtain $\partial \mathbf{q}/\partial t$.
3. Perform the time integration.
4. Synchronise the blocks.

3.3.1 Small wavelengths treatment

Wavelength components that are too small to be accurately resolved by the grid are removed after every step of the Runge Kutta scheme from the solution using a filtering procedure [58],

$$\tilde{\mathbf{q}} = \mathbf{q} - \sigma D(\mathbf{q}), \tag{3.6}$$

where D is a spatial filter that retains only the small wavelength components and σ is an input parameter that controls its strength. The filter is defined as:

$$D(\mathbf{q}) = \sum_{n=-M}^{M} d_n \mathbf{q}(x + n\Delta x), \tag{3.7}$$

where d_n is a symmetric stencil ($d_n = d_{-n}$) and Δx the grid spacing. For a single wavenumber component $\mathbf{q} \sim \exp(i\kappa x)$, we get in wavenumber space:

$$\hat{D}(\alpha) = d_0 + 2\sum_{n=1}^{M} d_n \cos(n\alpha), \tag{3.8}$$

where $\alpha = \kappa \Delta x$. The stencil coefficients are determined by constrains on the filter:

- Do not increase the amplitude of the wavenumber components: $\hat{D}(\alpha) > 0$,
- Very long wavelength components should not be modified: $\hat{D}(0) = 0$,
- Short wavelength components should be filtered: $\hat{D}(\pi) = 1$.

3.3.2 Boundary condition along the airfoil

The sources of noise are introduced as a hard-wall boundary condition along the airfoil using the characteristics formulation of Kim *et al.* [59].

First we need to define the characteristic waves in the normal direction to the airfoil surface. Along the boundary of the airfoil, we note $\boldsymbol{n} = (n_x, n_y)$ the unit normal vector pointing towards the wall and $\boldsymbol{\tau} = (-n_y, n_x)$ is the tangential vector. Eq. (3.5) can then be written[2]

$$\frac{\partial \mathbf{q}}{\partial t} + \frac{\partial \mathbf{C}\mathbf{q}}{\partial n} + \frac{\partial \mathbf{D}\mathbf{q}}{\partial \tau} = \mathbf{s}, \tag{3.9}$$

where $\mathbf{C} = \mathbf{A}n_x + \mathbf{B}n_y$ and $\mathbf{D} = -\mathbf{A}n_y + \mathbf{B}n_y$. $\mathbf{C}\mathbf{q}$ represents the flux in the direction normal to the airfoil. The previous equation can be rewritten yielding

$$\frac{\partial \mathbf{q}}{\partial t} + \mathbf{C}\frac{\partial \mathbf{q}}{\partial n} = \mathbf{r} \quad \text{with} \quad \mathbf{r} = \mathbf{s} - \frac{\partial \mathbf{D}\mathbf{q}}{\partial \tau} - \mathbf{q}\frac{\partial \mathbf{C}}{\partial n}. \tag{3.10}$$

$\mathbf{C}$ can be diagonalised as $\mathbf{C} = \mathbf{W}^{-1}\mathbf{\Lambda}\mathbf{W}$, where $\mathbf{\Lambda}$ is a diagonal matrix storing the eigenvalues and $\mathbf{W}$ is the matrix of eigenvectors. Therefore, multiplying by $\mathbf{W}^{-1}$ the above equations

$$\frac{\partial \tilde{\mathbf{q}}}{\partial t} + \mathbf{\Lambda}\frac{\partial \tilde{\mathbf{q}}}{\partial n} = \tilde{\mathbf{r}}, \tag{3.11}$$

where $\tilde{\mathbf{q}}$ denotes the amplitudes of the characteristics which are given by $\tilde{\mathbf{q}} = \mathbf{W}^{-1}\mathbf{q}$ and their phase speeds are determined by $\mathbf{\Lambda}$.

We now have to specify how to modify the amplitude of the acoustic wave travelling into the computational domain. We note $\tilde{\mathbf{q}} = (q_v, q_e, q_a^-, q_a^+)$ the amplitude of the characteristics corresponding to vorticity, entropy and acoustic waves, respectively. Using $\mathbf{q} = \mathbf{W}\tilde{\mathbf{q}}$ and $\boldsymbol{u}_0 \cdot \boldsymbol{n} = 0$ we can get

$$\rho_0 \boldsymbol{u}' \cdot \boldsymbol{n} = c_0 q_a^+ - c_0 q_a^- . \tag{3.12}$$

Then, the boundary condition can be imposed by rewritten the amplitude of the characteristic acoustic wave travelling into the computational domain in terms of the amplitude of the characteristic acoustic wave travelling out:

$$q_a^- = q_a^+ - \frac{\rho_0}{c_0}(\boldsymbol{u}' \cdot \boldsymbol{n}). \tag{3.13}$$

We then use $\mathbf{q} = \mathbf{W}\tilde{\mathbf{q}}$ to compute the modified value of the solution along the airfoil. This is done at every stage of the Runge Kutta scheme between tasks (3) and (4).

Note that we solve the linearised Euler equation for the scattered field only, therefore $\boldsymbol{u}' \cdot \boldsymbol{n}$ in Eq. (3.13) stands for the scattered turbulent velocity normal to the airfoil. Relating this with section 3.2.2, we find that Eq. (3.13) can be rewritten as

$$q_a^- = q_a^+ + \frac{\rho_0}{c_0}(\boldsymbol{u}_i' \cdot \boldsymbol{n}), \tag{3.14}$$

where $\boldsymbol{u}_i'$ is the incident turbulent velocity field which is computed along the airfoil with the random-vortex-particle method.

[2]Note that curvature terms are neglected in Eq. (3.9) since in this thesis we will only consider flat plates.

Another approach to implement the boundary condition along the airfoil was considered in this work. Instead of modifying the amplitudes of the characteristics, the rates of change of the amplitudes were modified. If we note $\mathbf{l} = (l_v, l_e, l_a^-, l_a^+)$ the rate of change of the characteristics corresponding to vorticity, entropy and acoustic waves respectively, we can write $\partial\mathbf{q}/\partial t = \mathbf{W}\mathbf{l}$. Proceeding as above, the boundary condition can be implemented on $\partial\mathbf{q}/\partial t$ by using

$$l_a^- = l_a^+ + \frac{\rho_0}{c_0}\frac{\partial}{\partial t}(\boldsymbol{u}_i' \cdot \boldsymbol{n}). \tag{3.15}$$

The reason for imposing for using Eq. (3.14) instead of Eq. (3.15) is that Eq. (3.15) requires second derivatives of the filter used to compute the synthetic velocity field, while Eq. (3.14) requires only first derivatives. In this study we work with filters corresponding to Gaussian, Liepmann and von Kármán spectra. The Gaussian filter is smooth and its derivatives can be computed up to any order. However, Liepmann and von Kármán filters are not differentiable at zero. This lack of smoothness has proved to introduce a significant source of error when implementing the boundary condition in terms of $\partial\mathbf{q}/\partial t$.

3.3.3 Non-reflecting boundary conditions

For isolated airfoils sounds propagates to infinity. To mimic this non-reflecting boundary conditions are implemented. The implementation is based on the use of a buffer zone in a region close to the boundary [60]. The actual size of the buffer zone is an input parameter. Along the grid points on the buffer zone the amplitude of the characteristic wave travelling into the simulation domain, q_a^-, is scaled by a factor α decreasing from 1 to 0: $q_a^-(1-\alpha)$. This means that the amplitude of the characteristic travelling into the domain is set to zero at the boundary of the computational domain and it is not modified at the beginning of the buffer zone providing a smooth transition to remove spurious reflections as the width of buffer zone increases [60].

3.3.4 Ffowcs-Williams Hawkings formulation

The acoustic solution in the far field is obtained with the Ffowcs-Williams Hawkings (FWH) formulation using a fixed control surface surrounding the sources and assuming a uniform mean flow outside the control surface.

The solution $\mathbf{q}$ along the control surface is stored at the required time steps during the simulation and then post-processed in Matlab using the FWH formulation in the frequency domain.

3.4 Validation

The validation of the linearised Euler equations solver for the study of broadband fan interaction noise is presented in this section. Since our aim in this section is to validate the LEE code, the random-vortex-particle method is not used. Instead we consider incident frozen gusts at different frequencies interacting with a flat plate with zero angle of attack. We are therefore checking that the LEE simulations are able to reproduce accurately the response function of the airfoil.

The parameters considered for this validation are the grid resolution, the pollution due to poorly resolved small wavelengths, the non-reflective boundary conditions, and the location of the Ffowcs-Williams Hawking control surface.

The influence of these parameters on the accuracy of the LEE solver is assessed by comparing the pressure jump along the airfoil and the far-field directivities against the analytical solutions obtained by Amiet in Ref. [17] modified for a fully two-dimensional problem. More information on Amiet's analytical solution can be found in section 3.1.1.

Sound Pressure Levels (SPL) in the far field shown here (and throughtout this thesis) are normalised by the distance d between the observer and the centre of the airfoil and by the turbulent kinetic energy K:

$$\mathrm{SPL} = 10 \log_{10} \left(\frac{d\ S_{pp}}{K} \right), \tag{3.16}$$

where S_{pp} is the Power Spectral Density (PSD) of the acoustic pressure field computed on a circular arc centred on the airfoil where angles are measured from the trailing edge. Due to the symmetry of the problem with respect to the x-axis, far-field acoustic results are shown for angles from 0 to 180 degrees only.

3.4.1 Problem definition

The problem is made non-dimensional using the chord of the airfoil, c, mean flow density, ρ_0, and sound speed, c_0. The mean flow velocity u_0 is parallel and uniform and its Mach number is set to 0.362 to considered the same test case as in Ref. [17].

The incident velocity field is a collection of frozen gusts excited at different frequencies and amplitudes, see Eq. (3.2). In this validation, we assume that the incident velocity field is the sum of three gusts with the same amplitude at the frequencies corresponding to the Strouhal numbers $St_1 = 6$, $St_2 = St_1/2$ and $St_3 = 2St_1$, respectively where $St_i = f_i c/u_0$ with f_i the frequency of the i^{th} gust. These frequencies were selected to cover the typical range of interest of broadband noise. Therefore, the incident turbulent

field imposed as a boundary condition along the airfoil (see section 3.3.2) is defined as:

$$u'_y(x,0,t) = \sum_{i=1}^{3} \cos\left[2\pi f_i(x/u_0 - t)\right]. \tag{3.17}$$

3.4.2 Computational setup

The simulation domain is $[-1.5, 1.5] \times [-1, 1]$ with the flat plate located at $[-0.5, 0.5] \times \{0\}$. This domain is divided into 6 blocks as shown in Figure 3.1. Each block is discretised with uniform grid using the same grid resolution for all blocks. Non-reflecting boundary conditions are implemented everywhere on the simulation domain by using buffer zones as explained in section 3.3.3.

The following baseline configuration is considered. Each block is discretised by with 200×200 points per block yielding a CFL number of 0.69. The size of the buffer zone is 10 grid points in every boundary apart from the outflow boundary where due to larger outgoing acoustic wavelengths a buffer zone of 40 points is used. The strength of the selective filter is set to 0.6 and the FWH control surface is the *'configuration 1'* shown in 3.2.

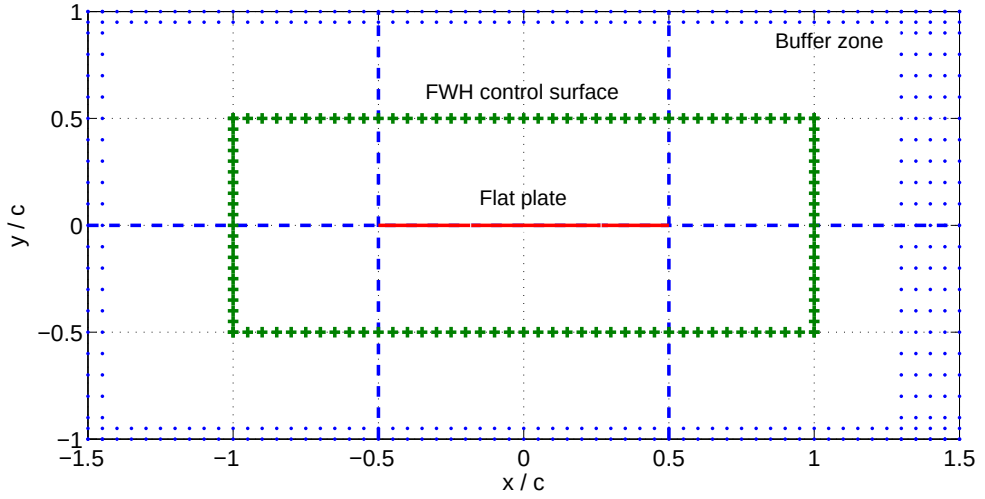

FIGURE 3.1: Sketch of the computational domain showing the flat plate location (—), the FWH control surface (+), the block distribution (– –), and the buffer zone (···).

3.4.3 Validation of FWH formulation

The Ffowcs-Williams Hawking formulation is employed to compute far-field results. The influence of the choice of control surface on the far-field results is assessed by considering three different control surface configurations. Each one of the configurations is a rectangle surrounding the airfoil as shown in Figure 3.2. Results obtained with each of these

are compared in order to assess the sensitivity of the far-field solution to the choice of control surface. Simulation results shown here correspond to the computational setup described above and with each block discretised by a uniform grid with 200 points in each direction.

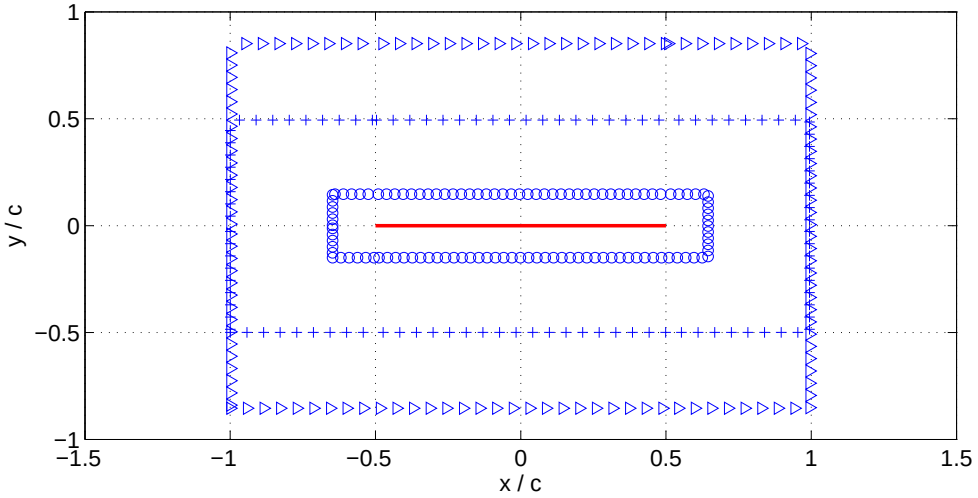

FIGURE 3.2: Configurations of the FWH control surface: *'configuration 1'* (+), *'configuration 2'* and (∘), and *'configuration 3'* (▷).

Figure 3.3 shows the error incurred with the different control surfaces at the highest Strouhal number St_3. The error shown is the relative error given by $|p_i(\theta) - p_j(\theta)|/|p_i(\theta)|$ where p stands for the PSD of the acoustic pressure field in the far-field and the subscripts i and j refer to different control surfaces. It is found that the relative error is larger when considering *'configuration 2'*. This suggests that this control surface is too close to the airfoil and that the solution at the FWH control surface is polluted due to the presence of vortices, see Figure 3.6. The relative error between *'configuration 1'* and *'configuration 3'* is of the order of 2%. This shows that provided that the control surface is located far enough from the turbulent flow surrounding the airfoil, it has little influence on far-field acoustic results computed with the Ffowcs-Williams Hawking formulation. Similar levels of error are obtained for the Strouhal numbers St_1 and St_2. Due to the smaller amount of data storage required by *'configuration 1'* compared to *'configuration 3'*, the former is selected.

3.4.4 Non-reflecting boundary conditions

In order to test the presence of spurious reflection at the boundaries due to the non-reflecting boundary condition, a larger computational domain is considered. This computational domain is $[-4.5, 4.5] \times [-2, 4]$ with the flat plate located at $[-0.5, 0.5] \times \{0\}$, see Figure 3.4. The same configuration as for the baseline case is used but with increased size. Due to the symmetry of the problem with respect to the x-axis, the upper

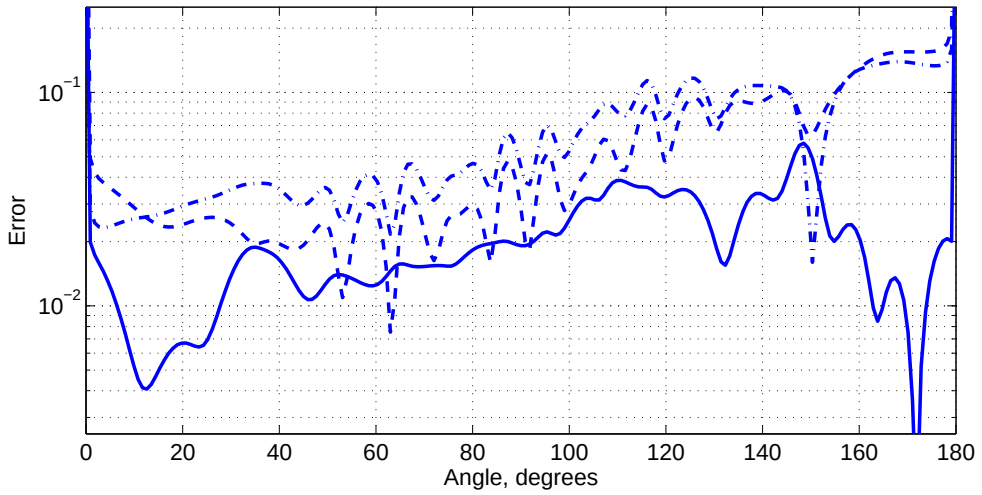

FIGURE 3.3: Relative error in directivity for Strouhal number St_3 obtained from three different configurations of the FWH control surface. *'configuration 1'* vs *'configuration 2'* (– –), *'configuration 1'* vs *'configuration 3'* (——) and *'configuration 2'* vs *'configuration 3'* (– · –).

side of the flat plate was further extended than the lower side, in order to reduce the computational cost.

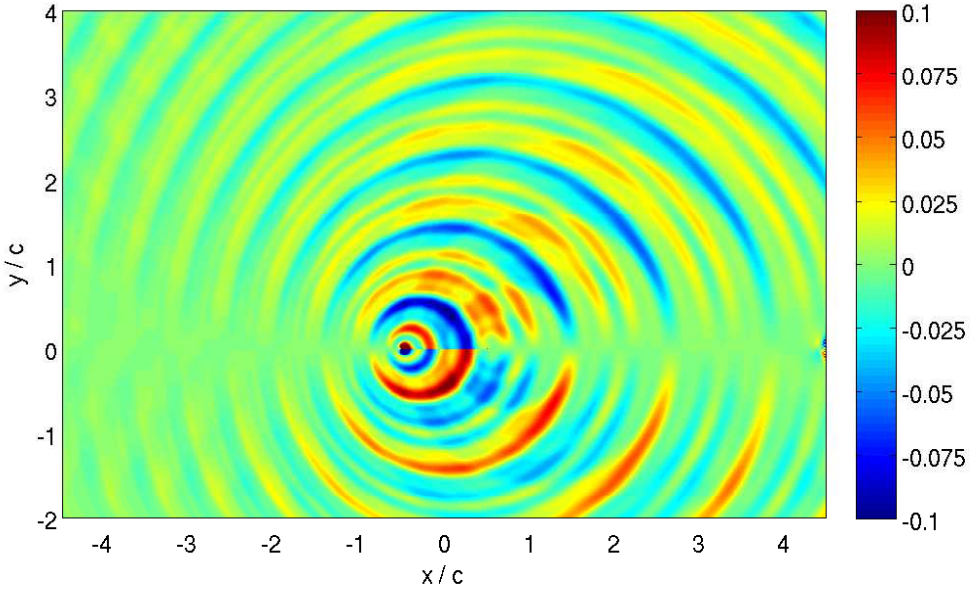

FIGURE 3.4: Snapshot of the acoustic pressure field for incident frozen gusts at Strouhal numbers $St_1 = 6$, $St_2 = St_1/2$ and $St_3 = 2St_1$.

Sound pressure levels obtained directly using the larger simulation domain at a distance $d = 3$ from the centre of the flat plate are compared against the FWH far-field solution given by *'configuration 1'* in Figure 3.5. Directivities predicted with the FWH formulation are in very good agreement with those obtained directly for Strouhal numbers St_1 and St_2. This suggests that at $d = 3$ we already observe the $1/r$ decay characteristic

of the PSD associated with cylindrical spreading of 2D waves. This distance captures at least 3 acoustic wavelengths for the smallest Strouhal number (based on zero Mach number). For the highest Strouhal number St_3 similar patterns are predicted by both methods, but the noise levels computed directly decrease faster as the angle increases compared to results obtained with FWH formulation. This corresponds with the smallest acoustic wavelengths we have (highest frequency and waves travelling upstream), therefore the difference observed can be related to the dissipation caused by the selective filter to remove small wavelengths, see section 3.3.1. Acoustic waves must travel the computational domain longer if computed directly at $d = 3$, and the selective filter seems to have a noticeable effect on these particular waves. (The effects of the filter strength are examined in the next section.)

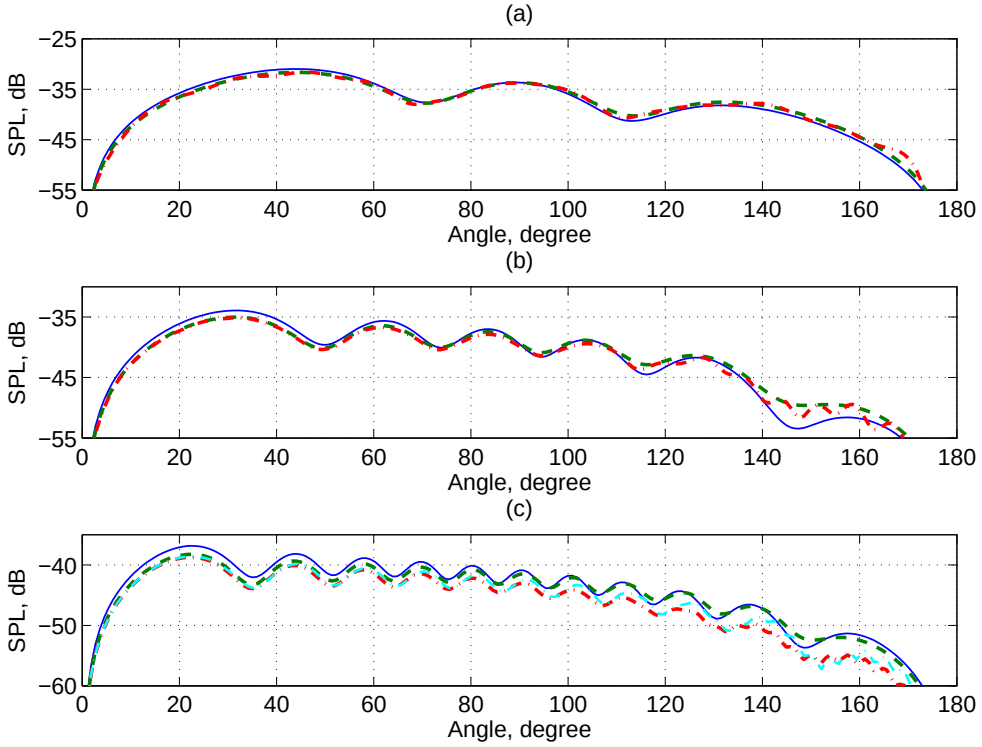

FIGURE 3.5: Directivity at Strouhal numbers $St_2 = St_1/2$ (a), St_1 (b), and $St_3 = 2St_1$ (c) obtained using Amiet's analytical solution (——), FWH formulation (– –) and computing directly (– · –). For St_3, (– · –) corresponds to results obtained with the selective filter strength set to 0.4.

If we now compare numerical results against Amiet's analytical solution, we can see that SPL predicted by the FWH formulation are in good agreement with analytical SPL for the three frequencies in a margin of 2 dB. In addition to possible pollution due to the selective filter, another explanation for the disagreement in amplitude between the acoustic pressure field computed with FWH formulation and Amiet's analytical solution is the vortex shedding. Vortex shedding is produced at the trailing edge due to the pressure discontinuity between the upper and lower sides of the flat plate, as illustrated in Figure 3.6. However the presence of vortices crossing the FWH control

surface downstream of the airfoil can introduce spurious noise sources. This pollution due to vortex shedding, although small, could be significant at high frequencies, relative to the noise levels.

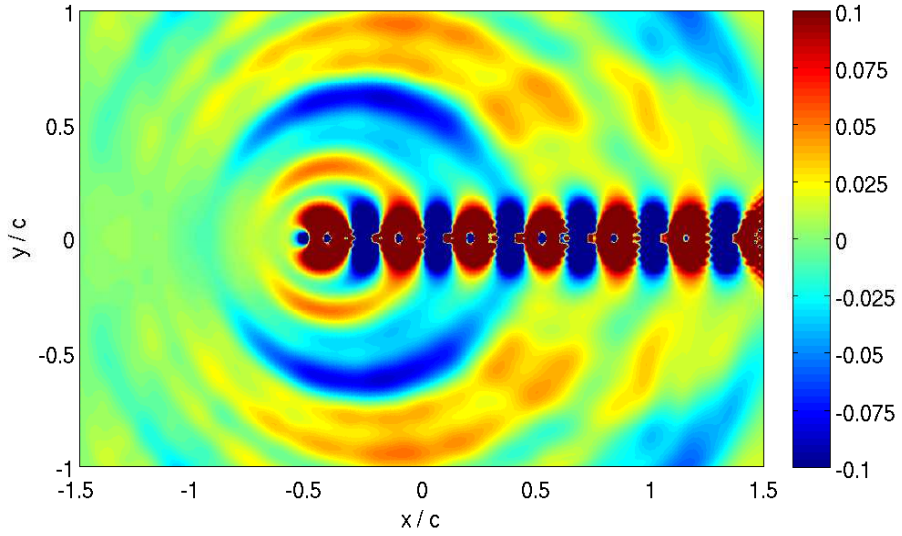

FIGURE 3.6: Snapshot of the velocity in the normal direction incident frozen gusts at Strouhal numbers $St_1 = 6$, $St_2 = St_1/2$ and $St_3 = 2St_1$.

3.4.5 Selective filter strength

As explained in section 3.3.1, poorly resolved wavelengths are removed by a selective filter which is grid-dependent. The influence of the strength of the filter is measured here by comparing numerical far-field directivities against Amiet's analytical solution. To illustrate this, Figure 3.7 shows the influence of the filter strength on the far-field acoustic pressure for the highest Strouhal number, St_3, as it is more sensitive to the choice of filter strength than both St_1 and St_2. In this case the simulation domain is discretised by a uniform grid with 200×200 points on each block. One can see that the PSD is sensitive to the filter strength, especially at upstream locations. The best approximation to Amiet's analytical solution is provided by the filter strength 0.6. This suggests that by selecting the filter strength too low poorly resolved wavelengths introduce pollution in the solution and if the strength is set too high dissipation occurs, as shown in Figure 3.5.

3.4.6 Grid resolution

A parametric study is also performed on the grid resolution by considering 100×100, 200×200, and 300×300 points per block. This yields a grid resolution of at least 7 points per hydrodynamic wavelength and 13 points per acoustic wavelength for the grid

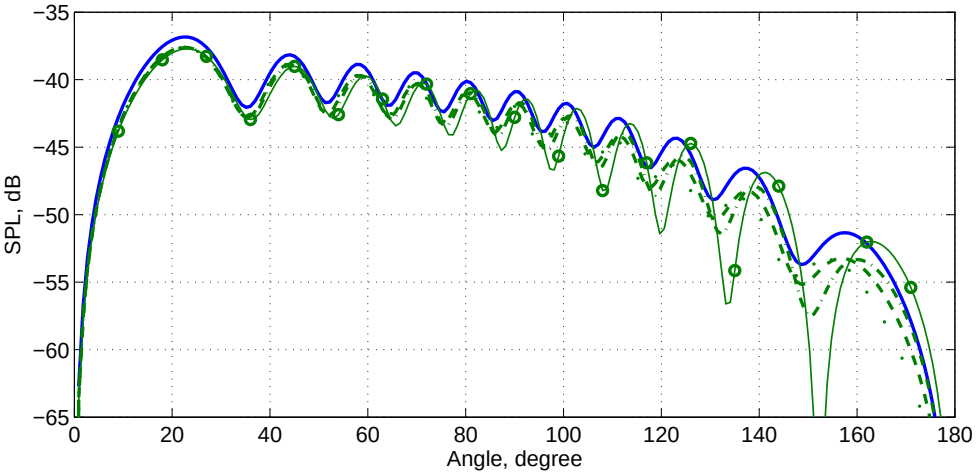

FIGURE 3.7: Influence of the filter strength for uniform grid with 200×200 points per block. Analytical (——) directivity at Strouhal number $St_3 = 2St_1$ versus numerical results for the filter strengths: 0.2 (– ∘ –), 0.4 (– · –), 0.6 (– –), and 1 (· · ·).

with 100×100 points. The time step is left constant and the CFL number corresponding to each grid is 0.23, 0.46, and 0.69, respectively. The strength of the filter that removes poorly resolved wavelengths is grid dependent, therefore for each grid the filter strength is selected by performing a parametric study as shown in the previous section yielding the strengths 0.4, 0.6, and 0.8, respectively.

Far-field directivities obtained using the grids under investigation are compared in Figure 3.8. While the grid with 100×100 points is too coarse to provide an accurate approximation of Amiet's solution, similar levels of error are found between the far-field directivities obtained with the grid with 200×200 points and 300×300 points with respect to the analytical solution. Due to the limited improvement in accuracy and substantial increase in computational cost, the grid with 200×200 points is preferred over the grid with 300×300 points.

3.4.7 Pressure jump along the airfoil

The pressure jump along the airfoil is now used to fully validate the airfoil response function. For this test case, each block uses a uniform grid of 200×200 points and a selective filter strength 0.6.

The amplitude of the pressure jump along the flat plate is shown in Figure 3.9. Numerical results are in good agreement with Amiet's analytical solution for the three Strouhal numbers under investigation. Amplitude levels are well captured along the airfoil with a slight change in local maxima, especially on the front half of the airfoil. Note that the leading edge of the flat plate is a pressure singularity which is particularly difficult to handle in numerical methods.

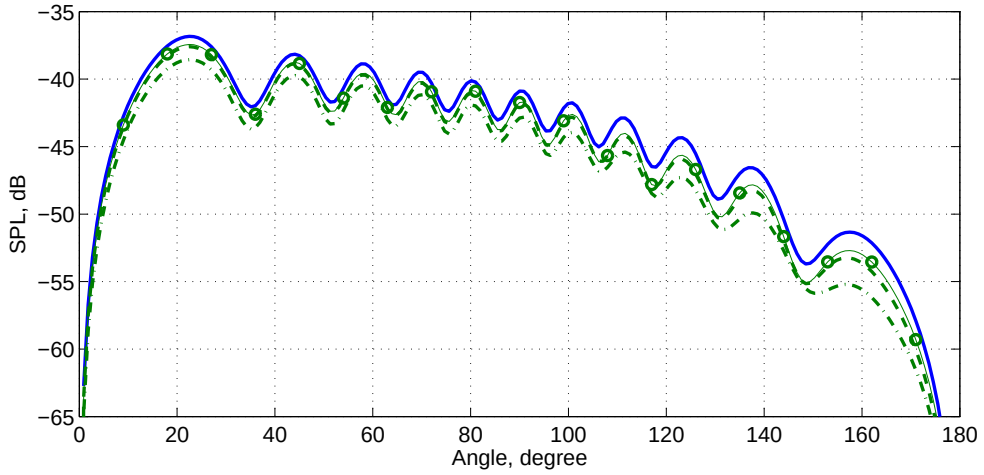

FIGURE 3.8: Comparison of uniform grids with different number of points per block. Analytical (——) directivity at Strouhal number $St_3 = 2St_1$ versus numerical results for grids with 100×100 (– · –), 200×200 (– –), and 300×300 (– ○ –) points.

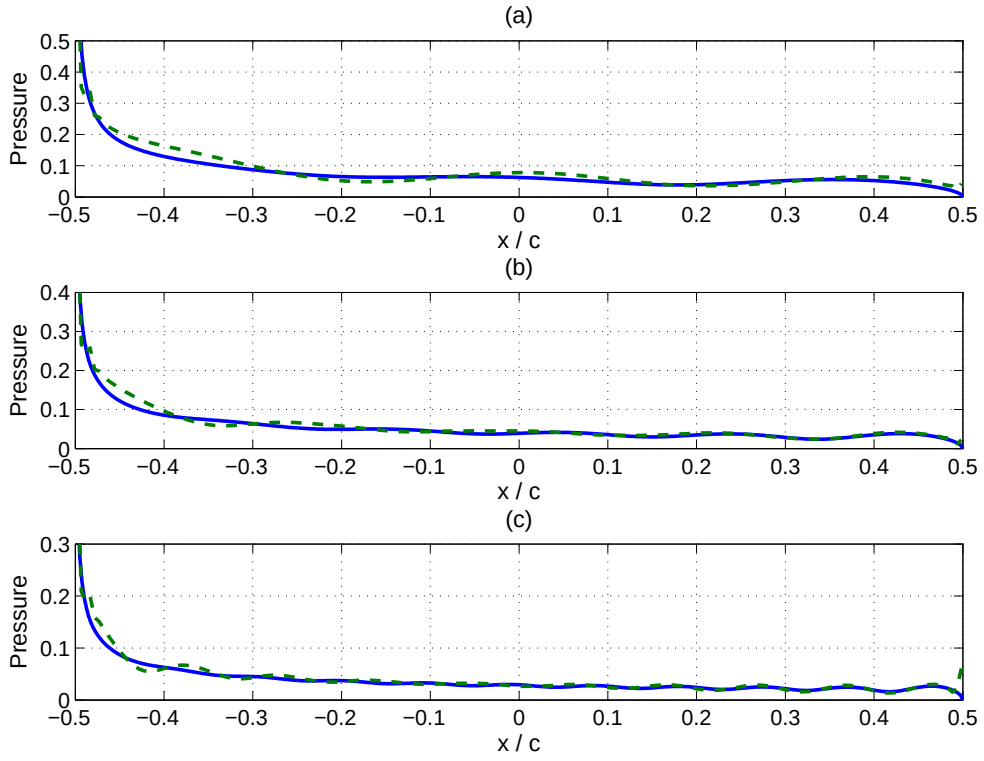

FIGURE 3.9: Analytical (——) versus numerical (– –) amplitude of the pressure jump along the airfoil at Strouhal numbers $St_2 = St_1/2$ (a), $St_1 = 6$ (b), and $St_3 = 2St_1$ (c).

Another feature that can be observed in Figure 3.9 is that the Kutta condition (zero pressure jump) at the trailing edge is not fully satisfied by the LEE solver. The accuracy of this trailing-edge boundary condition is not critical for interaction noise as the sound production is dominated by the leading edge. However, the treatment of the trailing edge changes the interference pattern between acoustic waves scattered at the trailing edge and noise radiated at the leading edge[3].

3.4.8 Conclusions

The LEE solver has been validated and it was shown that the response of an airfoil to incident frozen gust can be very accurately predicted. In addition, from the parametric study presented in this section the following guidelines are obtained. Each block on the simulation domain is discretised by a uniform grid of 200×200 points using a selective filter to remove poorly resolved small scale components with strength 0.6. Far-field results are obtained using FWH formulation with the control surface defined by *'configuration 1'*.

Numerical solutions for the pressure jump along the airfoil and far-field directivities obtained for this choice of parameters are in good agreement with Amiet's analytical solution. Regarding the pressure jump along the airfoil, the overall shape is recovered although the local maxima are not located at the same positions. This could be caused by a lack of resolution of the trailing edge where acoustic waves are scattered back towards the leading edge and the numerical difficulties associated with the singularity at the leading edge. Far-field directivities are also very well captured by the numerical method, see Figure 3.10. Numerical SPL slightly differs from Amiet's analytical solution upstream of the airfoil as the frequency increases. It is our understanding that the pollution introduced by the vortex shedding crossing the FWH control surface could also affect the results in the far field.

From the detailed tests shown in this chapter, we are confident that the numerical solutions provided by the LEE solver are accurate for the parameter values described above. In the next chapters of this thesis, the linearised LEE solver is combined with the random-vortex-particle method to predict broadband fan interaction noise.

[3] Two numerical approaches were considered in an attempt to improve the resolution of the trailing edge. The first of them is the numerical treatment of the trailing edge proposed by Sandberg *et al.* in Ref. [49] where for the first two grid points downstream of the trailing edge the streamwise derivatives are determined employing the same central finite-difference scheme as everywhere else in the domain but with values of the upstream points being specified as the average of the top and bottom surfaces. This smoothes the pressure discontinuity at the trailing edge. The second approach considered consisted in applying a window filter to the synthetic velocity field along the flat plate so that the amplitude of the wall velocity is not modified near the leading edge and then it is smoothly reduced reaching zero before the trailing edge. None of these approaches led to a significant improvement in far-field accuracy and were therefore rejected.

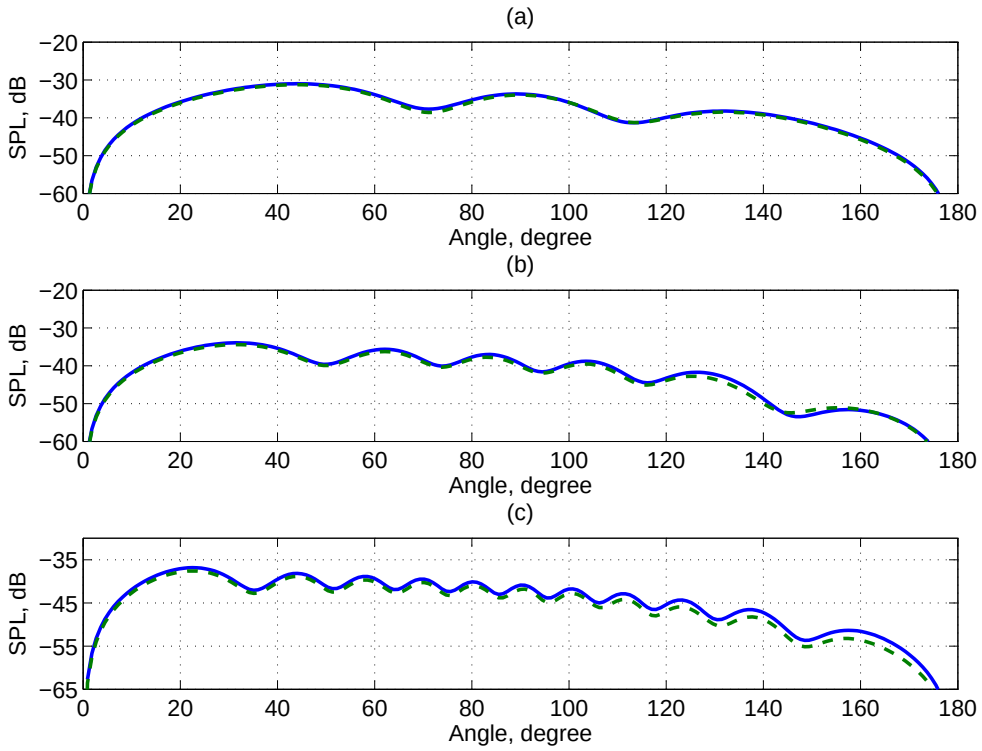

FIGURE 3.10: Analytical (——) versus numerical (– –) far-field directivities at Strouhal numbers $St_2 = St_1/2$ (a), $St_1 = 6$ (b), and $St_3 = 2St_1$ (c).

Chapter 4

Frozen Turbulence

In this chapter, the generation of broadband noise due to the interaction of frozen turbulence with a flat plate and its propagation are discussed. By frozen turbulence we mean that not only the statistical behaviour of the flow is frozen but also the turbulent velocity field is frozen with respect to a frame of reference moving with the mean flow. So there is no loss of correlation with time and the velocity field seen by an observer moving with the mean flow is constant.

Parametric studies are performed to test both the quality of the synthetic turbulent flow and the accuracy of the predicted sound field. Therefore, this chapter serves as a validation of the stochastic method presented in chapter 2 and also to the complete sound propagation method described in chapter 3. The computational performance of the method for the Gaussian, Liepmann and von Kármán energy spectra is also discussed.

4.1 Definition of the test case

The test case considered is a flat plate with zero angle of attack interacting with homogeneous isotropic frozen turbulence. The problem is made non-dimensional using the chord of the airfoil c, mean flow density ρ_0 and sound speed c_0. The parameters are chosen to be similar to the test case previously presented by Amiet in Ref. [17] with both his analytical solution and experimental data. For this test case the mean flow Mach number is set to 0.362 and the turbulence integral length scale is $\lambda = 0.07$. Note that the inputs for the stochastic method are not provided by RANS but instead the turbulence is specified upstream independently of the airfoil.

This test case is very well suited for the validation of the numerical method because analytical solutions are available. Amiet's analytical solution in Eq. (3.1) is used to

assess the accuracy of the method and also to determine trade-offs between accuracy and computational costs.

4.2 Computational setup

The simulation domain is $[-1.5, 1.5] \times [-1, 1]$ with the airfoil located at $[-0.5, 0.5] \times \{0\}$. The domain is divided into 6 blocks, each of them discretised by a Cartesian grid with 200 points in each direction. The time step is such that the CFL number is 0.8.

This computational domain was already used to validate the linearised Euler equations solver, and therefore the guidelines obtained from the parametric study performed in section 3.4 apply here. The strength of the selective filter is set to 0.6 and far-field results are obtained using FWH formulation with the control surface defined by *'configuration 1'* as shown in Figure 3.2.

Vortex particles are launched from a vertical segment upstream of the flat plate and convected with the mean flow. Due to the assumption of frozen turbulence, the vortex strengths remain constant in time and they are randomly chosen using a Gaussian distribution with zero mean and standard deviation determined by the vortex density, see section 2.3.1. Vortices are removed once they are out of the range of influence of the flat plate in order to reduce the computational cost.

4.3 Results

We begin by validating the turbulent field generated by the random-vortex-particle method in Eq. (2.61). We then assess the accuracy of the acoustic far field by comparing sound pressure levels against Amiet's analytical solution for a fully two-dimensional problem, see Eq. (3.1). The derivation of the analytical solution can be found in Appendix C.1.

4.3.1 Synthetic turbulence

The validation of the stochastic method performed in section 2.5 was restricted to separable filters and included no time-dependence. Here, however, neither of these constrains are considered. In addition, while the method was implemented in a grid-based discretisation in the previous validation, in this case a purely Lagrangian approach is used. The validation of the correlations along the flat plate will therefore act as a validation of the method to generate synthetic turbulence on its Lagrangian version.

4.3.1.1 Two-point correlations and one-dimensional spectra

In this section, the quality of the synthetic turbulence generated by the random-vortex-particle method is assessed by evaluating two-point correlations and one-dimensional spectra along the airfoil. Extensive parametric studies are performed for Gaussian, Liepmann and von Kármán filters in order to find the optimum parameters for the method. For the sake of brevity, details of the parametric study are shown for the Gaussian spectra and then only the main results are presented for Liepmann and von Kármán spectra.

At this point, it might be useful to highlight two features of the synthetic turbulence. First, the use of random number generators in the numerical method has an impact on assessing the influence of the parameter values on the statistical behaviour of the turbulence[1]. The other issue is that there is no clear criteria to state when the statistics are sufficiently accurate. Because this is a validation, we consider more samples that needed in practice. Due to this, we focus on the trends of the statistical properties and simply examine their sensitivity to the different parameters involved in the generation of synthetic turbulence.

The influence of the parameters involved in generating synthetic turbulence with the random-vortex-particle method can be divided in two categories. The first one is how to distribute the vortices. This is controlled by two parameters: the maximum distance r_{max} from the flat plate at which the vortex particles still contribute to the velocity field and the distance Δ between vortices, see Figure 4.1. The maximum distance r_{max} essentially defines the size of the region around the airfoil where random vortices need to be distributed. Within this region, vortices are located following a Cartesian distribution determined by the distance Δ. Hence, the number of vortices varies roughly as $(r_{max}/\Delta)^2$. The accuracy of the method is improved by considering large r_{max} and increasing the density of vortices (small Δ), but this has an influence on the computational cost. The second category is how to sample the numerical solution to obtained reliable statistics. This is controlled by the number of samples, N_s, the sampling rate, Δ_s, and the total number of time steps that needs to be considered, N_f. The Central Limit Theorem shows that the accuracy of the statistics increases as more random data is considered [35]. This also has an influence on the computational cost of the method (running the simulation for a large number of time steps N_f and storing many samples N_s).

[1] Random number generators use computational algorithms that produce sequences of pseudorandom numbers determined by a seed. By using different seeds, the random-vortex-particle yields different velocity fields even when selecting the same parameter values which will be reflected in the statistics. Using the same seed provides the same series of random numbers but a change in the parameters of method has an influence on how they are used and hence different velocity fields are obtained. These aspects complicate assessing the influence of the different parameter values in the statistics of the turbulence.

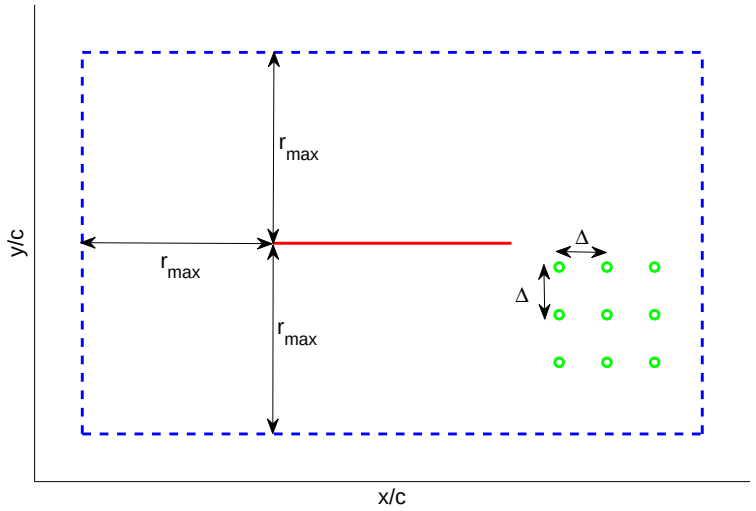

FIGURE 4.1: Sketch of the region around the airfoil where vortices are distributed showing the maximum distance r_{max} at which vortices must be located and the distance Δ between vortices.

We first discuss trade-offs between computational cost and accuracy due to the vortex distribution and we then consider the sampling of the numerical solution.

The maximum distance at which a vortex is yet significantly contributing to the velocity field is defined in terms of the integral length scale of the turbulence as $z_{max} = r_{max}/\lambda$. The influence of the filter in the velocity field is controlled by z_{max} – see Eqs. (2.86), (2.89) and (2.92) – and it decreases as z_{max} increases, see Figure 2.2. Therefore, we can get a cutoff for z_{max} that depends on the filter. This cutoff is set at 10^{-4}; a vortex is no longer contributing to the velocity field when the amplitude of the first derivative of filter at the distance at which the vortex is located is smaller than 10^{-4}. As it has been argued in section 2.4.4, Liepmann and von Kármán filters have a slower rate of decay with distance than the Gaussian filter, see Figure 2.2. That means that vortices further away from a given location on the flat plate will no longer contribute to the velocity field when using a Gaussian filter but they will do with any of the other two filters. In particular, $r_{max} = 2.43\lambda$ for Gaussian filter, $r_{max} = 4.57\lambda$ for Liepmann filter and $r_{max} = 5.43\lambda$ for von Kármán filter.

The distance Δ between vortices determines the density of vortices surrounding the flat plate. The effect of the density of vortices on the quality of the synthetic turbulence along the flat plate is examined by assessing the two-point correlations R_{11} and R_{22} (see Eq. (2.36)) and the one-dimensional energy spectra E_{11} and E_{22}. Note that the one-dimensional energy spectrum E_{ij} is defined as twice the one-dimensional Fourier transform of R_{ij} (see Ref. [14])

$$E_{ij}(\kappa) = 2 \int_{\mathbb{R}} R_{ij}(r) \exp(-i\kappa r) \mathrm{d}r. \tag{4.1}$$

Figure 4.2 compares stochastic and theoretical two-point correlations R_{11} and R_{22} and one-dimensional energy spectra E_{11} and E_{22} computed using the Gaussian filter for vortex density corresponding to $\Delta = \lambda/2$, $\Delta = \lambda/6$, $\Delta = \lambda/10$, and $\Delta = \lambda/16$. It appears that the statistics of the synthetic velocity field are not highly sensitive to the distance between vortices provided that they are at least $\Delta = \lambda/6$ close to each other. If we focus on the correlations obtained for the case $\Delta = \lambda/2$, we see that the stochastically generated correlations have problems capturing the peak at $r = 0$ and also the fact that the correlation tends to zero as the distance increases. However, similar levels of error are found by distributing the vortices at distances $\Delta < \lambda/6$. Since the synthetic velocity field at each point is computed as the sum of the contributions of the vortices closer than r_{max}, the smaller Δ is, the more expensive the method is from a computational point of view. As a trade-off between accuracy and computational cost, for the synthetic velocity field computed with the Gaussian filter, we propose to distribute the vortices every $\Delta = \lambda/6$.

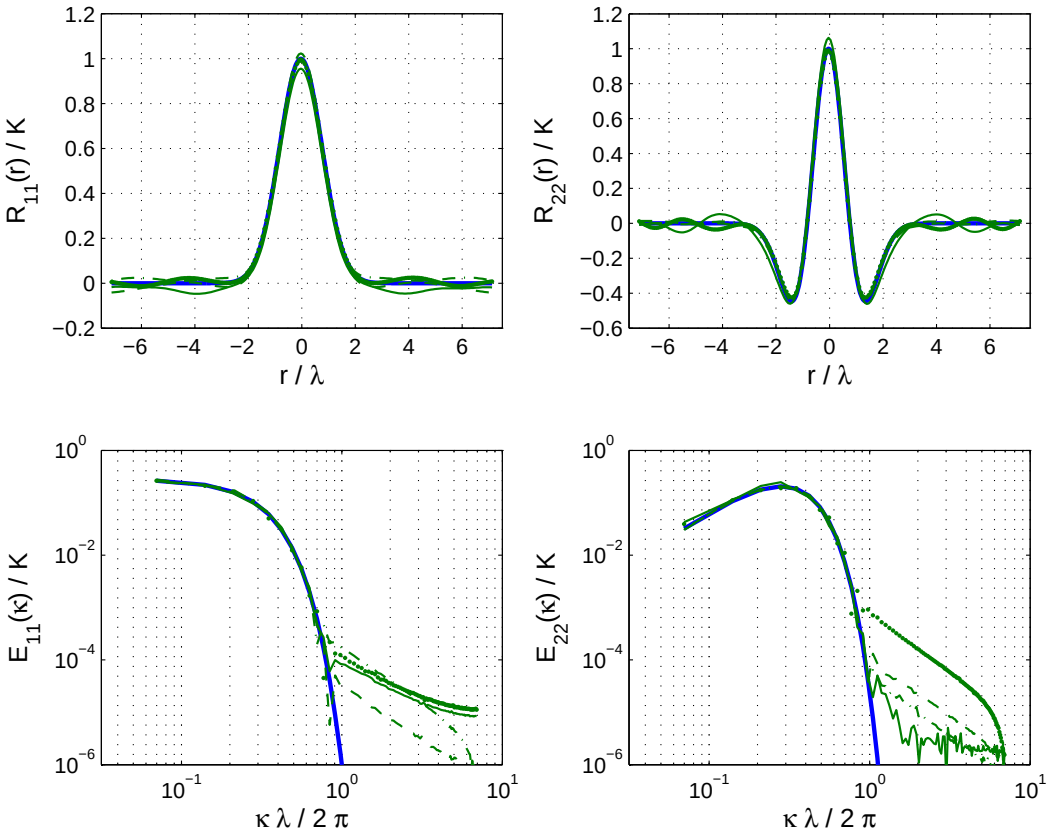

FIGURE 4.2: Analytical solution (—) against numerical results obtained with the Gaussian filter for vortex distance $\Delta = \lambda/2$ (—), $\Delta = \lambda/6$ (– · –), $\Delta = \lambda/10$ (– –) and $\Delta = \lambda/16$ (∗). Top: correlations R_{11} and R_{22} computed with respect to the central point of the airfoil. Bottom: one-dimensional energy spectra E_{11} and E_{22}. Averages taken over $N_s = 2,500$ samples at a sampling rate $\Delta_s = 40\Delta t$.

Another important aspect is the way the numerical solution is sampled to compute reliable statistics. If averages are taken over N_s number of samples at a sampling rate

Δ_s, then it means that the simulation runs for at least $N_f = N_s\Delta_s/\Delta t$ time steps, or equivalently the total simulation time is $T_f = \Delta_s N_s$. (Note that the total simulation time here does not include the initial time required to clean the computational domain.) Therefore, on the one hand, the more samples and the further apart they are picked, the more computationally expensive the method is. On the other hand, one has to ensure that enough different random data is contributing to the time series in order to obtained meaningful statistics. In this case, we have to ensure that different vortex particles are contributing to the time series. The sensitivity to the sampling parameters is now evaluated for a fixed distance between vortices Δ and distance of influence r_{max}.

Figure 4.3 shows the influence of increasing the number of samples N_s from $1,000$ to $20,000$ on the two-point correlations R_{11} and R_{22} and the one-dimensional energy spectra E_{11} and E_{22}. While the behaviour of the analytical correlation R_{22} is captured using $5,000$ samples, the R_{11} correlation is yet not well approximated. The numerical correlation R_{11} computed with $5,000$ samples is neither able to reproduce the peak as $r \to 0$ neither the decay as $r \to \infty$; in fact at least $20,000$ samples are required to have a good approximation as $r \to 0$. Regarding the one-dimensional energy spectra, more than $10,000$ samples have to be considered in order to capture the behaviour of E_{11} for small wavenumbers. Note that the larger the number of samples, the more expensive the method is as the simulation will need to run longer.

The influence of the sampling rate Δ_s is now assessed by fixing the number of samples to $N_s = 20,000$. Figure 4.4 shows that the stochastic two-point correlations R_{11} and R_{22} and the one-dimensional energy spectra E_{11} and E_{22} of the synthetic turbulence tend to theoretical results as the sampling rate increases, although little sensitivity to a change of sampling rate from $\Delta_s = 5\Delta t$ to $\Delta_s = 20\Delta t$ is found. The explanation for this phenomena is related to the constrain of frozen turbulence. As it has been previously discussed, the synthetic velocity field is frozen in the sense that if we move along with the flow we always see the same velocity pattern. By considering a sampling rate small in comparison with the time that it takes to a vortex to travel a distance r_{max}, the velocity field captured by two consecutive samples is essentially the same. Therefore, there are samples carrying redundant information. This can be solved by increasing the sampling rate which implies that for the same number of samples the simulation must be run longer and it is therefore more expensive.

We now fix the total computational time of the simulation and examine the influence of the sampling rate on the statistics of the turbulence along the airfoil. Figure 4.5 shows the influence of the sampling rate from $\Delta_s = 5\Delta t$ to $200\Delta t$ for a fixed number of time steps $N_f = 100,000$. Note that in this case the number of samples is not constant. The larger the sampling rate, the smaller the time series to compute the statistics is. A sampling rate larger than $100\Delta t$ does not capture the two-point correlations. If we focus on the stochastic R_{11} correlation, it does not tend to zero as the distance increases.

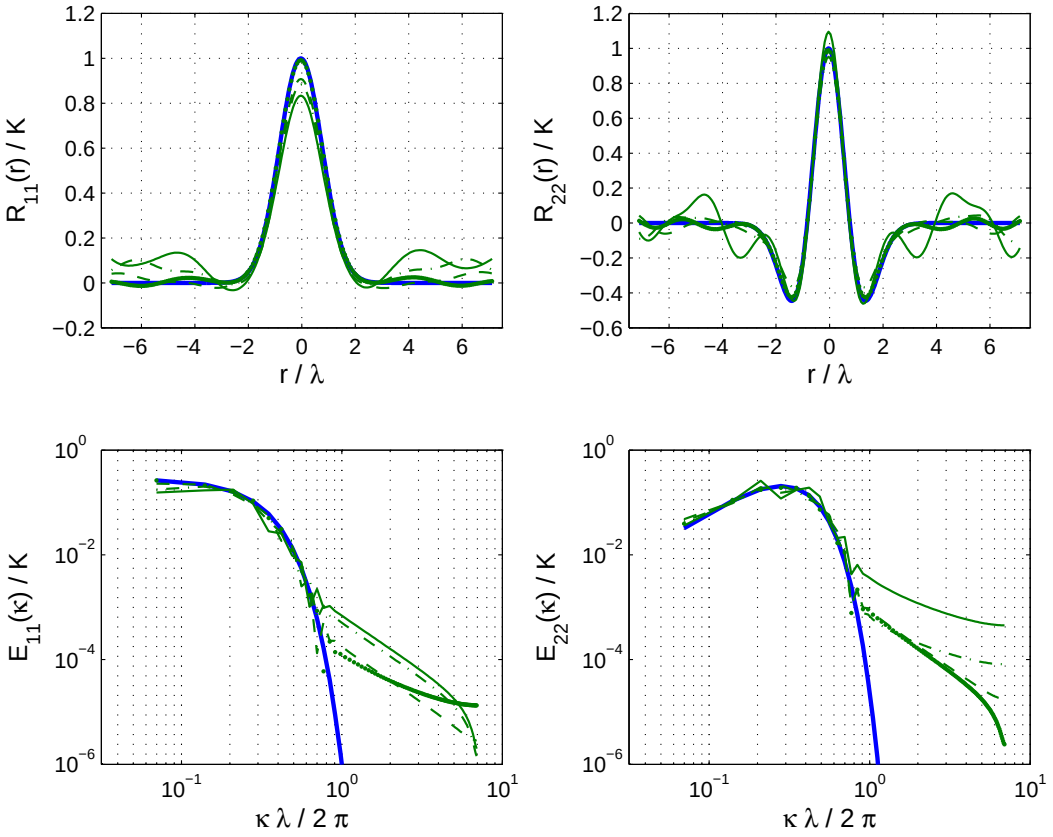

FIGURE 4.3: Analytical solution (—) against numerical results obtained with the Gaussian filter for number of samples $N_s = 1,000$ (—), $N_s = 5,000$ ($- \cdot -$), $N_s = 10,000$ ($- -$), and $N_s = 20,000$ ($*$). Top: correlations R_{11} and R_{22} computed with respect to the central point of the airfoil. Bottom: one-dimensional energy spectra E_{11} and E_{22}. Vortices distributed every $\Delta = \lambda/16$ and sampling rate $\Delta_s = 5\Delta t$.

However, neither the correlations nor the spectra are sensitive to a sampling rate smaller than $50\Delta t$ which corresponds to $N_s = 2,000$.

From this parametric study, it can be concluded that the parameter values $r_{max} = 2.43\lambda$ and $\Delta = \lambda/6$ generate synthetic turbulent velocity fields computed using the Gaussian filter that accurately reproduce the two-point correlations and one-dimensional energy spectra when considering $N_s = 2,500$ samples at a rate $\Delta_s = 40\Delta t$, see Figure 4.6.

Similar parametric studies have been carried out for Liepmann and von Kármán filters and they provide the following results. For the Liepmann filter, a sufficient level of agreement between the stochastically generated correlations R_{11} and R_{22} and the one-dimensional energy spectra E_{11} and E_{22} with their corresponding analytical expressions is achieved for the parameter values: $r_{max} = 4.57\lambda$, $\Delta = \lambda/8$, $N_s = 8,000$ and $\Delta_s = 60\Delta t$ as shown in Figure 4.7. Regarding the von Kármán filter, $r_{max} = 5.43\lambda$, $\Delta = \lambda/8$, $N_s = 8,000$ and $\Delta_s = 60\Delta t$ have been selected in order to obtain satisfactory agreement with analytical results, see Figure 4.8.

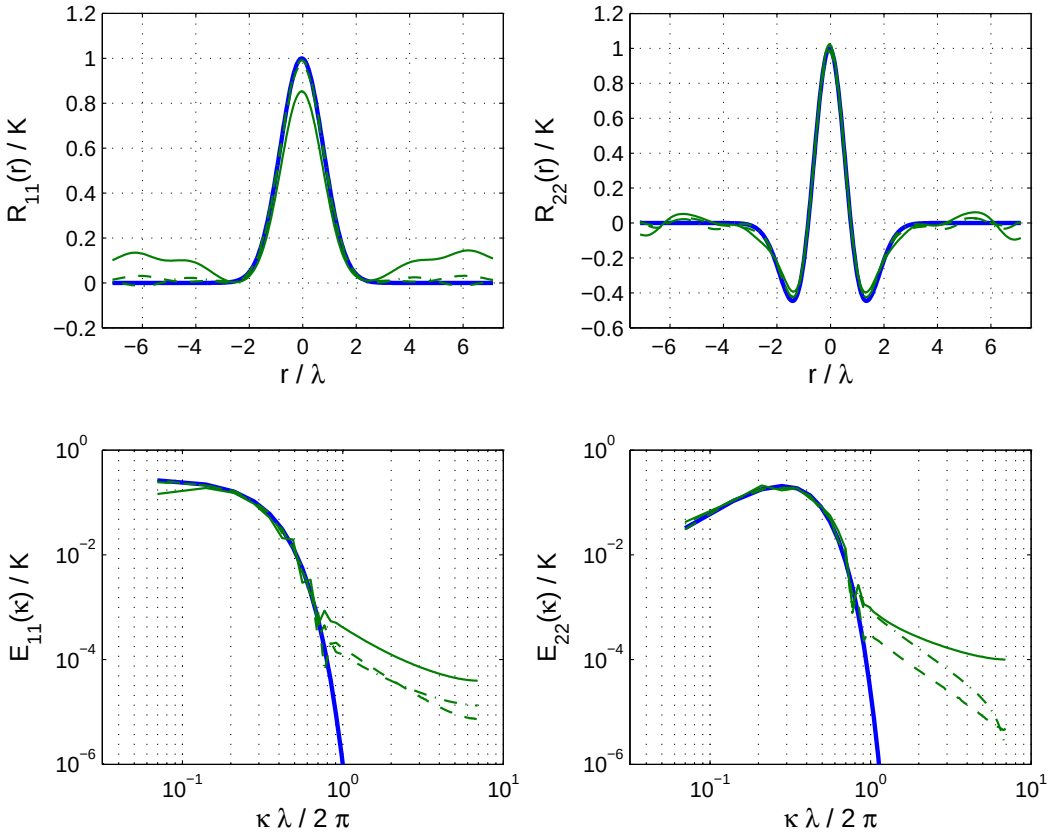

FIGURE 4.4: Analytical solution (—) against numerical results obtained with the Gaussian filter with sampling rate $\Delta_s = 1\Delta t$ (—), $\Delta_s = 5\Delta t$ (– · –), and $\Delta_s = 20\Delta t$ (– –). Top: correlations R_{11} and R_{22} computed with respect to the central point of the airfoil. Bottom: one-dimensional energy spectra E_{11} and E_{22}. Vortices distributed every $\Delta = \lambda/16$ and number of samples $N_s = 20,000$.

Note that the for Liepmann and von Kármán filters vortices are distributed at a smaller distance Δ compared to that selected for the Gaussian filters. This choice relates with the larger content of large wavenumbers present in Liepmann and von Kármán models. Compare for instance the one-dimensional energy spectra in Figures 4.6, 4.7 and 4.8. Large wavenumbers – or high frequency – content is produced by small vortices and the size of a vortex is controlled by the distance Δ, see Eq. (2.68).

Finally note that methods to generate synthetic turbulence based on Fourier modes (SNGR methods) are somehow criticised due to the large number of modes that must be considered in order to compute the velocity field, see section 2.1. However, it appears from the parametric studies performed in this section that methods based on filtering random data present a similar problem requiring large amounts of vortex particles.

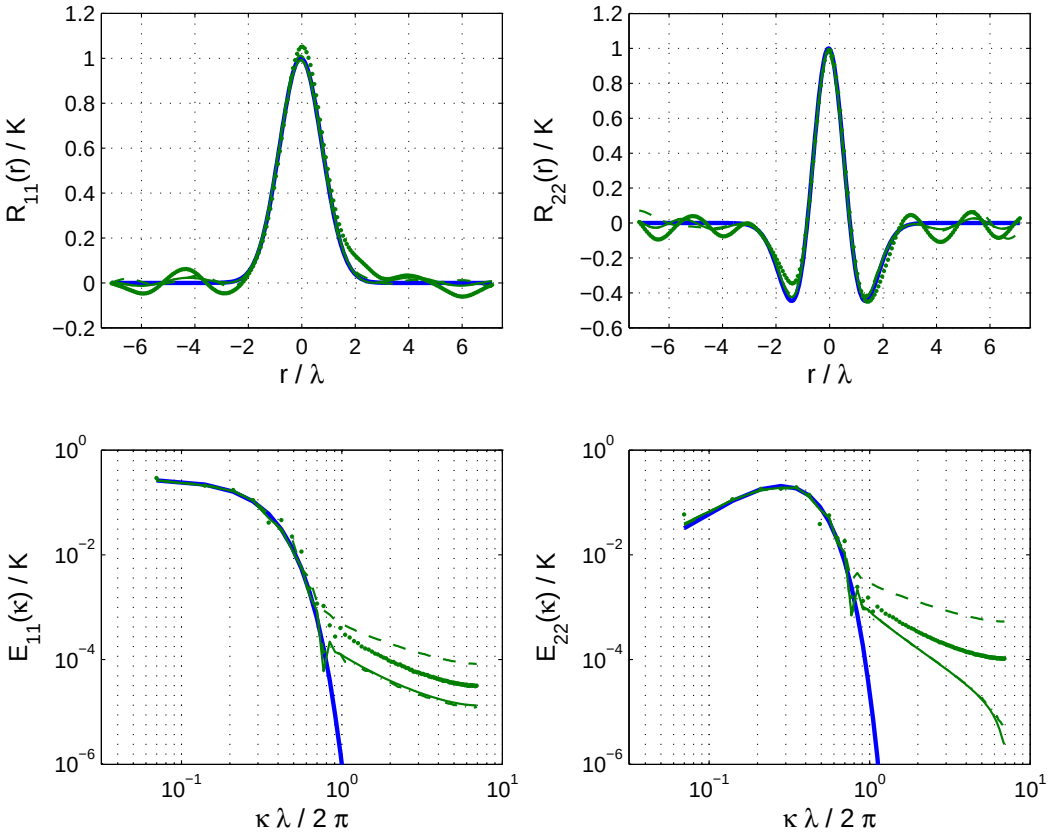

FIGURE 4.5: Analytical solution (—) against numerical results obtained with the Gaussian filter and sampling rate $\Delta_s = 5\Delta t$ (—), $\Delta_s = 50\Delta t$ (– · –), $\Delta_s = 100\Delta t$ (– –) and $\Delta_s = 200\Delta t$ (∗). Top: correlations R_{11} and R_{22} computed with respect to the central point of the airfoil. Bottom: one-dimensional energy spectra E_{11} and E_{22}. Vortices distributed every $\Delta = \lambda/16$ and number of time steps $N_f = 100,000$.

4.3.1.2 Two-point two-time correlations

The statistical properties of the synthetic turbulence can also be assessed by considering two-point two-time correlations along the airfoil: $R_{ij}(r,t) = \langle u_i'(\boldsymbol{x}_1, t_1)\ u_j'(\boldsymbol{x}_2, t_2)\rangle$ where $r = |\boldsymbol{x}_2 - \boldsymbol{x}_1|$ and $t = |t_2 - t_1|$. The synthetic turbulent velocity field $\boldsymbol{u}'$ generated by the stochastic method in Eq. (2.61) yields

$$R_{ij}(r,t) = \int_{\mathbb{R}^2}\int_{\mathbb{R}^2} G_i(|\boldsymbol{x}_1 - \boldsymbol{x}'|)G_j(|\boldsymbol{x}_2 - \boldsymbol{x}''|)\langle U(\boldsymbol{x}', t_1)\ U(\boldsymbol{x}'', t_2)\rangle \mathrm{d}\boldsymbol{x}'\mathrm{d}\boldsymbol{x}'', \tag{4.2}$$

where G_i stands for the i^{th} component of $\boldsymbol{G} = \nabla \times (0,0,G)$. Using the properties of the stochastic field U in Eq. (2.55), one finds that the general expression for the two-point two-time correlation tensor is

$$R_{ij}(r,t) = R_U(t) \int_{\mathbb{R}^2} G_i(|\boldsymbol{x}_1 - \boldsymbol{x}'|)G_j(|\boldsymbol{x}_1 - \boldsymbol{x}' + \boldsymbol{r} - t\boldsymbol{u}_c|)\mathrm{d}\boldsymbol{x}', \tag{4.3}$$

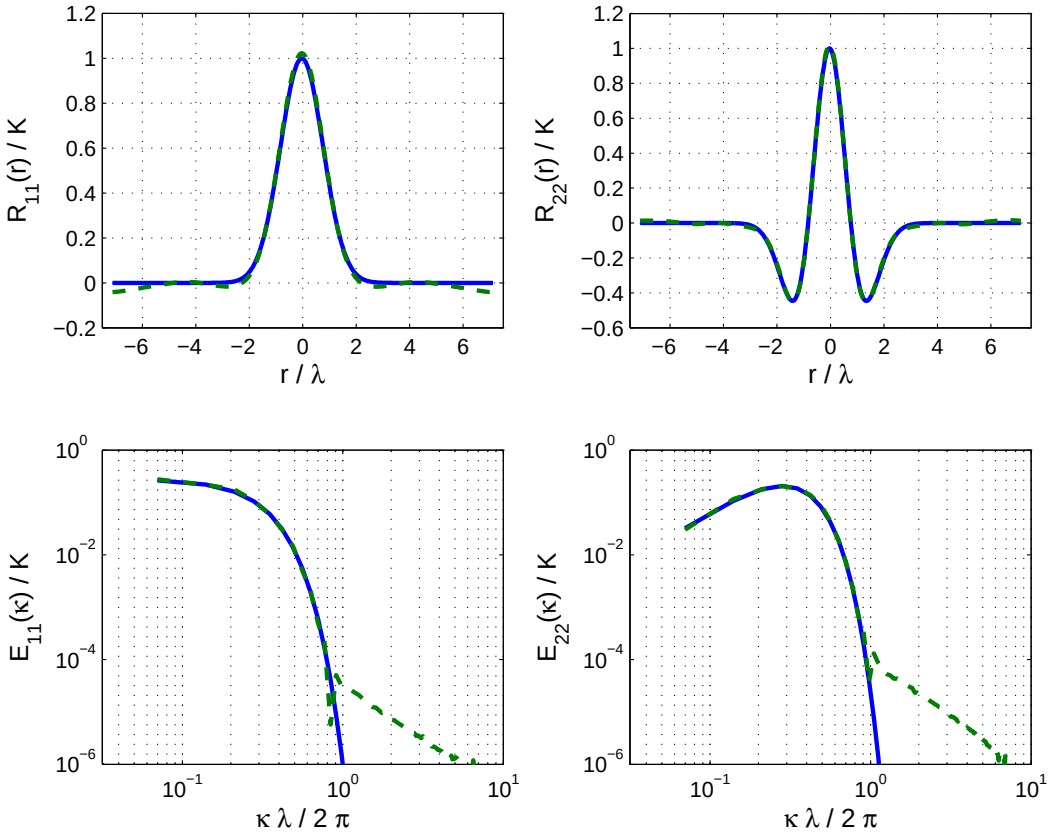

FIGURE 4.6: Analytical solution (—) against numerical results (– –) obtained for Gaussian filter with vortices every $\Delta = \lambda/6$, sampling rate $\Delta_s = 40\Delta t$, and number samples $N_s = 2,500$. Top: correlations R_{11} and R_{22} computed with respect to the central point of the airfoil. Bottom: one-dimensional energy spectra E_{11} and E_{22}.

with $R_U(t) = \langle U(\boldsymbol{x}, t_1)\, U(\boldsymbol{x}, t_2)\rangle$ the time correlation of U. For a fixed time delay, the two-point correlation has the shape inherited by the filter with amplitude scaled by the time correlation of U.

Since the synthetic turbulent velocity field is used as a boundary condition in the linearised Euler equations along the flat plate, we are focussing on the two-point two-time correlations R_{11} and R_{22} on the direction $\boldsymbol{r} = r\boldsymbol{e}_1$. By combining Eqs. (2.45), (2.47) and (2.57) we get:

$$R_{11}(r,t) = -\frac{1}{r}\frac{\mathrm{d}}{\mathrm{d}r}(G * G)(|\boldsymbol{r} - t\boldsymbol{u}_c|, t) R_U(t), \tag{4.4}$$

$$R_{22}(r,t) = -\frac{\mathrm{d}^2}{\mathrm{d}r^2}(G * G)(|\boldsymbol{r} - t\boldsymbol{u}_c|, t) R_U(t). \tag{4.5}$$

Assuming a model of the energy spectrum of the turbulence, it is possible to provide explicit expressions for the two-point two-time correlations R_{11} and R_{22} in Eqs. (4.4) and (4.5) along the airfoil. For instance, for the case of the Gaussian energy spectrum

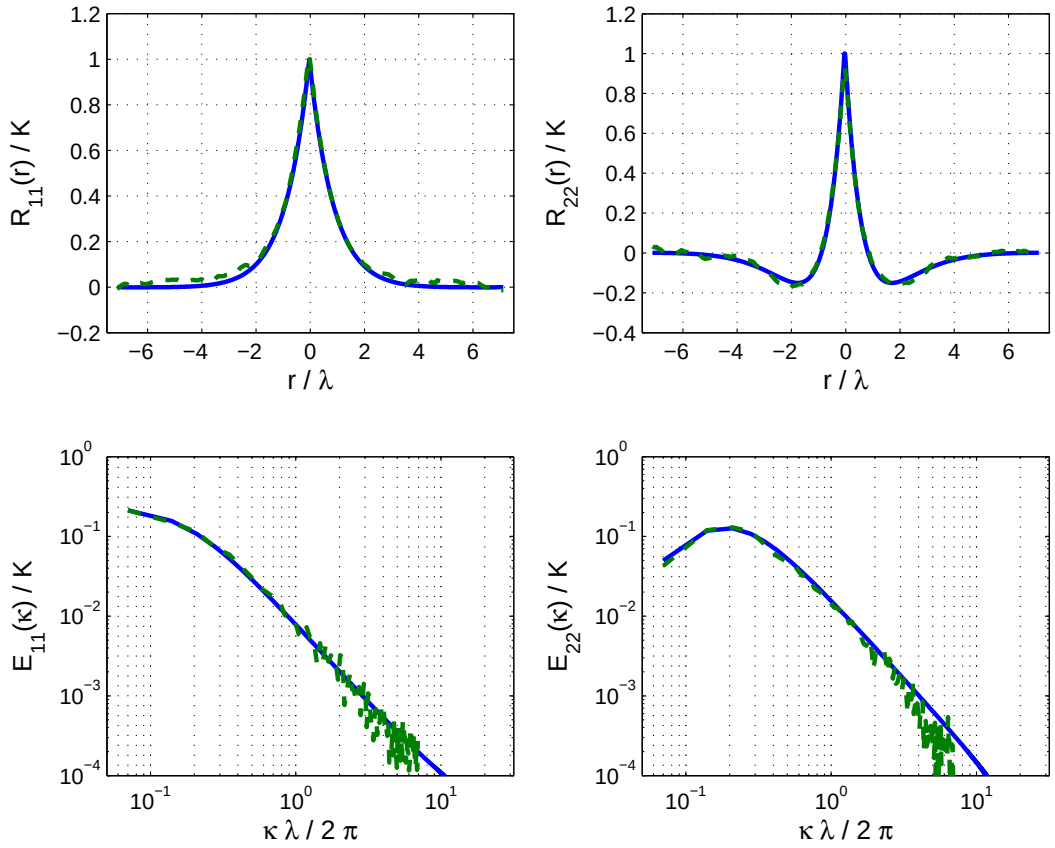

FIGURE 4.7: Analytical solution (—) against numerical results (– –) obtained for Liepmann filter with vortices every $\Delta = \lambda/8$, sampling rate $\Delta_s = 60\Delta t$, and number samples $N_s = 8,000$. Top: correlations R_{11} and R_{22} computed with respect to the central point of the airfoil. Bottom: one-dimensional energy spectra E_{11} and E_{22}.

we have:

$$R_{11}(r,t) = K \exp\left[\frac{\pi(r-u_0t)^2}{4\lambda^2}\right] R_U(t), \tag{4.6}$$

$$R_{22}(r,t) = K \exp\left[\frac{\pi(r-u_0t)^2}{4\lambda^2}\right]\left[1 - \frac{\pi(r-u_0t)}{2\lambda^2}\right] R_U(t). \tag{4.7}$$

Note that for the case of frozen turbulence the time correlation of the stochastic field U is $R_U(t) = 1$.

Figure 4.9 shows the numerical and theoretical correlations R_{11} and R_{22} plotted against time for several spatial separations $r/c = 0$, 0.2, 0.4, 0.6, 0.8 and 1. Good level of agreement is obtained when comparing numerical and analytical two-point two-time correlations R_{11} and R_{22} for the different locations. For any fixed distance r, the correlations have a Gaussian shape inherited from the filter used to generate the synthetic velocity field.

If we focus on the two-point two-time correlation at a specific non-zero distance, for instance $r/c = 1$, Figure 4.9 shows that the correlation peaks at the time that it takes for

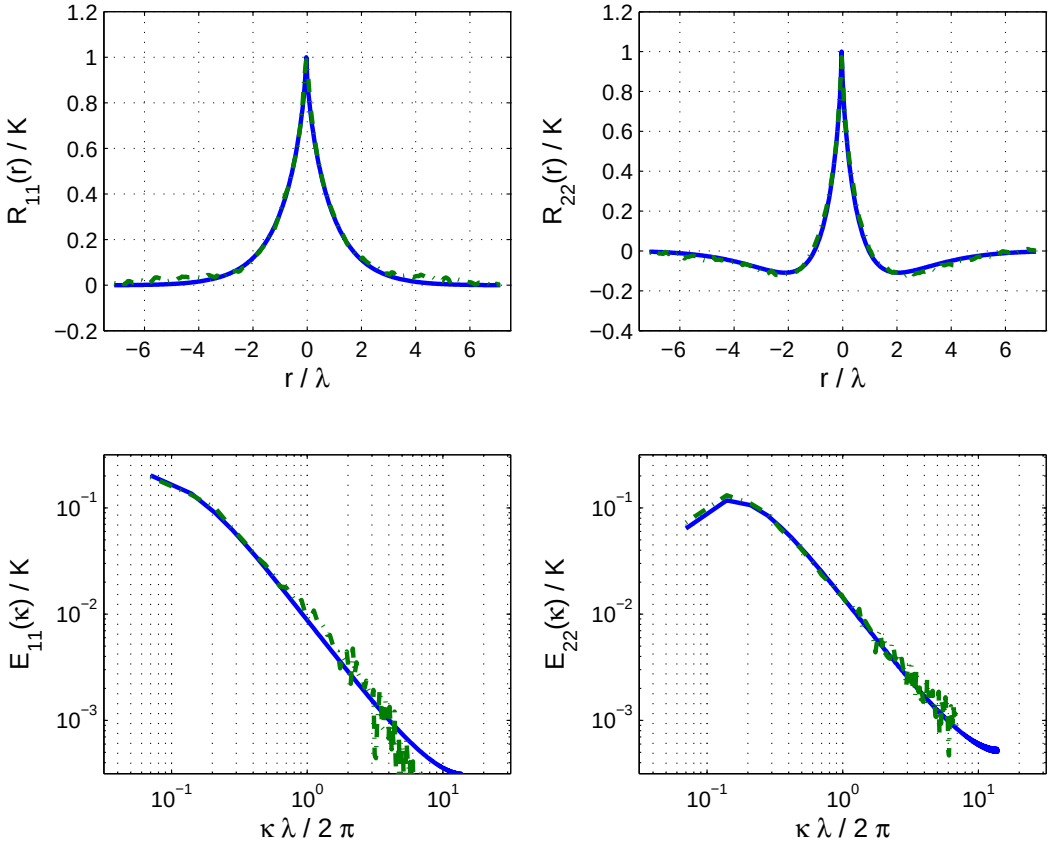

FIGURE 4.8: Analytical solution (—) against numerical results (– –) obtained for von Kármán filter with vortices every $\Delta = \lambda/8$, sampling rate $\Delta_s = 60\Delta t$, and number samples $N_s = 8,000$. Top: correlations R_{11} and R_{22} computed with respect to the central point of the airfoil. Bottom: one-dimensional energy spectra E_{11} and E_{22}.

a vortex particle to travel the distance $r/c = 1$. This means that the highest correlation is achieved when the velocity field is actually generated by the same set of vortices. In addition, there is no loss of correlation between a vortex at a given time and the same vortex at a later time since the maximum value of the correlation is K. Note that for the case of frozen turbulence the strength of each vortex is kept constant in time.

Similar levels of accuracy are obtained for Liepmann and von Kármán filters.

4.3.2 Acoustic pressure

Now that the quality of the synthetic turbulence along the flat plate has been assessed and guidelines on how to choose the parameters involved were obtained, we focus on the sound propagation.

Figure 4.10 depicts a snapshot of the acoustic pressure field around the airfoil for the Gaussian spectrum. It illustrates that most of the noise is radiated from the leading edge. Although it is not obvious here, acoustic waves generated at the leading edge

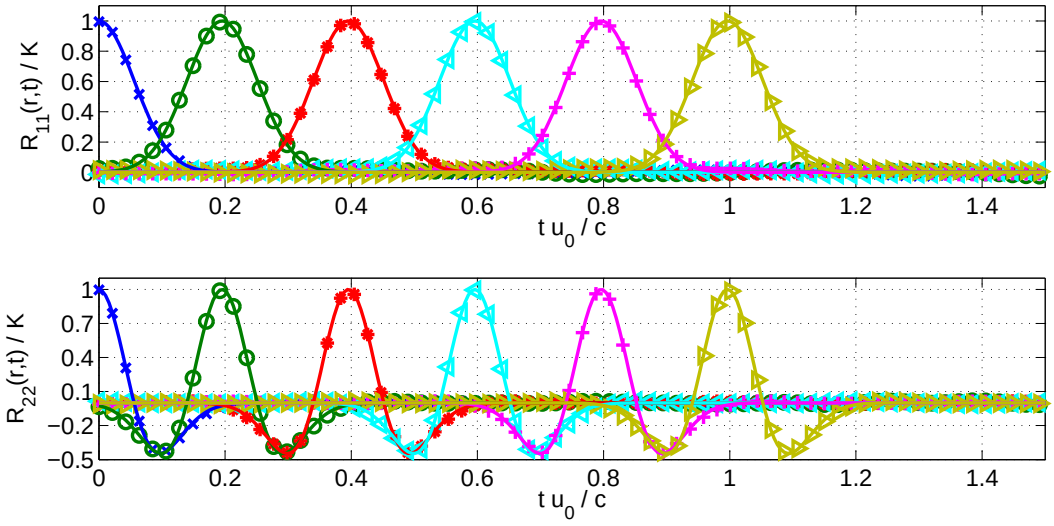

FIGURE 4.9: Two-point two-time correlations R_{11} (top) and R_{22} (bottom) for separations: $r/c = 0$ (—), $r/c = 0.2$ (—), $r/c = 0.4$ (—), $r/c = 0.6$ (—), $r/c = 0.8$ (—), and $r/c = 1$ (—). Solid lines represent analytical results and symbols stochastic results. Averages taken from 25,000 samples with sampling rate $\Delta_s = 20\Delta t$.

are scattered at the trailing edge. Note that even though numerical pollution can be observed in the outgoing boundary of the domain, a parametric study on the size of the buffer zone has been performed to ensure that it does not influence far-field noise levels.

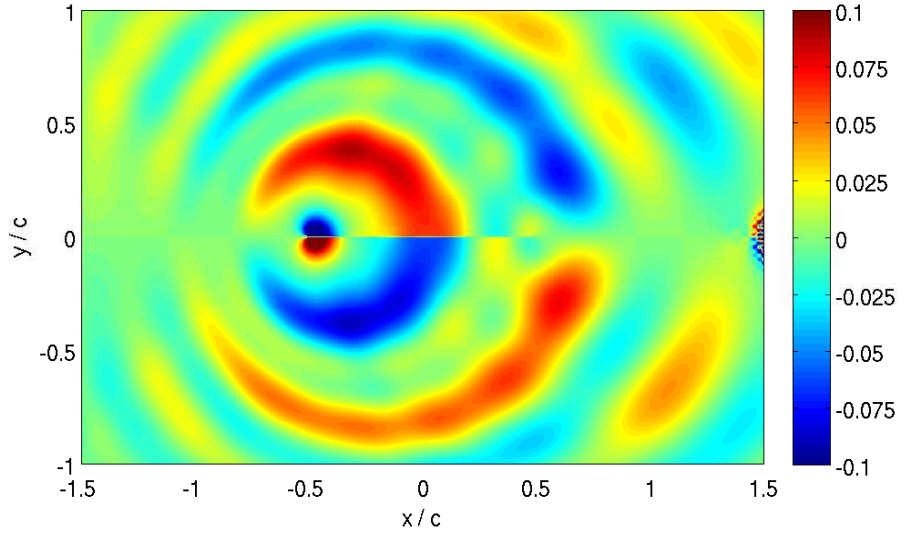

FIGURE 4.10: Snapshot of the acoustic pressure field for the Gaussian spectrum.

Far-field results are obtained with the Ffowcs-Williams Hawkings formulation by locating a control surface around the airfoil as described in section 3.4. In contrast with far-field results obtained in the validation of the LEE solver, here Thompson's multitaper method [61] is used to compute the numerical Power Spectral Density (PSD). The Thompson's multitaper method uses as input a time-domain signal which can be

obtained as the Fourier transform of the Ffowcs-Williams Hawkings formulation. The statistical behaviour of the far-field noise is obtained by sampling over 16,384 time steps so that results lie within a confidence interval of 1.16 dB.

The frequency range of interest is found to correspond to Strouhal numbers between 0 and 10 based on 20 dB difference with peak noise levels. For this highest frequency, the smallest hydrodynamic wavelengths are resolved by 17 points per wavelength and the smallest acoustic wavelengths by 35 points per wavelength.

The power spectral density in the far field obtained from Gaussian, Liepmann and von Kármán spectra is compared against Amiet's analytical solution for a fully two-dimensional problem, Eq. (3.1), in terms of noise spectrum and directivity. The PSD is computed on a circular arc centred on the airfoil where angles are measured from the downstream direction. Sound Pressure Levels (SPL) in the far field are normalised by the distance between the observer and the centre of the flat plate and the kinetic energy, see Eq. (3.16).

Figure 4.11 shows sound pressure levels for the Gaussian spectrum compared against analytical results for observers located at 30, 60, 120, and 150 degrees from the downstream direction. Figures 4.12 and 4.13 depict SPL at the same locations but computed using synthetic turbulent velocity field generated with the Liepmann and von Kármán spectra respectively. Noise levels are in good agreement with the analytical solution for the three spectra at all locations, especially for the Gaussian spectrum. For upstream locations, numerical results obtained with Liepmann and von Kármán spectra do not capture as accurately the shape of the noise spectra for Strouhal numbers larger than 6. Note however that these discrepancies are observed when the noise levels are already more than 15 dB bellow what is observed downstream. Similar issues for high frequencies at upstream directions were found during the validation of the LEE solver and possible reasons were also identified, see section 3.4.

Sound pressure levels obtained with the three energy spectra are shown in Figure 4.14 for an observer located in the far field at 90 degrees. Differences on the acoustic far field are observed by considering different energy spectra of the turbulence. Liepmann and von Kármán spectra predict similar noise levels over the whole range of frequencies with a maximum difference smaller than 2 dB. Regarding the Gaussian spectrum, we can see that the peak is located at a higher frequency and it decays faster. The trends of the sound pressure levels for the different filters can be directly linked with those of the energy spectra shown in Figure 2.1. Note that in Amiet's analytical solution, Eq. (3.1), it can be observed that the energy spectrum acts as an amplitude factor in the sound pressure levels.

Directivities for Strouhal numbers $St = 4$ and $St = 8$ are shown in Figure 4.15 for the Gaussian spectrum. Good agreement is obtained when comparing numerical results against the proposed analytical solution. The fit between analytical and numerical

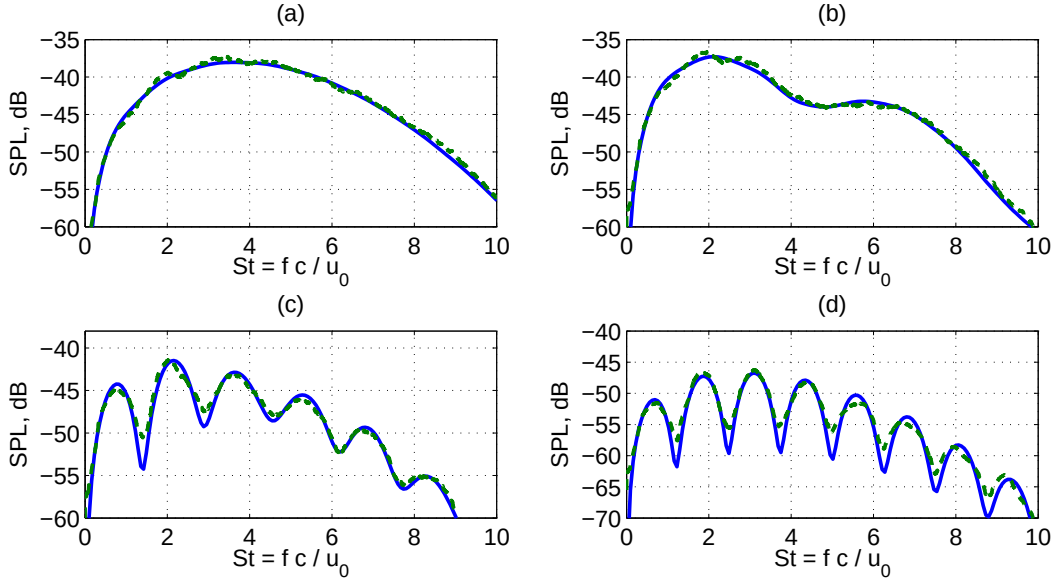

FIGURE 4.11: Analytical (—) versus numerical (– –) SPL for the Gaussian spectrum. Observers located at 30° (a), 60° (b), 120° (c), and 150° (d).

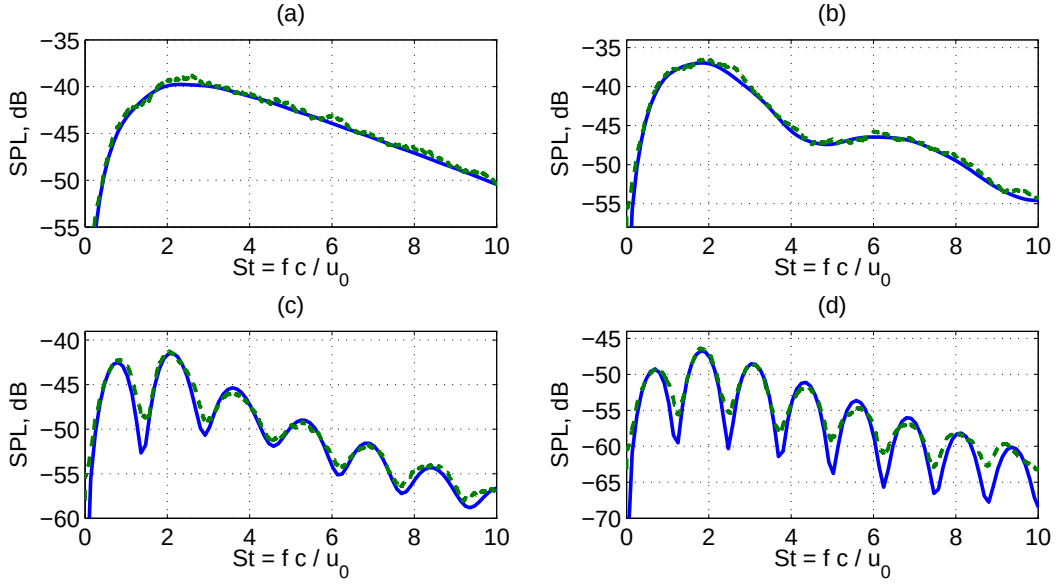

FIGURE 4.12: Analytical (—) versus numerical (– –) SPL for Liepmann spectrum. Observers located at 30° (a), 60° (b), 120° (c), and 150° (d).

results is slightly poorer at angles corresponding to upstream locations. This is thought not to be related with the performance of the method to generate synthetic turbulence but with the linearised Euler equations solver. Note that the small level of error observed here is in concordance with results obtained on the validation of the LEE solver in section 3.4. Similar results in terms of accuracy are obtained when considering either Liepmann or von Kármán spectrum due to the fact that the turbulence spectrum only affects the absolute level of the directivity at any given frequency.

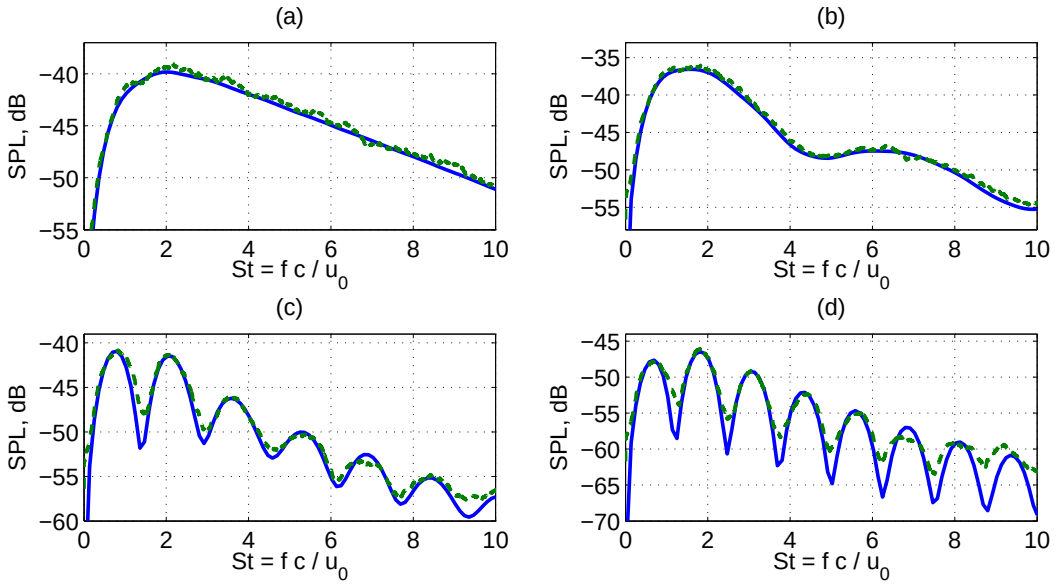

FIGURE 4.13: Analytical (—) versus numerical (– –) SPL for von Kármán spectrum. Observers located at 30° (a), 60° (b), 120° (c), and 150° (d).

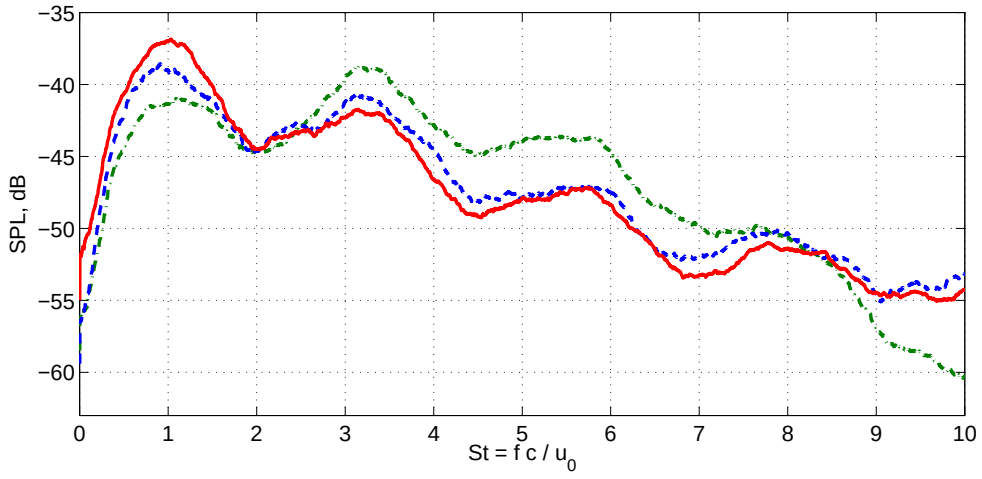

FIGURE 4.14: SPL corresponding to Gaussian (– · –), Liepmann (– –) and von Kármán (—) spectra for an observer located in the far field at 90°.

The accuracy of the acoustic propagation method is also tested in terms of Sound Power Levels (PWL). The acoustic power in a circular arc of radius r enclosing the airfoil can be computed by (see Ref. [62])

$$\mathrm{PWL} = \frac{1-M^2}{2\rho_0 c_0}\int_0^{2\pi} \frac{\sqrt{1-M^2\sin\theta^2}}{\left[\sqrt{1-M^2\sin\theta^2}-M\cos\theta\right]^2}\, S_{pp}(r,\theta)\; r\; \mathrm{d}\theta. \tag{4.8}$$

Figure 4.16 shows the overall acoustic power radiated from the airfoil for Gaussian,

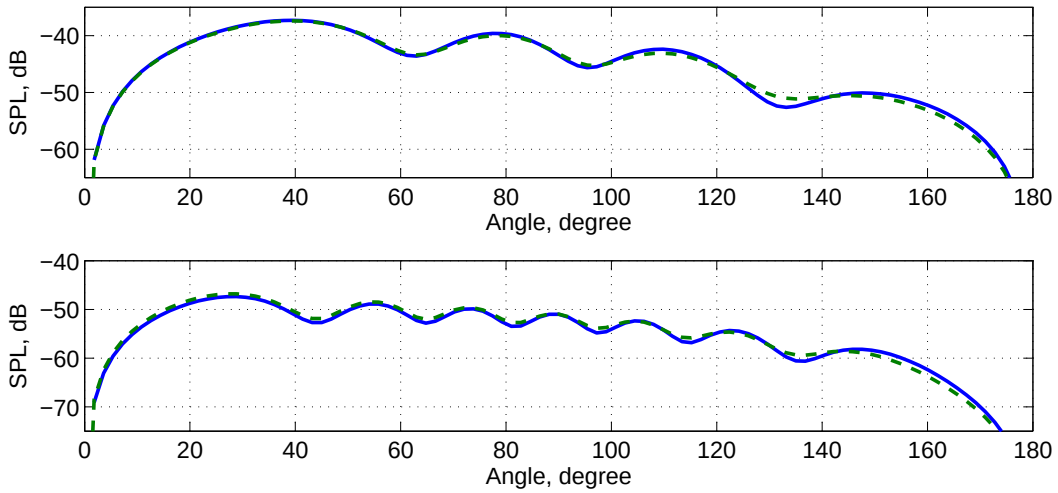

FIGURE 4.15: Analytical (—) versus numerical (– –) far-field directivity using the Gaussian filter at $St = 4$ (top) and $St = 8$ (bottom).

Liepmann and von Kármán energy spectra respectively. Good agreement is found between numerical and theoretical results with a maximum error smaller than 1 dB. This shows that discrepancies observed for Liepmann and von Kármán spectra at upstreams directions can be considered negligible compared to the overall acoustic power.

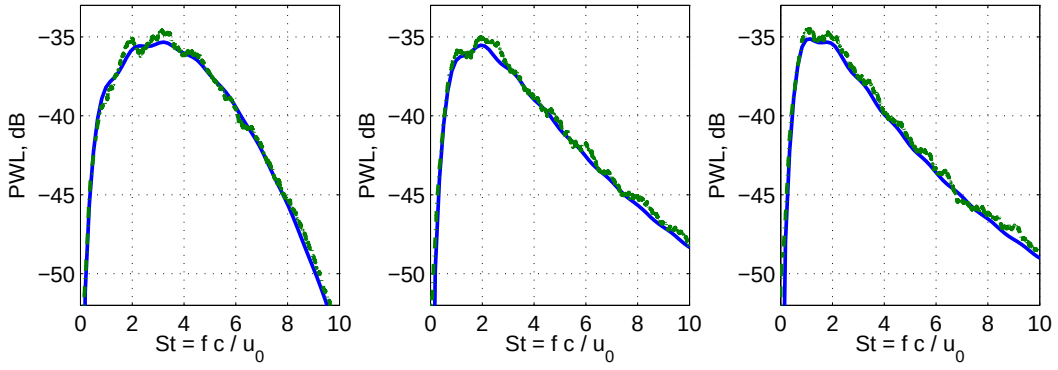

FIGURE 4.16: Analytical (—) versus numerical (– –) sound power levels for Gaussian (left), Liepmann (centre) and von Kármán (right) spectra.

Finally note that because this is intended as a validation of the numerical method, far-field noise results are computed by averaging over 16,384 samples so that results lie within a confidence interval of 1.16 dB. In practice the confidence interval could be relaxed to reduce the number of samples required. For instance, numerical results computed with 8,192 and 4,096 samples lie within confidence intervals of 1.5 and 1.83 dB, respectively. Sound pressure levels computed by averaging over 16,384, 8,192 and 4,096 samples for an observer located at 90 degrees are shown in Figure 4.17. Sound pressure levels predicted with the three sampling procedures are in good agreement with Amiet's analytical solution.

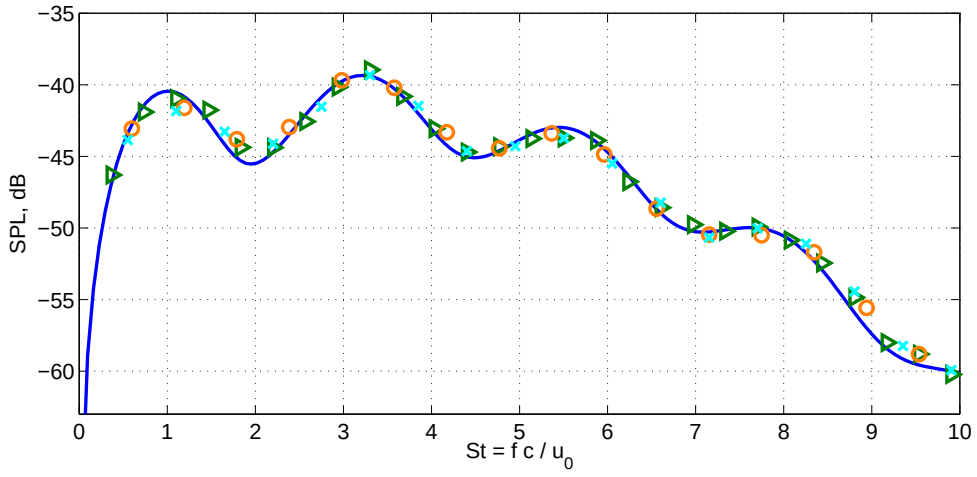

FIGURE 4.17: SPL with Gaussian spectrum for an observed in the far field at 90°. Amiet's analytical solution (—). Numerical results computed with 16,384 samples (▷), 8,192 samples (○) and 4,096 samples (×).

4.4 Computational performance

For each spectrum, three aspects have to be considered to assess the computational time of the stochastic method: the time required to evaluate the filter, the density of vortex particles, and the sampling of the numerical results to obtain accurate statistics.

Due to the use of interpolated functions that are much faster to compute than the exact expressions defining the filters (see section 2.4.5), the computational times required to evaluate Gaussian, Liepmann and von Kármán filters for a given vortex particle are almost identical.

The density of vortex particles is controlled by the maximum distance r_{max} from the flat plate at which vortices have to be distributed and the distance Δ between vortices. For each spectrum, guidelines for choosing the optimum values for r_{max} and Δ have been identified in section 4.3.1. It has been shown that the number of vortex particles is larger for the von Kármán spectrum, followed by the Liepmann spectrum and the Gaussian spectrum, see table 4.1. However, this increase in vortex particles does not have a significant impact on the computational time required to compute the velocity field. In particular, an increase in computational time of less than 2% is observed when computing the velocity field either with Liepmann or von Kármán filters compared to the Gaussian filter. In addition, the computational times associated with Liepmann and von Kármán filters are very similar.

The computational time appears to present a stronger sensitivity to the energy spectra when sampling the numerical results to obtain accurate statistics of the turbulence along the airfoil. The parametric studies presented in section 4.3.1 show that similar levels of accuracy with theoretical results are obtained when increasing the total number of

	Computational times		Number of vortex particles
	LEE (gust)	Synthetic turbulence	
Gaussian	1	0.1	$3,812$
Liepmann	1	0.12	$14,282$
von Kármán	1	0.12	$18,304$

TABLE 4.1: Comparison of the computational cost of the method when considering different energy spectra. Computational times are normalised by the computational time required by the LEE simulation alone.

time steps by 5 for Liepmann and von Kármán filters compared to the Gaussian filter. The time increase is related to the larger content of energy at high frequencies found in Liepmann and von Kármán spectra. This is not an issue of how we represent the energy spectra but of capturing the larger high frequency content of realistic energy spectra.

Computational times discussed above referred to computing the synthetic velocity field alone (LEE are not solved at the same time). Compared to the computational time of the LEE simulation when imposing a deterministic gust along the airfoil, the computational time required to compute the synthetic velocity field is about 10% for the Gaussian spectrum and 12% for the Liepmann and von Karman spectra, as illustrated in table 4.1. When the synthetic field is computed as part of the LEE simulation, some inconsistencies in the computational times have been found and computational times of the LEE simulation alone and computing the synthetic turbulence do not add up. The total computational time of the simulation is significantly larger than the sum of the computational time required to generate synthetic turbulence and the computational time to compute the sound propagation. The increase in computational time varies depending on the energy spectra and it is larger for the von Kármán spectrum. An issue with the efficiency of the cache memory has been identified as the cause of this problem.

4.5 Conclusions

In this chapter broadband fan interaction noise due to frozen turbulence impinging on an isolated airfoil has been studied by combining the linearised Euler equations solver described in chapter 3 with the random-particle method presented in chapter 2.

The statistical behaviour of the synthetic turbulence along the airfoil is accurately captured by the stochastic method. We have identified two aspects that have an impact on the accuracy of the statistics: the density of vortex particles and the sampling of the simulation results. Parametric studies on the number of vortices required by the Gaussian, Liepmann and von Kármán filters show that the von Kármán filter requires more vortices to compute the velocity field at a given location followed by the Liepmann and Gaussian filters. The increase on the number of vortices is caused by a slower rate

of decay of the filter with distance and a larger content of energy at high wavenumbers, see Figure 2.2. In addition, Liepmann and von Kármán filters require a larger sampling rate to obtain similar levels of accuracy with theoretical results than the Gaussian filters. This results in a longer simulation time for Liepmann and von Kármán spectra than for the Gaussian spectrum. The increase in computational time is explained by the large content of energy at high wavenumbers found in realistic energy spectra and does not relate with the technique used to represent the energy spectrum in the method.

Far-field noise levels predicted by the stochastic method are in good agreement with Amiet's analytical solution. Sound pressure levels are accurately predicted for the three spectra at different far-field locations. Small discrepancies with the analytical solution can be observed at high frequencies for upstreams locations, but they do not significantly influence the overall acoustic power radiated from the airfoil.

As expected, the choice of the energy spectrum – or the filter – to generate the synthetic velocity field has an impact on the predicted acoustic far field. Noise levels predicted with Liepmann and von Kármán energy spectra peak are similar frequencies but different trends can be observed. However, when considering the Gaussian spectra the predicted sound pressure levels peak at a higher frequency and present a faster rate of decay. For this test case, up to an average 5 dB difference is found between numerical results predicted with von Kármán and Gaussian spectra.

Regarding the computational performance of the method, the computational times required to compute the velocity field itself is almost independent of the energy spectra. However, in order to obtain reliable statistics along the airfoil, longer simulation times are required for the von Kármán and Liepmann spectra than for the Gaussian spectrum. This is related to the larger content of energy at high frequencies found in Liepmann and von Kármán spectra. It has been observed that when the stochastic method is combined with the LEE solver, computational times required to predict the acoustic field are not consistent with the individual computational times of the stochastic method and the LEE solver using a deterministic source. An issue with the use of cache memory has been identified as the cause.

Chapter 5

Evolving Turbulence

In the previous chapters it was assumed that the incident turbulent field was a frozen velocity pattern in time and was simply convected along with the mean flow. However, the velocity field associated to a turbulent flow is a random process in time. It is expected that for an observer moving with the mean flow, the velocity field will evolve and is also a random process with an associated decorrelation in time.

In this chapter, the effects of temporal decorrelation observed in real turbulent flows are included in the stochastic method to generate synthetic turbulence. We will refer the synthetic turbulent flow as "evolving turbulence" if the effects of time decorrelation are modelled. This is a generalisation of frozen turbulence where only convection effects are included and where the resulting turbulent velocity field seen by an observer moving with the base flow is a frozen pattern.

Time decorrelation is modelled in the stochastic method through the use of first and second-order Langevin models. First-order Langevin models –or Langevin equations– are commonly used to represent the fluid dynamics involved in turbulent diffusion processes at large Reynolds numbers. However, it will be shown here that numerical issues arise when a standard Langevin equation is coupled with the linearised Euler solver described in section 3.3. As proposed by Siefert and Ewert [15] a second-order Langevin model is considered to overcome the numerical issues derived from Langevin equations. Note that in this work a different second-order model from that in Ref. [15] is proposed and validated.

Simulation results for broadband fan interaction noise are presented for the same test case as in the previous chapter. Sound pressure levels in the far field are also compared against the analytical solution and numerical results obtained for the case of frozen turbulence. In addition, the influence of the integral time scale of the turbulence in the acoustic pressure field radiated from the airfoil is assessed. Since our aim is to evaluate the effects of including temporal decorrelation in the method, only the Gaussian spectrum will be used as input.

5.1 Langevin Equation

In a first attempt to include the effects of evolving turbulence in the stochastic method to generate synthetic turbulence, a standard Langevin equation is used to model the evolution in time of the synthetic velocity field.

Langevin equations are stochastic differential equations originally derived to represent Brownian motions and now widely used to model the fluid dynamics involved in turbulent diffusion at large Reynolds numbers [14]. In the field of aeroacoustics, Ewert *et al.* [27] considered a Langevin equation to model the effects of time correlation on synthetic turbulence, see section 2.1.2.3.

5.1.1 Model

The method to generate synthetic turbulence introduced in section 2.2 is based on computing the velocity field $\boldsymbol{u'}$ using $\boldsymbol{u'} = \nabla \times (0, 0, \eta)$ and:

$$\eta(\boldsymbol{x}, t) = \int_{\mathbb{R}^2} G(|\boldsymbol{x} - \boldsymbol{x'}|, t) U(\boldsymbol{x'}, t) \mathrm{d}\boldsymbol{x'}. \tag{5.1}$$

The spatial statistics of the synthetic turbulence are controlled by the filter G while the random field U determines the temporal properties of the flow.

The velocity field associated to a turbulent flow can be understood as a random process in time and its temporal properties can be included in the stochastic method by defining the time evolution of the stochastic field U as a Langevin equation of the form

$$\frac{\mathrm{D}_0}{\mathrm{D}t} U = -\alpha U + \beta \zeta, \tag{5.2}$$

with initial condition $U(0) = U_0$ where U_0 is also a random variable. The material derivative is given by $\mathrm{D}_0/\mathrm{D}t = \partial/\partial t + \boldsymbol{u}_c \cdot \nabla$ with $\boldsymbol{u}_c$ the convection velocity along the stream lines. ζ is a statistically stationary Gaussian white noise source. The coefficients α and β of the Langevin equation can be related to the statistical properties of the turbulence, as we shall do later in this section.

Eq. (5.2) is a stochastic differential equation representing two aspects. A deterministic part, $-\alpha U$, causes the average drift of the solution from the initial condition to relax as $\alpha \to 0$ and a stochastic part, $\beta\zeta$, accounts for the inertial diffusion process adding a zero-mean random source of standard deviation β. The coefficient α can be interpreted as the parameter accounting for the correlation of the process: the larger α is, the quicker the process will become uncorrelated with its initial condition. The coefficient β controls the strength of the random source such that U is statistically stationary.

The stochastic source ζ in Eq. (5.2) is defined as the time derivative of a Wiener process $\tilde{\zeta}$, which is a continuous Gaussian process with independent increments such that (see Ref. [63] for more details)

$$\langle\tilde{\zeta}(\boldsymbol{x},t)\rangle = 0, \quad \langle[\tilde{\zeta}(\boldsymbol{x},t_1) - \tilde{\zeta}(\boldsymbol{x},t_2)]^2\rangle = |t_2 - t_1|. \tag{5.3}$$

Therefore, it can be shown that ζ is a white noise source that verifies:

$$\langle\zeta(\boldsymbol{x},t)\rangle = 0, \quad \langle\zeta(\boldsymbol{x}_1,t_1)\ \zeta(\boldsymbol{x}_2,t_2)\rangle = \delta(\boldsymbol{x}_1 - \boldsymbol{x}_2)\delta(t_2 - t_1), \tag{5.4}$$

where δ stands for the Dirac function. Note that strictly speaking the continuous Gaussian white noise process ζ does not exist as a conventional function of time since the Wiener process is not differentiable and the Eq. (5.2) should be understood in the sense of a stochastic differential equation as explained in Ref. [63].

The rate of change over time of a vortex particle along the streamlines defined by the convection velocity $\boldsymbol{u}_c$ can be derived from the Lagrangian version of Eq. (5.2):

$$\frac{\partial}{\partial t}U(\boldsymbol{x}'(\boldsymbol{x}_0,t),t) = -\alpha U(\boldsymbol{x}'(\boldsymbol{x}_0,t),t) + \beta\zeta(\boldsymbol{x}'(\boldsymbol{x}_0,t),t). \tag{5.5}$$

The material derivative in the mean flow, $\mathrm{D}_0/\mathrm{D}t$, is the derivative taken along a path moving with the mean flow, hence in a Lagrangian formulation it simply becomes the derivative with respect to time.

To simplify the notation, we consider the strength of each fluid particle as a function of time: $U(\boldsymbol{x}'(\boldsymbol{x}_0,t)) \sim U(t)$. The solution of the Langevin equation in Eq. (5.5) can then be written (see Ref. [64]):

$$U(t) = U_0\exp(-\alpha t) + \beta\exp(-\alpha t)\int_0^t \exp(\alpha t')\zeta(t')\mathrm{d}t', \tag{5.6}$$

or alternatively

$$U(t) = U_0\exp(-\alpha t) + \beta\exp(-\alpha t)\int_0^t \exp(\alpha t')\mathrm{d}\tilde{\zeta}(t'), \tag{5.7}$$

It can be shown that the sample paths determined by a Wiener process are not of bounded variation on any bounded time, therefore the integrals in Eqs. (5.6) and (5.7) cannot be defined as ordinary Riemann-Stieltjes integrals but as the Ito Integral, see Ref. [63].

By considering the solution of the Langevin equation in Eq. (5.6) at two different times and averaging, the time correlation of U, $R_U(t) = \langle U(t_1)\ U(t_2)\rangle$ where $t = |t_2 - t_1|$, is

given by

$$\begin{aligned} R_U(t) =& \langle U_0^2 \rangle \exp[-\alpha(t_1+t_2)] \\ &+ \beta^2 \exp[-\alpha(t_1+t_2)] \int_0^{t_1} \int_0^{t_2} \exp[\alpha(t'+\tilde{t})] \langle \zeta(t')\ \zeta(\tilde{t}) \rangle \mathrm{d}t' \mathrm{d}\tilde{t}. \end{aligned} \tag{5.8}$$

Note that the random variable U_0 and the white noise field ζ are uncorrelated.

From Eq. (5.6) and after using Eq. (5.4), one can show that the energy (or variance) of the random process U is

$$\langle U(t)^2 \rangle = \left(\langle U_0^2 \rangle - \frac{\beta^2}{2\alpha} \right) \exp(-2\alpha t) + \frac{\beta^2}{2\alpha}. \tag{5.9}$$

To ensure that the process is statistically stationary, its energy $\langle U(t)^2 \rangle$ must remain constant in time. This condition yields a unique definition for $\beta = \sqrt{2\alpha \langle U_0^2 \rangle}$.

A second constraint to be imposed on the stochastic field is concerned with the time correlation of U in Eq. (5.8). Various experimental data (such as Favre *et al.* [65]) support an exponential time correlation for the velocity field of turbulent flows. Therefore, it is logical to define the stochastic field U so that its correlation in time decays as $\exp(-t/\tau)$ where τ is the Lagrangian integral time scale of the flow [66]. This condition yields $\alpha = 1/\tau$ when comparing with Eq. (5.8) for $\beta = \sqrt{2\alpha \langle U_0^2 \rangle}$ and using the fact that ζ is a white noise field.

Therefore, the effects of evolving turbulence can be modelled by a Langevin equation by defining the rate of change of U as

$$\frac{\mathrm{D}_0}{\mathrm{D}t} U = -\frac{1}{\tau} U + \sqrt{\frac{2}{\tau} \langle U_0^2 \rangle}\ \zeta. \tag{5.10}$$

The initial condition U_0 is a random variable following a zero-mean Gaussian distribution with unit standard deviation, $\langle U_0^2 \rangle = 1$. Note that the random field U as defined by Eq. (5.10) is continuos but not time differentiable, we will show that this is an issue for predicting the sound field.

Changing the notation so that the stochastic field U defined through a Langevin equation is explicitly a function of position and time, we get that U satisfies the properties in Eq. (2.55):

$$\langle U(\boldsymbol{x}, t) \rangle = 0, \quad \langle U(\boldsymbol{x}_1, t_1)\ U(\boldsymbol{x}_2, t_2) \rangle = \delta(\boldsymbol{r} - t\boldsymbol{u}_c) \exp\left(-t/\tau\right), \tag{5.11}$$

where $\boldsymbol{r} = \boldsymbol{x}_2 - \boldsymbol{x}_1$. Note that U is defined as a zero-mean white noise field in space and in this case $R_U(t) = \exp(-t/\tau)$.

When assuming frozen turbulence, the time correlation tends to infinity, $\tau \to \infty$, and hence the right-hand side of Eq. (5.10) vanishes, indicating that the model is only representing convection effects, $\mathrm{D}_0 U/\mathrm{D}t = 0$.

The following input parameters are required to model the time evolution of the turbulence with the Langevin equation Eq. (5.10):

- Convection velocity of the flow, $\boldsymbol{u}_c$. It can be provided by steady RANS or LES simulations or by measurements.
- Integral time scale of the turbulence, τ. The Lagrangian time scale τ controls the temporal correlation of the turbulence. It is a function of the dissipation rate, ϵ, and a weak function of the Reynolds number. It can be estimated by the scaling procedure [14]:

$$\tau \approx \frac{2K}{C_0 \epsilon}, \tag{5.12}$$

  where C_0 is an empirical constant whose value is not yet exactly defined but is understood to be smaller than 6. We consider $C_0 = 2.1$ as proposed by Pope in Ref. [14] but the sensitivity of the results to this parameter will be investigated in section 5.3.

5.1.2 Numerical implementation

The implementation of the stochastic method to generate evolving turbulence is performed using a Lagrangian formulation. As shown in section 2.3.1, the method can be written as a sum of contributions from individual vortex particles:

$$\boldsymbol{u}'(\boldsymbol{x}, t) = \sum_{n=1}^{N} \boldsymbol{G}(|\boldsymbol{x} - \boldsymbol{x}_n(t)|, K(\boldsymbol{x}_n), \lambda(\boldsymbol{x}_n)) U_n(t), \tag{5.13}$$

where $\boldsymbol{G} = \nabla \times (0, 0, G)$ and U_n is the weighted average of U over the n^{th} fluid element $\mathbb{S}_{0n}$:

$$U_n(t) = \int_{\mathbb{S}_{0n}} U(\boldsymbol{x}'(\boldsymbol{x}_0, t), t) J \mathrm{d}\boldsymbol{x}_0. \tag{5.14}$$

The filter G controls the spatial statistics of the turbulence and it is fully defined by either the two-point correlation tensor or the energy spectra through either of the expressions in Eq. (2.59).

U_n can be understood as the strength of each vortex particle and its value can be deduced by relating Eq. (5.14) with the Langevin equation in Eq. (5.5). Integrating Eq. (5.5) over the fluid element $\mathbb{S}_{0n}$, we have:

$$\frac{\partial}{\partial t} U_n(t) = -\frac{1}{\tau} U_n(t) + \sqrt{\frac{2}{\tau}} \zeta_n(t), \tag{5.15}$$

where ζ_n is the weighted average of the random source over the fluid element $\mathbb{S}_{0n}$:

$$\zeta_n(t) = \int_{\mathbb{S}_{0n}} \zeta(\boldsymbol{x}'(\boldsymbol{x}_0, t), t) J \mathrm{d}\boldsymbol{x}_0.$$

Initial conditions for each U_n and values for ζ_n at each time step must be provided in order to define the strength of the vortex particles at each time. Since U_0 and ζ are independent random variables following a zero-mean Gaussian distribution with unit standard deviation, by definition $U_n(0)$ and $\zeta_n(t)$ follow a zero-mean Gaussian distribution with variance:

$$\int_{\mathbb{S}_{0n}} J^2 \mathrm{d}\boldsymbol{x}_0.$$

Note that for incompressible flows $J = 1$ and the variance of $U_n(0)$ and $\zeta_n(t)$ is equal to the area of the fluid element S_{0n}.

Finally, in order to implement Eq. (5.13) the discrete version of the Langevin equation in Eq. (5.15) must be provided. For small time steps Δt the time derivative of U can be approximated using a simple Euler scheme:

$$\frac{\partial}{\partial t} U_n(t) \approx \frac{U_n(t + \Delta t) - U_n(t)}{\Delta t}. \tag{5.16}$$

This approximation is also applied to the stochastic source ζ which is defined as the time derivative of the Wiener process $\tilde{\zeta}$:

$$\zeta_n(t) \approx \frac{\tilde{\zeta}_n(t + \Delta t) - \tilde{\zeta}_n(t)}{\Delta t}. \tag{5.17}$$

Inserting both approximations in Eq. (5.15)

$$U_n(t + \Delta t) = \left(1 - \frac{\Delta t}{\tau}\right) U_n(t) + \sqrt{\frac{2}{\tau}} \left[\tilde{\zeta}_n(t + \Delta t) - \tilde{\zeta}_n(t)\right]. \tag{5.18}$$

From the properties of the Wiener process $\tilde{\zeta}$ in Eq. (5.3), we see that the increment $\tilde{\zeta}_n(t + \Delta t) - \tilde{\zeta}_n(t)$ follows a zero-mean Gaussian distribution with variance determined by the time step Δt and the density of vortices. This term can then by rewritten as $\sqrt{\Delta t}\zeta_n$ where ζ_n follows a zero-mean Gaussian distribution with variance determined by the density of vortices. Therefore, Eq. (5.18) is rewritten as:

$$U_n(t + \Delta t) = \left(1 - \frac{\Delta t}{\tau}\right) U_n(t) + \sqrt{\frac{2\Delta t}{\tau}} \zeta_n(t), \tag{5.19}$$

where U_n and ζ_n are independent random variables picked from zero-mean Gaussian distributions with variance determined by the density of vortex particles.

Note that in order to be consistent with the time discretisation of the LEE solver (see section 3.3) the strength of the vortices is updated at every stage of the Runge-Kutta

method.

5.1.3 Results

Numerical simulations have been performed to investigate the effects of evolving turbulence on broadband fan interaction noise. The test case considered in the previous chapter to investigate the effects of frozen turbulence is now employed with the aim of comparing both sets of results.

The statistical behaviour of the synthetic velocity field along the airfoil and the acoustic pressure in the near and far field are examined in order to identify the influence of evolving turbulence on the predicted noise levels.

5.1.3.1 Problem definition

The test case considered is that of a flat plate with zero angle of attack interacting with homogeneous isotropic turbulence. The problem is made non-dimensional using the chord, mean density, and sound speed.

The parameters are the same as those used to validate the method for the case of frozen turbulence, see chapter 4. The turbulence is convected by a uniform mean flow with Mach number of 0.362 in the x-direction and it is characterised by an integral length scale $\lambda = 0.07$.

In order to include the effects of evolving turbulence, the method also requires the integral time scale of the turbulence. Following the scaling procedure proposed in Eq. (5.12) with the constant $C_0 = 2.1$, the Lagrangian integral time scale corresponding to the flow under consideration is $\tau = 20.86$.

5.1.3.2 Computational setup

The computational setup implemented for this test case is the same as for the simulation of frozen turbulence in chapter 4.

The simulation domain is $[-1.5, 1.5] \times [-1, 1]$ with the airfoil located at $[-0.5, 0.5] \times \{0\}$. The domain is divided into 6 blocks, each of them discretised by a Cartesian grid with 200 points in each direction. The time step is such that the CFL number is 0.8. Vortex-particles are launched from a vertical segment upstream of the flat plate, convected with the mean flow and removed once they are out of the range of influence of the flat plate.

In contrast with the case of frozen turbulence where the strength of each vortex particle remains constant, the strength of each particle now varies in time according to Eq. (5.19).

The initial strength of each vortex particle follows a Gaussian distribution with zero mean and standard deviation determined by the density of vortices in the domain. And it is updated at every stage of the Runge-Kutta method. Note that the time step used in the numerical discretisation is at least four orders of magnitude smaller than the integral time scale of the turbulence.

To simplify the discussion and focus on the effects of evolving turbulence compared to frozen turbulence, simulation results are only presented assuming that the energy spectrum of the turbulence is Gaussian.

The synthetic velocity field at each point is given by summing the contribution of vortices located in its vicinity. For the case of frozen turbulence, a parametric study over the distribution of vortices required to obtain reliable statistics has been performed, see section 4.3.1. The conclusions of this parametric study are also used for the case of evolving turbulence. Therefore, reliable statistics can be obtained for the Gaussian spectrum when generating vortices in the region determined by $r_{max} = 2.43\lambda$ with a distance between vortices of $\Delta = \lambda/6$.

5.1.3.3 Synthetic turbulence

The quality of the synthetic turbulence generated by the random-vortex-particle method in Eq. (5.13) is assessed by evaluating its statistical behaviour along the airfoil. Two-point correlations R_{11} and R_{22} and one-dimensional spectra E_{11} and E_{22} (defined by Eqs. (2.36) and (4.1)) computed along the flat plate are given in Figure 5.1 showing that the random-vortex-particle method is able to achieve very accurately the expected two-point correlation functions and energy spectra when the rate of change of the strength of the vortex particles is defined by the Langevin equation Eq. (5.19).

Since the temporal correlation of the turbulence is now included in the random-vortex-particle method, it is important to study the behaviour of the two-point two-time correlations R_{11} and R_{22} along the airfoil.

Figure 5.2 shows the two-point two-time correlations R_{11} and R_{22} plotted against time for several spatial separations $r/c = 0$, 0.2, 0.4, 0.6, 0.8, and 1 along the airfoil. Very good level of agreement is obtained when comparing numerical and analytical correlations R_{11} and R_{22} for the different locations.

The correlations for a spacial separation of $r/c = 1$ corresponds to two points that are one chord away. That is correlations between the leading and the trailing edge of the airfoil. As one would expect, the maximum correlation between them occurs at the time that it takes for the vortices to travel the chord of the airfoil. In contrast with the case of frozen turbulence (see Figure 4.9) the correlation is no longer unit, but decreases due to the temporal decorrelation of U modelled by the Langevin equation as $\exp(-t/\tau)$.

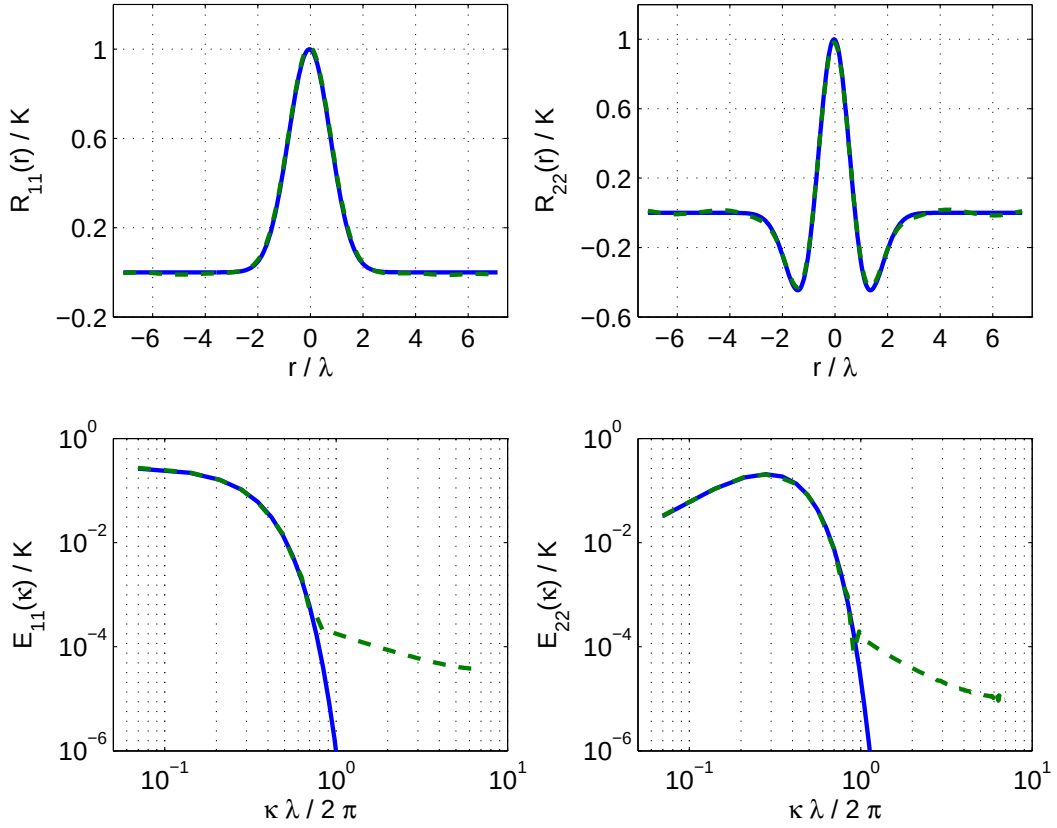

FIGURE 5.1: Analytical solution (—) against numerical results (– –) obtained for Gaussian spectrum. Top: two-point correlations R_{11} and R_{22} computed with respect to the centre of the airfoil. Bottom: one-dimensional energy spectra E_{11} and E_{22}.

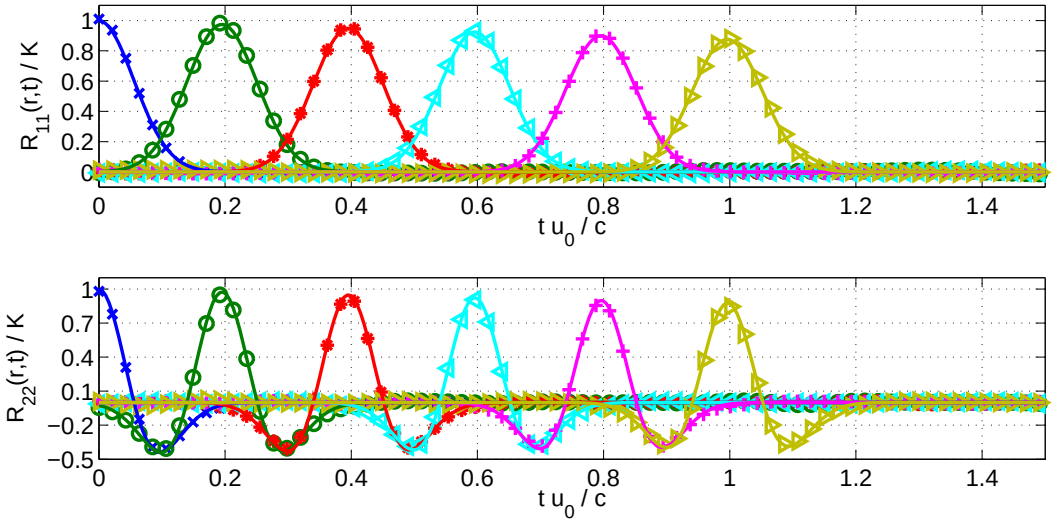

FIGURE 5.2: Two-point two-time correlations R_{11} (top) and R_{22} (bottom) for separations: $r/c = 0$ (—), $r/c = 0.2$ (—), $r/c = 0.4$ (—), $r/c = 0.6$ (—), $r/c = 0.8$ (—), and $r/c = 1$ (—). Solid lines represent analytical results and symbols stochastic results obtained with a standard Langevin equation. Averages taken from 25,000 samples with sampling rate $\Delta_s = 20\Delta t$.

Therefore, for this test case, the integral time scale of the turbulence $\tau = 20.86$ yields about 12% loss of temporal correlation for points that are one chord apart.

5.1.3.4 Acoustic pressure field

Now that the quality of the synthetic turbulence has been validated, we look at the scattered acoustic field. The acoustic pressure field surrounding the flat plate generated by its interaction with the evolving turbulence is depicted in Figure 5.3. In comparison with the acoustic pressure field generated by frozen turbulence shown in Figure 4.10, it features additional sound waves with small wavelengths radiating from the plate. For the case with frozen turbulence, most of the noise is radiated from the leading edge and then is scattered at the trailing edge. However, in this case, there are significant additional sound sources located mostly along the middle of the flat plate.

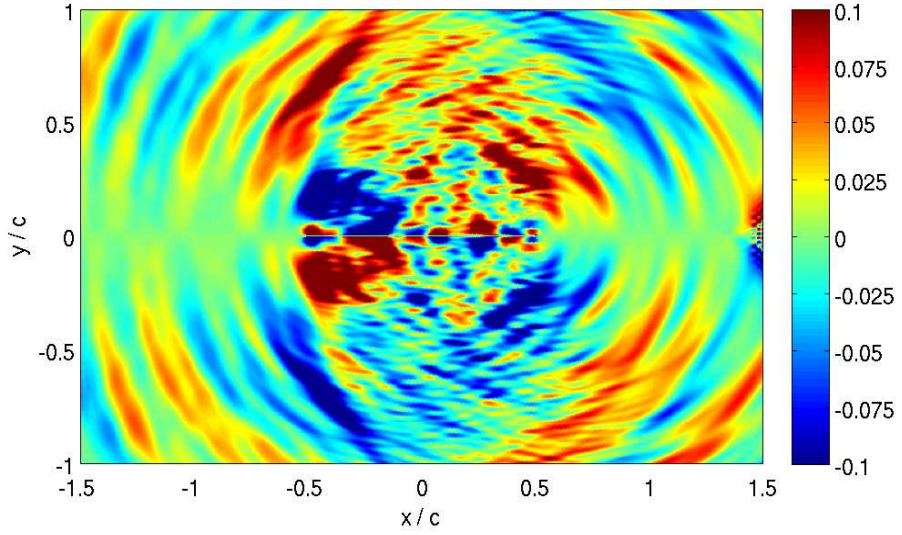

FIGURE 5.3: Snapshot of the acoustic pressure field for the Gaussian spectrum generated with a standard Langevin equation.

Noise levels in the far field are also computed using the same procedure as in chapter 4.

Figure 5.4 shows sound pressure levels compared against numerical and analytical results for the case of frozen turbulence ($\tau \to \infty$) for observers in the far field at 30, 60, 90, 120, and 150 degrees from the downstream direction. For observers located downstream, noise levels are very similar to those of the case of frozen turbulence for Strouhal numbers smaller than 6 and there are increased noise levels at higher frequencies. A much more significant increase between frozen and evolving turbulence is observed for upstream locations. Noise levels at 120 and 150 degrees are larger for evolving turbulence than those generated with frozen turbulence over the whole range of frequencies. In particular, at 150 degrees an almost flat spectrum is found for Strouhal numbers larger than 4 and the interference pattern originally generated by the interaction between the noise

radiated from the leading edge and the scattering at the trailing edge is no longer present. Even though the overall sound pressure levels in the upstream direction are about 10 dB lower that the levels downstream, the large content of sound at high frequencies is significant.

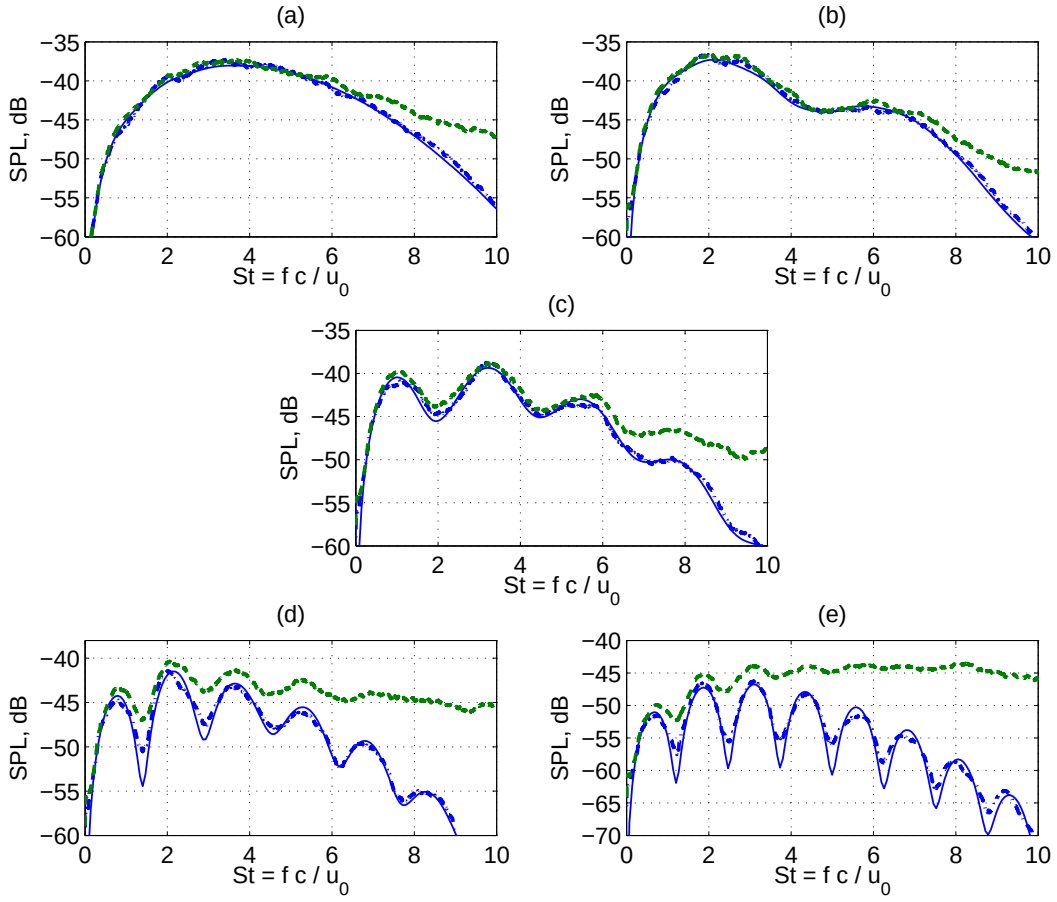

FIGURE 5.4: Analytical (—) and numerical (– · –) SPL for frozen turbulence versus numerical (– –) SPL for evolving turbulence. Observers located at 30° (a), 60° (b), 90° (c), 120° (d), and 150° (e).

Directivities at the Strouhal numbers $St = 4$ and $St = 8$ are shown in Figure 5.5. Numerical results obtained for evolving turbulence are plotted against numerical and analytical results for the case of frozen turbulence. From 0 to 90 degrees the same trends and similar noise levels are obtained compared with frozen turbulence. However, for upstream directions there is a dramatic change between results obtained with frozen and evolving turbulence. For the latter case, sound pressure levels at $St = 8$ are larger upstream than downstream.

Finally if we plot the overall acoustic power radiated by the airfoil as shown in Figure 5.6, we can also see that including the effects of temporal decorrelation with the Langevin equation (5.10), the method predicts a significant increase at high frequencies compared to frozen turbulence.

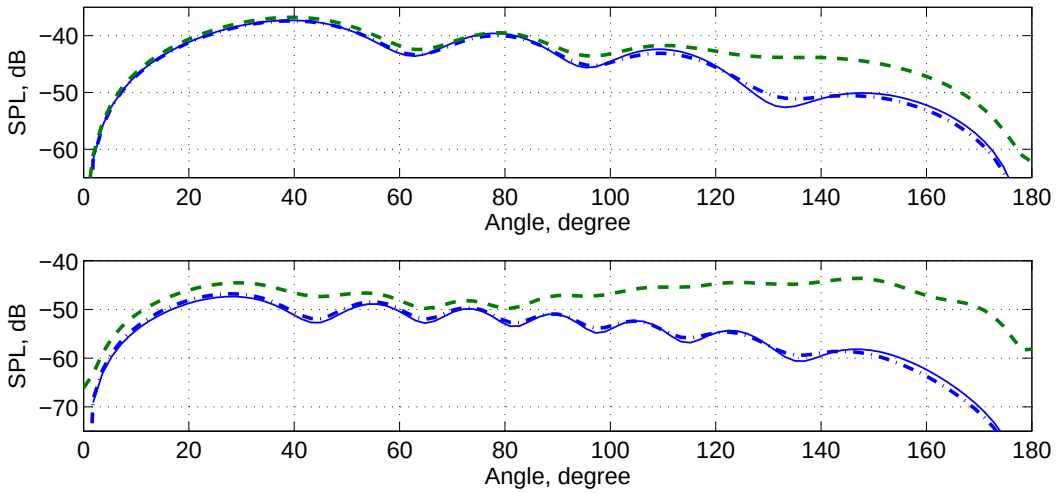

FIGURE 5.5: Analytical (—) and numerical (– · –) far-field directivity for frozen turbulence versus numerical (– –) directivity for evolving turbulence at $St = 4$ (top) and $St = 8$ (bottom).

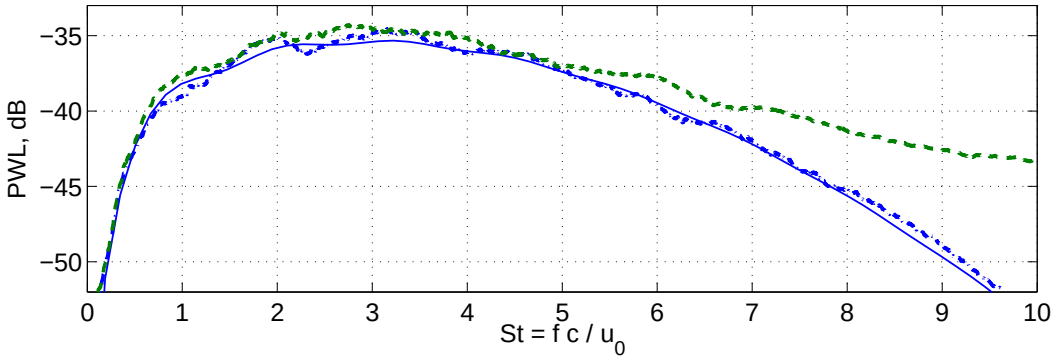

FIGURE 5.6: Analytical (—) and numerical (– · –) acoustic power for frozen turbulence versus numerical results (– –) for evolving turbulence.

5.1.4 Discussion

At this point one might question whether the higher noise levels observed at high frequencies are a genuine effect of introducing time correlation in the synthetic velocity field or instead represent spurious sources introduced by the time discretisation of the model.

A possible explanation for the larger amplitude of noise levels at high frequencies could be a lack of numerical resolution in space or time, but this has been ruled out. First of all, in the frequency range of interest ($St < 10$) the smallest hydrodynamic wavelengths are resolved by at least 17 points per wavelength and the smallest acoustic wavelengths by 35 points per wavelength. In addition, the solution seems also independent of the time step used in the numerical integration. Figure 5.7 shows the SPL for observers located at 30, 60, 90, 120, and 150 degrees. Results for frozen turbulence are compared

against numerical results for evolving turbulence computed using three different time steps corresponding to CFL numbers of 0.8, 0.4 and 0.2. (Numerical results are all obtained with the same sampling frequency and number of samples.) We can see that reducing the time step does not change the noise levels at high frequencies. This suggests that the larger amplitude of noise levels at high frequencies is not caused by a lack of numerical resolution.

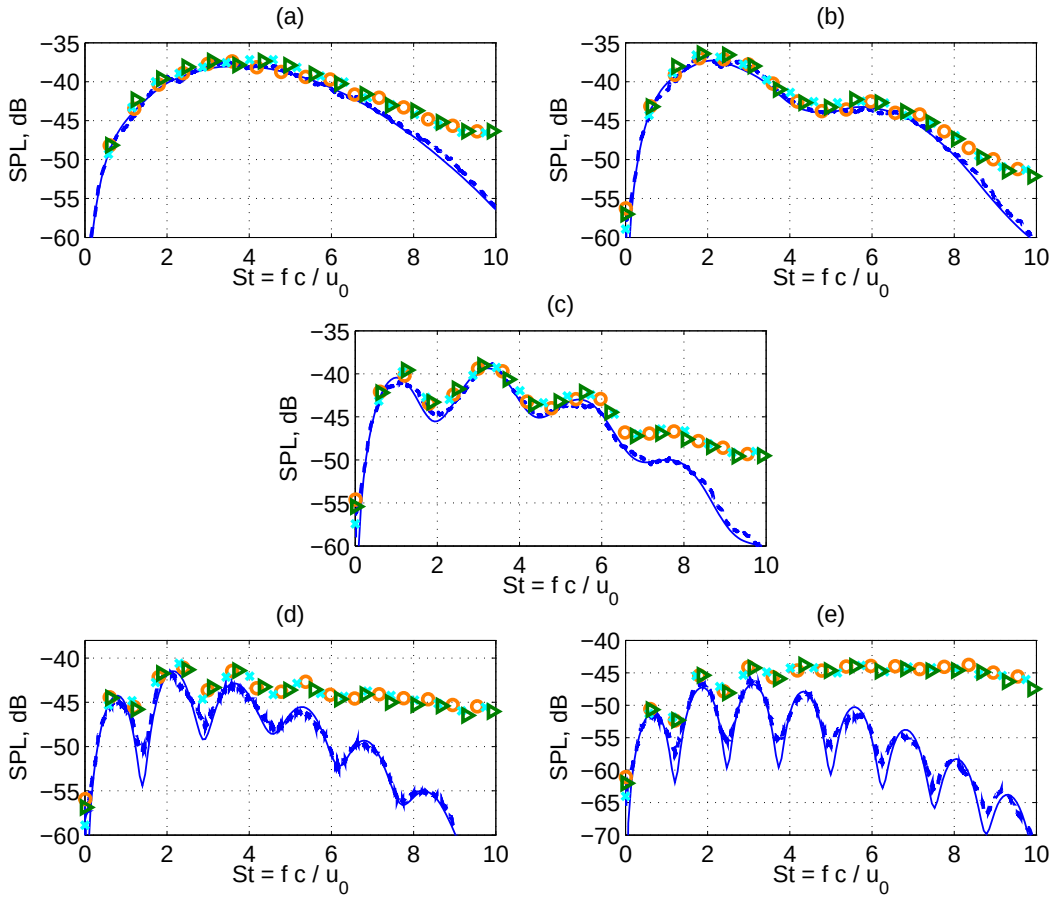

FIGURE 5.7: Analytical (—) and numerical (– · –) SPL for frozen turbulence versus numerical SPL for evolving turbulence obtained with numerical time steps corresponding to CFL numbers of 0.8 (○), 0.4 (×) and 0.2 (▷). Observers located at 30° (a), 60° (b), 90° (c), 120° (d), and 150° (e).

Given that the stochastic method for evolving turbulence and the high-order LEE solver have both been validated, another explanation is that numerical issues arise when coupling the two to perform the time integration of the differential equations. The time evolution of the strength of each vortex particle modelled by Eq. (5.10) is continuous but not differentiable and therefore the resulting synthetic turbulent velocity field along the flat plate is not differentiable in time, as illustrated in Figure 5.8. The Runge-Kutta scheme used for the time integration of the linearised Euler equations could be modified so as to deal with stochastic differential equations more accurately (see Ref. [63]), but

that would require to use a different time integration scheme for only a few grid points, which could be rather cumbersome to implement.

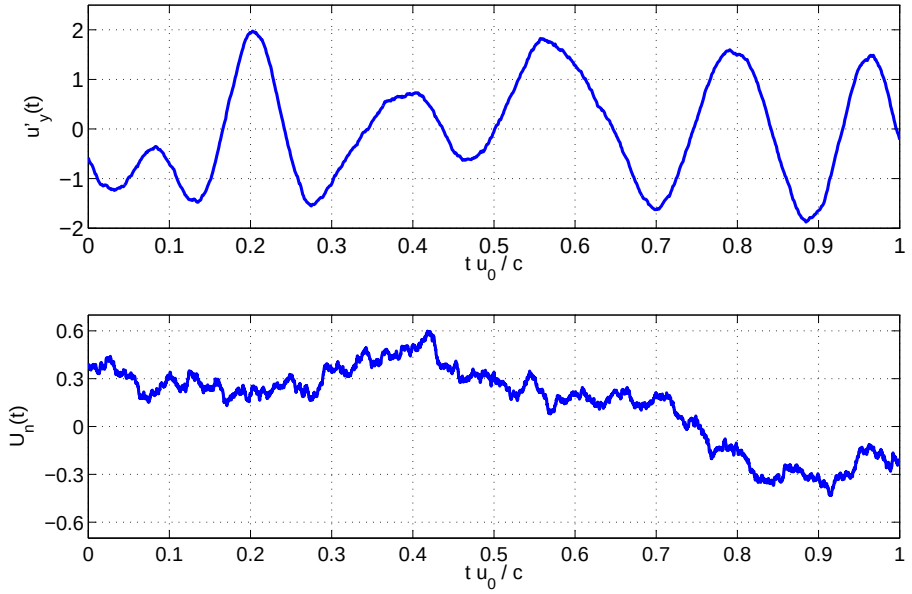

FIGURE 5.8: Top: Synthetic turbulent velocity field computed at the centre of the flat plate versus time. Bottom: Time evolution of the strength of a given vortex particle modelled by the Langevin equation in Eq. (5.10).

A possible alternative to modifying the Runge-Kutta scheme is to smooth the evolution of the synthetic velocity field by adding a filter in time. In order to implement such a filter it will be necessary to store several previous time steps, so this approach is not used here due to the associated computational cost.

Yet another alternative is to model the time correlation of the turbulence in such a way that the resulting synthetic velocity field is a differentiable function in time. This can be achieved from two different approaches. One approach is to smooth the random field U given by the Langevin equation by filtering it with the help on a second Langevin equation. This approach has been proposed by Ewert and Siefert in Ref. [15]. Another approach is to modify the stochastic source in the Langevin equation. The stochastic field U is not differentiable in time due to the lack of continuity of the stochastic source ζ. Therefore, we propose to replace ζ in the Langevin equation (5.10) by a continuous random source. Both approaches result in second-order Langevin models but with different set of parameters. While in Ref. [15] just an overview of the second-order Langevin model is included, in the next section the model proposed here is presented in detail.

5.2 Second-order Langevin model

In this section the stochastic source in a standard Langevin equation is modified so that it is a continuous function in time. The objective is that the resulting stochastic field U

would be a differentiable function in time and hence the numerical issues discussed in the previous section would be overcome.

5.2.1 Model

The numerical issues introduced by the standard Langevin equation in Eq. (5.10) are related with the lack of continuity of the source term ζ. Here the theory is generalised by considering a stochastic source W which is assumed to be a continuous function in time (so it is not pure white noise) and it is also assumed to be correlated with U. This yields the Langevin equation

$$\frac{\mathrm{D}_0}{\mathrm{D}t}U = -\frac{1}{\tau}U + W, \tag{5.20}$$

with initial condition $U(0) = U_0$ where U_0 is also a random variable. We begin by deriving the conditions on W and U_0 for the random process to be statistically stationary. Then we describe how W can be generated.

Proceeding as for the standard Langevin equation in Eq. (5.10), the rate of change over time of the stochastic field U along the streamlines defined by the convection velocity, $\boldsymbol{u}_c$, can be derived from the Lagrangian version of Eq. (5.20):

$$\frac{\partial}{\partial t}U(\boldsymbol{x}'(\boldsymbol{x}_0,t),t) = -\frac{1}{\tau}U(\boldsymbol{x}'(\boldsymbol{x}_0,t),t) + W(\boldsymbol{x}'(\boldsymbol{x}_0,t),t). \tag{5.21}$$

This is similar to Eq. (5.5) but now the source term is continuous in time and correlated with U.

For each fluid element, the solution of Eq. (5.21) as a function of time can be written:

$$U(t) = U_0\exp(-t/\tau) + \exp(-t/\tau)\int_0^t \exp(t'/\tau)W(t')\mathrm{d}t'. \tag{5.22}$$

Note that in contrast with the standard Langevin equation, the integral can be defined in the standard way (it is not an stochastic integral) since W is continuous in time. Its energy (or variance), $\langle U(t)^2\rangle$, is therefore given by:

$$\begin{aligned}\langle U(t)^2\rangle =& \langle U_0^2\rangle\exp(-2t/\tau) + 2\exp(-2t/\tau)\int_0^t \exp(t'/\tau)\langle U_0\ W(t')\rangle\mathrm{d}t' \\ &+ \exp(-2t/\tau)\int_0^t \exp(t'/\tau)\int_0^t \exp(\tilde{t}/\tau)\langle W(t')\ W(\tilde{t})\rangle\mathrm{d}t'\mathrm{d}\tilde{t}.\end{aligned} \tag{5.23}$$

From the requirement that the random process U is statistically stationary, we can use that $\langle U(t)^2\rangle = \langle U_0^2\rangle$ to get:

$$\langle U_0\ W(t)\rangle = \frac{\langle U_0^2\rangle}{\tau}\exp(t/\tau)\left[1 - \frac{\tau}{\langle U_0^2\rangle}\int_0^t \exp(-s/\tau)R_W(s)\mathrm{d}s\right], \tag{5.24}$$

where R_W is the time correlation of W: $R_W(t) = \langle W(t_1)\, W(t_2)\rangle$ with $t = |t_2 - t_1|$. W is also a random process in time, therefore it can be assumed that its correlation with U_0 vanishes with time. Hence, we can impose the condition that $\langle U_0\, W(t)\rangle \to 0$ as $t \to \infty$. For this condition to be verified, the term in brackets in Eq. (5.24) must be of the order of $\exp[-t(1+A)/\tau]$ where A is a constant such that $A < 0$. Following Krasnoff *et al.* [67], this condition can be achieved by defining:

$$R_W(t) = \langle W_0^2\rangle \exp(-\gamma t), \tag{5.25}$$

with $\langle W_0^2\rangle = \langle U_0^2\rangle/(\tau\tau_d)$ and $\gamma = (1/\tau_d - 1/\tau)$ where an additional time scale τ_d such that $\tau_d \ll \tau$ has been introduced. With these choices we get:

$$\langle U_0\, W(t)\rangle = \frac{\langle U_0^2\rangle}{\tau\langle W_0^2\rangle} R_W(t), \tag{5.26}$$

which, when combined with Eq. (5.23), yields a constant energy of U.

The resulting time correlation, $R_U(t) = \langle U(t_1)\, U(t_2)\rangle$, is

$$R_U(t) = \frac{\exp(-t/\tau)\,\langle U_0^2\rangle}{\tau - 2\tau_d}\left\{\tau - \tau_d - \tau_d \exp\left[\left(\frac{2}{\tau} - \frac{1}{\tau_d}\right) t\right]\right\}. \tag{5.27}$$

It converges to $\langle U_0^2\rangle \exp(-t/\tau)$ as $\tau_d \to 0$ verifying Eq. (5.11). The influence of the additional parameter τ_d will be described in section 5.2.3.2.

The stochastic source W in the Langevin equation Eq. (5.20) is now fully defined and it can be generated using a second Langevin equation (similar to the one used in section 5.1):

$$\frac{\mathrm{D}_0}{\mathrm{D}t} W = -\alpha' W + \beta'\zeta, \tag{5.28}$$

where ζ is a continuous white noise source that can be defined as the time derivative of a Wiener process verifying Eq. (5.4):

$$\langle \zeta(\boldsymbol{x}, t)\rangle = 0, \quad \langle \zeta(\boldsymbol{x}_1, t_1)\, \zeta(\boldsymbol{x}_2, t_2)\rangle = \delta(\boldsymbol{x}_2 - \boldsymbol{x}_1)\delta(t_2 - t_1). \tag{5.29}$$

Following the same analysis as for the standard Langevin equation Eq. (5.2), the random source W is statistically stationary with time correlation $R_W(t) = \langle W_0^2\rangle \exp(-\gamma t)$ if one defines $\beta' = \sqrt{2\alpha'\langle W_0^2\rangle}$ and $\alpha' = \gamma$.

The initial condition $W(0) = W_0$ is by definition a random variable following a zero-mean Gaussian distribution with variance $\langle W_0^2\rangle = \langle U_0^2\rangle/(\tau\tau_d)$. It follows from Eq. (5.26) that W_0 and U_0 are correlated verifying $\langle U_0\, W_0\rangle = \langle U_0^2\rangle/(\tau\langle W_0^2\rangle)$. These constraints can be met by defining W_0 such that:

$$W_0 = \frac{1}{\tau} U_0 + \sqrt{\frac{\gamma}{\tau}}\, \xi, \tag{5.30}$$

where ξ is an independent zero-mean random variable with unit variance.

Note that the integral time scale of the source W is $1/\gamma$. Since $\tau_d \ll \tau$, the characteristic time scale of W is of the order of τ_d. Following Krasnoff *et al.* [67], from a physical point of view the source W can be understood to represent the viscous diffusion process of the smallest turbulent motions which occur at the Kolmogorov time scale. Based on this interpretation, the ratio τ/τ_d scales as the Reynolds number.

To summarise, the combination of Eq. (5.20) and Eq. (5.28) forms a second-order Langevin model given by:

$$\begin{cases} \dfrac{\mathrm{D}_0}{\mathrm{D}t}U = -\dfrac{1}{\tau}U + W, \\ \dfrac{\mathrm{D}_0}{\mathrm{D}t}W = -\gamma W + \sqrt{2\gamma\langle W_0^2\rangle}\ \zeta, \end{cases} \tag{5.31}$$

with $\gamma = 1/\tau_d - 1/\tau$. W is continuous but not differentiable in time. U is therefore smoother when generated by the second-order Langevin model in Eq. (5.31) than if it were generated by the standard Langevin equation in Eq. (5.10) with noise source a white noise field.

For the case of frozen turbulence, both time scales τ and τ_d tend to infinity. Hence the right-hand sides in the system Eq. (5.31) are equal to zero and the model is only representing convection effects, $\mathrm{D}_0U/\mathrm{D}t = 0$ and $\mathrm{D}_0W/\mathrm{D}t = 0$. Note that Eq. (5.30) verifies $W_0 = 0$ for the case of frozen turbulence ($\tau, \tau_d \to \infty$).

The second-order Langevin model, Eq. (5.31), requires the following input parameters to model the time evolution of the turbulence:

- Convection velocity of the flow, $\boldsymbol{u}_c$. It can be provided by steady RANS or LES simulations or by measurements.
- Integral time scale of the turbulence, τ. τ is the Lagrangian time scale of the turbulence. It is a function of the dissipation rate, ϵ, and a weak function of the Reynolds number. Its value is given throughout the scaling procedure proposed by Pope [14] to define the integral length scale of the turbulence for the Langevin equation. See Eq. (5.12) and the related discussion in section 5.3.
- Characteristic time scale of the viscous dissipation process, τ_d. From the point of view of the physics of turbulent flows, τ_d is of the order of the Kolmogorov time scale [67]. However, τ_d is used here as a numerical parameter to smooth the time evolution of the strength of the vortices. A discussion of how this parameter is chosen will be given in section 5.2.3.2.

5.2.2 Numerical implementation

The numerical discretisation of the second-order Langevin model is performed following the same approach as for the first-order Langevin model.

The Lagrangian formulation of the second-order Langevin model, Eq. (5.31), reads

$$\begin{cases} \dfrac{\partial}{\partial t}U(\boldsymbol{x}'(\boldsymbol{x}_0,t),t) = -\dfrac{1}{\tau}U(\boldsymbol{x}'(\boldsymbol{x}_0,t),t) + W(\boldsymbol{x}'(\boldsymbol{x}_0,t),t), \\ \dfrac{\partial}{\partial t}W(\boldsymbol{x}'(\boldsymbol{x}_0,t),t) = -\gamma W(\boldsymbol{x}'(\boldsymbol{x}_0,t),t) + \sqrt{2\gamma\langle W_0^2\rangle}\ \zeta(\boldsymbol{x}'(\boldsymbol{x}_0,t),t). \end{cases} \tag{5.32}$$

The rate of change of the strength of the vortex particle U_n can be derived by integrating Eq. (5.32) over the n^{th} fluid element $\mathbb{S}_{0n}$,

$$\begin{cases} \dfrac{\partial}{\partial t}U_n(t) = -\dfrac{1}{\tau}U_n(t) + W_n(t), \\ \dfrac{\partial}{\partial t}W_n(t) = -\gamma W_n(t) + \sqrt{2\gamma\langle W_0^2\rangle}\ \zeta_n(t), \end{cases} \tag{5.33}$$

where W_n and ζ_n are the weighted averages over $\mathbb{S}_{0n}$ of W and ζ, respectively

$$W_n(t) = \int_{\mathbb{S}_{0n}} W(\boldsymbol{x}'(\boldsymbol{x}_0,t),t)J\mathrm{d}\boldsymbol{x}_0, \quad \text{and} \quad \zeta_n(t) = \int_{\mathbb{S}_{0n}} \zeta(\boldsymbol{x}'(\boldsymbol{x}_0,t),t)J\mathrm{d}\boldsymbol{x}_0.$$

In order to determine the strength of the n^{th} vortex particle at each time, values for ζ_n at each time step must be provided together with initial conditions for U_n and W_n. Since U_0 and ζ are random variables following a zero-mean Gaussian distribution with unit standard deviation, by definition $U_n(0)$ and $\zeta_n(t)$ follow a zero-mean Gaussian distribution with variance:

$$\int_{\mathbb{S}_{0n}} J^2\mathrm{d}\boldsymbol{x}_0.$$

W_0 is a random variable following a zero-mean Gaussian distribution with variance $\langle W_0^2\rangle = \langle U_0^2\rangle/(\tau\tau_d)$, therefore $W_n(0)$ follows a zero-mean Gaussian distribution with variance:

$$\frac{1}{\tau\tau_d}\int_{\mathbb{S}_{0n}} J^2\mathrm{d}\boldsymbol{x}_0.$$

Note that for incompressible flows we have $J = 1$.

The numerical discretisation of the second-order Langevin model in Eq. (5.33) is also based on a forward Euler scheme, yielding:

$$U_n(t+\Delta t) = \left(1 - \frac{\Delta t}{\tau}\right) U_n(t) + \Delta t W_n(t), \tag{5.34a}$$

$$W_n(t+\Delta t) = (1-\gamma\Delta t)\, W_n(t) + \sqrt{2\gamma\Delta t\langle W_0^2\rangle}\ \zeta_n(t). \tag{5.34b}$$

Note that while the rate of change of W_n is defined by a Langevin equation with source term a white noise field (and therefore the analysis performed in section 5.1.2 applies), the rate of change of the stochastic field U_n is determined by a Langevin equation with a continuous source term. This is why the factor $\sqrt{\Delta t}$ on the right hand side of Eq. (5.34b) is not found in Eq. (5.34a).

In summary, the second-order Langevin model proposed in this section can be combined with the random-vortex-particle method to generate synthetic evolving turbulence in a Lagrangian formulation yielding Eq. (2.67).

5.2.3 Validation

Numerical simulations are performed to evaluate the statistical behaviour of the turbulence along the airfoil and far-field noise levels. As in chapter 4, acoustic predictions in the far field are compared against Amiet's analytical solution for the case of frozen turbulence but also against the results obtained for evolving turbulence modelled with the standard Langevin equation.

It is shown in this section that provided the small time scale τ_d is selected properly, the second-order Langevin model provides with synthetic turbulent velocity fields with the same statistical behaviour as the standard Langevin equation. However, by modelling the rate of change of the vortex strengths with the proposed second-order Langevin model, the spurious high frequency sound sources observed with the Langevin equation are not present.

5.2.3.1 Problem definition and computational set up

The test case and corresponding computational set up used to investigate broadband interaction noise in the previous section is also considered here. Please refer to section 5.1.3.1 and section 5.1.3.2 for a full description.

The only difference with the previous computational set up, is that the strength of each vortex particle is now modelled by the second-order Langevin model in Eq. (5.34). In this case, the method requires as input an additional time scale, τ_d. We begin by defining some guidelines to adjust the value of τ_d.

5.2.3.2 Influence of the additional time scale τ_d

The second-order Langevin model in Eq. (5.31) relies on a stochastic source W with integral time scale $1/\gamma \approx \tau_d$ to model the time evolution of the strengths of the vortex particles. In this work the time scale τ_d is used merely as a numerical parameter that

controls the smoothness of the strength of the vortex particles over time. Two constraints are imposed over τ_d:

- The first constraint is that τ_d must be sufficiently smaller than the integral time scale of the turbulence τ so that the time correlation of the vortex strength U given by Eq. (5.27) is a good approximation of $\exp(-t/\tau)$.
- The second issue is that the numerical time step used to discretise Eq. (5.33) must be sufficiently small compared to τ_d in order to discretise Eq. (5.33) accurately. The smaller the time scale τ_d is, the smaller the numerical time step has to be, and so the more computationally demanding the method is. An effort is therefore made to select the largest τ_d possible such that reliable statistics are obtained at an acceptable computational cost.

A parametric study is therefore performed to adjust the value of τ_d. The list of cases included in the parametric study is depicted in table 5.1. For these cases the statistical behaviour of the turbulence along the flat plate and the acoustic pressure in the far field are assessed.

	τ	τ/τ_d	$\tau_d/\Delta t$
Test case 1	20.86	700	10
Test case 2	20.86	150	50
Test case 3	20.86	150	100
Test case 4	20.86	70	100
Test case 5	20.86	70	200
Test case 6	20.86	20	350

TABLE 5.1: List of cases considered to adjust the value of τ_d.

Figure 5.9 shows the theoretical time correlation of U given by Eq. (5.27) as produced by the second-order Langevin model for different values of τ_d against the target time correlation $\exp(-t/\tau)$ that we aim to capture. We can see that for ratios τ/τ_d larger than 70 the error is smaller than 2%, however for ratios τ/τ_d around 20 the error increases to about 4%. An important feature is that by increasing the value of τ_d ($\tau/\tau_d \to 1$), the time correlation of U is overpredicted by the second-order Langevin model. This means that if τ_d is not sufficiently small compared to τ, the effects of loss of correlation in time determined by the integral length scale of the turbulence are partially neglected.

Figure 5.10 depicts both theoretical and numerical two-point two-time correlations R_{11} and R_{22} for points along the airfoil at distance $r/c = 0.6$. Overall, good agreement is obtained when comparing numerical and analytical correlations. Numerical results capture the shape inherited from the Gaussian filter and also the loss of correlation due to the random change in the strength of the vortices. The worst fit between numerical

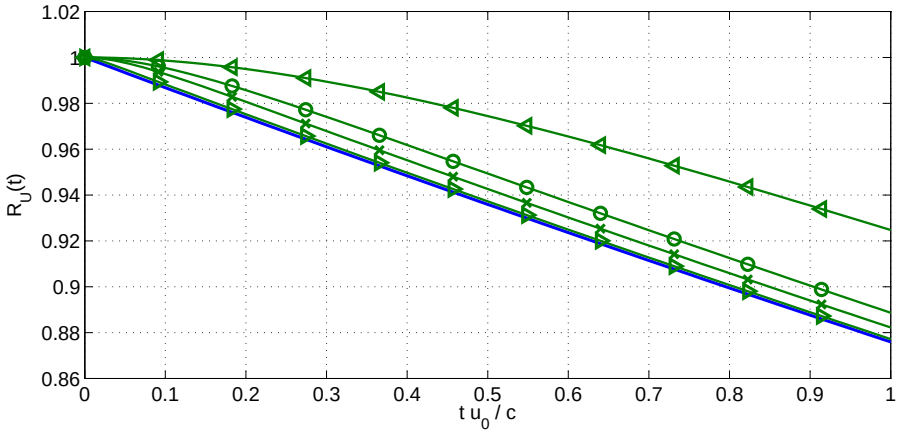

FIGURE 5.9: Target exponential time correlation of U (—) versus theoretical correlation given by the second-order Langevin model for different values of τ_d. $\tau/\tau_d \approx 700$ (▷), $\tau/\tau_d \approx 150$ (×), $\tau/\tau_d \approx 70$ (○), and $\tau/\tau_d \approx 20$ (◁).

and analytical results is found for $\tau/\tau_d \approx 20$ due to the poor approximation of $\exp(-t/\tau)$ by the time correlation of U, as seen in Figure 5.9.

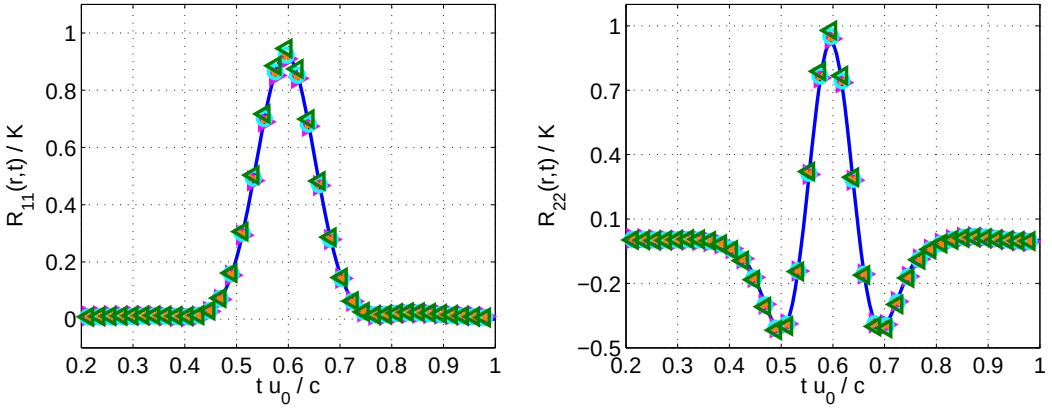

FIGURE 5.10: Two-point two-time correlations R_{11} (left) and R_{22} (right) for $r/c = 0.6$. Solid lines represent analytical results. Symbols stand for numerical correlations obtained with the second-order Langevin model for $\tau/\tau_d \approx 700$ (▷), $\tau/\tau_d \approx 150$ (×), $\tau/\tau_d \approx 70$ (○), and $\tau/\tau_d \approx 20$ (◁). Averages taken from 25,000 samples at a sampling every $20\Delta t$.

It has been shown that if τ_d is not sufficiently small compared to τ then the second-order Langevin model in Eq. (5.31) overpredicts the correlation in time of the vortex strength. This can also be illustrated by plotting the time evolution of the strength of the vortex particles for the different values of τ_d. In Figure 5.11 the time evolution of a given vortex particle modelled with the second-order Langevin model for different values τ_d is compared against the time evolution of the same vortex particle modelled with the standard Langevin equation in Eq. (5.10). We can see that a much smoother behaviour is obtained with the second-order model compared to the standard Langevin equation.

The larger the value of the τ_d is, the smoother the solution is until the point where the strength is almost independent of time.

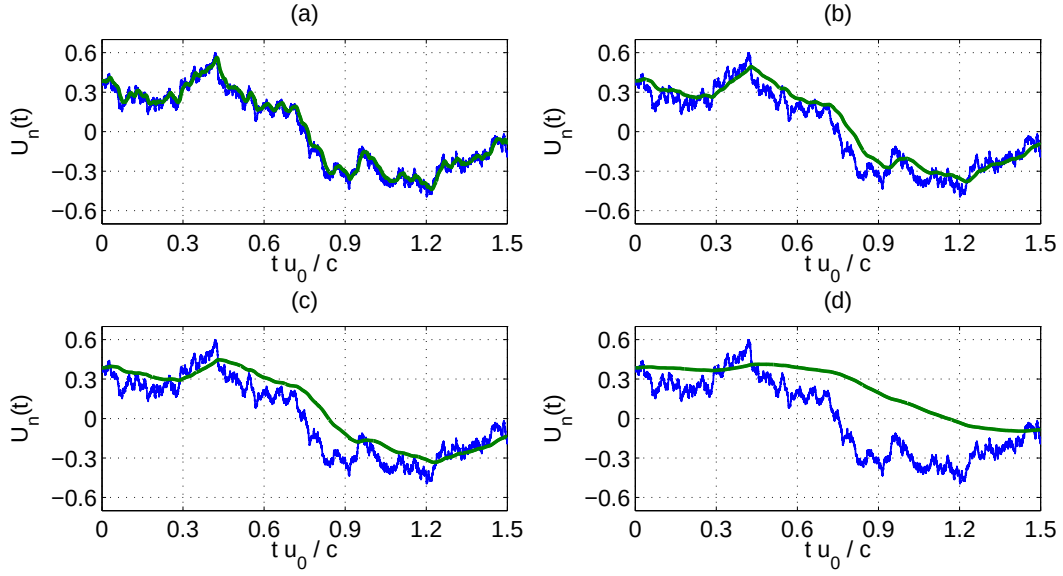

FIGURE 5.11: Time evolution of the strength of a given vortex particle modelled by the standard Langevin equation (—) versus the second-order Langevin model (—). $\tau/\tau_d \approx 700$ (a), $\tau/\tau_d \approx 150$ (b), $\tau/\tau_d \approx 70$ (c), and $\tau/\tau_d \approx 20$ (d).

Therefore, we can conclude that provided that the small time scale τ_d is properly selected the exponential time decorrelation of the turbulence can be captured by modelling the rate of change of the vortex particles with the second-order Langevin model in Eq. (5.31).

We now focus on the acoustic field predicted when using the second-order Langevin model for different ratios τ/τ_d and in how the spurious sound sources radiating at high frequencies introduced by the standard Langevin equation can be removed. Noise levels in the far field are computed using the same procedure as for the results obtained for the case of frozen turbulence in chapter 4.

Figure 5.12 depicts the sound pressure levels for an observer at five different locations: 30, 60, 90, 120, and 150 degrees from the downstream direction. Numerical and analytical results for frozen turbulence are compared against numerical sound pressure levels obtained with the second-order Langevin model for the values of τ_d under investigation. For the smallest ratio, $\tau/\tau_d \approx 20$, similar SPL are predicted either by assuming frozen or evolving turbulence. However, for this case, τ_d is too large and the second-order Langevin model underestimates the loss of correlation in time as shown in Figure 5.9. In contrast, for the smallest value of τ_d considered here, $\tau/\tau_d \approx 700$, sound pressure levels in the far field are similar to those obtained with the standard Langevin equation showing large sound levels at high frequencies especially for upstream locations, see Figure 5.4.

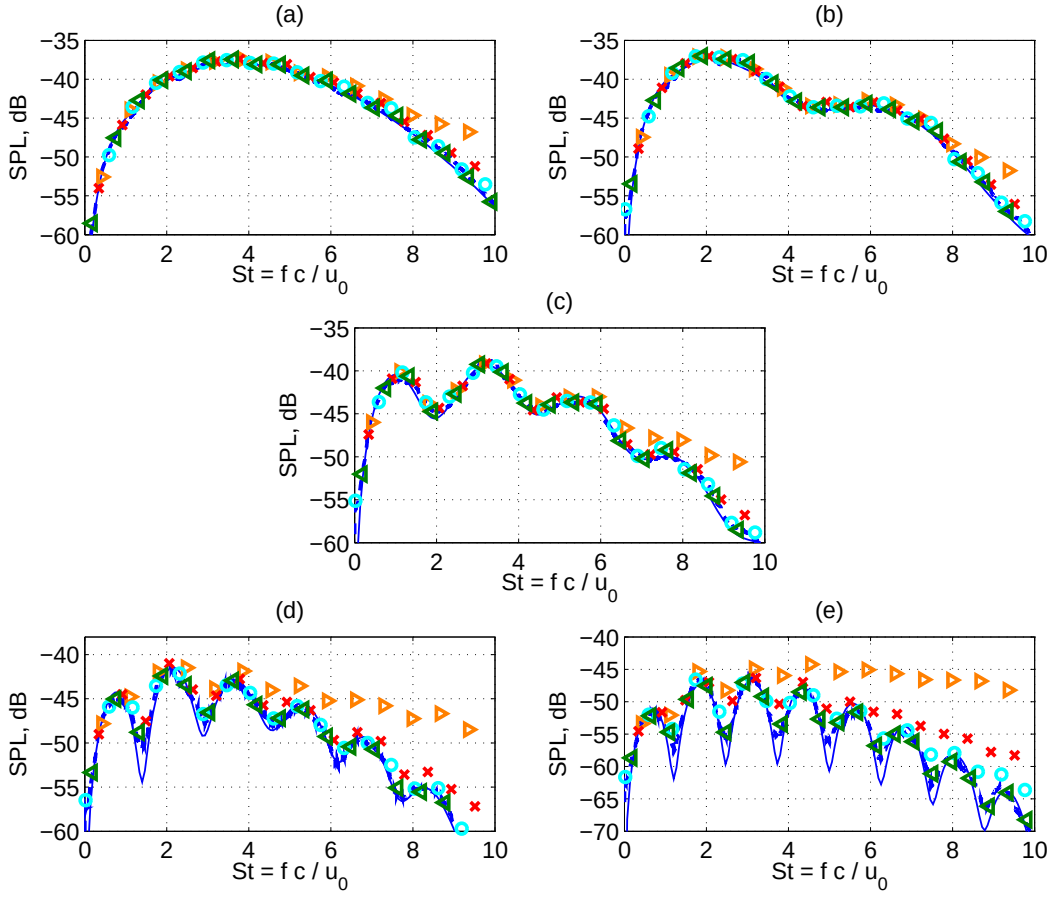

FIGURE 5.12: Analytical (—) and numerical (– · –) SPL for frozen turbulence versus numerical results for the case of evolving turbulence computed with $\tau/\tau_d \approx 700$ (▷), $\tau/\tau_d \approx 150$ (×), $\tau/\tau_d \approx 70$ (○), and $\tau/\tau_d \approx 20$ (◁). Observers located at 30° (a), 60° (b), 90° (c), 120° (d), and 150° (e).

5.2.3.3 Influence of the numerical time step

We now investigate the sensitivity of the results to the numerical time step Δt. Numerical results depicted in Figure 5.12 have all been computed using the same time step for the numerical integration corresponding to a CFL number of 0.8 and it is four orders of magnitude smaller than the integral time scale τ of the turbulence.

The small time scale τ_d should be sufficiently large compared to the numerical time step in order to discretise Eq. (5.31) accurately. Therefore, the influence of the ratio $\tau_d/\Delta t$ in far-field noise levels is now discussed for the ratios $\tau/\tau_d \approx 70$ and $\tau/\tau_d \approx 150$.

Sound pressure levels for the ratio $\tau/\tau_d \approx 70$ computed with numerical time steps corresponding to $\tau_d/\Delta t \approx 100$ and $\tau_d/\Delta t \approx 200$ are depicted in Figure 5.13. Simulation results obtained with both time steps predict the similar levels of noise for the five locations considered and only at 150 degrees a disagreement of about 1 dB in amplitude is found. Note that sound pressure levels at 150 degrees are at least 15 dB bellow what

it is observed at downstream locations. This suggest that the numerical results converge for the largest time step, $\tau_d/\Delta t \approx 100$.

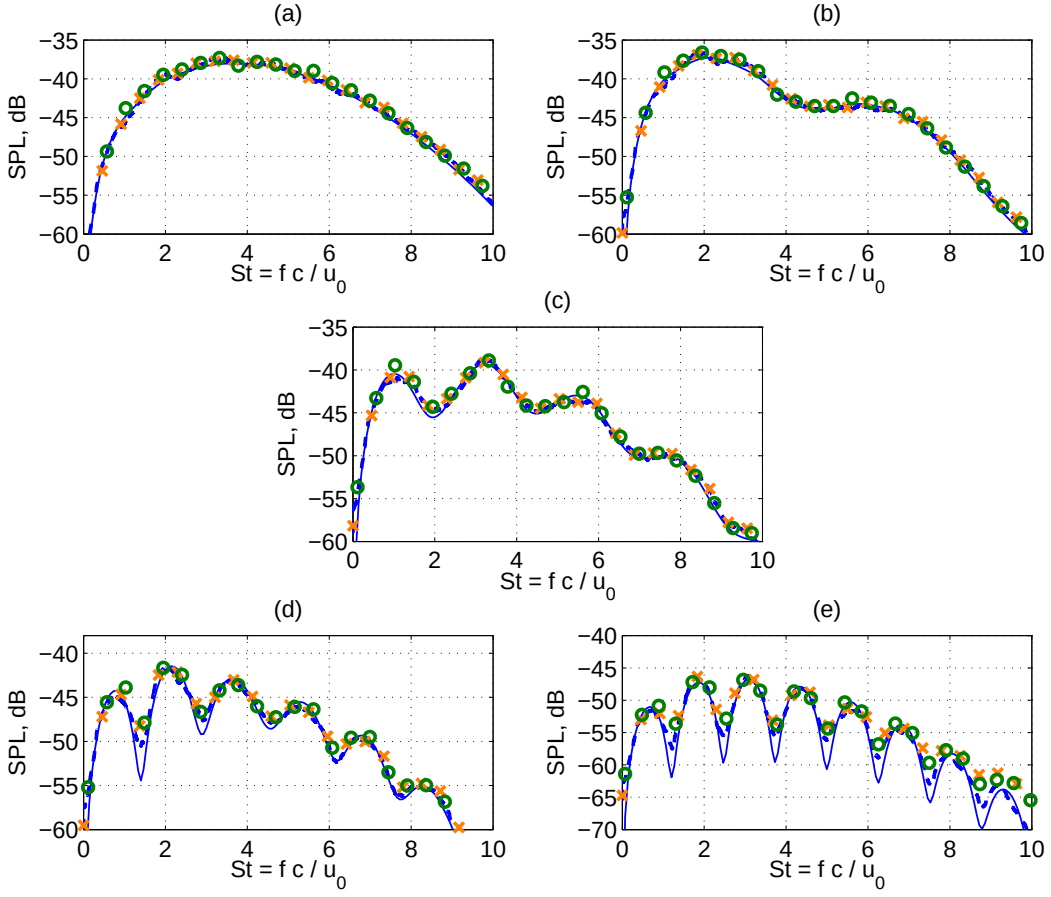

FIGURE 5.13: Analytical (—) and numerical (– · –) SPL for frozen turbulence versus numerical results for the case of evolving turbulence computed with $\tau/\tau_d \approx 70$ and numerical time steps corresponding to $\tau_d/\Delta t \approx 100$ (×) and $\tau_d/\Delta t \approx 200$ (○). Observers located at 30° (a), 60° (b), 90° (c), 120° (d), and 150° (e).

Figure 5.14 shows far-field sound pressure levels for different locations computed with $\tau/\tau_d \approx 150$ and numerical time steps corresponding $\tau_d/\Delta t \approx 50$ and $\tau_d/\Delta t \approx 100$. Similar SPL are predicted for downstream locations, however at upstream locations (especially at high frequencies) they are still dependent on the numerical time step showing that numerical results have not converged for $\tau_d/\Delta t \approx 50$. (This implies that results shown in Figure 5.12 for $\tau/\tau_d \approx 700$ were also dependent on the time step.)

Figure 5.15 compares far-field results for $\tau/\tau_d \approx 70$ against $\tau/\tau_d \approx 150$ where for each case the time step is approximately a hundred times smaller than the corresponding τ_d. We can see that similar sound pressure levels are predicted in both cases. Therefore, the method is not highly dependent on the value of the small time scale τ_d provided that the time step used in the discretisation is small enough. The computational cost of the method is higher as the numerical time step decreases; hence one could argue that selecting the small time scale τ_d such that $\tau/\tau_d \approx 70$ is more desirable than $\tau/\tau_d \approx 150$.

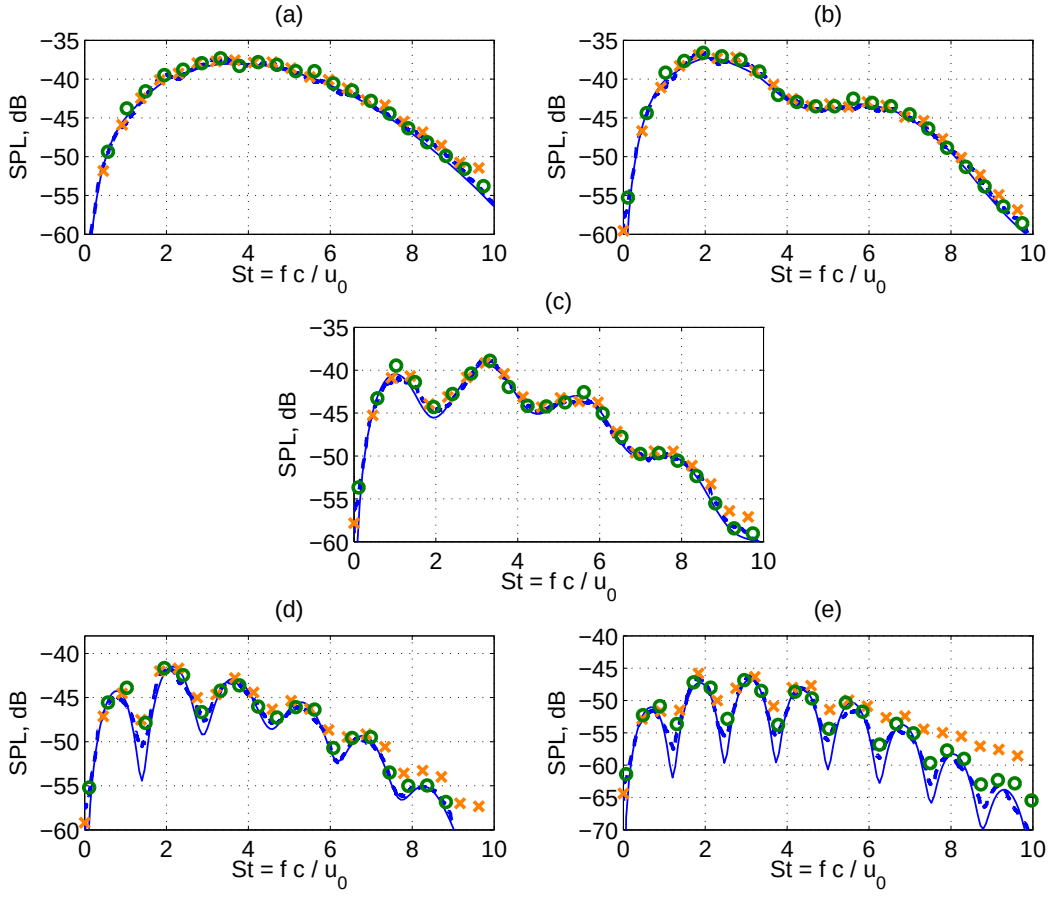

FIGURE 5.14: Analytical (—) and numerical (– · –) SPL for frozen turbulence versus numerical results for the case of evolving turbulence computed with $\tau/\tau_d \approx 150$ and numerical time steps corresponding to $\tau_d/\Delta t \approx 50$ (×) and $\tau_d/\Delta t \approx 100$ (○). Observers located at 30° (a), 60° (b), 90° (c), 120° (d), and 150° (e).

In addition, note the numerical time step corresponding to $\tau/\tau_d \approx 70$ yields a CFL number of 0.8.

5.2.3.4 Conclusions

From the validation of the second-order Langevin model in Eq. (5.31) performed in this section it can be concluded that reliable far-field noise levels are predicted by the stochastic method when ensuring that the small time scale τ_d is at least about 70 times smaller than the integral time scale τ and about a hundred times larger than the numerical time step Δ. For these parameter values, the second-order Langevin model achieves accurate two-point two-time correlations along the airfoil but the large amplitude of noise levels at high frequencies associated with spurious sound sources predicted by the standard Langevin equation in Eq. (5.10) are no longer present.

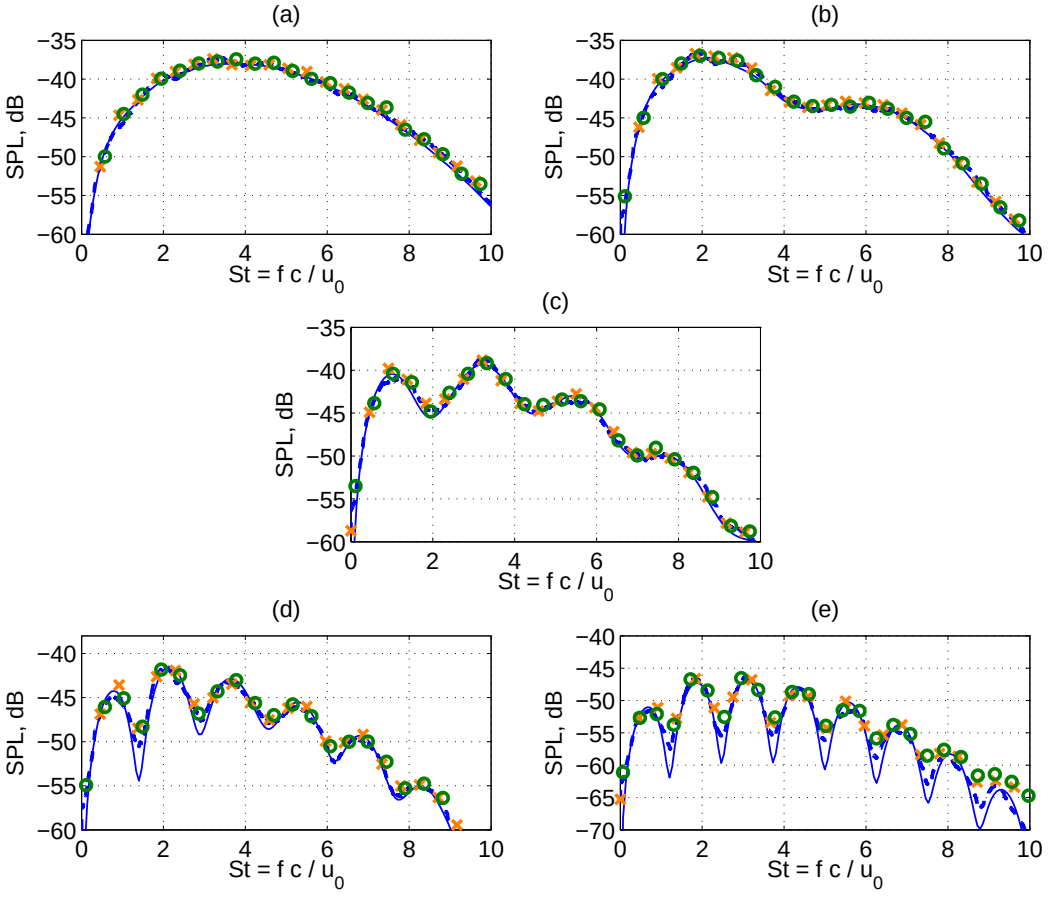

FIGURE 5.15: Analytical (—) and numerical (– · –) SPL for frozen turbulence versus numerical results for the case of evolving turbulence computed with $\tau/\tau_d \approx 70$ and time step Δt (○) and with $\tau/\tau_d \approx 150$ and $\Delta t/2$ (×). Observers located at 30° (a), 60° (b), 90° (c), 120° (d), and 150° (e).

Figure 5.16 shows a snapshot of the acoustic pressure field around the airfoil obtained by the second-order Langevin model. It can be observed that the large content of sound waves with small wavelengths radiating from the plate predicted when using the standard Langevin equation are not found in this case, see Figure 5.3.

Far-field directivities at the Strouhal numbers $St = 4$ and $St = 8$ are shown in Figure 5.17 where angles are measured from the downstream direction. It can be seen that for both Strouhal numbers larger noise levels are found at downstream locations. This is in contrast with directivities predicted by the standard Langevin equation where larger amplitudes are predicted for upstream locations (especially for the highest Strouhal number), see Figure 5.5.

Figure 5.18 depicts the overall acoustic power radiated from the airfoil showing that the larger amount of power at high frequencies predicted when using the standard Langevin equation (see Figure 5.6) is not present when modelling the time correlation of the turbulence with the second-order Langevin model provided that the small time scale τ_d

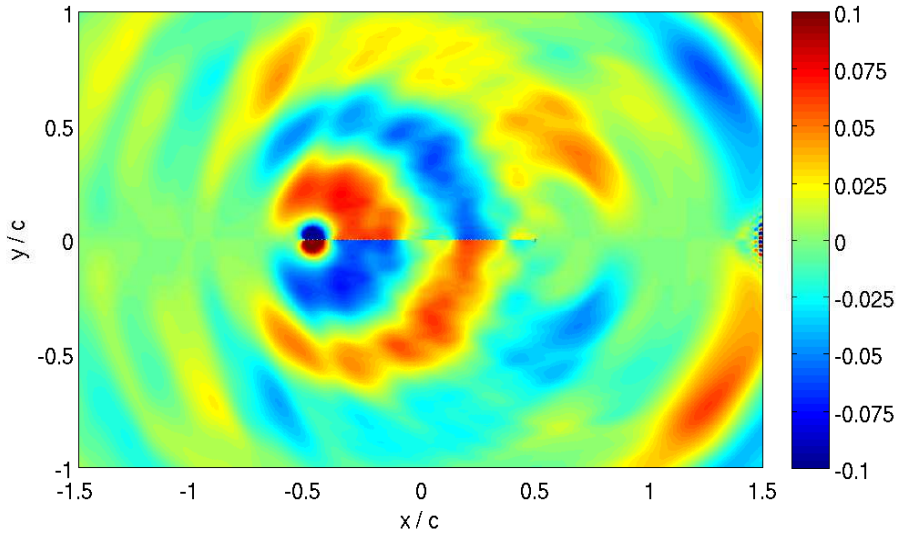

FIGURE 5.16: Snapshot of the acoustic pressure field for the Gaussian spectrum generated with a second-order Langevin model.

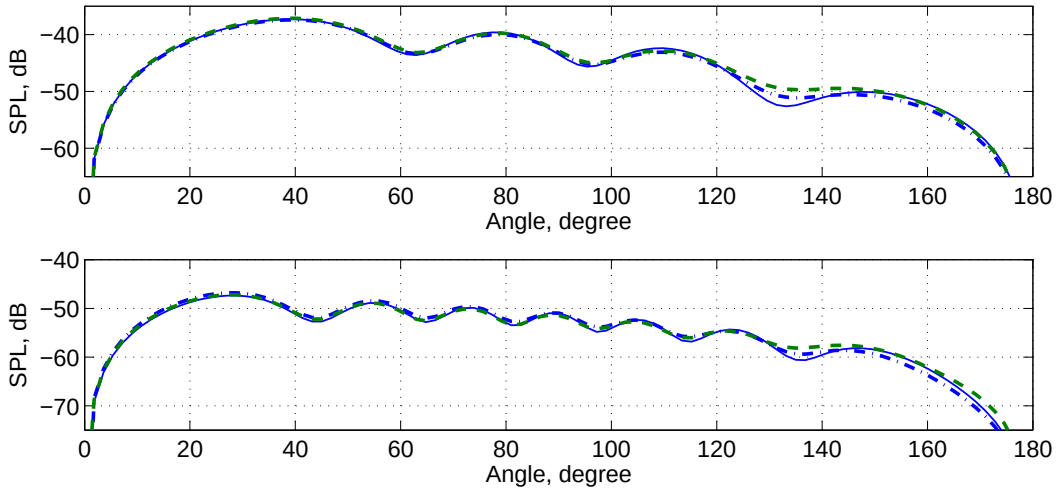

FIGURE 5.17: Far-field directivity at $St = 4$ (top) and $St = 8$ (bottom). Analytical (—) and numerical (– · –) directivity for frozen turbulence versus evolving turbulence (– –) with $\tau/\tau_d \approx 70$.

and the numerical time step Δt are properly selected. Therefore, it is our understanding that the higher amplitude of noise levels predicted by the standard Langevin equation at high frequencies (especially significant at upstream locations) are due to spurious sound sources related with the time discretisation of the sound sources.

We are now confident that the stochastic method predicts reliable far-field noise levels when modelling the time correlation of the turbulence with the second-order Langevin model in Eq. (5.31), so we look at the influence of evolving turbulence.

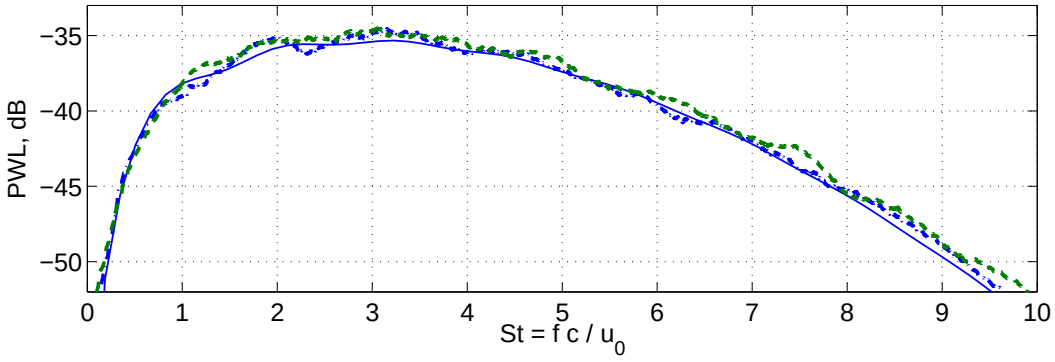

FIGURE 5.18: Analytical (—) and numerical (–·–) acoustic power for frozen turbulence versus numerical results (– –) for the case of evolving turbulence.

5.3 Influence of the integral time scale of the turbulence

In this section the sensitivity of the far-field noise levels to the integral time scale τ of the turbulence is evaluated. The integral time scale of the turbulence is a function of the dissipation rate, ϵ, and a weak function of the Reynolds number. The value of the integral time scale used so far in this work is based on the scaling procedure proposed by Pope [14]:

$$\tau \approx \frac{2K}{C_0 \epsilon}, \tag{5.35}$$

where C_0 is an empirical constant. This scaling procedure relies on the experimental constant C_0 whose value is not precisely established, therefore it is worth to evaluate the sensitivity of the results obtained so far to such empirical constant, or in other words the sensitivity of the results to the integral time scale of the turbulence.

Numerical results presented so far in this chapter for evolving turbulence were obtained by assuming that the empirical constant C_0 was 2.1. The value $C_0 = 2.1$ was obtained from measurements of a thermal wake at low Reynolds numbers and even though τ is only a weak function of the Reynolds number a different estimate might be required in this case. In addition, from a theoretical point of view, the derivation of the scaling process indicates that C_0 should be a good estimate of the Kolmogorov universal constant $\mathcal{C}_0$ which is thought to be greater than 4 and possibly around 6 [14].

By selecting different values of C_0, different integral time scales τ are obtained. The smaller C_0 is, the larger the integral time scale is, and therefore the more similarities should be with the case of frozen turbulence ($\tau \to \infty$). In contrast, as $C_0 \to \mathcal{C}_0$ the smaller the integral time scale becomes emphasising the effects of the time decorrelation. We now assess the dependency of the scattered acoustic field on the constant C_0 and therefore on the integral time scale of the turbulence.

Two additional test cases are considered to investigate the sensitivity of the far-field radiated sound on the integral time scale of the turbulence, see table 5.2. The first one,

assumes $C_0 = 0.66$. This choice is in agreement with Krasnoff *et al.* [67] who proposed that $\tau \approx 3K/\epsilon$. For this case the integral time scale is larger than for $C_0 = 2.1$. Therefore, in order to emphasis the effects of the time correlation in the turbulence, a second test case with a smaller integral time scale corresponding to $C_0 = 3.54$ is considered.

As an estimate of the influence of the integral time scale on the statistical behaviour of the turbulence, the loss of correlation in time for points that are one flat plate away corresponding to each of the integral time scales under investigation is stated in table 5.2. Note that the values of the small time scale τ_d and the numerical time step Δt corresponding to each integral time scale τ in table 5.2 are selected following the guidelines obtained in the previous section.

	C_0	τ	τ/τ_d	$\tau_d/\Delta t$	Time decorrelation	$u_0\tau/\lambda$
Test case 1	0.66	66.40	220	100	5%	340
Test case 2	2.1	20.86	70	100	12%	100
Test case 3	3.54	12.38	70	180	20%	65

TABLE 5.2: List of cases considered to assess the influence of the integral time scale of the turbulence in the scattered acoustic field.

Sound pressure levels in the far field obtained with the three integral time scales under consideration are shown in Figure 5.19. Sound pressure levels at downstream locations appear to be independent of the integral time scale of the turbulence. If we focus on SPL at upstream locations, we can see that by reducing the integral time scale of the turbulence there is a slight increase of sound levels at high frequencies. Noise levels with larger amplitudes are still 15 dB below of what is observed at downstream locations and therefore their contribution to the overall sound power at that frequency is not significant, as shown in Figure 5.20.

In summary, a maximum of 20% loss of correlation between the leading and the trailing edge has been considered. For this test case, the smallest integral time scale of the turbulence, $\tau = 12.38$, is still much larger than the typical time scale of a vortex passing near the leading edge, $\lambda/u_0 = 0.19$. Since most of the noise is radiated from the leading edge, it is plausible to think that noise levels produced by interaction with frozen turbulence should be similar to those produced by a turbulent flow characterised by $\tau = 12.38$. The ratios between the integral length scales of the turbulence considered here and and the typical time scale of a vortex passing near the leading edge are given in table 5.2.

Note that for the integral time scale of the turbulence to be of the order of the typical time scale of a vortex passing next to the leading edge, the scaling procedure in Eq. (5.35) would require $C_0 \approx 230$. Even though the value of C_0 is not well defined, it is a weak function of the Reynolds number so such a large value is rather unrealistic. In

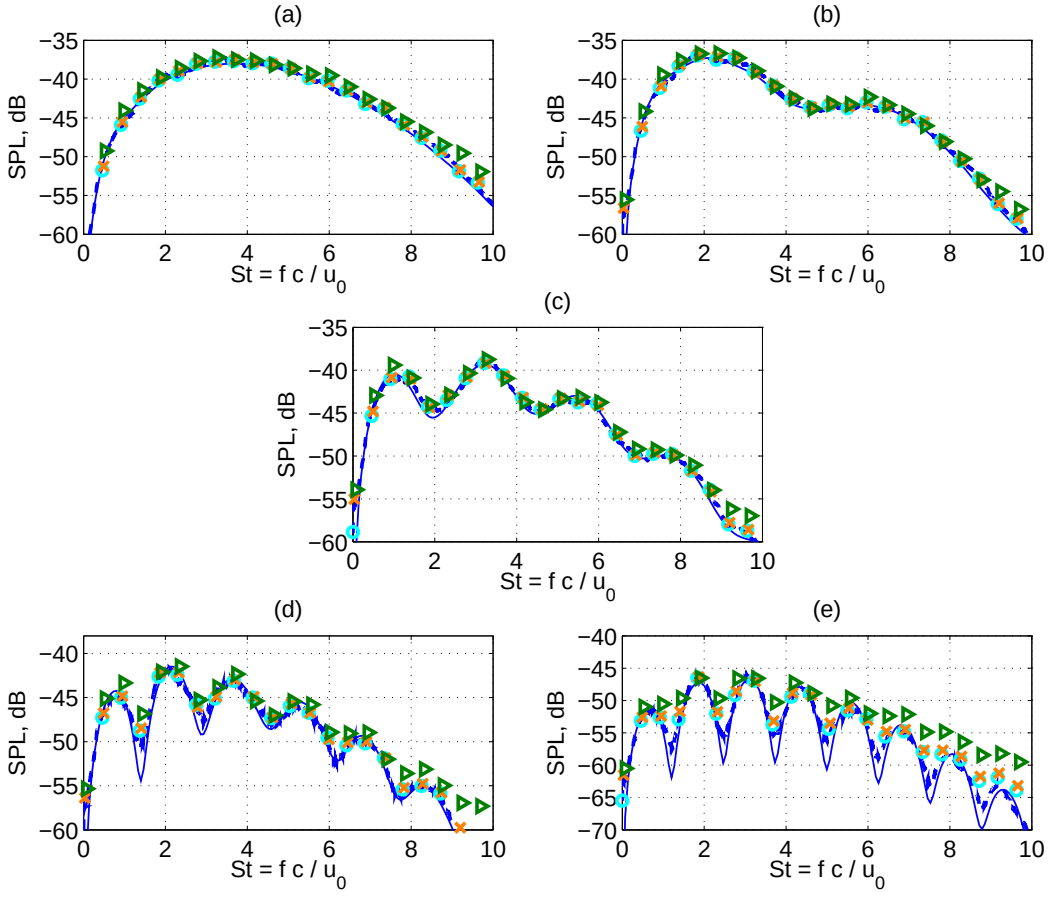

FIGURE 5.19: Analytical (—) and numerical (– · –) SPL for frozen turbulence versus numerical results for the case of evolving turbulence computed with the largest (○), the intermediate (×) and the smallest (▷) integral time scale. Observers located at 30° (a), 60° (b), 90° (c), 120° (d), and 150° (e).

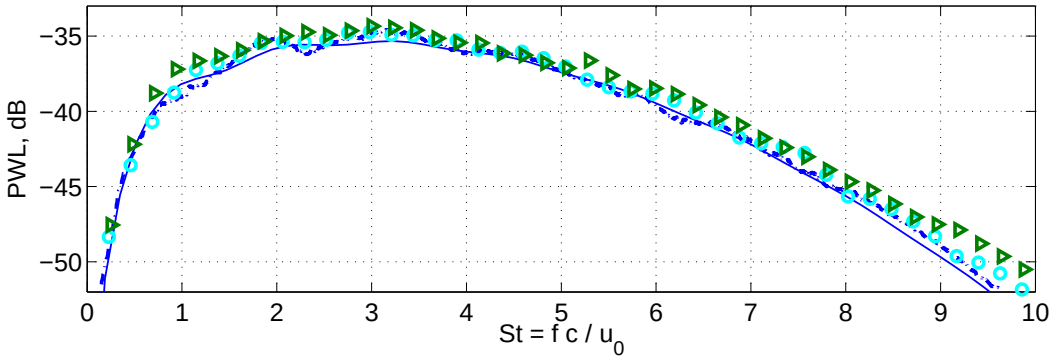

FIGURE 5.20: Analytical (—) and numerical (– · –) acoustic intensity for frozen turbulence versus numerical results for the case of evolving turbulence computed with the smallest (○) and the largest (▷) integral time scale.

addition, the scaling procedure is based on the fact that C_0 should be of the order of the Kolmogorov universal constant which is thought to be between 4 and 6.

5.4 Conclusions

The effects of evolving turbulence have been included in the method to generate synthetic turbulent flows by introducing time-dependence in the strength of each vortex-particle.

Time correlation in synthetic turbulence is usually modelled by Langevin equations, however a standard Langevin equation is not suitable for coupling with the linearised Euler equations solver used in this work due to the lack of smoothness of the resulting synthetic velocity field. It has been shown here that by modelling the time-dependence of the strength of the vortex-particles with a standard Langevin equation significant spurious noise sources are generated at high frequencies.

A possible solution to avoid modifying the LEE solver (such as modifying the Runge-Kutta scheme performing the time integration) is to implement a filter in time that removes the smallest wavelength components. This possibility was disregarded due to the computational complexity associated to it.

A second-order Langevin model has been proposed instead. The second-order Langevin model captures the statistical properties of turbulent flows when assuming that the integral time scale of the turbulence is large compared to a smaller time scale which is used here as a numerical parameter. In contrast with standard Langevin equations, second-order Langevin models describe the turbulent diffusion as a smooth process. Therefore they are suitable for coupling with the Runge-Kutta scheme implemented in the LEE solver to perform the time integration.

The effects of evolving turbulence on broadband fan interaction noise have been assessed for the same test case considered in chapter 4. Reliable far-field results have been obtained using the second-order Langevin model. They show a very limited increase in noise levels when compared with the case of frozen turbulence apart from very high frequencies at upstream locations where noise is negligible. The limited influence of modelling the time correlation of the turbulence can be explained by noting that most of the noise is generated at the leading edge and that the physical integral time scale of the turbulence is much larger than the typical time scale of a vortex-particle passing near the leading edge. The disparity between these time scales implies that the strength of the vortex particles varies very little as they pass near the leading edge generating almost the same turbulent velocity field at that point.

In this chapter, the numerical method has been validated only for the Gaussian spectrum. Note however, that the conclusions reached apply as well for the Liepmann and von Kármán filters as the integral time scale of the turbulence and the typical time scale of a vortex-particle passing near the leading edge are independent of the energy spectra.

Chapter 6

Inhomogeneous Non-stationary Turbulence

In this chapter the stochastic method is modified to provide a more realistic description of rotor-stator interaction noise. Broadband noise is produced when the rotor turbulent wakes impinge on the outlet guide vanes (OGVs or stator vanes) and it is considered one of the main sources of broadband fan noise in modern turbofan engines.

The turbulence downstream of the fan is strongly inhomogeneous and non-stationary. In contrast with Fourier-mode methods which are difficult to apply to model inhomogeneous turbulence [4], we shall demonstrate that random-vortex-particle methods are general enough to deal with inhomogeneous non-stationary turbulence accurately.

The random-vortex-particle method is extended to represent non-stationary inhomogeneous turbulence by combining it with the wake model proposed by Jurdic [18]. This wake model allows for strong variations of the turbulent kinetic energy. Three different implementations of the stochastic method are developed and validated. In addition, to illustrate the capabilities of the method, the statistical properties of the synthetic turbulence along the OGV and far-field noise levels are assessed for different wake configurations.

6.1 Synthetic inhomogeneous non-stationary turbulence

In this section, the random-vortex-particle method originally introduced in section 2.2 is extended to generate synthetic inhomogeneous non-stationary turbulence. In contrast with the case considered in the previous chapters of statistically stationary homogeneous turbulent flows, all statistical quantities of the turbulence such as kinetic energy will now be considered position and time dependent.

We begin by discussing different implementations of the random-vortex-particle method to generate synthetic inhomogeneous non-stationary turbulence. Then a wake model describing the turbulent flows found in the interstage between the fan and the OGVs is used to obtain the input parameters for the stochastic method. Finally, theoretical two-point two-time correlations for each of the implementations are presented.

6.1.1 Random-Vortex-Particle Method

In chapter 2 it was shown that the random-vortex-particle method generate turbulence by summing up the contributions of a series of vortex particles with random strengths, see section 2.3.1. The velocity field reads:

$$u_i'(\boldsymbol{x},t) = \varepsilon_{ij} \sum_{n=1}^{N} \frac{\partial}{\partial x_j} G(|\boldsymbol{x} - \boldsymbol{x}_n(t)|, K, \lambda) U_n(t), \tag{6.1}$$

where ε_{ij} stands for the alternating symbol. G is the spatial filter that controls the spatial correlation and spectrum of the turbulence. $U_n(t)$ can be interpreted as the strength of the vortex particle located at $\boldsymbol{x}_n$ and controls the temporal properties of the turbulence.

In previous chapters, we focussed on statistically stationary homogeneous turbulence and hence the kinetic energy K and the integral length scale λ of the turbulence were constant. Here, our aim is to generate synthetic inhomogeneous non-stationary turbulence in which case the statistics of the turbulence are position and time dependent. Based on the fact that the filter G is a function of the point $\boldsymbol{x}$ at which the velocity field is computed and a function of the vortex location $\boldsymbol{x}_n$, different implementations of the random-vortex-particle method in Eq. (6.1) can be considered[1]. This consideration was also pointed out by Ewert in Ref. [55] when comparing broadband trailing edge noise predicted with the RPM method (see section 2.1.2.3) against laboratory experiments. In contrast with Ref. [55], where the influence of the implementation on the predicted noise levels is not discussed, here different implementations are formulated and validated in details.

We first present the implementations of the stochastic method to generate synthetic inhomogeneous non-stationary turbulence, and the differences between them are then discussed.

[1]The implementations of the stochastic method to generate synthetic inhomogeneous non-stationary turbulence are presented here directly in a Lagrangian formulation. Note that the derivation of the stochastic method in a continuous frame performed in chapter 2 still holds here but the definition of the statistics of the turbulence (correlations, spectra,...) depend now not only on distance and time delay but also on position and time.

6.1.1.1 Implementations

Implementation 1

The first extension of the random-vortex-particle method in Eq. (6.1) to deal with inhomogeneous non-stationary turbulence is based on the assumption that the statistics of the turbulence are defined at the vortex location $\boldsymbol{x}_n$. Using that $K^{1/2}$ is a scaling factor in the filter (see Eq. (2.60)), $G = K^{1/2}\tilde{G}$ and we get:

$$u_i'(\boldsymbol{x},t) = \varepsilon_{ij} \sum_{n=1}^{N} K^{1/2}(\boldsymbol{x}_n,t) \frac{\partial}{\partial x_j} \tilde{G}(r_n, \lambda(\boldsymbol{x}_n,t)) U_n(t), \tag{6.2}$$

where $r_n = |\boldsymbol{x} - \boldsymbol{x}_n(t)|$.

Implementation 2

The second extension of the stochastic method assumes that the statistics of the turbulence are specified at the point $\boldsymbol{x}$ yielding:

$$u_i'(\boldsymbol{x},t) = \varepsilon_{ij} \sum_{n=1}^{N} \frac{\partial}{\partial x_j} \left[K^{1/2}(\boldsymbol{x},t) \tilde{G}(r_n, \lambda(\boldsymbol{x},t)) \right] U_n(t). \tag{6.3}$$

Implementation 3

There is yet another possible implementation of the random-vortex-particle method to generate synthetic inhomogeneous turbulence. In this case, the statistics of the turbulence are defined at the point $\boldsymbol{x}$ but instead of specifying the kinetic energy directly within the stream function, it is imposed to the velocity field itself. Thus, the velocity field is first generated with Eq. (6.1) defining the integral time scale by its local value $\lambda(\boldsymbol{x},t)$ and constant unit kinetic energy, and then it is scaled to achieve the target value of kinetic energy $K(\boldsymbol{x},t)$:

$$u_i'(\boldsymbol{x},t) = \varepsilon_{ij} K^{1/2}(\boldsymbol{x},t) \sum_{n=1}^{N} \frac{\partial}{\partial x_j} \tilde{G}(r_n, \lambda(\boldsymbol{x},t)) U_n(t). \tag{6.4}$$

6.1.1.2 Discussion

For the special case of locally homogeneous turbulence (the statistics of the turbulence are slow varying functions of position), the derivatives of K and λ with respect to position can be neglected and Implementations 2 and 3 lead to the same formulation. In addition, the support of the filter is of the order of the integral length scale and for vortex particles located at distances $r_n < \lambda$ we get that $\lambda(\boldsymbol{x}_n,t) \approx \lambda(\boldsymbol{x},t)$ and $K^{1/2}(\boldsymbol{x}_n,t) \approx K^{1/2}(\boldsymbol{x},t)$. Therefore results obtained with Implementation 1 are expected to be similar to those obtained with any of the other two implementations.

The sensitivity of the synthetic velocity field to the implementation might be larger for strongly inhomogeneous turbulence as large variations of kinetic energy and integral length scale are observed for distances that are small compared to the integral length scale. The influence of the implementation for strongly inhomogeneous non-stationary turbulence on the statistical properties of the synthetic turbulence and radiated sound field will be evaluated in section 6.2.

It is our understanding that Implementation 1 provides a better representation of the physics of the problem than Implementations 2 and 3. It models the turbulence as a cloud of vortex particles where each vortex accounts for the actual properties of the turbulence at its location. However, Implementations 2 and 3 might have computational advantages for the application of broadband fan interaction noise. While Implementation 1 enforces the definition of the statistics on the whole region where vortex particles are distributed, Implementations 2 and 3 require the values of the statistics only at a few grid points. In this sense, Implementation 3 is the most desirable since Implementation 2 entails computing the spatial derivative of the kinetic energy.

Another aspect to highlight is that if the input parameters of the stochastic method are provided by RANS simulations, then defining the kinetic energy and the integral length scale at the boundaries present an added difficulty since the velocity field is zero at the boundary. One would have then to chose an alternative location to pick the values of the statistics. In the approach followed in this work, the turbulence is fully specified upstream of the airfoil and then computed with the random-vortex-particle method as if there were no airfoil. Therefore, in this case the statistics of the turbulence can be defined as a function of physical point or of vortex location without ambiguity.

6.1.2 Application to rotor-stator interaction

In order to illustrate the capabilities of the random-vortex-particle method in generating inhomogeneous non-stationary turbulence, the problem of broadband fan noise due to rotor-stator interaction has been selected. The turbulence generated by the rotor blades impinging on the stator vanes is strongly inhomogeneous and non-stationary. In addition, existing analytical models describing the statistics of the turbulence upstream of the OGVs can be used to obtain input parameters for validating the stochastic method.

Firstly, the general problem is briefly described. Then the wake model used here to specify the statistics of the turbulence downstream of a rotor is presented and implemented within the different extensions of the random-vortex-particle method discussed in the previous section.

6.1.2.1 Turbulence downstream a rotor

Turbulent flows behind a rotor are non-stationary but their properties are periodic over one full rotation or from blade to blade if it is assumed that the blades are statistically identical. Therefore, the statistics of the turbulence downstream of a rotor can be described as cyclo-stationary [18]. In stationary signals the statistical properties are independent of time. In contrast, for the case of cyclo-stationary signals the statistical properties of the signal depend on time.

A sketch of a typical rotor-stator configuration where the geometry of the rotor blades and the stator vanes are modelled as flat plates is shown in Figure 6.1. This sketch shows the turbulent wakes of the rotor blades which are convected with the mean flow towards the stator vanes. For each turbulent wake the maximum turbulence intensity coincides with the wake centreline and varies across the wake following approximately a Gaussian distribution [68]. In addition, the turbulent wakes spread as they travel away from the rotor blades. The width of the wake can be used to estimate the integral length scale of the turbulence [18].

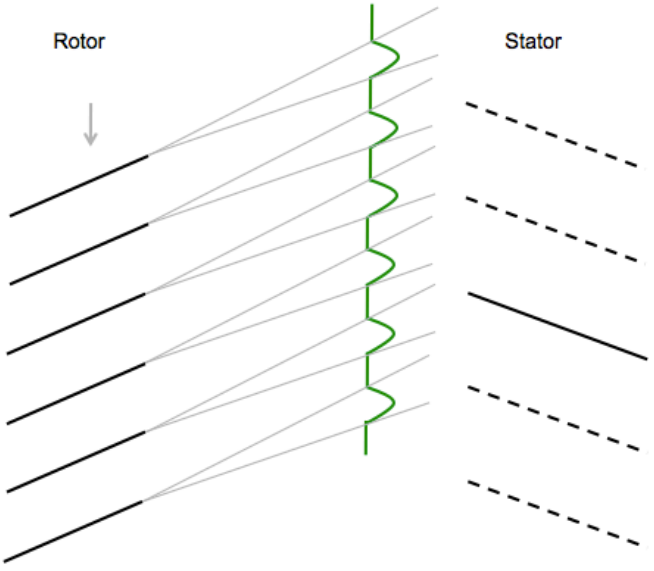

FIGURE 6.1: Sketch of a rotor-stator cascade model showing the variation of kinetic energy due to the rotor turbulent wakes.

The flow upstream of the fan is already turbulent, so the flow in the region between the wakes is also turbulent although its intensity is weaker than the wake turbulence. The integral length scale of the background turbulence is thought to be smaller than the integral length scale of the wake turbulence (vortices within the wake are larger than those in the background turbulence) but the ratio between them is not well established.

6.1.3 Wake model

In this thesis, the turbulent flow in the rotor-stator interstage is analytically described by a wake model proposed by Jurdic in Ref. [18]. The wakes generated by the rotor blades are statistically identical and modelled as a train of Gaussian functions. The model assumes that background turbulence and wake turbulence are uncorrelated. The background turbulence is isotropic, stationary and homogeneous. The spectral characteristics of the turbulence within the wake are also modelled as homogeneous and isotropic but modulated by a periodic train of Gaussian functions leading to cyclo-stationary non-homogeneous turbulence.

Jurdic proposed two implementations. The first implementation is based on a modulation of homogeneous isotropic velocity fields by a train of Gaussian functions. The second implementation models directly the statistics of the turbulence in the rotor-stator interstage section. Both models provide similar levels of accuracy with measurements. Since our aim is to obtain a description of the kinetic energy and the integral length scale, the second implementation is more straightforward. It models the kinetic energy as the sum of the background mean square velocity $\overline{w_b^2}$ and the wake mean square velocity $\overline{w_w^2}$ at the wake centreline modulated by a train of Gaussian functions:

$$K(\boldsymbol{x},t) = \overline{w_b^2} + \overline{w_w^2} \sum_{m=-\infty}^{\infty} \exp\left[-\ln(2) \left(\frac{x - u_0 t - m u_0 T}{L_w} \right)^2 \right]. \tag{6.5}$$

L_w is the half-wake width. T is the period between two consecutive wakes and it is determined by the rotor blade spacing and speed of the rotor. u_0 is the convection velocity of the wakes. Note that here the directivity effects on wake propagation are neglected and the turbulent kinetic energy is described as it arrives parallel to the OGV.

The wake model in Eq. (6.5) is valid for rotor-stator configurations where there is no overlapping between adjacent wakes. As shown in Ref. [62], if the period between wakes T is small compared to the half-wake width L_w so that adjacent wakes overlap, the model leads to unphysical correlation between the wakes.

Following Jurdic's approach, the integral length scale of the wake turbulence is estimated using the half-wake width L_w as $\lambda = 0.42 L_w$. In addition, background and wake turbulence are assumed to be characterised by the same integral length scale. This assumption has previously been considered, for instance in Refs. [18, 69].

In this work, the wake model in Eq. (6.5) is used to define the values of turbulent kinetic energy and integral length scale upstream of the OGV which are then introduced as input parameters in the random-vortex-particle method. We assume that the spreading of the wakes along the OGV is negligible and hence the integral length scale of the turbulence remains constant. Therefore, for an observer moving with the mean flow the train of turbulent wakes form a frozen pattern moving along the stator vanes.

6.1.4 Statistical properties of the turbulence

Analytical expressions for the two-point two-time correlations of the turbulence are now presented and will be later used to validate the implementations of the random-vortex-particle method presented in Eqs. (6.2) - (6.4) with input parameters provided by the wake model in Eq. (6.5).

For non-stationary inhomogeneous turbulence, the two-point two-time correlation tensor is defined as $R_{ij}(\boldsymbol{x}_1, \boldsymbol{r}, t_1, t) = \langle u_i'(\boldsymbol{x}_1, t_1)\, u_j'(\boldsymbol{x}_2, t_2)\rangle$, where $\boldsymbol{r} = \boldsymbol{x}_2 - \boldsymbol{x}_1$ and $t = |t_2 - t_1|$. For each implementation of the random-vortex-particle method in Eqs. (6.2) - (6.4), different analytical expressions are obtained.

For velocity fields obtained with Implementation 1 in Eq. (6.3) based on the definition of the statistics of the turbulence as functions of the vortex location $\boldsymbol{x}_n$, the two-point two-time correlations R_{11} and R_{22} in the streamwise direction, $\boldsymbol{r} = r\boldsymbol{e}_1$, are given by:

$$R_{ii}(\boldsymbol{x}_1, \boldsymbol{r}, t_1, t) = R_U(t) \sum_{n=1}^{N} K(\boldsymbol{x}_n, t_1) \tilde{G}_{,j}(r_n) \tilde{G}_{,j}(r_n + r - u_0 t), \tag{6.6}$$

where $r_n = |\boldsymbol{x}_1 - \boldsymbol{x}_n(t)|$. The subscript $,j$ denotes the partial derivative with respect to the j^{th} component. Closed-form expressions for R_{11} and R_{22} are obtained by providing specific expressions for the energy spectrum.

If the turbulence is obtained with Implementation 2 in Eq. (6.2) based on the definition of the kinetic energy at point $\boldsymbol{x}$, we get:

$$R_{11}(\boldsymbol{x}_1, \boldsymbol{r}, t_1, t) = -R_U(t) K(\boldsymbol{x}_1, t_1) K^{1/2}(\boldsymbol{x}_1 + \boldsymbol{r}, t_2) (\tilde{G}_{,2} * \tilde{G}_{,2})(r - u_0 t), \tag{6.7}$$

$$\begin{aligned} R_{22}(\boldsymbol{x}_1, \boldsymbol{r}, t_1, t) = -R_U(t) \Bigg\{ & \Bigg(\left[K^{1/2}\right]_{,1} (\boldsymbol{x}_1, t_1) K(\boldsymbol{x}_1 + \boldsymbol{r}, t_2) \\ & - K^{1/2}(\boldsymbol{x}_1, t_1) \left[K^{1/2}\right]_{,1} (\boldsymbol{x}_1 + \boldsymbol{r}, t_2) \Bigg) (\tilde{G} * \tilde{G}_{,1})(r - u_0 t) \\ & + \left[K^{1/2}\right]_{,1} (\boldsymbol{x}_1, t_1) \left[K^{1/2}\right]_{,1} (\boldsymbol{x}_1 + \boldsymbol{r}, t_2) (\tilde{G} * \tilde{G})(r - u_0 t) \\ & - K^{1/2}(\boldsymbol{x}_1, t_1) K^{1/2}(\boldsymbol{x}_1 + \boldsymbol{r}, t_2) (\tilde{G}_{,1} * \tilde{G}_{,1})(r - u_0 t) \Bigg\}. \end{aligned} \tag{6.8}$$

Finally, the two-point two-time correlations R_{11} and R_{22} in the streamwise direction for Implementation 3 in Eq. (6.4), are given by:

$$R_{11}(\boldsymbol{x}_1, \boldsymbol{r}, t_1, t) = -R_U(t) K^{1/2}(\boldsymbol{x}_1, t_1) K^{1/2}(\boldsymbol{x}_1 + \boldsymbol{r}, t_2) (\tilde{G}_{,2} * \tilde{G}_{,2})(r - u_0 t), \tag{6.9}$$

$$R_{22}(\boldsymbol{x}_1, \boldsymbol{r}, t_1, t) = -R_U(t) K^{1/2}(\boldsymbol{x}_1, t_1) K^{1/2}(\boldsymbol{x}_1 + \boldsymbol{r}, t_2) (\tilde{G}_{,1} * \tilde{G}_{,1})(r - u_0 t). \tag{6.10}$$

Note that since the kinetic energy defined in Eq. (6.5) does not vary in the normal direction, when combining Implementations 2 and 3 with Eq. (6.5) the same expression is obtained for the streamwise component of the velocity field. Hence both implementations yield the same theoretical correlation R_{11}. In contrast, expressions for correlation of the normal velocity component, R_{22}, differ in the terms involving spatial derivatives of the kinetic energy in the streamwise direction.

6.2 Validation

In this section, the implementations in Eqs. (6.2) - (6.4) of the random-vortex-particle method for inhomogeneous non-stationary turbulence are applied to the same test case to assess the difference in predicted acoustic field.

The sensitivity of the numerical results to the implementation is first tested on the statistics of the synthetic turbulence and then sound pressure levels in the far field are compared against Amiet's analytical solution modified to account for the effect of the turbulent wakes impinging on the stator vanes. More details on the modified analytical solution can be found in Appendix C.2.

6.2.1 General problem

Due to the complexity of the rotor-stator configuration, a number of simplifications are usually made, see Figure 6.1. A general approach is to unroll the rotor-stator configuration to form a periodic system and then use strip theory for each section of the stator span to reduce the geometry of the vanes to two dimensions. In a further simplification the stator vanes can be assumed to be identical and their geometry simplified to a flat plate. Under these constraints and above a critical frequency at which the acoustic power approximately scales with the number of stator vanes [70], the rotor-stator interaction problem can be reduced to an isolated flat plate.

It is also assumed here that the effects of the duct enclosing the rotor-stator configuration are negligible and therefore consider that the noise radiates in the free field. This assumption is reasonable if the acoustic wavelength is small compared to the distance between the noise sources and the duct wall [18].

6.2.2 Test case

The test case considered is an isolated flat plate with zero angle of attack interacting with inhomogeneous non-stationary turbulence. The problem is made non-dimensional using the chord of the airfoil, mean flow density and sound speed.

The parameters used in this validation are similar to those considered in previous chapters, see for instance section 4.1. The turbulence is convected by a uniform mean flow with Mach number 0.362 in the x-direction. In contrast with previous chapters, the turbulent kinetic energy is now a function of position and time which is specified upstream of the OGV by the wake model introduced in section 6.1.3. The half-wake width L_w upstream of the OGV is set to about 17% of the chord of the flat plate and the effects of wake spreading are neglected. The period between adjacent wakes is set to $T = 10L_w/u_0$ and the level of background turbulence to 10%. Using the relation between the half-wake width and the integral length scale proposed by Jurdic we have $\lambda = 0.07$.

Note that for this test case the period between wakes represents about ten times the characteristic time of travelling along the wake L_w/u_0 ensuring that there are no overlapping wakes.

6.2.3 Computational setup

The computational setup implemented for this test case coincides with that used for the simulation of frozen turbulence in chapter 4. To simplify the discussion and focus on the effects of inhomogeneous non-stationary turbulence, simulation results are presented only for a Gaussian spectrum. Please refer to section 4.2 for a full description of the computational set up.

In contrast with the test cases considered in previous chapters, the kinetic energy of the turbulence now varies in time according to Eq. (6.5). Even though the background and the wake turbulence are assumed incoherent, the same set of vortex particles is used to recreate background and wake turbulence. Due to the linearity of the problem it could be possible to consider two sets of uncorrelated vortices and then sum up their contributions to the velocity field, however from a computational point of view it is more efficient to use one single set.

Also in contrast with previous chapters, the acoustic pressure is now non-stationary. Following the usual treatment of experimental data, the power spectral density of numerical results is obtained by computing the time average. Therefore, the sound pressure levels correspond to the first harmonic of the time series. Note that to obtain accurate statistics a sufficiently large amount of wakes must be captured within the time series.

6.2.4 Synthetic turbulence

The time variation of the kinetic energy at a fixed point on the flat plate is shown in Figure 6.2. Since the typical size of the vortices is λ, roughly five vortices fit within the wake width. Therefore, large variations of kinetic energy are observed at small distances yielding strongly inhomogeneous turbulence.

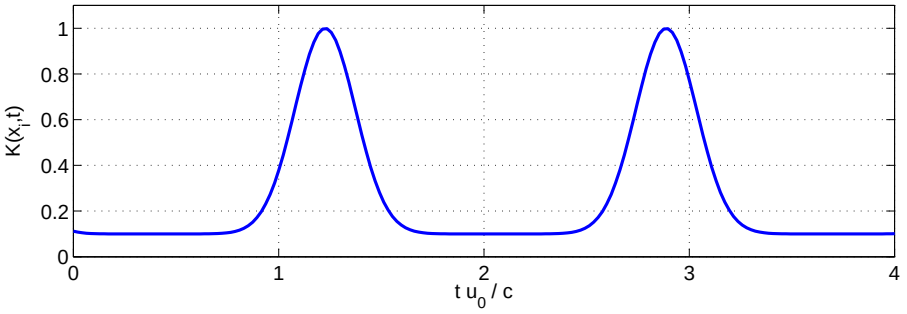

FIGURE 6.2: Turbulent kinetic energy at a given point $\boldsymbol{x}_i$ versus time. Wake model with $L_w = 0.17/c$, $T = 10L_w/u_0$, and 10% level of background turbulence.

The synthetic velocity fields obtained with each of the three implementations proposed in Eqs. (6.2) - (6.4) are shown in Figure 6.3. The three velocity fields are found to be very similar. Note that the velocity component in the streamwise direction is defined by the same equation with either Implementation 2 in Eq. (6.3) or Implementation 3 in Eq. (6.4).

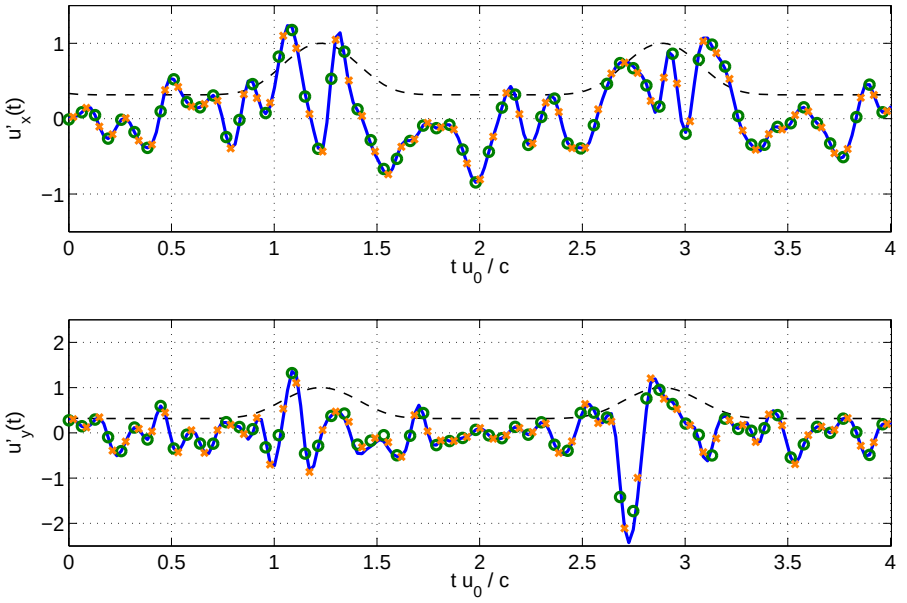

FIGURE 6.3: Synthetic turbulent velocity in the streamwise direction (top) and normal direction (bottom) versus time. Implementation 1 (—). Implementation 2 (○). Implementation 3 (×). Dashed line shows the square root of the turbulent kinetic energy. Wake model with $L_w = 0.17/c$, $T = 10L_w/u_0$, and 10% level of background turbulence.

The effects of the variation of kinetic energy in time can be observed in the velocity field (especially in the normal component) but the largest amplitudes of the instantaneous velocity field do not necessarily coincide with the maximum of the kinetic energy. For a particular time, an increase in kinetic energy can be balanced by small vortex strengths or vice versa, and hence the amplitude of the velocity is not totally controlled by the amplitude of the kinetic energy. Note that since the vortex strengths follow a zero-mean

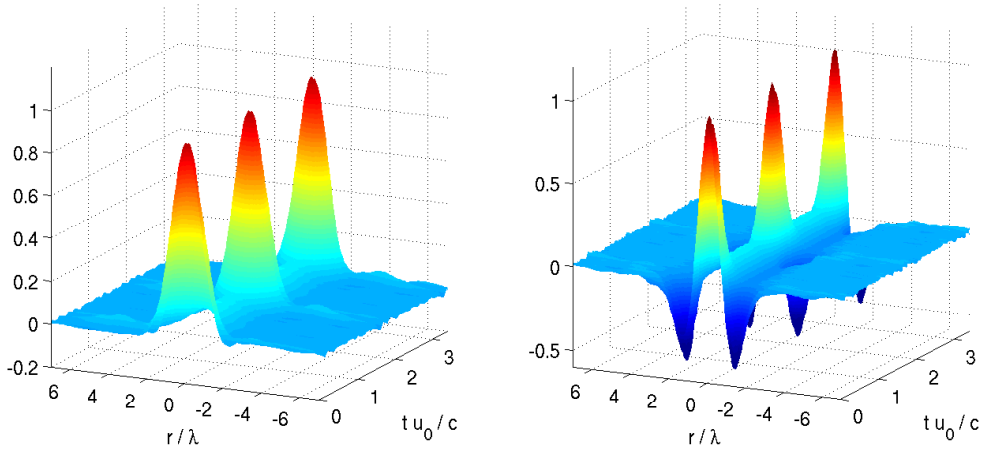

FIGURE 6.4: Contour plots of the numerical correlations R_{11} (left) and R_{22} (right) computed with Implementation 1. Wake model with $L_w = 0.17/c$, $T = 10L_w/u_0$, and 10% level of background turbulence.

distribution, the statistical properties of the velocity field are not affected, as illustrated in Figure 6.4.

Figure 6.4 shows the time evolution of the numerical two-point correlations R_{11} and R_{22} with respect to the centre of the flat plate computed with Implementation 1. The modulation of the kinetic energy can be observed in the correlation featuring strong peaks when the centre of the wakes reaches the centre of the flat plate.

The statistical properties of the turbulence along the flat plate are now assessed. We first evaluate the impact of implementation on the statistical properties by comparing the theoretical correlations in Eqs. (6.6) - (6.10). We then validate the numerical results by comparing the stochastically generated correlations against the corresponding analytical expression.

Figure 6.5 shows the difference between analytical correlations corresponding to the implementations of the stochastic method over one period T. The two-point correlation R_{11} appears to be only slightly influenced by the definition of kinetic energy. Note that Implementations 2 and 3 lead to the same theoretical correlations R_{11}. The correlation of the normal component R_{22} seems to be more sensitive to the implementations. The largest difference is found between Implementations 1 and 2 with an error of up to 6%.

To better illustrate these differences, the two-point correlation R_{22} is shown in Figure 6.6 at a time when the centre of the wake reaches the centre of the airfoil. We can see that similar correlations are predicted from the different implementations.

In order to estimate the numerical error for the three implementations in Eqs. (6.2) - (6.4), the numerical correlations R_{11} and R_{22} are now compared against the corresponding analytical correlations. Figure 6.7 shows a snapshot of the difference between theoretical and numerical two-point two-time correlations R_{11} and R_{22} computed with

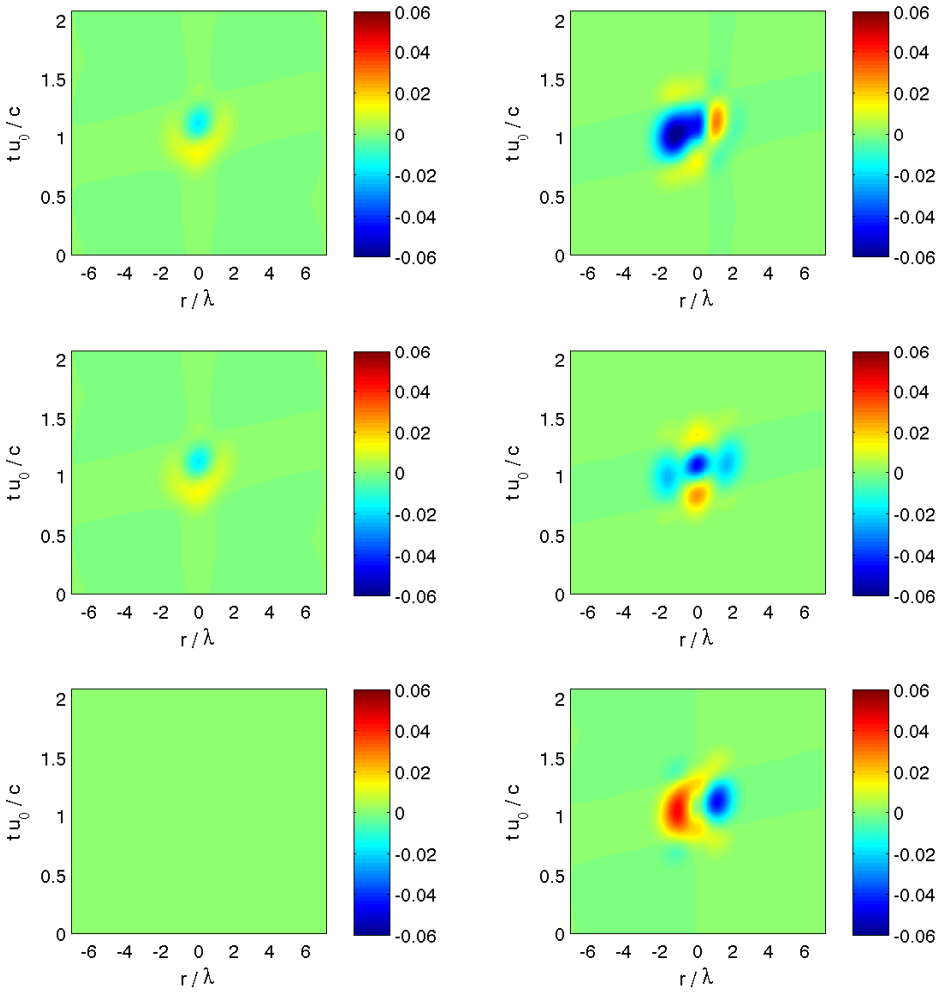

FIGURE 6.5: Contour plots of the difference between analytical two-point correlations R_{11} (left) and R_{22} (right) computed with respect to the centre of the flat plate. Top: Difference between Implementations 1 and 2. Centre: Difference between Implementations 1 and 3. Bottom: Difference between Implementations 2 and 3. Wake model with $L_w = 0.17/c$, $T = 10L_w/u_0$, and 10% level of background turbulence.

respect to the centre of the flat plate over one period T. The numerical method seems to have more difficulties in capturing the correlation of the streamwise component over the normal component, especially near the peak at $r = 0$. Good agreement is obtained for all three implementations showing similar levels of error of about 4%.

In a further attempt to clarify this error, analytical and numerical two-point correlations are compared in Figure 6.8 for a time when the centre of the wake reaches the centre of the airfoil. It can be observed that numerical results follow closely the theoretical correlations. It appears that the most difficult features to capture are the peak at $r = 0$ and that the correlation tends to zero as the distance increases.

Note that the level of error observed here between numerical and analytical correlations is slightly larger than in the previous chapters. Due to the cyclo-stationary nature of the

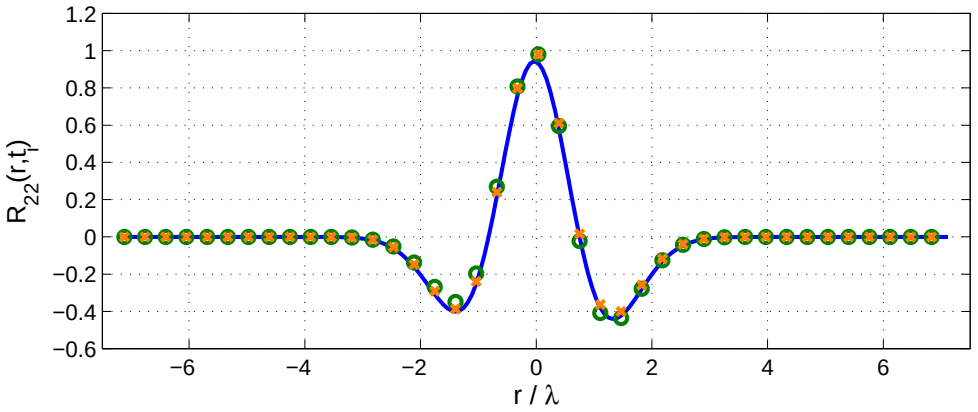

FIGURE 6.6: Analytical correlations R_{22} computed with respect to the centre of the flat plate at time t_i when the centre of the wake reaches the centre of the airfoil. Implementation 1 (—). Implementation 2 (○). Implementation 3 (×). Wake model with $L_w = 0.17/c$, $T = 10L_w/u_0$, and 10% level of background turbulence.

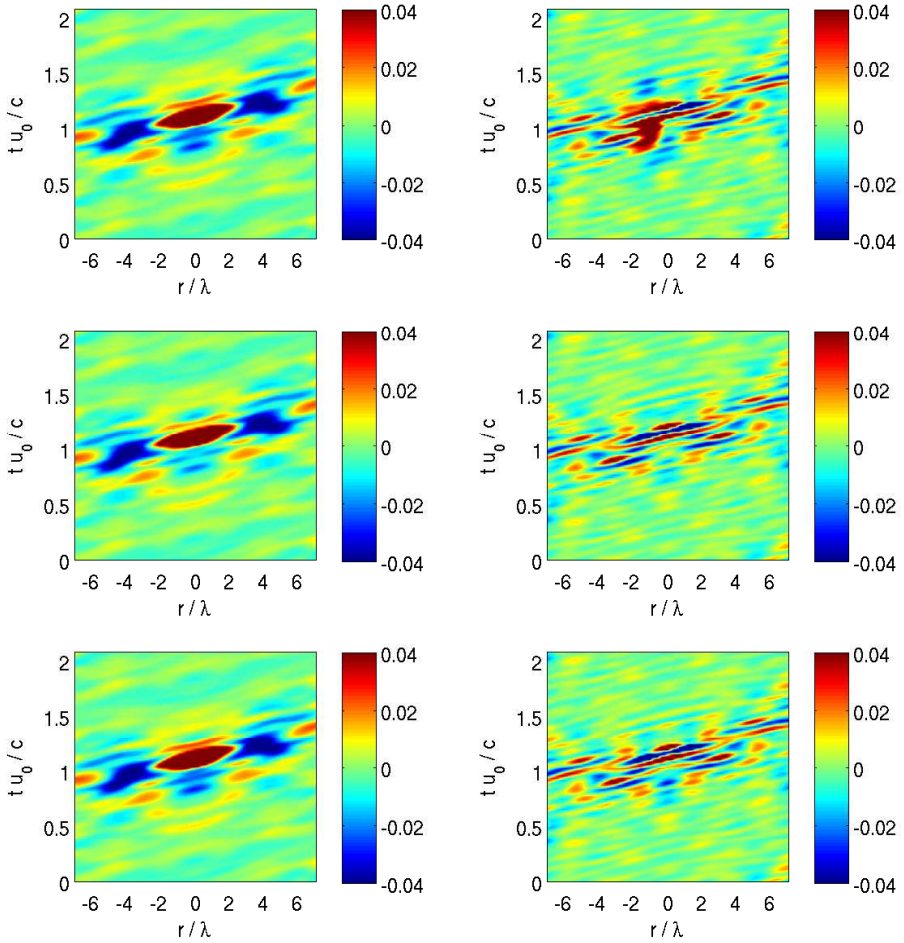

FIGURE 6.7: Contour plots of the difference between analytical and numerical two-point correlations R_{11} (left) and R_{22} (right) computed with respect to the centre of the flat plate over one period T. Top: Implementation 1. Centre: Implementation 2. Bottom: Implementation 3. Wake model with $L_w = 0.17/c$, $T = 10L_w/u_0$, and 10% level of background turbulence.

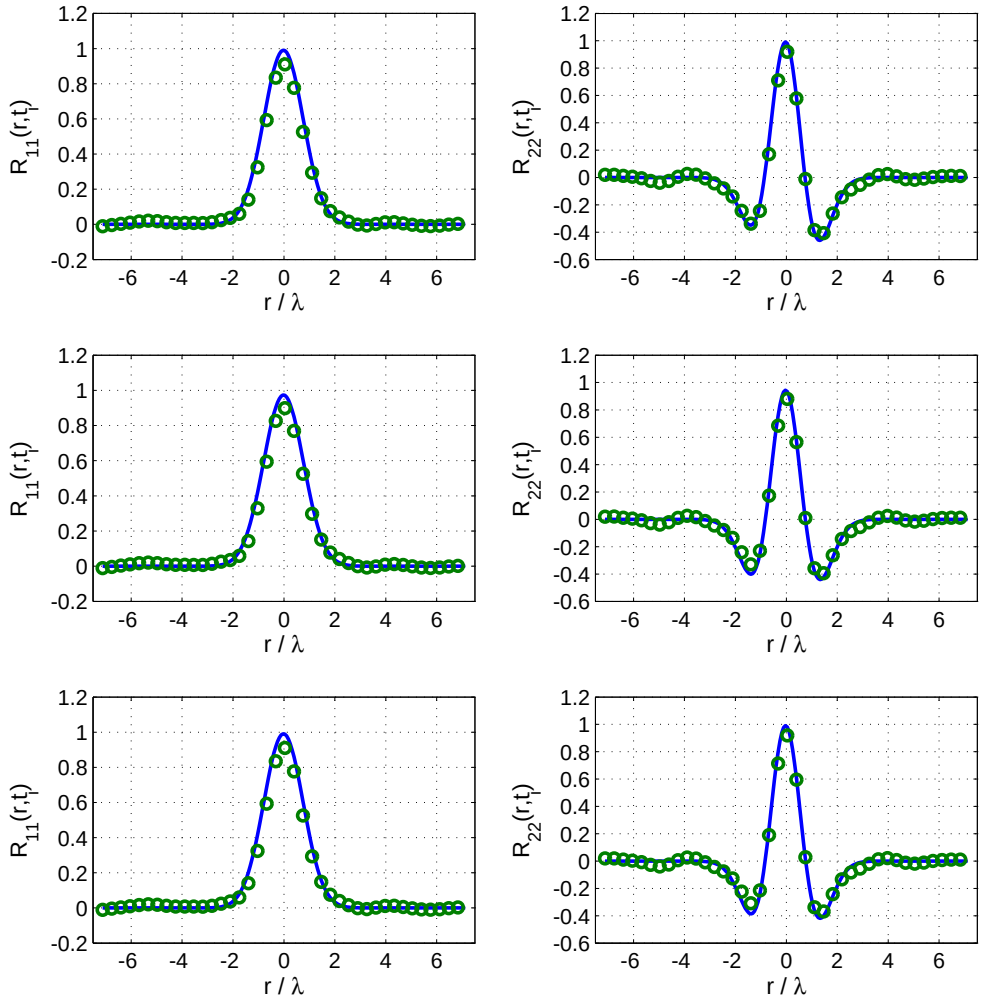

FIGURE 6.8: Analytical (—) and numerical (○) two-point correlations R_{11} (left) and R_{22} (right) computed with respect to the centre of the flat plate at time t_i when the centre of the wake reaches the centre of the airfoil. Top: Implementation 1. Centre: Implementation 2. Bottom: Implementation 3. Wake model with $L_w = 0.17/c$, $T = 10L_w/u_0$, and 10% level of background turbulence.

turbulence longer time series would be required here to maintain the level of accuracy, as shown in Figure 4.6, however an error in the 4% margin is not expected to significantly affect the reliability of predicted far-field noise levels.

6.2.5 Acoustic pressure

Now that the statistical properties of the turbulence have been validated, the sensitivity of the predicted sound field to the implementation of the stochastic method is assessed.

A snapshot of acoustic pressure in the near field of the flat plate is depicted in Figure 6.9. It cannot be appreciated here but the evolution of the acoustic pressure shows a cyclic variation of the sound intensity due to the wakes passing near the flat plate.

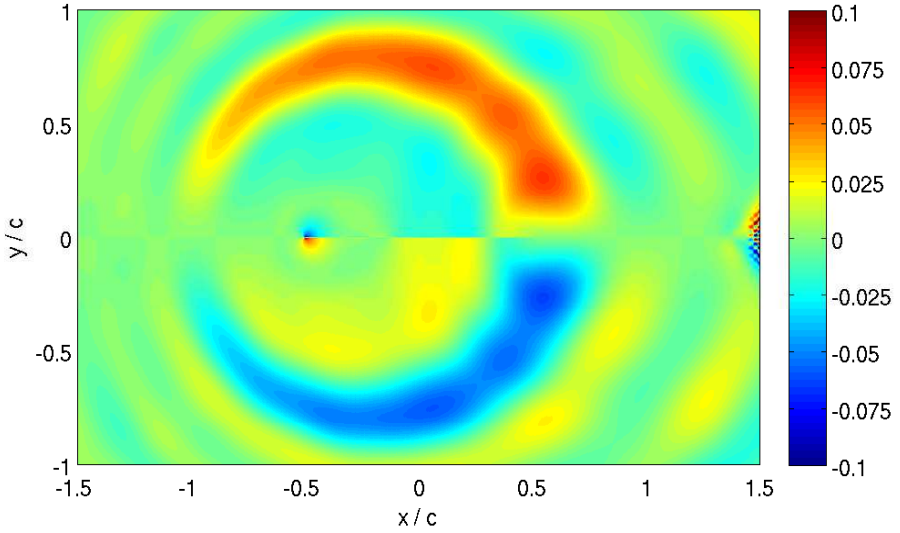

FIGURE 6.9: Snapshot of the acoustic pressure predicted assuming that the statistics of the turbulence are specified at the vortex location. Wake model with $L_w = 0.17/c$, $T = 10L_w/u_0$, and 10% level of background turbulence.

Figure 6.10 shows sound pressure levels for observers located at 30, 60, 90, 120 and 150 degrees from the downstream direction. Similar noise levels are predicted by all three implementations in Eqs. (6.2) - (6.4). Therefore, the predicted acoustic field is not significantly affected by the implementation considered. In addition, numerical results are in very good agreement with Amiet's analytical solution.

Far-field directivities for Strouhal numbers $St = 4$ and 8 are shown in Figure 6.11. Numerical results obtained with the proposed implementations of the stochastic method predict similar far-field directivities. They are in very good agreement with Amiet's analytical solution and it is only for $St = 8$ at upstream locations that a slight under-prediction is found. These discrepancies are consistent with what was observed with homogeneous turbulence in chapter 4.

6.2.6 Conclusions

In this section, the random-vortex-particle method has been validated for the case of inhomogeneous non-stationary turbulence. The three implementations of the stochastic method described in Eqs. (6.2) - (6.4) have been used to simulate the same test case and hence assess the sensitivity of synthetic velocity field and acoustic field to the choice of implementation.

Differences can be observed on the statistical properties of the turbulence depending on the implementation of the stochastic method. The influence of the implementation is stronger for the normal component of the velocity field, especially when computed by

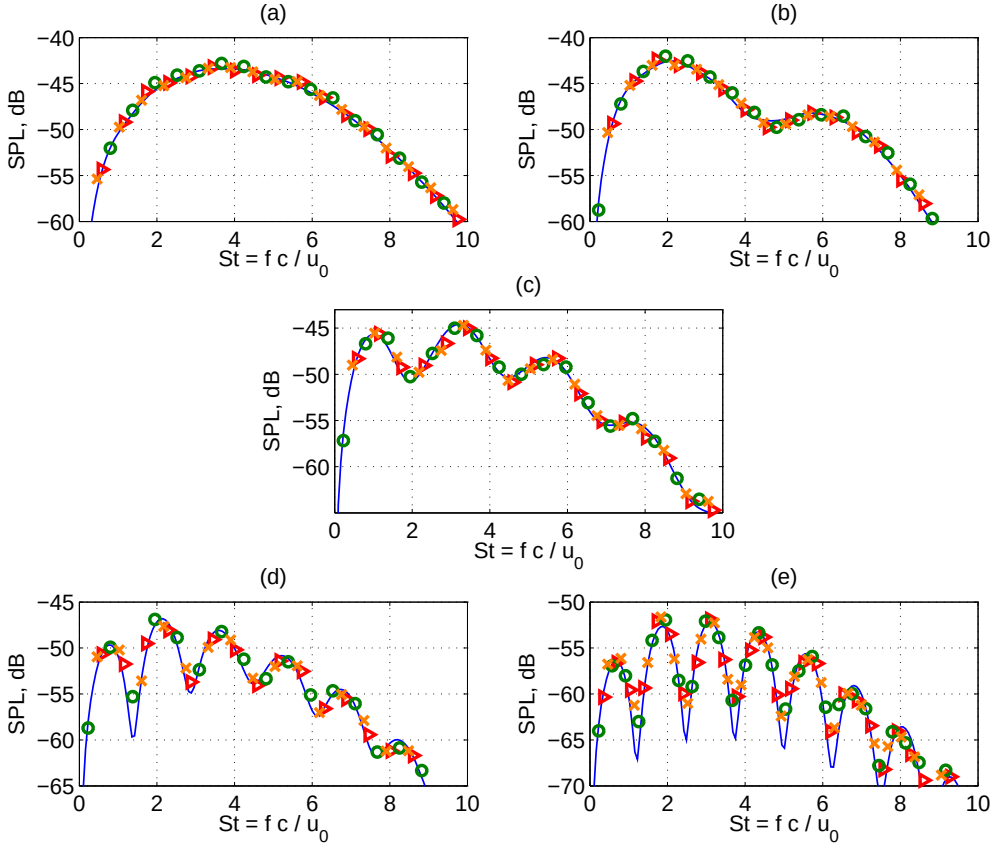

FIGURE 6.10: Analytical (—) SPL against numerical results computed with Implementation 1 (▷), Implementation 2 (○) and Implementation 3 (×). Observers located at 30° (a), 60° (b), 90° (c), 120° (d), and 150° (e). Wake model with $L_w = 0.17/c$, $T = 10L_w/u_0$, and 10% level of background turbulence.

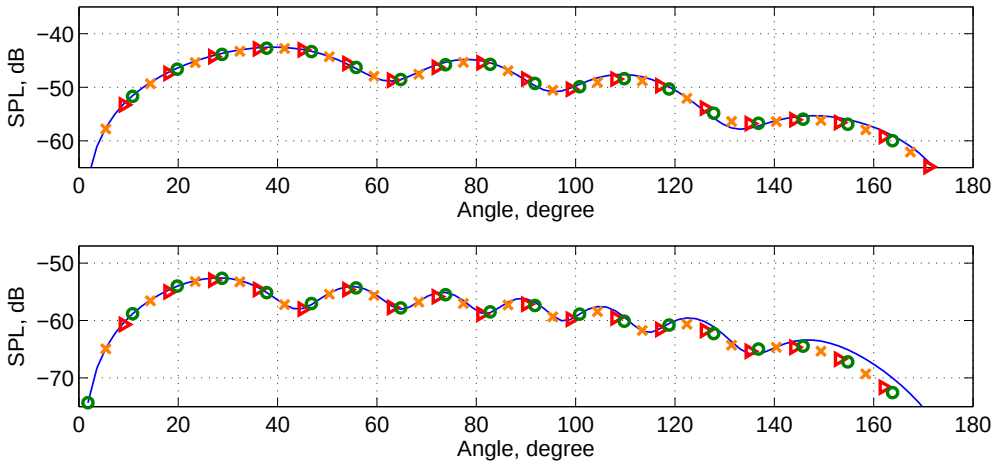

FIGURE 6.11: Directivity at Strouhal numbers $St = 4$ (top) and $St = 8$ (bottom). Amiet's analytical solution (—). Numerical results computed with Implementation 1 (▷), Implementation 2 (○) and Implementation 3 (×). Wake model with $L_w = 0.17/c$, $T = 10L_w/u_0$, and 10% level of background turbulence.

Implementations 1 and 2. However, the differences are rather limited with the largest amplitude difference being within a 6% margin.

The sensitivity of predicted far-field noise levels to the implementation of the stochastic method has also been found negligible and analytical sound pressure levels are accurately predicted for observes at different far-field locations.

In conclusion, the random-vortex-particle method is general enough to accommodate for non-stationary inhomogeneous turbulence. For the test case considered here, where no RANS simulations were used, all three implementations provide reliable far-field noise predictions.

6.3 Influence of the wake configuration

We now focus on the description of the turbulent wakes generated by the rotor blades impinging on the stator vanes. The sensitivity of predicted noise levels to the choice of input parameters for the wake model in Eq. (6.5) is assessed by considering the influence of the wake separation, followed by the ratio between background and wake turbulence, and finally the sensitivity to the wake width.

6.3.1 Test case and computational setup

The test case considered here and corresponding computational setup are similar to those described in section 6.2.2 to assess the sensitivity of the numerical results to the implementation of the stochastic method. But now all the numerical results presented are obtained with Implementation 1 of the random-vortex-particle method in Eq. (6.2) combined with the wake model in Eq. (6.5) for different input parameters.

6.3.2 Influence of the wake separation

In order to evaluate the sensitivity of the predicted noise levels to the wake separation, three periods are considered: $10L_w/u_0$, $15L_w/u_0$ and $20L_w/u_0$, see table 6.1. For each case the half-width L_w of the wake is set to 17 % of the stator chord and the integral length scale can be estimated as $\lambda = 0.07$. The level of background turbulence is set to 10%. The kinetic energy corresponding with these cases is shown in Figure 6.12 as a function of time. Note that due to the restriction imposed by the wake model Eq. (6.5), we only consider cases where the wakes are not overlapping.

The statistical properties of the synthetic turbulence along the flat plate are assessed by computing two-point two-time correlations R_{11} and R_{22} defined by Eq. (6.6) with respect to the centre of the flat plate. Figure 6.13 shows the difference between theoretical and

	T	L_w	$\overline{w_2^2}$	$\overline{w_1^2}$
Test case 1	$10L_w/u_0$	$0.17/c$	90%	10%
Test case 2	$15L_w/u_0$	$0.17/c$	90%	10%
Test case 3	$20L_w/u_0$	$0.17/c$	90%	10%

TABLE 6.1: List of test cases considered to assess the influence of the wake separation.

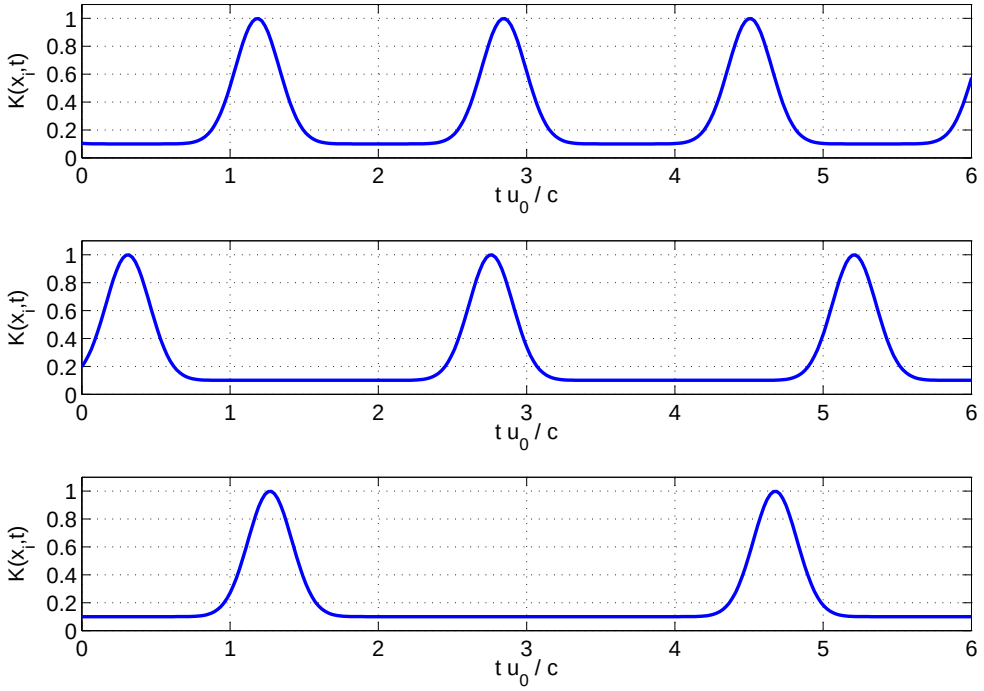

FIGURE 6.12: Time evolution of the kinetic energy with periods $T = 10L_w/u_0$ (top), $T = 15L_w/u_0$ (centre) and $T = 20L_w/u_0$ (bottom) at a given point $\boldsymbol{x}_i$. Wake model with $L_w = 0.17/c$ and 10% level of background turbulence.

numerical correlations R_{11} and R_{22} corresponding to $T = 15L_w/u_0$ and $T = 20L_w/u_0$, respectively. As observed for the period $T = 10L_w/u_0$ in Figure 6.7, the error is slightly larger for the correlation of the streamwise component than for the normal component. Yet, in both cases, the statistics of the turbulence are well captured by the stochastic method, as illustrated in Figure 6.14 where two-point correlations along the flat plate are shown for a time when the centre of the wakes reaches the centre of the flat plate.

Figure 6.15 shows SPL for observers in the far field at different locations. Numerical results obtained for each period are in very good agreement with Amiet's analytical solution. Predicted noise levels follow the same trends independently of the period but an increase in amplitude is observed as the period decreases. Hence, if the turbulent wakes are closer to each other more noise is generated. In fact, the increase in noise levels scales with the mean-square velocity of the turbulence u_{rms}^2, as illustrated in Figure 6.16.

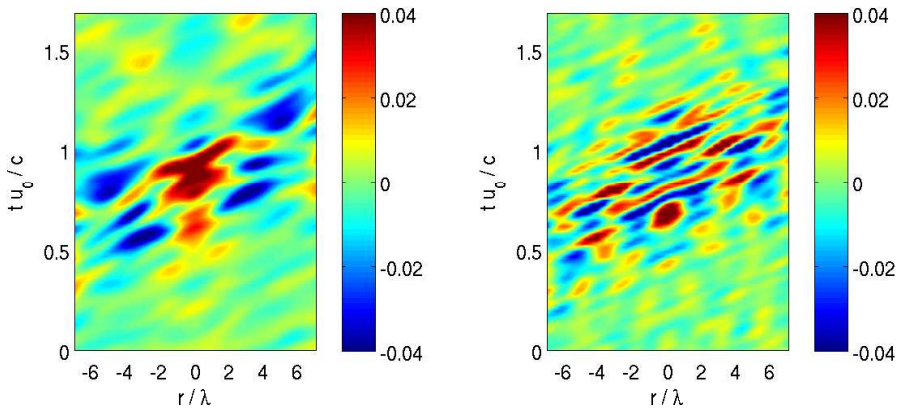

(a) Wake model with $T = 15L_w/u_0$, $L_w = 0.17/c$ and 10% level of background turbulence.

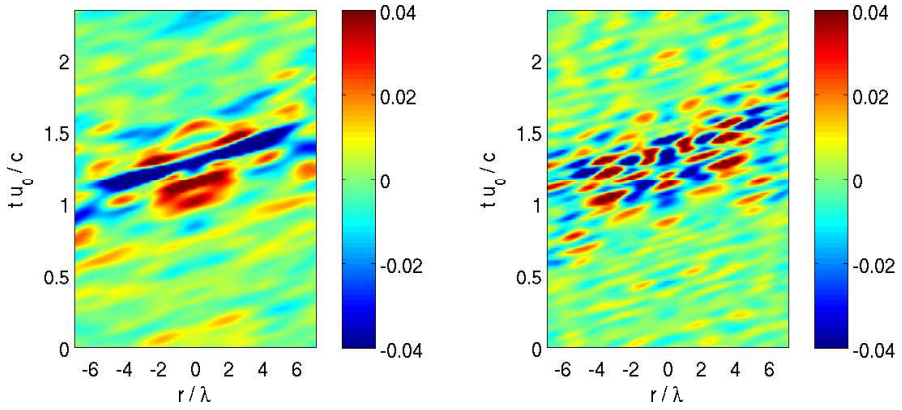

(b) Wake model with $T = 20L_w/u_0$, $L_w = 0.17/c$ and 10% level of background turbulence.

FIGURE 6.13: Contour plots of the difference between analytical and numerical two-point correlations R_{11} (left) and R_{22} (right) computed with respect to the centre of the flat plate over one period T.

6.3.3 Influence of the background turbulence

As described in section 6.1.2.1, turbulent flows impinging on the stator vanes are composed of background turbulence and wake turbulence generated by the rotor blades. The statistical properties of the background turbulence are not well established yet. It is assumed homogeneous and isotropic and it is characterised by a smaller integral length scale but here we assume the same length scale for the background and wake turbulence.

Three different levels of background turbulence are considered here to assess its influence on rotor-stator interaction noise, as shown in table 6.2 and in Figure 6.17. They vary from no background turbulence to account for the 30% of the total turbulence intensity. The period between wakes is set to $T = 10L_w/u_0$ and the half-wake width to the 17% of the airfoil chord.

As for the previous test cases, the statistics of the turbulence along the flat plate are very well captured by the random-vortex-particle method. Figure 6.18 shows numerical

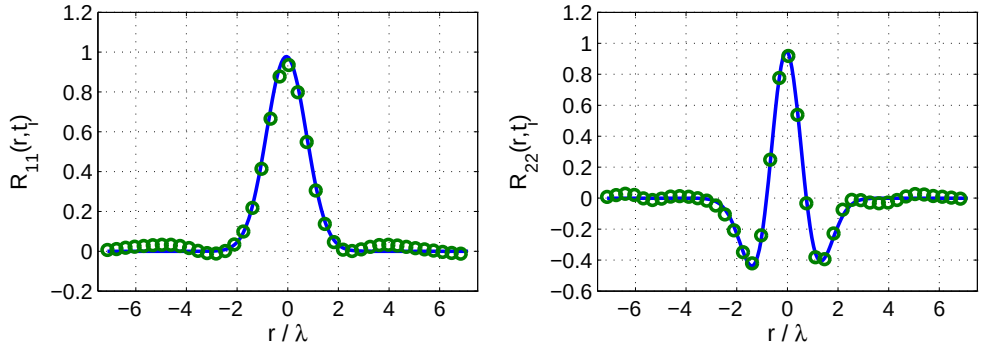

(a) Wake model with $T = 15L_w/u_0$, $L_w = 0.17/c$ and 10% level of background turbulence.

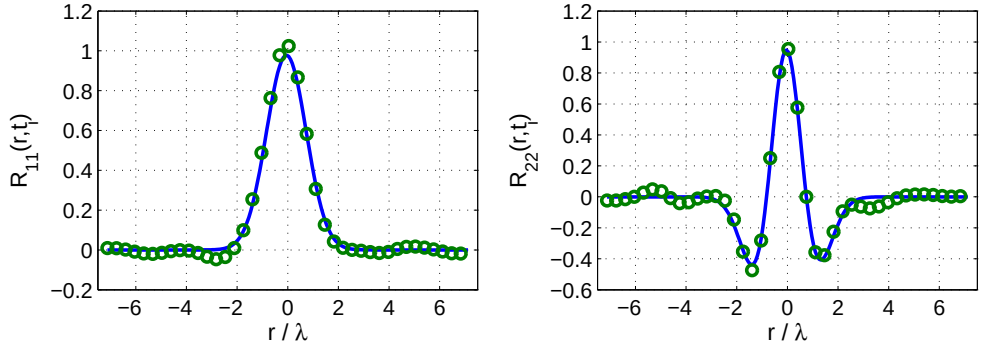

(b) Wake model with $T = 20L_w/u_0$, $L_w = 0.17/c$ and 10% level of background turbulence.

FIGURE 6.14: Analytical (—) and numerical (○) two-point correlations R_{11} (left) and R_{22} (right) computed with respect to the centre of the flat plate at time t_i when the centre of the wake reaches the centre of the airfoil.

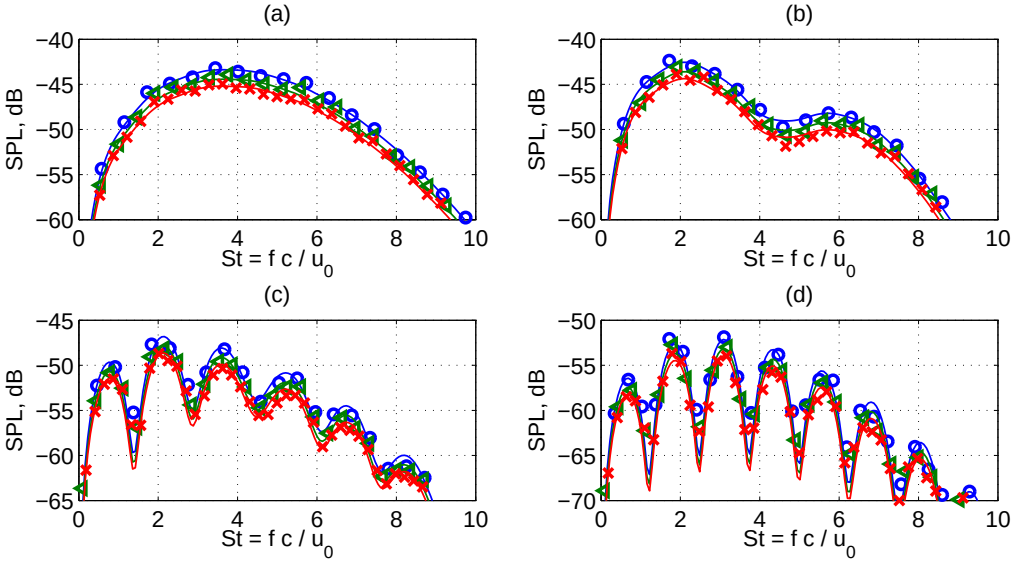

FIGURE 6.15: Far-field sound pressure levels for observers located at 30° (a), 60° (b), 120° (c), and 150° (d). Solid lines represent analytical results. Symbols correspond to numerical results obtained with $T = 10L_w/u_0$ (○), $T = 15L_w/u_0$ (◁) and $T = 20L_w/u_0$ (×). Wake model with $L_w = 0.17/c$ and 10% level of background turbulence.

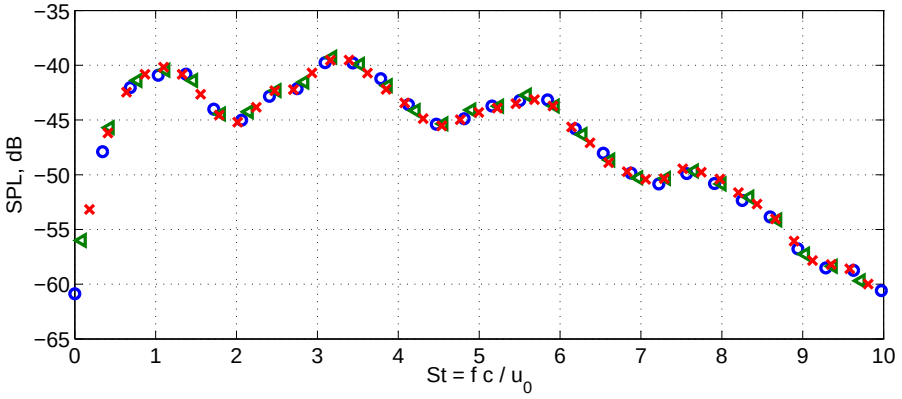

FIGURE 6.16: Numerical SPL normalised by the mean-square velocity for an observed at 90°. Periods $T = 10L_w/u_0$ (○), $T = 15L_w/u_0$ (◁) and $T = 20L_w/u_0$ (×). Wake model with $L_w = 0.17/c$ and 10% level of background turbulence.

	T	L_w	$\overline{w_2^2}$	$\overline{w_1^2}$
Test case 1	$10L_w/u_0$	$0.17/c$	100%	0%
Test case 2	$10L_w/u_0$	$0.17/c$	90%	10%
Test case 3	$10L_w/u_0$	$0.17/c$	70%	30%

TABLE 6.2: List of test cases considered to assess the influence of the level of background turbulence.

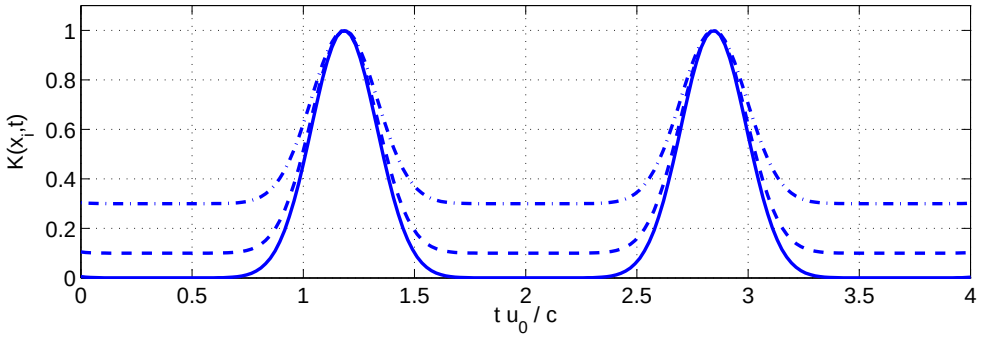

FIGURE 6.17: Time evolution of the kinetic energy with 0 % (—), 10 % (– –) and 30 % (– · –) levels of background turbulence. Wake model with $L_w = 0.17/c$ and $T = 10L_w/u_0$.

and analytical two-point correlations R_{11} and R_{22} with respect to the centre of the airfoil for the test cases corresponding to 0% and 30% background turbulence.

If we now look at the acoustic pressure radiated from the flat plate for each of the three test cases in table 6.2, we see that numerical sound pressure levels in the far field are in agreement with Amiet's analytical solution as shown in Figure 6.19. It can also be observed that the SPL increase with the level of background turbulence and it also scales with the mean-square velocity of the turbulence, as shown in Figure 6.20.

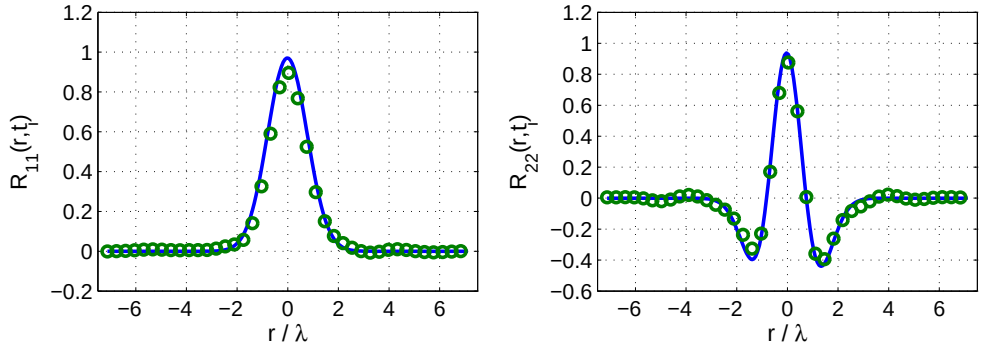

(a) Wake model with $T = 10L_w/u_0$, $L_w = 0.17/c$ and 0% level of background turbulence.

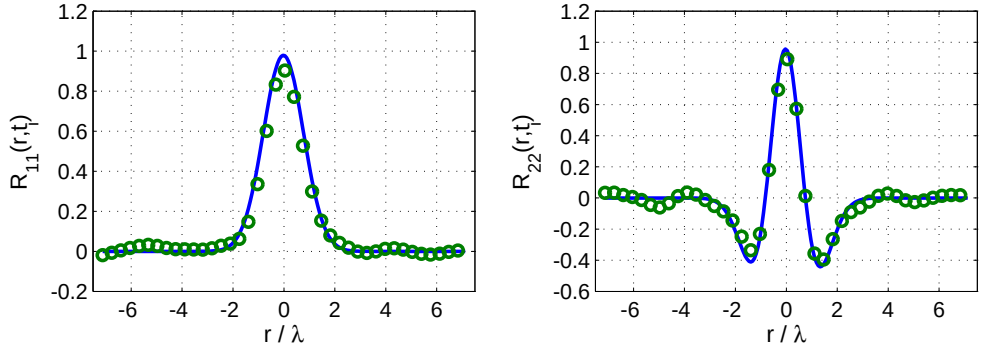

(b) Wake model with $T = 10L_w/u_0$, $L_w = 0.17/c$ and 30% level of background turbulence.

FIGURE 6.18: Analytical (—) and numerical (○) two-point correlations R_{11} (left) and R_{22} (right) computed with respect to the centre of the flat plate at time t_i when the centre of the wake reaches the centre of the airfoil.

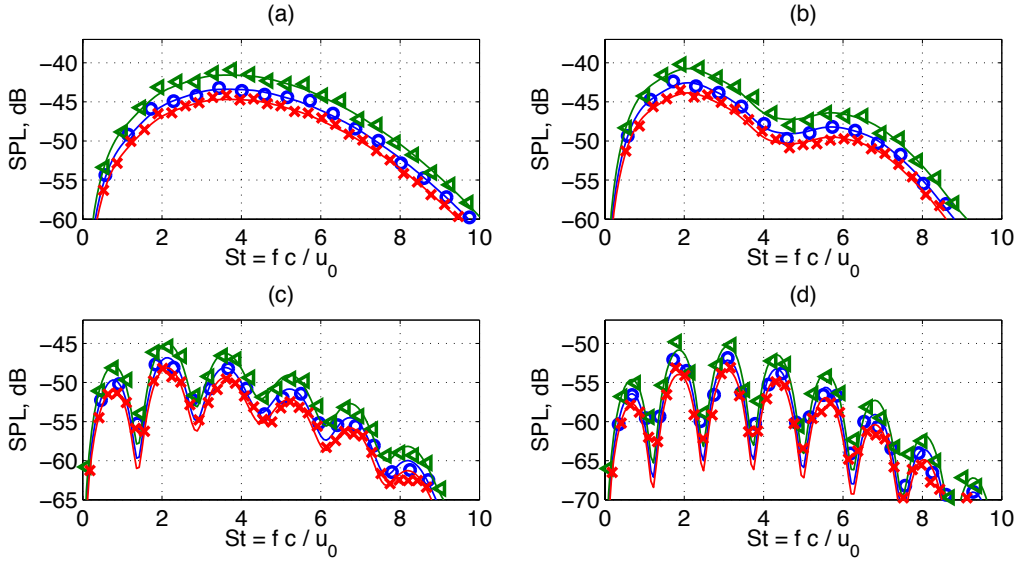

FIGURE 6.19: Far-field SPL for observers located at 30° (a), 60° (b), 120° (c), and 150° (d). Solid lines represent analytical results. Symbols correspond to numerical results obtained with 0% (×) , 10% (○) and 30% (◁). Wake model with $L_w = 0.17/c$ and $T = 10L_w/u_0$.

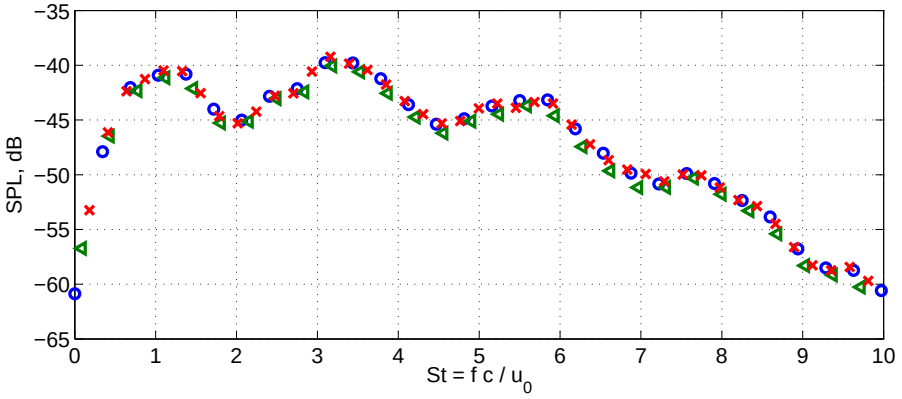

FIGURE 6.20: Numerical SPL normalised by the mean-square velocity for an observed at 90°. Levels of background turbulence: 0% (×) , 10% (○) and 30% (◁). Wake model with $L_w = 0.17/c$ and $T = 10L_w/u_0$.

From the results shown here it appears that an increase in background turbulence produces the same effect in noise levels as a smaller period between wakes. This conclusion is explained by the fact that the integral length scales of the background turbulence and the wake turbulence are chosen identical. However if they were different, each turbulence component would contribute differently to the energy spectrum of the turbulence and hence the overall noise levels would not scale only with the mean-square velocity.

6.3.4 Influence of the wake width

The turbulent wakes generated by the rotor blades spread as they move away from the rotor. The width of the wake is therefore a function of the distance from the rotor. To evaluate the influence of the wake width on the predicted noise levels the three test cases shown in table 6.3 and Figure 6.21 are considered. The wake half-width L_w varies from 8% of the OGV chord to 24%. The period of the wakes is set to $T = 15L_w/u_0$ and the level of background turbulence to 10%.

	T	L_w	λ	$\overline{w_2^2}$	$\overline{w_1^2}$
Test case 1	$15L_w/u_0$	$0.08/c$	0.035	90%	10%
Test case 2	$15L_w/u_0$	$0.17/c$	0.07	90%	10%
Test case 3	$15L_w/u_0$	$0.24/c$	0.1	90%	10%

TABLE 6.3: List of test cases considered to assess the influence of the wake width.

The integral length scale of the turbulence within the wake is estimated by its relation with the half-wake width ($\lambda = 0.42L_w$) and hence as the wake spreads the integral length scale of the turbulence increases. Therefore, each test case uses a different distribution of vortices which is based on the guidelines defined in chapter 4.

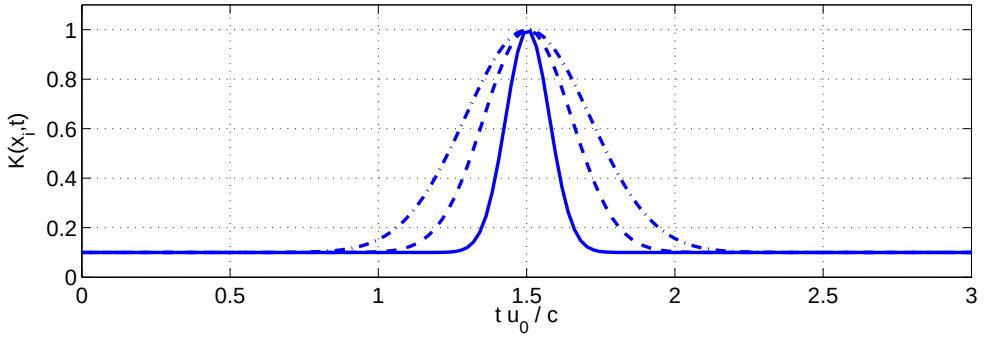

FIGURE 6.21: Time evolution of the kinetic energy of the turbulence with half-wake widths $L_w = 0.08/c$ (—), $L_w = 0.17/c$ (– –) and $L_w = 0.24/c$ (– · –). Wake model with a period $T = 15L_w/u_0$ and 10% background turbulence.

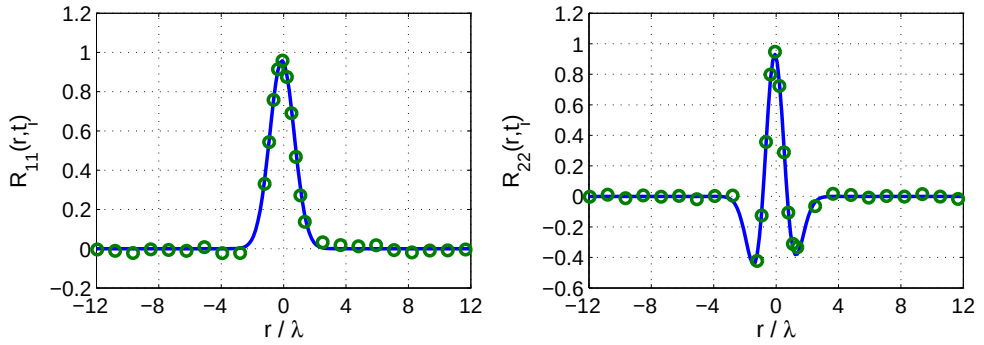

(a) Wake model with $T = 10L_w/u_0$, $L_w = 0.08/c$ and 10% level of background turbulence.

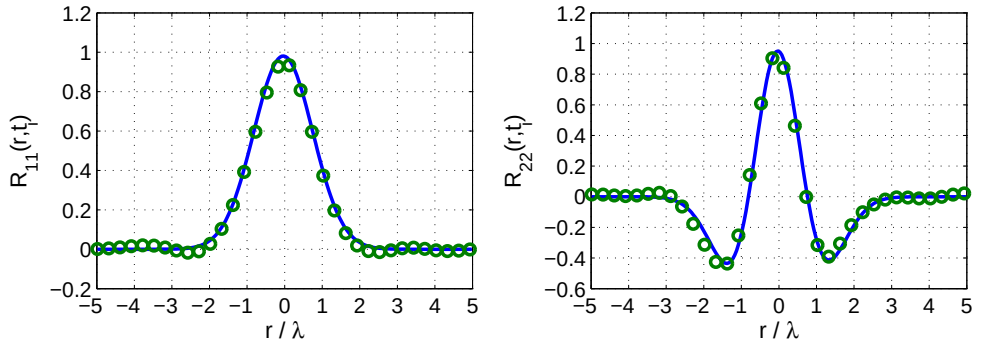

(b) Wake model with $T = 10L_w/u_0$, $L_w = 0.24/c$ and 10% level of background turbulence.

FIGURE 6.22: Analytical (—) and numerical (○) two-point correlations R_{11} (left) and R_{22} (right) computed with respect to the centre of the flat plate at time t_i when the centre of the wake reaches the centre of the flat plate.

The accuracy of the statistical properties of the turbulence for the half-wake width $L_w = 0.17/c$ have already been assessed in the previous section and it was shown that the numerical error is negligible, see Figures 6.13(a) and 6.14(a).

The two-point two-time correlations R_{11} and R_{22} for the half-wake widths $L_w = 0.08/c$ and $L_w = 0.24/c$ are compared against analytical results in Figure 6.22. As for the previous cases, the numerical results follow closely the theoretical correlations.

Figure 6.23 shows sound pressure levels for observers at different far-field locations predicted for the test cases in table 6.3. For each value of L_w numerical SPL are in very good agreement with Amiet's analytical solution. It can be observed that the wake width has an strong impact on noise levels. As expected a larger wake width leads to an increase in noise levels at lower frequencies and a decrease of noise levels at higher frequencies.

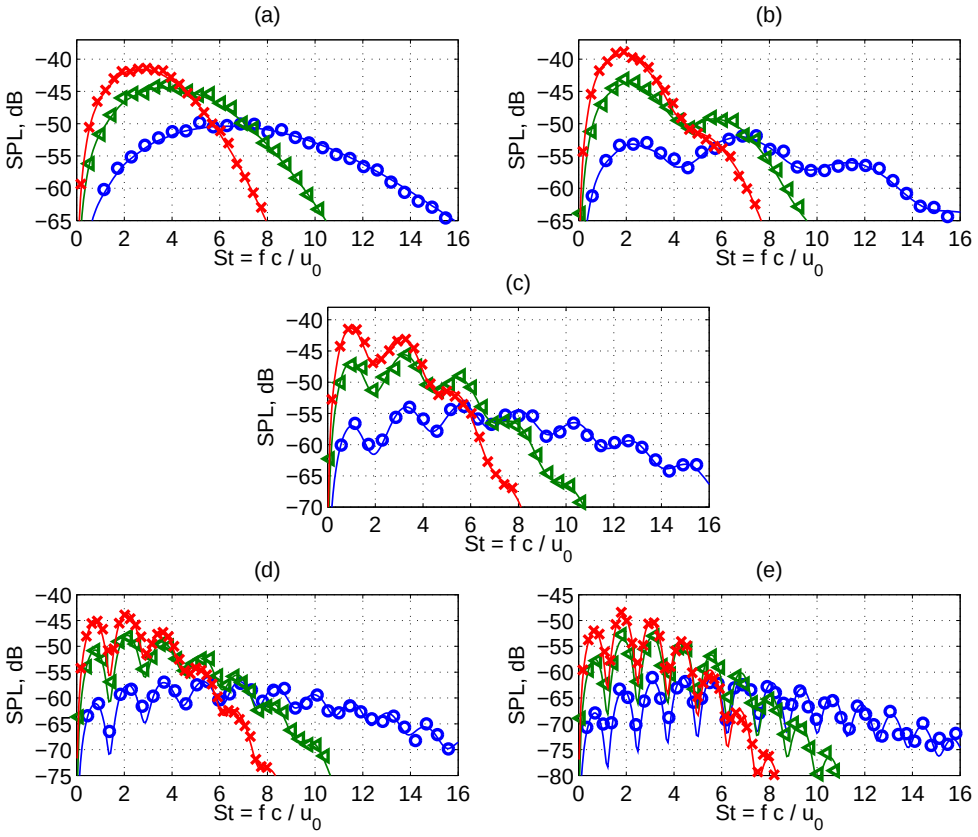

FIGURE 6.23: Far-field sound pressure levels for observers located at 30° (a), 60° (b), 90° (c), 120° (d), and 150° (e). Solid lines represent analytical results. Symbols correspond to numerical results obtained with $L_w = 0.08/c$ (○), $L_w = 0.17/c$ (◁), and $L_w = 0.24/c$ (×). Wake model with a period $T = 15L_w/u_0$ and 10% background turbulence.

Far-field directivities are shown in Figure 6.24 for Strouhal numbers $St = 3$ and 6. Again, numerical predictions are consistent with analytical results. The width of the wakes does not to modify the shape of the directivities but only changes the absolute levels.

6.4 Conclusions

In this chapter, the stochastic method has been extended to describe inhomogeneous non-stationary turbulence. Three different implementations of the random-vortex-particle

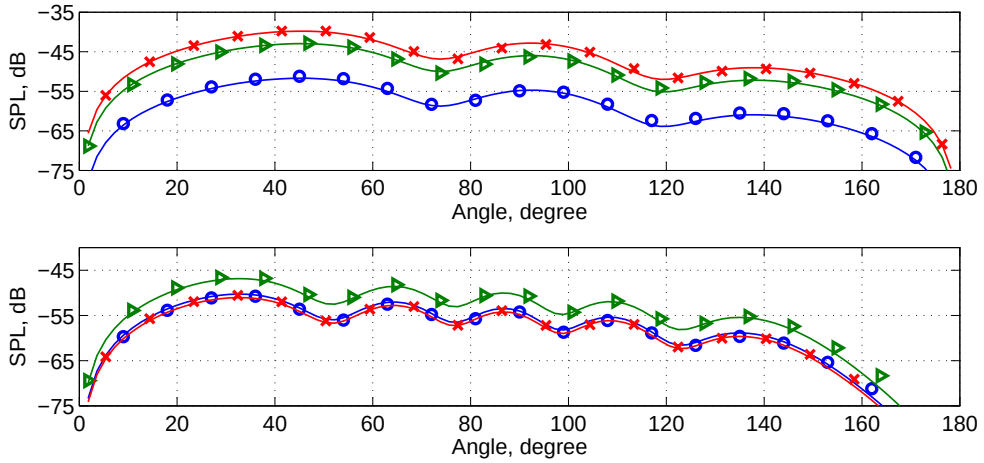

FIGURE 6.24: Directivity at Strouhal numbers $St = 3$ (top) and $St = 6$ (bottom). Solid lines represent analytical results. Symbols correspond to numerical results obtained with $L_w = 0.08/c$ (○), $L_w = 0.17/c$ (◁), and $L_w = 0.24/c$ (×). Wake model with a period $T = 15L_w/u_0$ and 10% background turbulence.

method for inhomogeneous non-stationary turbulence have been proposed and validated. Implementation 1 is based on the definition of the statistics of the turbulence (kinetic energy and integral length scale) at the vortex locations. Implementations 2 and 3 are based on the definition of the kinetic energy and integral length scale at the grid points and they differ in if the target value of kinetic energy is imposed within the stream function (Implementation 2) or directly at the velocity field (Implementation 3).

The stochastic method has been applied to the problem of rotor-stator interaction noise by combining the random-vortex-particle method with an existing wake model. It has been shown that, for this test case, numerical results are not very sensitive to the choice of implementation. While Implementation 3 is computationally cheaper, it neglects the terms with spatial derivatives of the kinetic energy whose influence increases as the turbulence becomes more inhomogeneous. We argue that the implementation based on the definition of the kinetic energy of the turbulence at the vortex location is more realistic since the vortex strength is specified by the local values of the turbulence and the velocity field is then given by contributions from all the nearby vortices.

The sensitivity of far-field noise levels to the wake configuration has also been discussed. When modifying the wake separation or the ratio between background and wake turbulence sound pressure levels in the far field have been found to scale with the mean-square velocity. Variations of the wake width change significantly the frequency content of the noise spectrum. The larger integral length scales associated with wider wakes produce stronger noise levels at small frequencies. Note that considering different wake separations and levels of background turbulence could also have an impact on the noise spectrum if the integral length scales of the background turbulence and wake turbulence were different.

Chapter 7

Comparison with Experiments

The aim of this chapter is to compare sound pressure levels predicted by the stochastic method against existing experimental results for an isolated airfoil in a turbulent jet. This comparison provides another opportunity to validate the numerical method. It also demonstrates the benefits of using the von Kármán spectrum instead of a Gaussian spectrum to describe the turbulence energy spectrum.

Note that measurements were preformed for a real airfoil geometry but numerical simulations are carried out for a flat plate. This simplification is not due to a restriction of the method but the requirements of numerical implementation go beyond the scope of this project.

7.1 Description of the experiment

As part of the European project FLOCON, leading and trailing edge noise of an isolated airfoil were measured in the ISVR open jet wind tunnel by Gruber and Joseph [71]. This section describes the experimental setup and the aerodynamic and aeroacoustic measurements. We present only leading edge noise data that is relevant for the comparison with numerical results.

7.1.1 Experimental setup

Figure 7.1 shows pictures of the experimental set up. A more detailed description of the ISVR DARP quiet open jet wind tunnel facility can be found in Ref. [72].

Air is supplied by a centrifugal fan driven by a variable speed motor. Turbulence is generated by inserting a grid (visible in Figure 7.1(a)) in the contraction of the nozzle at 50 mm from the nozzle exit. The dimensions of the nozzle exit are 0.45 m width by 0.15

(a) Exterior view of the nozzle.

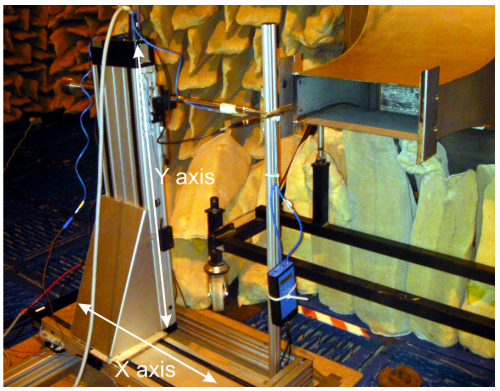

(b) Traverse unit.

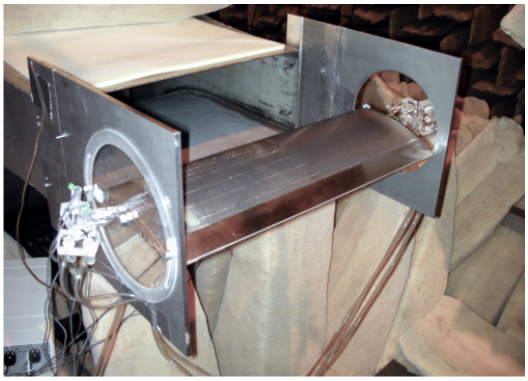

(c) Airfoil and side plates of the nozzle.

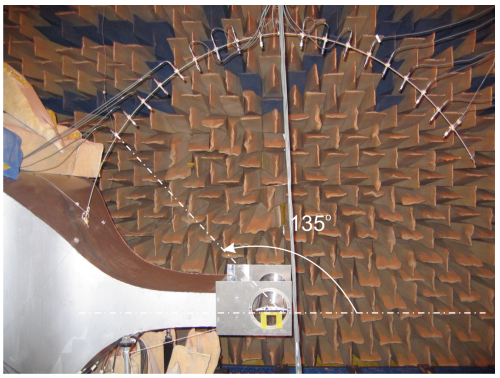

(d) Microphone array.

FIGURE 7.1: Sketch of the experimental set up.

m height. The streamwise velocity component was measured for jet velocities 20, 40 and 60 m/s (corresponding to Mach numbers 0.06, 0.11 and 0.17, respectively). Two grid designs were used so that the turbulence intensity at the nozzle exit is approximately 2 or 2.5%. Here, only results obtained for the mean flow velocity 60 m/s and the grid generating 2.5% turbulent intensity are discussed since this case corresponds with the highest leading edge noise levels.

The airfoil profile used in the experiment is a NACA651210 with 0.45 m of span and 0.15 m of chord. The leading edge of the airfoil is located at 0.145 m of the exit of the nozzle. Different angles of attack were measured but only data from zero angle of attack are used since it allows for a more direct comparison with the previous test case discussed in chapter 4.

7.1.2 Aerodynamic measurements

Aerodynamic measurements were performed using hot-wire probes and with the airfoil and side plates removed. We first describe the data measured and we then use it to characterise the statistical properties of the turbulence upstream of the airfoil. The aim is to extract from the data the input parameter values for the numerical simulation.

7.1.2.1 Measured data

Hot-wire measurements of the turbulent velocity component in the streamwise direction were carried out at two planes parallel to the nozzle exit and located at 0.095 m and at 0.145 m downstream of the nozzle exit, respectively. On each of these planes, hot-wire data were collected at 9 different locations arranged in a square 3×3 array with size 0.225×0.075 m. Note that the second plane coincides with the actual position of the leading edge of the airfoil when it is placed in front of the nozzle.

Tables 7.1 and 7.2 summarise the measured mean flow velocity and turbulence intensity ($TI = u_{rms}/u_0$) at each of the hot-wire probe locations (labelled from top to bottom and left to right). Measurements at different locations are consistent except those acquired at locations 7 and 8 in the first plane and location 8 in the second plane which are therefore rejected. For the remaining locations, the average mean flow velocity is 52.88 m/s and the average turbulence intensity is 2.12%. The variance of the measured mean flow velocity and the turbulent intensity in the streamwise direction over the 15 points are 0.18 m/s and 0.1%, respectively. Therefore, the mean flow is approximated as uniform and the turbulence intensity as statistically homogeneous in the streamwise component.

Location	1	2	3	4	5	6	(7)	(8)	9
Mean flow [m/s]	53.32	52.57	52.89	53.09	52.11	53.76	2.99	3.06	52.88
TI [%]	2.17	1.84	1.87	2.16	1.86	1.95	0.87	1.48	2.96

TABLE 7.1: Mean flow and turbulence intensity TI measured at the plane located at 0.095 m downstream of the nozzle.

Location	1	2	3	4	5	6	7	(8)	9
Mean flow [m/s]	53.34	52.63	52.83	53.17	52.28	52.80	52.80	3.05	52.62
TI [%]	2.25	1.78	2.01	2.19	1.85	2.08	2.24	1.19	2.55

TABLE 7.2: Mean flow and turbulence intensity TI measured at the plane located at 0.145 m downstream of the nozzle.

Note that the average of the measured mean flow is 52.88 m/s and not the expected mean flow velocity of 60 m/s. This discrepancy is thought to be related with the calibration of the hot-wire probes. In addition the average of the measured turbulence intensity is about 15% lower than expected. Calibration issues affect the reliability of the measurement to extract appropriate values of the statistical parameters describing the incoming turbulence (turbulent kinetic energy and integral length scale).

Another aspect to highlight is that no measurements of the turbulent velocity field in the spanwise and normal directions of the airfoil were performed. Therefore, it is not possible to verify if the turbulence is isotropic. The experiment was designed to produce isotropic turbulence, however due to the distance between the turbulence generating grid and the nozzle exit (50 cm) vortex stretching in the streamwise direction takes

place. One should expect a larger integral length scale of the normal component of the turbulence in the streamwise direction. Note that even though the turbulent flow is only suspected to be weakly anisotropic, analytical and numerical results presented later on in this chapter would be affected as in both cases it is the normal component of the turbulent velocity field that is used.

7.1.2.2 Estimation of the kinetic energy and integral length scale of the turbulence

Aerodynamic measurements can be used to estimate the kinetic energy K and the integral length scale λ of the turbulence in the streamwise direction. A way of estimating these is by fitting the velocity spectrum obtained from measurements to an analytical model for homogeneous isotropic turbulence. Such an analytical velocity spectrum can be related with a model for the energy spectrum and derived using either two- or three-dimensional formulations. While the nature of the experiments is three-dimensional, the numerical simulations are fully two-dimensional and therefore both approaches are considered here. Von Kármán and Gaussian energy spectra are used to derive analytical expressions of the velocity spectrum in an attempt to show that although Gaussian spectra are computationally more desirable, von Kármán spectrum provides more accurate predictions.

The von Kármán energy spectrum previously introduced in Eq. (2.90),

$$E_k(\kappa) = \frac{110}{27\pi} K \lambda \varsigma^4 \frac{\kappa^4}{(1+\varsigma^2\kappa^2)^{17/6}}, \tag{7.1}$$

is used to model the spectrum of two- and three-dimensional turbulence. However, different Gaussian energy spectra are used depending on the dimension of the problem. Following Kraichnan's approach [6], the Gaussian spectrum for two- and three-dimensional formulations are

$$E_g(\kappa) = \frac{2}{\pi^2} K \lambda^4 \kappa^3 \exp\left(-\frac{\lambda^2\kappa^2}{\pi}\right), \quad \text{(2D)} \tag{7.2}$$

$$E_g(\kappa) = \frac{8}{3\pi^3} K \lambda^5 \kappa^4 \exp\left(-\frac{\lambda^2\kappa^2}{\pi}\right), \quad \text{(3D)} \tag{7.3}$$

respectively. The Gaussian energy spectrum in Eq. (7.3) has also been considered by Atassi *et al.* [13] when discussing the effects of turbulence energy spectra in broadband fan noise. (See section 3.1 for more details on Atassi *et al.*'s method.)

We now present the different expressions for the velocity spectrum and then a parametric study is performed to estimate the kinetic energy and the integral length scale.

Velocity spectrum from measurements

The velocity spectrum of the measured turbulent field in the streamwise direction at a given location $\boldsymbol{x}$ is given by

$$\phi_{11}(\omega) = \int_{-\infty}^{\infty} \langle u_x'(\boldsymbol{x}, t_0) u_x'(\boldsymbol{x}, t) \rangle \exp(-i\omega t) \mathrm{d}t, \tag{7.4}$$

where ω is the angular frequency, and $\boldsymbol{u'}$ is the fluctuating component of the velocity. 512 samples of the fluctuating component of the velocity field at a sampling frequency $f_s = 20,012$ Hz are used. Similar velocity spectra are found at all locations (except at those excluded due to low values of mean flow) which contributes in showing that the streamwise component of the turbulence is statistically homogeneous.

Two-dimensional formulation

An analytical expression for the velocity spectrum of the streamwise component, ϕ_{11}, can be derived from its relation with the energy spectrum of the turbulence (see Ref. [14])

$$\phi_{11}(\kappa_x) = \int_{\mathbb{R}} \frac{4\pi E(\kappa)}{\kappa} \left(1 - \frac{\kappa_x^2}{\kappa^2}\right) \mathrm{d}\kappa_y. \tag{7.5}$$

Then, Taylor's hypothesis for frozen turbulence can be used to convert temporal to spatial statistics yielding $\phi_{11}(\omega) = \phi_{11}(\kappa_x)/2\pi u_0$.

Closed-form expressions for the velocity spectrum are given by inserting von Kármán and Gaussian energy spectra defined in Eqs. (7.1) and (7.2) in Eq. (7.5). This yields the following expressions:

$$[\phi_{11}]_g(\omega) = \frac{2K\lambda}{u_0} \exp\left(\frac{-\lambda^2\omega^2}{\pi u_0^2}\right), \tag{7.6}$$

$$[\phi_{11}]_k(\tilde{\omega}) = -\frac{110K\lambda\tilde{\omega}}{27u_0\pi^{3/2}} \left\{ \frac{\Gamma(-4/3)\Gamma(5/6)}{\tilde{\omega}^{4/3}} F_1 + \frac{\pi\Gamma(4/3)\left[(\tilde{\omega}^2 - 3)F_2 - 5\tilde{\omega}^2 F_3\right]}{3(1+\tilde{\omega}^2)\Gamma(17/6)} \right\}, \tag{7.7}$$

where subscripts g and k refer to the Gaussian and von Kármán spectrum respectively,

$$F_1 = {}_2\mathrm{F}_1\left(-\frac{5}{6}, \frac{17}{6}; \frac{7}{3}; 1 + \frac{1}{\tilde{\omega}^2}\right), \quad F_2 = {}_2\mathrm{F}_1\left(-\frac{1}{2}, \frac{1}{2}; -\frac{1}{3}; 1 + \frac{1}{\tilde{\omega}^2}\right),$$

$$F_3 = {}_2\mathrm{F}_1\left(-\frac{1}{2}, -\frac{1}{2}; -\frac{1}{3}; 1 + \frac{1}{\tilde{\omega}^2}\right), \quad \text{and} \quad \tilde{\omega} = \frac{\Gamma(1/3)\lambda}{\sqrt{\pi}\Gamma(5/6)u_0}\omega.$$

Three-dimensional formulation

For a three-dimensional turbulent flow, the velocity spectrum of the streamwise component, $\tilde{\phi}_{11}$, is related with the energy spectrum by (see Ref. [14])

$$\tilde{\phi}_{11}(\kappa_x, \kappa_z) = \int_{\mathbb{R}} \frac{2\pi^2 E(\kappa)}{\kappa^2} \left(1 - \frac{\kappa_x^2}{\kappa^2}\right) \mathrm{d}\kappa_y. \tag{7.8}$$

Using again Taylor's hypothesis for frozen turbulence yields (see Ref. [17])

$$\tilde{\phi}_{11}(\omega) = \frac{\phi_{11}(\kappa_x, 0)}{4\pi u_0 l_z}, \quad \text{with} \quad l_z = \frac{1}{R_{11}(\kappa_x, 0)} \int_0^\infty R_{11}(\kappa_x, z)\mathrm{d}z. \tag{7.9}$$

$R_{11}(\kappa_x, z)$ is the Fourier transform of $\tilde{\phi}_{11}(\kappa_x, \kappa_z)$ with respect to κ_z and hence l_z can be interpreted as a correlation length in the spanwise direction.

The velocity spectrum in the streamwise direction corresponding to the Gaussian energy spectrum in Eq. (7.3) is

$$\left[\tilde{\phi}_{11}\right]_g (\omega) = \frac{4K\lambda}{3u_0} \exp\left(\frac{-\lambda^2\omega^2}{\pi u_0^2}\right), \tag{7.10}$$

and the velocity spectrum in the streamwise direction corresponding to von Kármán energy spectrum in Eq. (7.1) is

$$\left[\tilde{\phi}_{11}\right]_k (\omega) = \frac{4K\lambda}{3u_0}(1 - \tilde{\omega}^2)^{-5/6}. \tag{7.11}$$

Parametric study

A parametric study is performed to estimate the integral length scale of the turbulence by fitting the measured velocity spectrum, Eq. (7.4), to the analytical velocity spectrum corresponding to von Kármán and Gaussian energy spectra in a two-dimensional formulation, Eqs. (7.6) and (7.7).

The measured velocity spectrum used in this parametric study corresponds to data collected at location 5 on the plane located at 0.145 m downstream of the nozzle (see table 7.2) since this location corresponds to the central position of the leading edge of the airfoil.

The velocity spectrum obtained from measurements is compared with von Kármán and Gaussian velocity spectra for integral length scales $\lambda = 0.005$, 0.1 and 0.2 m in Figures 7.2 and 7.3, respectively. In both cases, the turbulent kinetic energy is estimated through the measured root-mean-square velocity assuming isotropic homogeneous two-dimensional turbulence, that is $K = u_{rms}^2$. Von Kármán spectrum provides a good fit to measurements for $\lambda = 0.01$ m over the whole range of frequencies. In contrast, for the Gaussian spectrum neither of the proposed values of the integral length scale provides a good fit to the measured velocity spectrum. This is due to the fast decay of the exponential function in the Gaussian velocity spectrum, see Eq. (7.6).

The fit between the Gaussian analytical spectrum and measurements can be improved by tuning the kinetic energy together with the integral length scale of the turbulence, see Figure 7.4. The benefits of this strategy are limited to specific frequency ranges; for instance for $\lambda = 0.01$ m and $K = 0.6u_{rms}^2$ good agreement is found only between 500 and

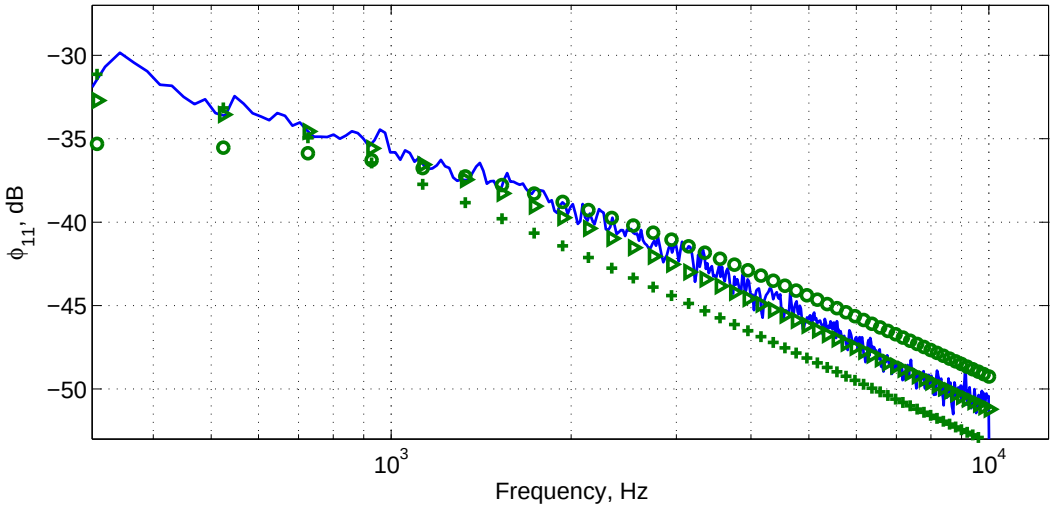

FIGURE 7.2: Measured velocity spectrum (—) against von Kármán velocity spectrum with $\lambda = 0.005$ m (○), $\lambda = 0.01$ m (▷), and $\lambda = 0.02$ m (+).

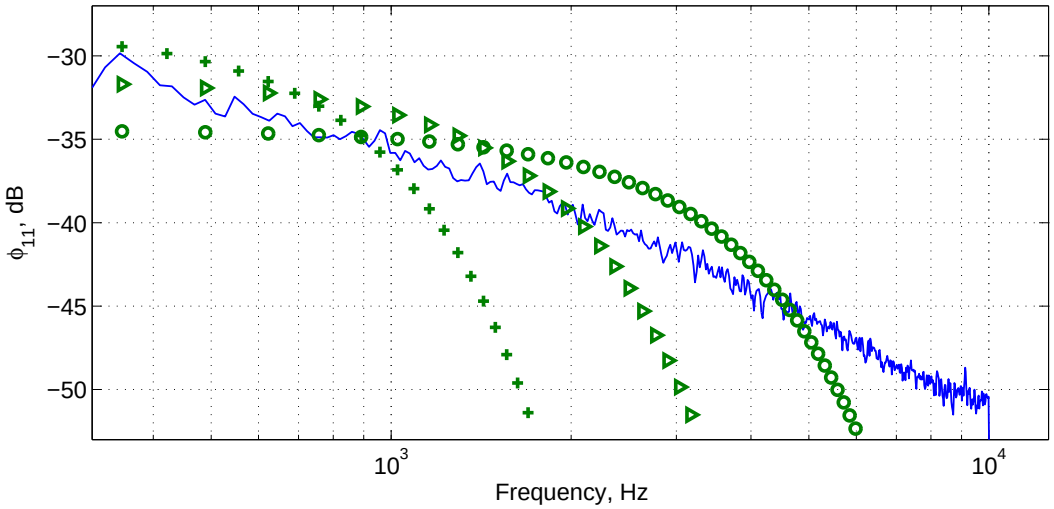

FIGURE 7.3: Measured velocity spectrum (—) against Gaussian velocity spectrum with $\lambda = 0.005$ m (○), $\lambda = 0.01$ m (▷), and $\lambda = 0.02$ m (+).

2,000 Hz. Therefore one option is to consider instead of one single Gaussian spectrum a series of Gaussian spectra so that by superimposing them a good approximation of the measured spectrum is achieved. This approach is proposed by Siefert and Ewert [15], the objective being to model non-Gaussian spectrum with a series of Gaussian filters. (See section 2.1.2.3 for further information on Ewert's method.)

In contrast with Siefert and Ewert's approach, in this thesis we propose the use of one single energy spectrum to describe the whole range of frequencies. Superimposing more than one Gaussian spectrum increases the computational cost of the method due to the associate increase in the number of vortices. Hence, by considering a more realistic

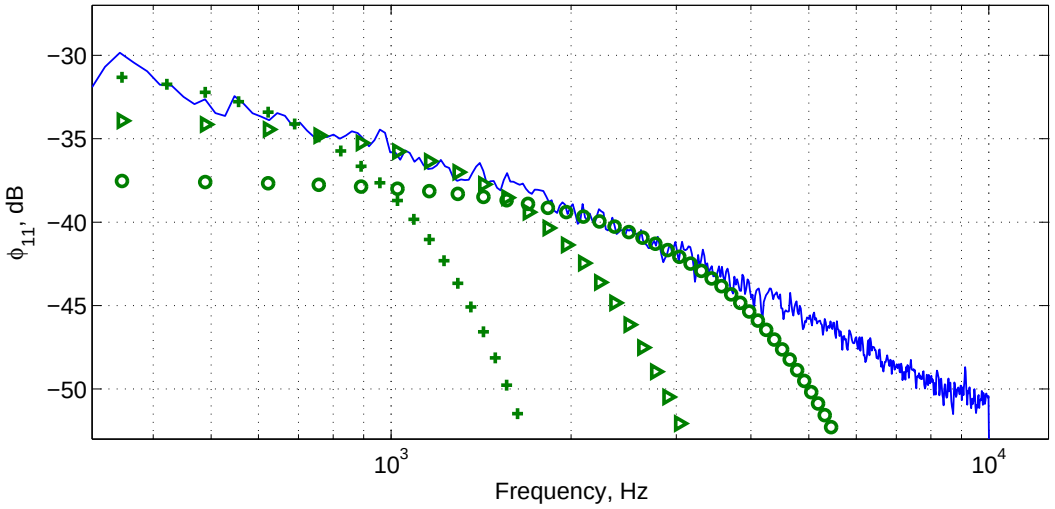

FIGURE 7.4: Measured velocity spectrum (—) against Gaussian velocity spectrum with $\lambda = 0.005$ m and $K = 0.5u_{rms}^2$ (○), $\lambda = 0.01$ m and $K = 0.6u_{rms}^2$ (▷), and $\lambda = 0.02$ m and $K = 0.65u_{rms}^2$ (+).

model for the energy spectrum the resulting numerical method is simpler and describes the whole range of frequencies of interest.

Finally, note that using the velocity spectrum to fit the measurements is more robust than the energy spectrum because it is independent of the number of dimensions. Figure 7.5 shows Gaussian and von Kármán velocity spectra derived in two dimensions, Eqs. (7.6) and (7.7), against the corresponding expressions derived in three dimensions, Eqs. (7.10) and (7.11). We can see that similar fit to the experimental data is obtained for the same choice of integral length scale and kinetic energy adjusted by a factor 1.5 for the three-dimensional formulation. (The factor 3/2 stems from the definition of the kinetic energy for isotropic turbulence as shown in Eq. (2.12).)

In summary, the von Kármán spectrum provides an accurate description of the measured velocity spectrum in the streamwise direction. An integral length scale of $\lambda = 0.01$ m is a good fit to the experimental data. In addition, the value of kinetic energy is consistent with that derived from the root-mean-square velocity. Regarding the Gaussian spectrum, only a specific range of frequencies can be approximated for any fixed value of integral length scale and the kinetic energy must be adjusted independently of the measured root-mean-square velocity in order to improve the fitting.

7.1.3 Acoustic measurements

The ISVR open jet wind tunnel is located in an anechoic chamber of dimensions $8 \times 8 \times 8$ m where noise measurements are performed using a circular array of microphones centred on trailing edge of the airfoil as shown in Figure 7.1(d). The array consisted of 19 microphones uniformly distributed between 45 degrees from the downstream direction

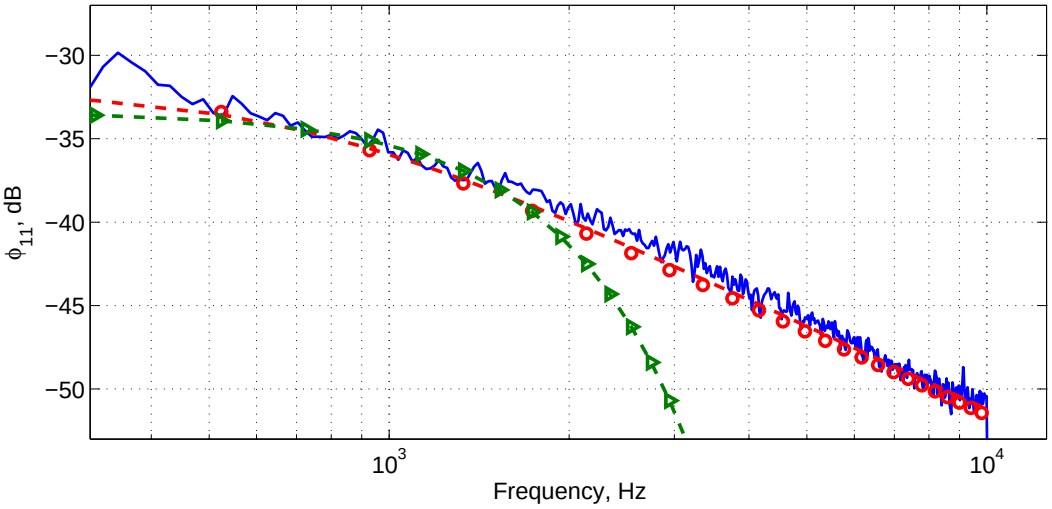

FIGURE 7.5: Measured velocity spectrum (—) against theoretical models. Von Kármán velocity spectrum derived from 2D (– –) and 3D (○) formulations with $\lambda = 0.01$ m and $K = u_{rms}^2$ and $K = 3u_{rms}^2/2$, respectively. Gaussian velocity spectrum from 2D (– –) and 3D (▷) formulations with $\lambda = 0.01$ m and $K = 0.6u_{rms}^2$ and $K = 0.9u_{rms}^2$, respectively.

to 135 degrees. The radius of the microphone array, 1.2 m, is almost three times larger than the span of the airfoil and captures at least one acoustic wavelength for Strouhal numbers larger than 0.37 (based on zero Mach number).

The sound spectral density at each microphone location is computed using as input 512 samples of the measured acoustic field at a sampling frequency $f_s = 51,200$ Hz. Data measured by the microphone located at 45 degrees is rejected due to a significant deviation of sound pressure level compared to the other microphones (noise levels being 70 dB lower than the others), see Figure 7.6. Background noise levels were found to be insignificant and no background correction was applied to the measured data.

An issue with such an open jet facility is that acoustic waves propagate through the jet shear layer before reaching the microphone, and when doing so waves are refracted as illustrated in Figure 7.7. This leads to a change in angle and amplitude in the far field. Thus, for a microphone located at position M outside the jet, due to the refraction of wavefronts at the shear layer, the angle Θ_m at which the microphone is located does not correspond to the angle Θ_c of propagation inside the jet. Measurements are performed in terms of Θ_m but numerical results and Amiet analytical solution are given in terms of Θ_c, so a relationship between the two has to be established before compering them.

The model proposed by Amiet [73] is used here to account for the effects of the shear layer on the angle of propagation and amplitude. The source position is located at the leading edge of the airfoil and corrections are made under the assumptions of zero-thickness shear layer, equal distance from present source position ($r_c = r_m$) and that the distance from the source to the shear layer ($h = 0.075$ m) is small compared to the

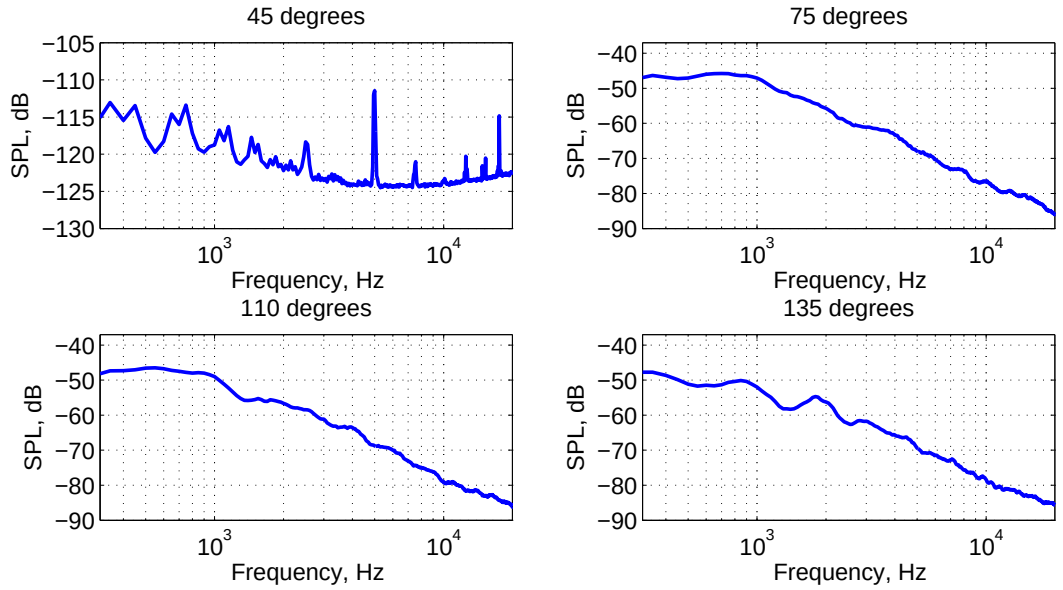

FIGURE 7.6: Sound power levels at 45°, 75°, 110° and 135° centred at the trailing edge. Note that SPL at 45° have a significant deviation from those at other locations suggesting a malfunction of the microphone.

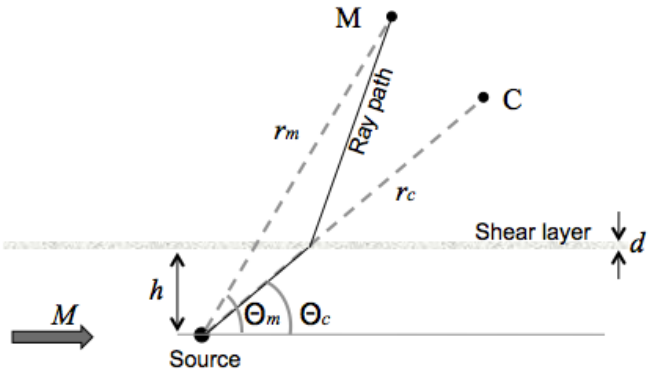

FIGURE 7.7: Sketch of the refraction of sound by a shear layer [73].

distance to the observer ($r_m = 1.2$ m). The relation between the propagation angle before the refraction Θ_c and the microphone angle Θ_m is:

$$\Theta_c = \arctan\left(\frac{C}{\beta^2 \cos\Theta_m + M}\right), \tag{7.12}$$

where $C^2 = (1 - M\cos\Theta_m)^2 - \cos^2\Theta_m$ and $\beta^2 = 1 - M^2$ with M the jet Mach number. The amplitude change caused by the shear layer can be account for by the correction factor:

$$A_c = \frac{\sqrt{1 + M^2C^2}}{2}\left[\frac{C}{\sin\Theta_m} + (1 - M\cos\Theta_m)^2\right]. \tag{7.13}$$

Angle and amplitude corrections corresponding to the microphone locations in the experiment are shown in Figure 7.8 where angles are centred at the leading edge of the airfoil and measured from the downstream direction. The correction in amplitude is rather limited with the largest amplitude difference being 1.5 dB for the microphone located at 40 degrees. In contrast, angles with and without shear layer correction differ by up to 10 degrees.

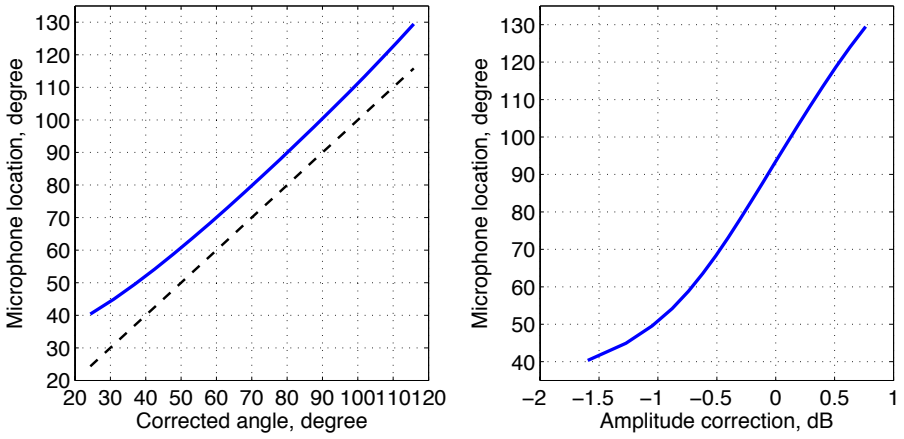

FIGURE 7.8: Left: Angle correction Θ_c versus microphone location Θ_m. Right: Amplitude correction in dB versus microphone location.

Measured noise levels are further discussed in section 7.3 when compared with Amiet's analytical solution and the numerical results. Note that Amiet's shear layer correction is applied to analytical and numerical results and noise levels computed from measurements are left unchanged.

7.2 Numerical Simulations

In this section the stochastic method proposed in this thesis to predict broadband fan interaction noise is used to simulate the experiment described above.

The following assumptions are made. The geometry of the airfoil is simplified to a flat plate. The turbulent flow interacting with the airfoil is assumed to be isotropic, homogeneous and two-dimensional. The turbulence is convected by a uniform mean flow in the x-direction $u_0 = 60$ m/s (Mach number 0.175).

Synthetic turbulence is generated with the random-vortex-particle method as in Eq. (2.67) using the Gaussian and von Kármán filters defined by Eqs. (2.86) and (2.92). For both filters, the turbulence is characterised by an integral length scale of 0.01 m. The turbulent kinetic energy for von Kármán filters is 0.93 m^2/s^2 while for Gaussian filters is 0.56

m^2/s^2, see section 7.1.2.2. The remaining parameter required for the random-vortex-particle method to generate synthetic turbulence is the Lagrangian time scale which can be estimated as $\tau = 0.522$ s using the scaling procedure in Eq. (5.12).

7.2.1 Problem definition

The parameters of the problem are made non-dimensional using the chord of the airfoil, the mean flow density and the sound speed. Table 7.3 summarises the parameters used in the numerical simulation.

	Experiment	Simulation
Airfoil geometry	NACA651210	Flat plate
Mean flow	60 m/s	0.175
Integral length scale	0.01 m	0.067
Kinetic energy for von Kármán filter	0.935 m^2/s^2	7.905e-06
Kinetic energy for Gaussian filter	0.561 m^2/s^2	4.776e-06

TABLE 7.3: Parameters used in the numerical simulation.

The typical time scale of a vortex passing near the leading edge λ/u_0 is various orders of magnitude smaller than the integral time scale of the turbulence, hence the effects of temporal decorrelation can be neglected and frozen turbulence is assumed. See section 5.4 for a detailed discussion of the assumption of frozen turbulence.

7.2.2 Computational setup

The computational domain is given by $[-3.5, 3.5] \times [-3, 3]$ with the flat plate located at $[-0.5, 0.5] \times \{0\}$, see Figure 7.9. The domain is divided in fourteen blocks, each with a uniform Cartesian grid of 200×600 grid points. This grid provides at least 10 points per hydrodynamic wavelength and 47 points per acoustic wavelength (based on a maximum Strouhal number $St = 20$). The time step selected corresponds to a CFL number of 0.8. Note that the computational domain considered here is significantly larger than the one used in the previous test case (see section 4.2) due to a larger content of noise at low frequencies observed in the measured sound pressure levels.

Buffer zones are implemented at the boundary of the simulation domain as explained in section 3.3.3. The size of the buffer zone is 100 grid points everywhere apart from the outflow boundary where a buffer zone of 190 points is used. Following a parametric study similar to that in section 3.4, the strength of the selective filter is set to 0.62. Far-field acoustic results are obtained using the FWH formulation with a rectangular control surface enclosing the flat plate as shown in Figure 7.9.

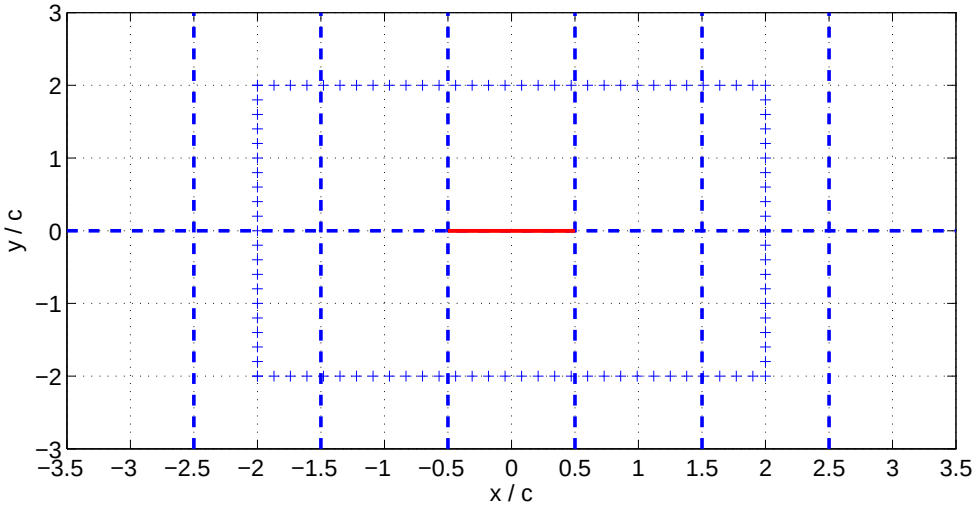

FIGURE 7.9: Sketch of the domain of simulation showing the block distribution (− −), the flat plate location (—) and the FWH-formulation control surface (+) .

The conclusions drawn from the parametric study performed in chapter 4 are used here to set up the vortex distribution and sampling procedure. The synthetic turbulence is generated with Gaussian and von Kármán filters. For the Gaussian filter, vortices are distributed on a region determined by $r_{max} = 2.43\lambda$ and at every $\Delta = \lambda/6$. For the von Kármán filter, vortices are distributed on a region determined by $r_{max} = 5.43/\lambda$ and at every $\Delta = \lambda/8$, see Figure 4.1. In both cases, the vortices are convected with the mean flow and their strength remains constant in time, representing frozen turbulence.

7.2.3 Numerical results

The statistical behaviour of the synthetic turbulence and noise levels in the far field are now examined in order to validate the numerical results.

7.2.3.1 Synthetic turbulence

The quality of the synthetic turbulence is assessed by evaluating its statistical properties along the flat plate. Two-point correlations R_{11} and R_{22} and one-dimensional energy spectra E_{11} and E_{22} (defined by Eqs. (2.36) and (4.1)) are computed along the flat plate with Gaussian and von Kármán filters. They are shown in Figures 7.10 and 7.11, respectively. In both cases, the statistical behaviour of the synthetic turbulence is in very good agreement with the corresponding analytical expressions.

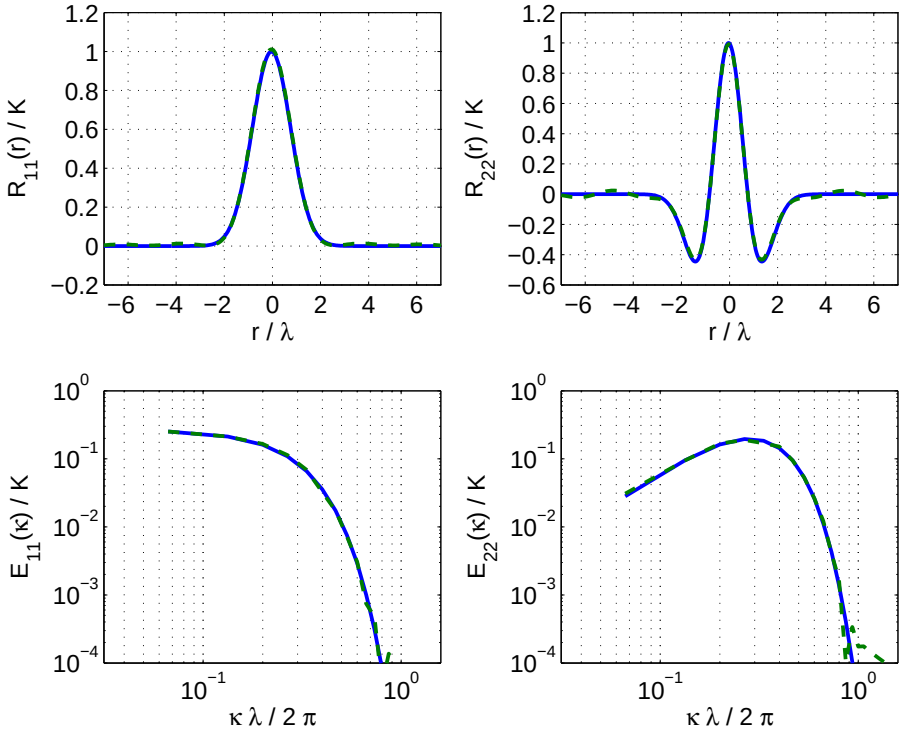

FIGURE 7.10: Analytical solution (—) against numerical results (– –) obtained with the Gaussian spectrum. Top: two-point correlations R_{11} and R_{22} computed with respect to the central point of the airfoil. Bottom: one-dimensional energy spectra E_{11} and E_{22}. Averages taken over $8,000$ samples at a sampling rate $40\Delta_t$.

7.2.3.2 Acoustic pressure

A snapshot of the acoustic pressure field around the flat plate is shown in Figure 7.12 for the Gaussian spectrum. As seen in the previous test case, most of the noise is radiated from the leading edge and acoustic waves are also scattered at the trailing edge.

Noise levels in the far field are also computed using the same procedure as in chapter 4 but with a sampling frequency adjusted to this test case.

Figure 7.13 shows sound pressure levels for the Gaussian spectrum for observers located at 30, 60, 90, 120, and 150 degrees centred at the centre of the airfoil and meassured from the downstream direction. Figure 7.14 shows SPL at the same locations but computed using the von Kármán spectrum. For both spectra, noise levels are in good agreement with the fully two-dimensional Amiet's analytical solution at all locations, and especially at downstream locations. For upstream locations, numerical results do not capture as accurately the shape of the noise spectra predicted by the analytical solution. Note that these discrepancies were already discussed in the previous test case (see chapter 4) and also that they are observed when the noise levels are more than 15 dB below what is observed downstream.

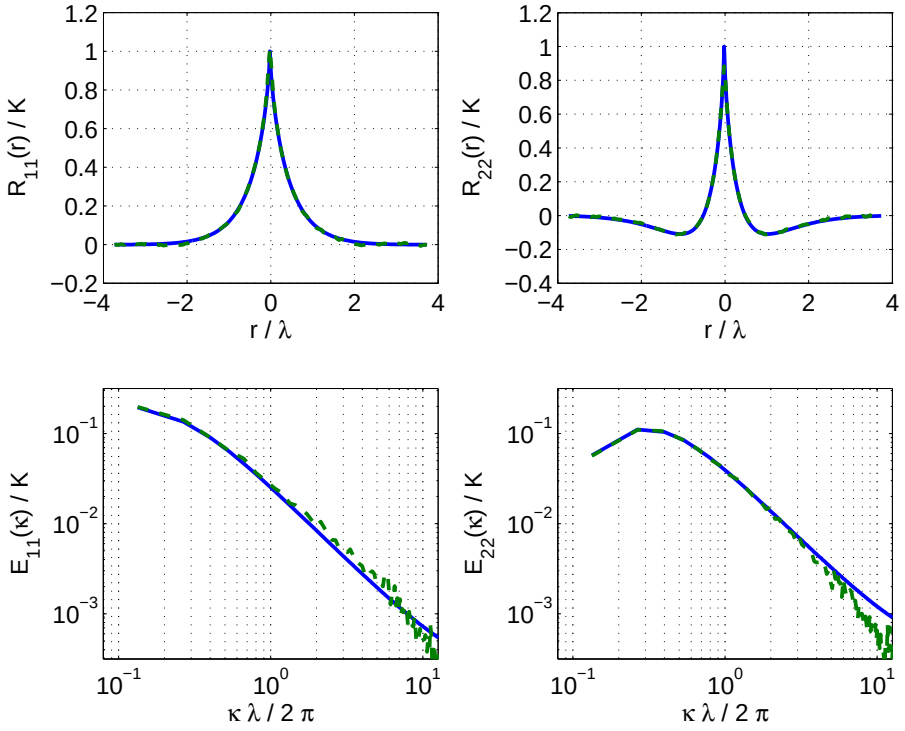

FIGURE 7.11: Analytical solution (—) against numerical results (– –) obtained with von Kármán filter. Top: two-point correlations R_{11} and R_{22} computed with respect to the central point of the airfoil. Bottom: one-dimensional energy spectra E_{11} and E_{22}. Averages taken over $8,000$ samples at a sampling rate $40\Delta_t$.

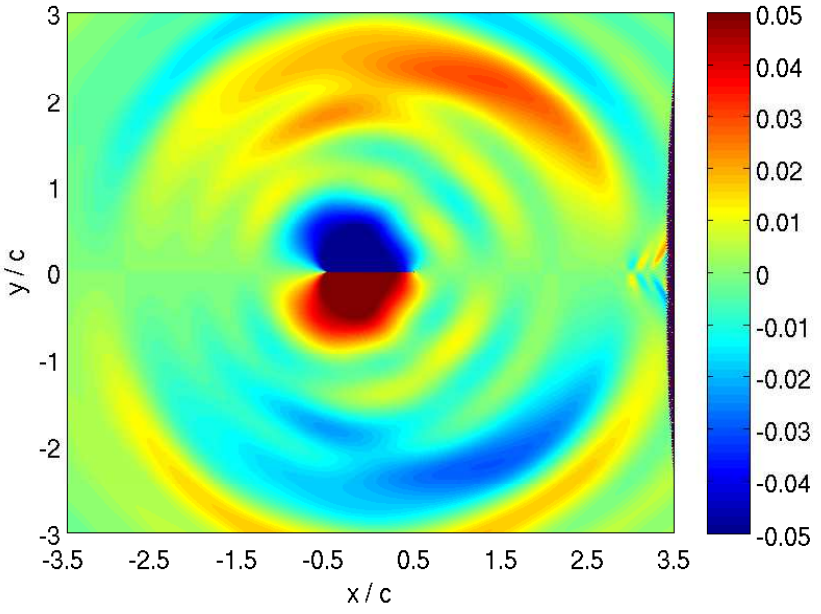

FIGURE 7.12: Snapshot of the acoustic pressure field for the Gaussian spectrum.

We now compare sound pressure levels for this test case against sound pressure levels predicted for the test case considered in chapter 4, for instance Figure 7.13 against Figure 4.11 and Figure 7.14 against Figure 4.13. We can see that in both cases the noise levels peak at similar Strouhal numbers. But, since the present test case has a slower mean flow velocity than the previous one, large noise levels are found at a lower frequencies justifying the use of a larger computational domain to accommodate for the larger wavelength.

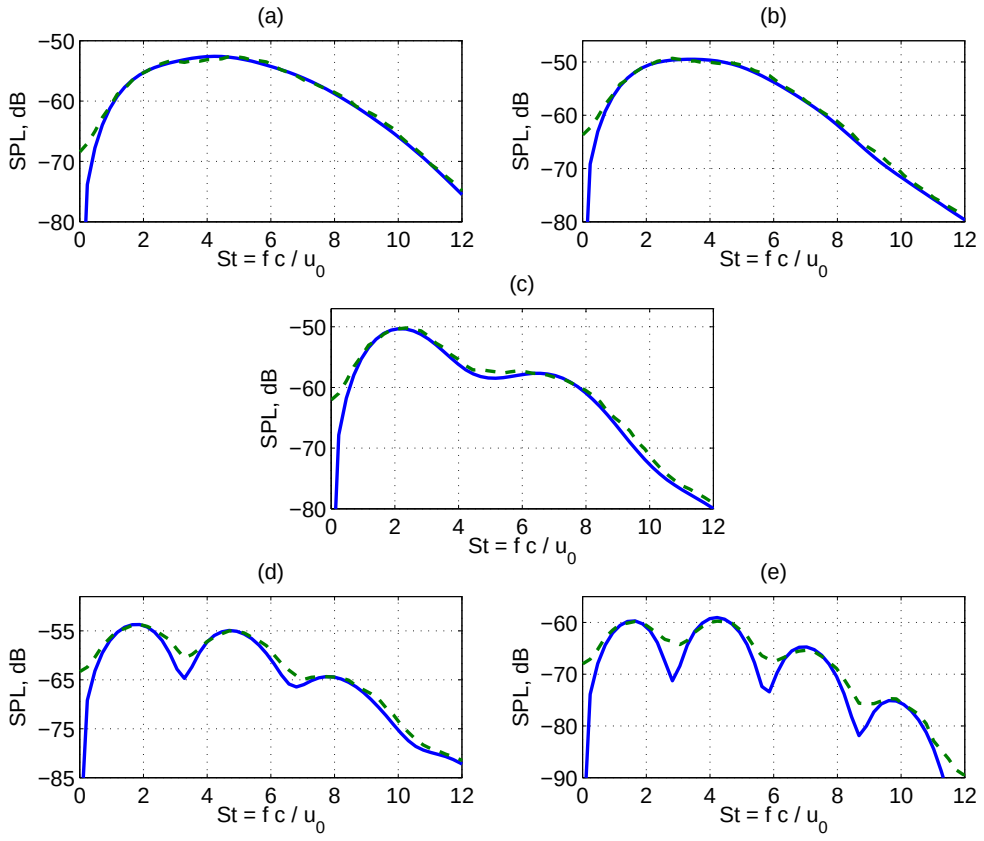

FIGURE 7.13: Far-field SPL obtained with the Gaussian spectrum for observers located at 30° (a), 60° (b), 90° (c), 120° (d), and 150° (e). Amiet's analytical solution (—). Numerical results (– –).

7.3 Comparison with experiments

Numerical results obtained in the previous section are now compared with experimental data. We first discuss the statistical behaviour of the turbulence by comparing the velocity spectrum against measurements and then predicted and measured sound pressure levels are compared.

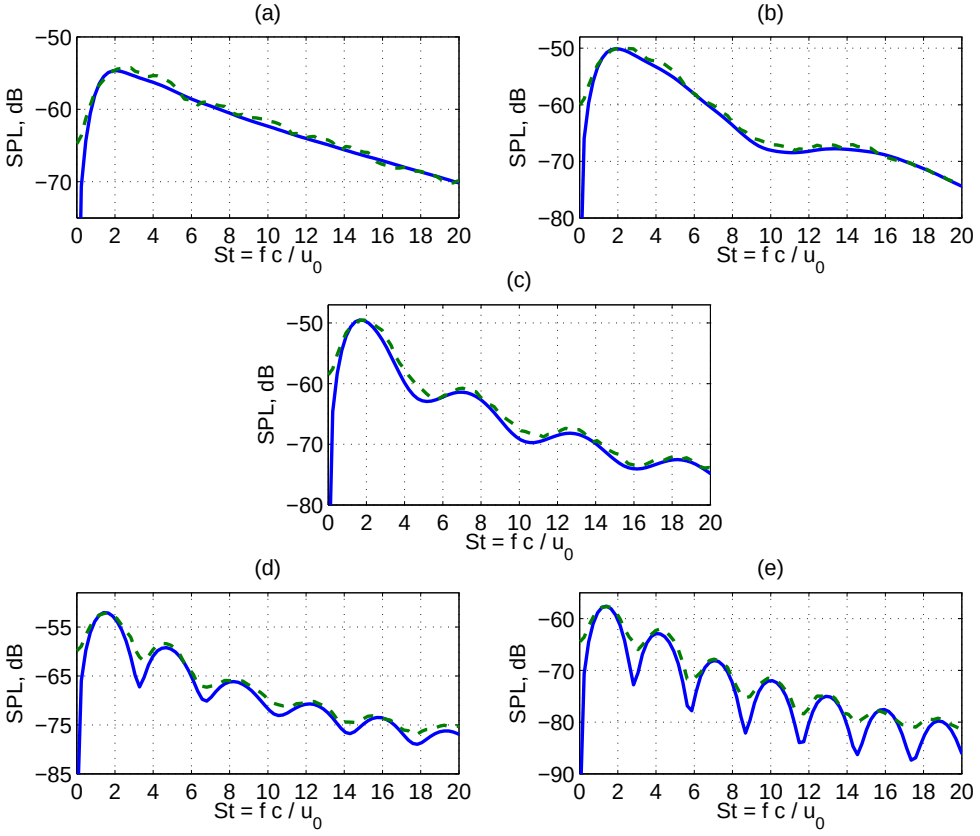

FIGURE 7.14: Far-field SPL obtained with the von Kármán spectrum for observers located at 30° (a), 60° (b), 90° (c), 120° (d), and 150° (e). Amiet's analytical solution (—). Numerical results (– –).

7.3.1 Statistical behaviour of the turbulence

In order to verify if the synthetic turbulent velocity field accurately reproduces the statistical behaviour of the fluctuating component of the velocity field measured in the experiment, numerical results are compared against the measured velocity spectrum at the leading edge of the airfoil.

Stochastically generated and measured velocity spectra in the streamwise direction are compared in Figure 7.15. The velocity spectrum obtained using von Kármán spectrum provides a good approximation of the measured and analytical velocity spectra for frequencies up to 3 kHz but at higher frequencies larger amplitudes are found. Note that a slight overprediction of energy levels at high frequencies was also found when comparing the stochastic one-dimensional energy spectrum in the streamwise direction against its theoretical expression (see Figure 7.11), but it was shown not to have a significant effect on the prediction of noise levels (see Figure 7.14) which is our ultimate purpose.

The stochastically generated Gaussian velocity spectrum is in very good agreement with its analytical expression, but as expected does not fit the measured velocity spectrum

showing a much faster rate of decay at high frequencies, see section 7.1.2.

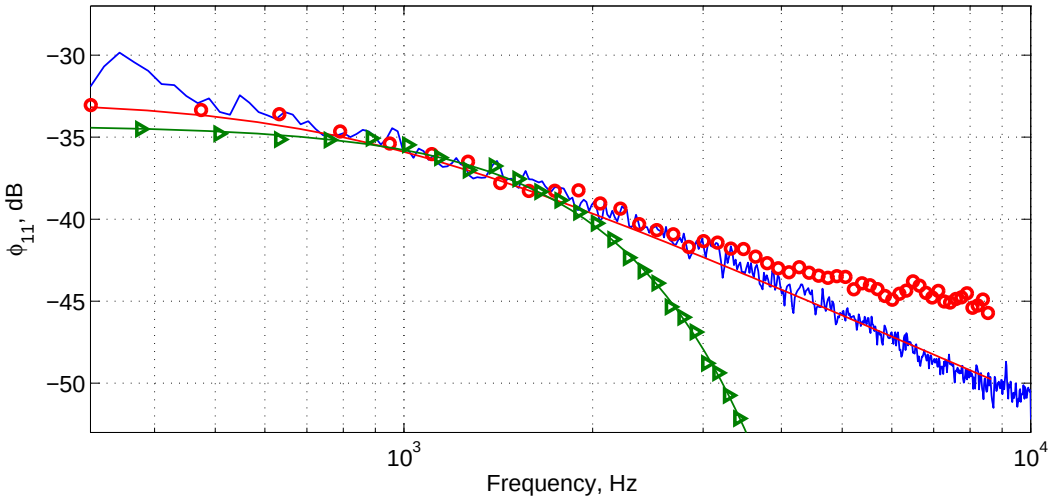

FIGURE 7.15: Measured velocity spectrum (—) against analytical (—) and numerical (○) von Kármán velocity spectra and analytical (—) and numerical (▷) Gaussian velocity spectra at the leading edge.

7.3.2 Noise levels

In previous chapters sound pressure levels in the far field were validated against the fully two-dimensional Amiet's analytical solution in Eq. (3.1). Here, due to the three-dimensional nature of the measured sound pressure levels, a correction factor that accounts for the difference between 2D and 3D must be applied in order to compare experimental data against the numerical results. The correction factor can be deduced by comparing Amiet's analytical solution in equation (17) of Ref. [42], $\tilde{S}_{pp}$, with the fully two-dimensional solution derived in Appendix C.1, S_{pp}, yielding

$$\tilde{S}_{pp}(x,y,0,\omega) = \frac{\kappa_0 L \tilde{\phi}_{22}(\kappa_x,0)}{\sigma \phi_{22}(\kappa_x)} S_{pp}(x,y,\omega), \tag{7.14}$$

where ω is the angular frequency, $\kappa_0 = \omega/c_0$ is the free-field acoustic wavenumber, $\kappa_x = \omega/u_0$ is the hydrodynamic wavenumber in the streamwise direction, L is the span of the airfoil, $\sigma = \sqrt{x^2 + (1-M^2)y^2}$ and $\tilde{\cdot}$ refers to a three-dimensional formulation. Note that Eq. (7.14) accounts for the difference in sound radiation between two and three dimensions and also for the difference in the definition of the sound source corresponding to the ratio $\tilde{\phi}_{22}(\kappa_x,0)/\phi_{22}(\kappa_x)$. A correction factor to compare two-dimensional simulations against experiments was also considered by Ewert *et al.* in Ref. [55] when predicting broadband trailing edge noise.

In addition to the three-dimensional correction, analytical and numerical results presented in this section are corrected to include the refraction effects of the open jet shear

layer as discussed in section 7.1.3. Thus the PSD of the numerical solution and its theoretical expression in Eq. (7.14) are not computed directly at the microphone locations but at the corrected angles defined by Eq. (7.12) and the amplitude of the noise levels is corrected using Eq. (7.13).

In Figure 7.16 measured sound pressure levels at 50, 90 and 130 degrees from the trailing edge of the airfoil are compared against analytical and numerical results obtained with Gaussian and von Kármán spectra. Numerical SPL computed with Gaussian spectrum do not capture the overall trend of the measured SPL and significant differences are found for Strouhal numbers larger than 10 due to the fast exponential decay. The agreement is better for the middle frequency range (where the fitting of the velocity spectra was optimised for) and especially for upstream locations.

Better agreement is found between predicted sound pressure levels with von Kármán spectrum and measurements, see Figure 7.16. At downstream locations, the shape of the noise spectrum is well predicted even though the slope is slightly flatter yielding larger noise levels at high frequencies. At upstream locations, numerical results very well capture the trend and amplitude of the measured sound pressure levels. However, at all locations a slight change of local maxima can be observed and it appears that the discrepancies between numerical results and measurements increase with frequency.

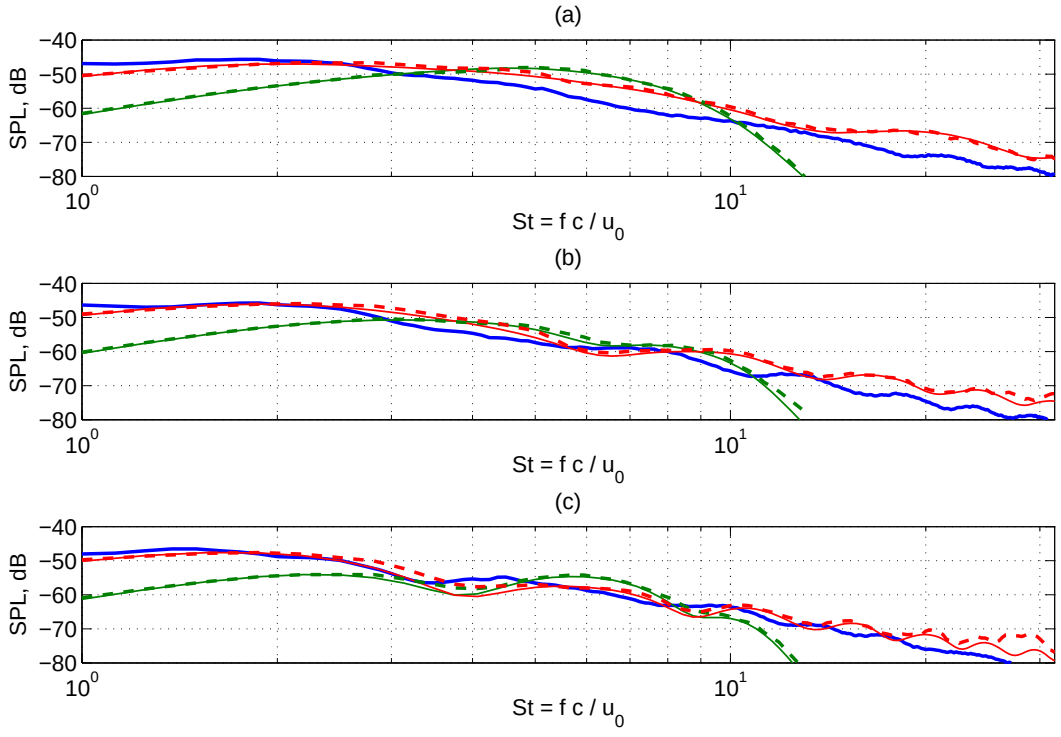

FIGURE 7.16: Sound pressure levels for observers located at 50° (a), 90°(b), and 130° (c). Measured SPL (—). Amiet's analytical solution (—) and numerical (– –) SPL computed with von Kármán spectrum. Amiet's analytical solution (—) and numerical (– –) SPL computed with Gaussian spectrum.

Directivities for Strouhal numbers $St = 2.5$, 5 and 10 are shown in Figure 7.17 for the von Kármán spectrum. Good agreement is observed when comparing numerical results against the proposed analytical solution with average error of about 1 dB. For the lowest Strouhal number, the numerical directivity predicts very well the measurements. Reasonable agreement is found at all locations and for Strouhal numbers $St = 5$ and $St = 10$. However, as observed in Figure 7.16, differences between measurements and numerical results are more noticeable as the frequency increases and for downstream locations.

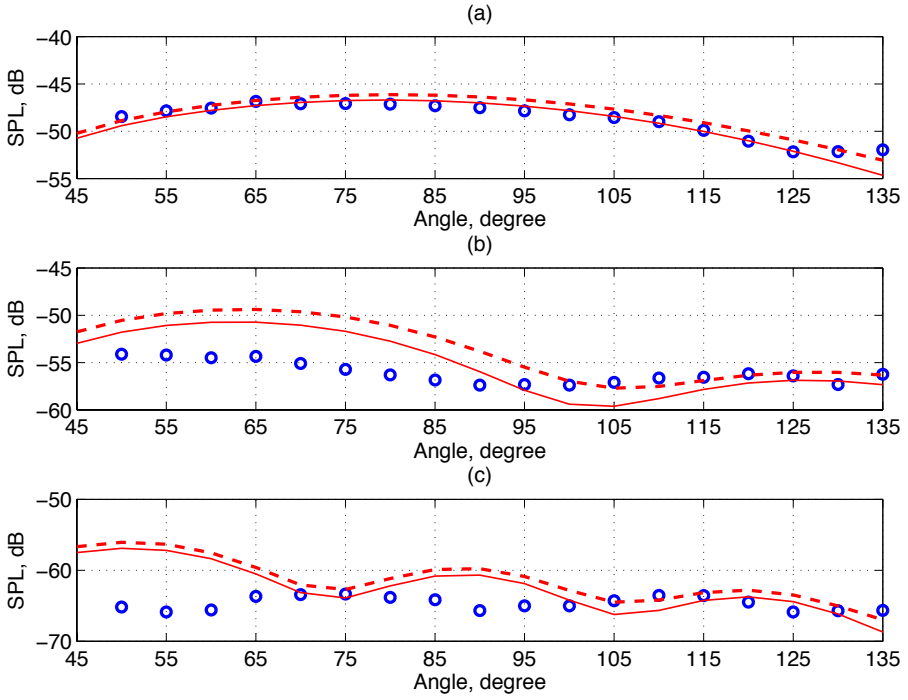

FIGURE 7.17: Directivities at Strouhal numbers $St = 2.5$ (a), $St = 5$ (b) and $St = 10$ (c). Measured (○), analytical (—) and numerical (– –) computed with von Kármán spectrum.

The acoustic power per unit length radiated between 50 and 135 degrees from the trailing edge of the airfoil is computed using Eq. (4.8). Numerical PWL computed with Gaussian spectrum provides only limited agreement with measurements, overpredicting the acoustic power by up to 8 dB from $St = 3$ to $St = 10$ and underpredicting it everywhere else. In contrast, good agreement is found between measured and predicted PWL for the von Kármán spectrum. Numerical results computed with the von Kármán spectrum capture the rate of decay of the acoustic pressure for the whole frequency range even though with a slightly different slope.

The faster rate of decay of the measured noise levels suggests that the turbulent flow should be characterised by a larger integral time scale of the turbulence (which would increase noise levels at low frequencies and decrease them at high frequencies). There are two reasons why this could actually be the case. Firstly, the mean flow velocity is chosen

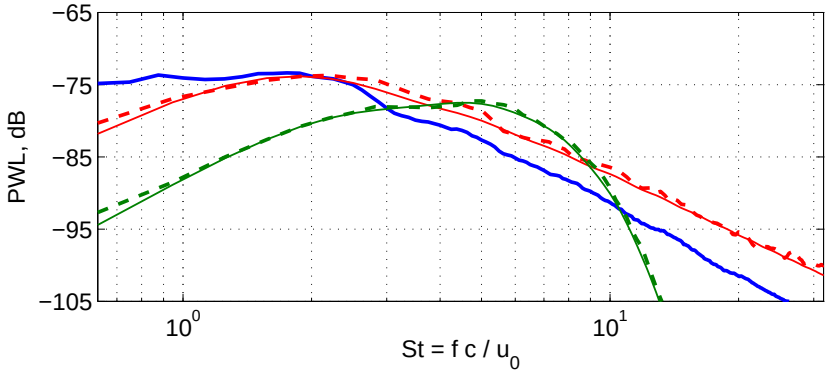

FIGURE 7.18: Acoustic power per unit of length between 50 and 135 degrees from the trailing edge. Measured PWL (—). Amiet's analytical solution (—) and numerical (– –) PWL computed with von Kármán spectrum. Amiet's analytical solution (—) and numerical (– –) PWL computed with Gaussian spectrum.

from the specification provided for the fan and not from hot-wire measurements due to calibration problems, so one might argue that the values of the integral length scale and kinetic energy estimated from hot-wire measurements could be affected by these calibration issues. Secondly, the integral length scale of the turbulence was estimated using the velocity field in the streamwise direction, however the numerical method (see Eq. (3.14)) and Amiet's analytical solution (see Eq. (3.1)) require information of the normal component of the turbulent velocity. Since in the experimental setup the grid is located in the contraction of the nozzle, vortex stretching in the streamwise direction occurs between the grid location and the nozzle exit (50 cm downstream) resulting a integral length scale which could be larger for the normal component of the turbulence than for the streamwise component.

Another possible source of error between the measurements and the numerical results is the geometry of the airfoil. While Amiet's analytical solution and numerical results assume a flat plate, experiments were conducted using a NACA651210. This change in geometry results in a different interference pattern between the noise generated at the leading and its scattering at the trailing edge. The chord of the flat plate is directly estimated from the chord of the airfoil, however due to the camber of the NACA651210 numerical results underpredict the time that it takes for an acoustic wave scattered at the trailing edge to reach the leading edge of the airfoil. In addition, Amiet and Patterson [39] argued that the thickness of the airfoil, t_A, significantly reduces noise levels for frequencies larger than the ratio u_0/t_A. For this test case, this ratio suggests that noise levels predicted with a flat plate are higher than those obtained with the NACA651210 for Strouhal numbers larger than 10.

7.4 Conclusions

In this chapter numerical results obtained with the stochastic method proposed in this thesis to predict broadband fan interaction noise have been compared against experimental data for an isolated fixed NACA651210 in a turbulent jet.

Aerodynamic measurements were used to estimate the input parameters for the numerical method. Measurements were only performed for the streamwise component of the velocity while the numerical method requires as input statistical parameters of the turbulent velocity field normal to the flat plate. This leads to some uncertainty on the parameters chosen here since the turbulence might be anisotropic.

This experimental data provides the opportunity to validate the numerical method for a different test case than that used in chapters 4, 5 and 6. For this additional test case, the statistics of the turbulence along the flat plate and the predicted noise levels in the far field are in very good agreement with the corresponding theoretical results.

This test case also shows that the von Kármán spectrum is better suited to predict broadband fan interaction noise than the Gaussian spectrum. Numerical results obtained with the Gaussian spectrum show a good agreement with measurements only within a limited frequency range. In contrast, numerical SPL obtained with the von Kármán spectrum show a relatively good agreement with measurements over the whole range of frequencies. In addition, the value of kinetic energy obtained by fitting the velocity spectrum to the theoretical von Kármán spectrum is consistent with the root-mean-square velocity of the turbulence whilst for the Gaussian spectrum the kinetic energy is used as a numerical parameter.

The approach proposed by Siefert and Ewert [15] of modelling the turbulence spectrum by superimposing a series of Gaussian spectra has also been discussed. It is feasible to approximate the measured velocity spectrum by superimposing a series of Gaussian spectra each with parameter values chosen to fit the measurements at specific frequency ranges. By doing so, it seems that each Gaussian spectrum in the series would actually provide a reasonable prediction of the acoustic field at the corresponding frequency range.

In this thesis we argue that due to the increase of computational cost associated with superimposing a series of Gaussian spectra (the number of vortex particles increases roughly proportionally to the number of Gaussian spectra), it can potentially be cheaper to use one single von Kármán spectrum. In addition, noise predictions provided by the von Kármán spectrum were more accurate with measurements than those obtained with the single Gaussian spectrum for the relevant frequency range.

It is our understanding that the disagreement found between numerical sound pressure levels predicted here with the von Kármán spectrum and measurements relates to the

lack of measurements of the normal component of the turbulence and also due to the use of a flat plate instead of a NACA651210 geometry. Due to the vortex stretching that occurs between the turbulence generating grid and the nozzle exit, the integral time scale for the normal component of the turbulence could be significantly larger than for the streamwise component. A larger integral length scale would actually improve the fitting between numerical and measured noise levels. Another factor that influences the comparison with measurements is that numerical results are obtained for a flat plate. The thickness of the NACA651210 is thought to reduce noise levels for Strouhal numbers larger than 10 and the interference pattern between acoustic waves radiated from the leading edge and those scattered at the trailing edge is modified by the camber of the airfoil.

Chapter 8

Conclusions

Areas covered in this thesis and the corresponding conclusions are summarised here. In addition, recommendations for future work are presented.

8.1 Synthetic turbulence

The stochastic method developed and validated in this thesis generates synthetic two-dimensional incompressible isotropic turbulent flows. It is based on filtering random data and stems from the works of Careta *et al.* [9] and Ewert *et al.* [10]. Once the method is discretised, the synthetic velocity field can be interpreted as the sum of contributions of random vortex particles moving with the mean flow.

The spatial statistical properties of the synthetic turbulence are controlled by a filter which can be determined either by the two-point correlation tensor or by the energy spectrum. In contrast with most filter-based methods, this work has focussed on filters specified by the energy spectrum of the turbulence. New non-Gaussian filters have been developed to model more realistic energy spectra such as Liepmann and von Kármán spectra. This is a departure from Ewert *et al.*'s work where non-Gaussian spectra are modelled using series of Gaussian filters. The influence of the energy spectra on the synthetic turbulence has been investigated in details. It has been shown that the quality of the synthetic turbulence depends on how the vortex particles are distributed. Parametric studies have been performed for each spectrum to establish guidelines for distributing the vortex particles in the computational domain. From these guidelines, it can be concluded that more particles has to be considered for the von Kármán spectrum, followed by the Liepmann spectrum and Gaussian spectrum. The increase in number of vortex particles is explained by a higher frequency content which also has an impact on the numerical sampling of the velocity field to capture the statistical properties of the turbulence. It has been shown that the simulation has to be run for longer to obtain

accurate statistics for turbulence obtained with von Kármán and Liepmann spectra than with the Gaussian spectra. The increase in vortex density and simulation time is a consequence of representing more realistic energy spectra and not of the technique used to represent the spectra. Therefore, the same features would be observed if a series of Gaussian filters were used to model realistic energy spectra.

The temporal properties of the synthetic turbulence are controlled by a stochastic field. The cases of frozen and evolving turbulence have been studied in details. In the case of frozen turbulence – where only convection effects are modelled – vortex particles are convected with the mean flow with constant strength. The resulting velocity field seen by an observer moving with the mean flow is a frozen pattern. In the case evolving turbulence the temporal decorrelation present in turbulent flows has been included by updating the strengths of the vortices as they are convected with the mean flow. Langevin equations have been proposed to update the vortex strengths in time. It has been shown that standard Langevin equations capture the statistical properties of turbulent flows but lead to non-differentiable velocity fields. The lack of differentiability has proved to be an issue when coupling the stochastic method with the linearised Euler equations to predict broadband fan noise as spurious sound sources are introduced at high frequencies. A second-order Langevin model has been proposed and validated as an alternative to the standard Langevin equation. The second-order Langevin method can be interpreted as a filtering process to smooth the synthetic velocity field in time. It has been demonstrated that it reproduces accurately the statistics of the turbulence and, in contrast to standard Langevin equations, it is suitable to couple with high-order finite difference schemes.

The stochastic method has also been extended to generate strongly inhomogeneous non-stationary turbulence. Three different implementations of the stochastic method have been proposed and validated. They differ in the location at which the turbulent kinetic energy and the integral length scale are defined. For the special case of locally homogeneous turbulent flows, all three implementations were shown to lead to the same formulation. For inhomogeneous turbulent flows found in aeroacoustic applications, it has been demonstrated that the choice of implementation has little influence on the synthetic velocity field when the kinetic energy and integral length scale of the turbulence are provided by an analytical model.

The numerical implementation of the stochastic method has been performed following a purely Lagrangian approach. This is also a departure from Ewert et al.Õs work where vorticity is interpolated onto an auxiliary grid to compute the induced velocity field. In contrast, in a purely Lagrangian approach the synthetic velocity field is computed directly at the vortex locations determined freely due to the convection effects. The computational performance of the method has also been improved by implementing interpolated filters that are much faster to compute than the exact mathematical expressions defining the filters. With the use of interpolation functions, similar computational

times are required to compute the synthetic velocity field for any of the three energy spectra considered.

Filter-based methods were initially devised to improve the computational cost of the SNGR methods which is mainly caused by the large number of Fourier modes required to compute the velocity field and the large number of realisations required to capture the statistical properties of the turbulence. In this work, similar features have been identified in the filter-based methods. One has to ensure that the number of random vortices is sufficient to properly represent the turbulent velocity field. In addition, the simulation needs to be run for a long time in order to obtain accurate statistical properties. No thorough comparison between a SNGR method and the filter-based method has been performed, but both techniques have to accumulate sufficient random data to accurately reproduce the statistical properties of the turbulence. An important advantage of the method presented here with respect to SNGR methods is that it is very flexible when dealing with strongly inhomogeneous, or non-stationary, turbulence.

8.2 Broadband fan interaction noise

In this thesis the target application of the stochastic method has been broadband fan interaction noise. This is a new application of filter-based methods which has not been tackle with RPM methods before.

The LEE solver has been validated for a flat plate interacting with frozen gusts at different frequencies. Guidelines for choosing the numerical parameters have been identified and for those the response of an airfoil to incident deterministic frozen gusts can be very accurately predicted by the numerical method. Only at high frequencies and upstream locations where noise is negligible a slight disagreement between numerical and theoretical sound pressure levels can be observed. Possible reasons for the discrepancies are the selective filter that removes poorly resolved small wavelengths and vortex shedding crossing the FWH control surface.

The stochastic method has firstly been combined with the LEE solver to predict broadband interaction noise due to frozen turbulence impinging on a flat plate. Far-field noise levels predicted with Gaussian, Liepmann and von Kármán energy spectra have been validated against Amiet's analytical solution. For each energy spectra, the predicted noise spectrum and directivities are in very good agreement with the analytical solution. As expected, the choice of energy spectra has an impact on the radiated acoustic field. Noise spectra predicted with Liepmann and von Kármán spectra peak at similar frequencies but a slightly different trend is observed. Noise levels predicted with the Gaussian spectrum peak at a higher frequency and present a much faster rate of decay compared to results obtained with von Kármán and Liepmann spectra.

The sensitivity of broadband fan noise to the temporal decorrelation of the turbulence has also been evaluated by combining the stochastic method with a second-order Langevin model. It has been demonstrated that very limited increase in noise levels compared to the case of frozen turbulence is found apart from very high frequencies at upstream locations where noise is negligible. The limited influence of modelling the time correlation can be explained by the fact that the integral time scale of the turbulence is much larger that the typical time scale of a vortex passing near the leading edge. Therefore, the strength of the vortices vary very little as they pass near the leading edge generating almost the same velocity field as if the strengths remained constant. The effects of the time decorrelation could have a larger impact on the radiated acoustic field when considering realistic airfoil geometries. Whilst for a flat plate most of the noise is radiated from a point source, for realistic airfoil geometries noise sources are distributed along the leading edge. Hence, depending on the leading edge radius vortices would have more time to evolve as they pass near the leading edge. The influence of the temporal decorrelation it is expected to be perceived only at high frequencies.

The stochastic method has also been extended to model rotor turbulent wakes impinging on a stator vane by combining the random-vortex-particle method with an existing wake model. The sensitivity of noise levels to the upstream turbulence has been investigated by considering trains of wakes with different width and separation and assuming that background and wake turbulence have the same integral length scale. Noise levels were found to increase proportionally to the mean-square velocity of the turbulence for configurations with different intensity ratio between background and wake turbulence and for configurations with different periods between wakes. Changes of the wake width showed a stronger impact on the predicted noise spectrum. The larger the integral length scale associated with wider wakes leads to a shift of the noise spectrum towards lower frequencies.

Finally, numerical results have been compared against existing experimental results for an airfoil in a turbulent jet. This comparison demonstrates that the von Kármán spectrum is better suited to predict broadband fan interaction noise than the Gaussian spectrum. Whilst noise levels predicted with the Gaussian spectrum provide a reasonable fit to measurements only within a specific frequency range, noise levels predicted with the von Kármán spectrum are in good agreement with measurements over the whole range of frequencies of interest. Siefert and Ewert's approach of using a series of Gaussian filters to model non-Gaussian spectra has been discussed, but it is the author's opinion that the computational cost would increase to levels similar to those of the von Kármán filter and no improvement in accuracy would be obtained. The differences observed between measurements and predictions obtained with the von Kármán spectrum are thought to be caused by airfoil geometry effects and also anisotropy effects leading to a larger integral length scale of the normal component of the turbulence.

8.3 Future work

The stochastic method developed in this thesis has been validated as an accurate and computationally efficient tool to predict broadband fan interaction noise. However, there are areas where further work could significantly benefit the predictions of the method for broadband fan noise:

- More realistic geometries. This work has focussed on the development and validation of the method for turbulent flows interacting with flat plates. Considering more realistic airfoil geometries would provide more reliable noise predictions, especially at high frequencies where the effects of airfoil thickness and leading edge shape are relevant. In this case, the mean flow is non-uniform and hence it has to be specified in the computational domain for instance by performing RANS simulations. Note that when working with non-uniform mean flows more care is required to track the location of the vortex particles at each time.

- Three-dimensional simulations. Fully three-dimensional simulations would allow to consider realistic airfoil geometries and complex non-uniform flows with strong variations along the span of the airfoil. For instance the numerical method could then be used to assess the sensitivity of broadband predictions to leading and trailing-edge treatments such as serrations. In addition the ful three-dimensional character of the turbulent velocity field could be represented in the simulation.

- Thorough comparison with Fourier-mode methods. At the moment Fourier-mode methods and filter-based methods to generate synthetic turbulence coexist in CAA. Some advantages and disadvantages of both techniques have been reported but no thorough comparison between Fourier-mode methods and random-vortex-particle methods has been performed so far. Such a comparison would shed light on their relative capability to capture different physical properties of the turbulence, such as time decorrelation, inhomogeneity and realistic energy spectra, and the required computational cost.

- Implementation of the stochastic method within the LEE solver. An inconsistent increase in computational time has been observed when combining the random-vortex-particle method with the LEE solver. For any of the three filters considered in this work, computing the synthetic velocity field itself requires similar computational times. However, when stochastic method is combined with the LEE solver a dramatic change in computational time can be observed depending on the filter used. This issue has been identified with the management of the cache memory. The von Kármán energy spectrum requires larger arrays to store the vortex particles, followed by the Liepmann spectrum and the Gaussian spectrum. The

computational time for the von Kármán spectrum could be reduced by using a different implementation of the numerical method where better memory management is achieved.

Appendix A

Extensions to more general turbulent flows

The random-vortex-particle method presented so far in this thesis generates the velocity field of an incompressible, two-dimensional, isotropic and evolving turbulent flow. In this appendix, the method will be progressively generalised in order to cope with anisotropic three-dimensional turbulent flows.

A.1 Three-dimensional flows

A 3D extension of the random-vortex-particle method is possible by determining a three-dimensional stream function, $\boldsymbol{\eta}$, such that [10]

$$\boldsymbol{u}'(\boldsymbol{x},t) = \nabla \times \boldsymbol{\eta}(\boldsymbol{x},t) = \varepsilon_{ijk}\frac{\partial}{\partial x_j}\eta_k \boldsymbol{e}_i, \tag{A.1}$$

where $\boldsymbol{x}$ is a three-dimensional vector, ε_{ijk} is the alternating symbol, and η_i is the i^{th} component of $\boldsymbol{\eta}$.

The three-dimensional stream function is defined by considering three independent stochastic fields, U_i, such that

$$\langle U_i(\boldsymbol{x},0)\rangle = 0, \quad \langle U_i(\boldsymbol{x}_1,t_1)U_j(\boldsymbol{x}_2,t_2)\rangle = \delta(\boldsymbol{r}-t\boldsymbol{u}_c)\exp\left(-t/\tau\right)\delta_{ij}, \tag{A.2}$$

where $\boldsymbol{r} = \boldsymbol{x}_2 - \boldsymbol{x}_1$, $t = |t_1 - t_2|$, δ stands for the Dirac function and δ_{ij} is the Kronecker symbol yielding that each component of $\boldsymbol{\eta}$ is given by

$$\eta_i(\boldsymbol{x},t) = \int_{\mathbb{R}^3} G(|\boldsymbol{x}-\boldsymbol{x'}|,t)U_i(\boldsymbol{x'},t)\mathrm{d}\boldsymbol{x'}. \tag{A.3}$$

G is the filter use to obtain the required target values of the turbulent velocity field.

Following a similar scheme to the two-dimensional case (see section 2.2), the statistics of $\boldsymbol{u}'$ and $\boldsymbol{\eta}$ are related in order to obtain the expression for the filter in terms of either the correlation or the energy spectrum of the turbulent flow.

The stationary two-point two-time correlation tensor of $\boldsymbol{\eta}$ in a Lagrangian formulation is given by (see appendix B.5)

$$C_{ij}(\boldsymbol{r},t) = \delta_{ij} R_{U_i}(t)(G * G)(r), \quad \hat{C}_{ij}(\boldsymbol{\kappa},t) = \delta_{ij} R_{U_i}(t)\hat{G}(\kappa)^2, \tag{A.4}$$

where $*$ stands for the three-dimensional convolution.

In three dimensions, assuming isotropy, a given function can be written in terms of its Fourier transform and the spherical Bessel function of zeroth order, j_0, (see appendix B.6). In particular, from $C(\boldsymbol{r}) = (G * G)(r)$ we get:

$$C(\boldsymbol{r}) = \frac{1}{2\pi^2}\int_0^\infty \hat{G}(\kappa)^2 \mathrm{j}_0(\kappa r)\mathrm{d}\kappa. \tag{A.5}$$

where $r{=}|\boldsymbol{r}|$ and $\kappa{=}|\boldsymbol{\kappa}|$.

The stationary two-point correlation tensor of the three-dimensional velocity field $\boldsymbol{u}'$, $R_{ij}(\boldsymbol{r}) = \langle u_i'(\boldsymbol{x}_1)\, u_j'(\boldsymbol{x}_2)\rangle$, can be written in terms of the lateral, $f(r)$, and longitudinal, $g(r)$, autocorrelations as

$$R_{ij}(\boldsymbol{r}) = [f(r) - g(r)]n_i n_j + g(r)\delta_{ij}, \tag{A.6}$$

where the vector components n_i stand for the unit vector in the $\boldsymbol{x}_1 - \boldsymbol{x}_2$ direction and δ_{ij} is the Kronecker symbol. Mass conservation in 3D connects the autocorrelations f and g by

$$g(r) = f(r) + \frac{r}{2}\frac{\mathrm{d}f}{\mathrm{d}r}(r), \tag{A.7}$$

yielding (see appendix B.7)

$$f(r) = -\frac{2}{r}\frac{\mathrm{d}C}{\mathrm{d}r}(r), \quad g(r) = -\frac{\mathrm{d}^2C}{\mathrm{d}r^2}(r) - \frac{1}{r}\frac{\mathrm{d}C}{\mathrm{d}r}(r). \tag{A.8}$$

Therefore, in three-dimensions the quantity $R = R_{ii}/2$ reads

$$R(r) = -\frac{\mathrm{d}^2C}{\mathrm{d}r^2}(r) - \frac{2}{r}\frac{\mathrm{d}C}{\mathrm{d}r}(r). \tag{A.9}$$

Performing the corresponding derivatives of Eq. (A.5), the expression of R can be simplified

$$R(r) = \frac{1}{6\pi^2}\int_0^\infty \kappa^2\hat{G}(\kappa)^2\left[\frac{6}{\kappa r}\mathrm{j}_1(\kappa r) + \mathrm{j}_0(\kappa r) - 2\mathrm{j}_2(\kappa r)\right]\mathrm{d}\kappa, \tag{A.10}$$

where j_0, j_1 and j_2 are the spherical Bessel functions of zero, first and second order respectively. Using the relation $\mathrm{j}_1(\kappa r) = \kappa r \left[\mathrm{j}_0(\kappa r) + \mathrm{j}_2(\kappa r)\right]/3$, we get

$$R(r) = \frac{1}{2\pi^2} \int_0^\infty \kappa^2 \hat{G}(\kappa)^2 \mathrm{j}_0(\kappa r) \mathrm{d}\kappa. \tag{A.11}$$

Hence, due to the relation between the Fourier transform and the spherical Bessel function and by comparing with Eq. (A.5)

$$\hat{R}(\kappa) = \kappa^2 \hat{G}(\kappa)^2. \tag{A.12}$$

It also follows from Eq. (A.12) that in the physical space the filter reads

$$G(r) = \frac{1}{2\pi^2} \int_0^\infty \frac{\hat{R}(\kappa)^{1/2}}{\kappa} \mathrm{j}_0(\kappa r) \mathrm{d}\kappa. \tag{A.13}$$

In three dimensions the velocity spectrum, ϕ_{ij}, given by the inverse Fourier transform of the correlation function reads

$$\phi_{ij}(\boldsymbol{\kappa}) = \int_{\mathbb{R}^3} R_{ij}(\boldsymbol{r}) \exp(-i\boldsymbol{\kappa} \cdot \boldsymbol{r}) \mathrm{d}\boldsymbol{r}, \tag{A.14}$$

Hence, by definition of R, its expression in terms of the velocity spectrum in the wavenumber space is

$$\hat{R}(\kappa) = \frac{1}{2} \phi_{ij}(\boldsymbol{\kappa}). \tag{A.15}$$

Comparing Eq. (A.12) and Eq. (A.15),

$$\phi_{ii}(\boldsymbol{\kappa}) = 2\kappa^2 \hat{G}(\kappa)^2. \tag{A.16}$$

Finally, the filter can be connected to the energy spectrum, $E(\kappa)$, through its relation with the velocity spectrum. In a three-dimensional turbulent flow the velocity spectrum and the energy spectrum are connected by

$$E(\kappa) = \frac{1}{8\pi^3} \oint \frac{1}{2} \phi_{ii}(\boldsymbol{\kappa}) \mathrm{d}S(\kappa), \tag{A.17}$$

where $S(\kappa)$ denotes the sphere in the wavenumber space of radius κ centred at the origin. Hence,

$$E(\kappa) = \frac{1}{4\pi^2} \kappa^2 \phi_{ii}(\boldsymbol{\kappa}). \tag{A.18}$$

Inserting Eq. (A.16) into Eq. (A.18), the relation between the filter kernel and the energy spectrum in the wavenumber space is given by

$$E(\kappa) = \frac{1}{2\pi^2} \kappa^4 \hat{G}(\kappa)^2, \tag{A.19}$$

which yields in the physical space

$$G(r) = \frac{1}{\sqrt{2}\pi} \int_0^\infty \frac{E(\kappa)^{1/2}}{\kappa^2} \mathrm{j}_0(\kappa r) \mathrm{d}\kappa. \tag{A.20}$$

Summarising, in this section it has been shown how to generate a synthetic three-dimensional incompressible evolving turbulent flow under the constrains of homogeneity and isotropy. The equations that determine the synthetic velocity field of such flow are given by

$$\boldsymbol{u}'(\boldsymbol{x}, t) = \nabla \times \boldsymbol{\eta}(\boldsymbol{x}, t), \tag{A.21}$$

where

$$\eta_i(\boldsymbol{x}, t) = \int_{\mathbb{R}^3} G(|\boldsymbol{x} - \boldsymbol{x'}|) U_i(\boldsymbol{x'}, t) \mathrm{d}\boldsymbol{x'}, \tag{A.22}$$

U_1, U_2, and U_3 are three independent stochastic fields verifying Eq. (A.2), and G is recovered either from Eq. (A.13) or Eq. (A.20).

A.2 Anisotropic turbulence

The remaining constrain in random-vortex-particle method is isotropy. This restriction can be eliminated by transforming the generated velocity field into a field that matches the correlation of the desired anisotropic turbulent flow.

By solving the Reynolds-averaged Navier Stokes equations, for instance using a K-ϵ model, it is possible to applied a Reynolds stress model and hence recover the local Reynolds stress of the anisotropic turbulent flow. The set of transformations proposed by Lund *et al.* [31] or Smirnov *et al.* [32] can then be applied to the velocity field generated with the random-vortex-particle method, see section 2.1.3. The output is a turbulent anisotropic velocity field whose length and time scales and correlation functions correspond to those of the original flow.

Appendix B

Detailed derivation of equations

The derivation of some equations presented along this thesis that might require further explanation is presented in this appendix.

B.1 Derivation of Eq. (2.39)

The stationary two-point correlation of $\boldsymbol{u}'$ is $R_{ij}(\boldsymbol{r}) = \langle u_i'(\boldsymbol{x})\ u_j'(\boldsymbol{x}+\boldsymbol{r})\rangle$.

Inserting the definition of $\boldsymbol{u}'$,

$$R_{ij}(\boldsymbol{r}) = \langle (-1)^j \frac{\partial}{\partial x_j}\eta(\boldsymbol{x})\ (-1)^i \frac{\partial}{\partial x_i}\eta(\boldsymbol{x}+\boldsymbol{r})\rangle, \tag{B.1}$$

and applaying properties of the correlation function

$$R_{ij}(\boldsymbol{r}) = (-1)^{i+j}\langle \frac{\partial}{\partial x_j}\eta(\boldsymbol{x})\ \frac{\partial}{\partial x_i}\eta(\boldsymbol{x}+\boldsymbol{r})\rangle, \tag{B.2}$$

and properties of partial derivatives

$$R_{ij}(\boldsymbol{r}) = (-1)^{i+j}\langle \frac{\partial}{\partial x_j}\eta(\boldsymbol{x})\ \frac{\partial}{\partial r_i}\eta(\boldsymbol{x}+\boldsymbol{r})\rangle, \tag{B.3}$$

yields

$$R_{ij}(\boldsymbol{r}) = (-1)^{i+j}\frac{\partial}{\partial r_i}\langle \frac{\partial}{\partial x_j}\eta(\boldsymbol{x})\ \eta(\boldsymbol{x}+\boldsymbol{r})\rangle. \tag{B.4}$$

Since locally homogeneous flows are been considered, by hypothesis

$$\frac{\partial}{\partial x_j}\langle \eta(\boldsymbol{x})\ \eta(\boldsymbol{x}+\boldsymbol{r})\rangle = 0. \tag{B.5}$$

Hence, Eq. (B.4) is equivalent to

$$R_{ij}(\boldsymbol{r}) = (-1)^{i+j+1}\frac{\partial}{\partial r_i}\langle \eta(\boldsymbol{x})\ \frac{\partial}{\partial x_j}\eta(\boldsymbol{x}+\boldsymbol{r})\rangle. \tag{B.6}$$

By the same reasoning as in Eq. (B.3) and Eq. (B.4),

$$R_{ij}(\boldsymbol{r}) = (-1)^{i+j+1}\frac{\partial^2}{\partial r_i \partial r_j}\langle \eta(\boldsymbol{x})\ \eta(\boldsymbol{x}+\boldsymbol{r})\rangle, \tag{B.7}$$

Using that the correlation tensor of the stream function η is given by $C(\boldsymbol{r})$,

$$R_{ij}(\boldsymbol{r}) = (-1)^{i+j+1}\frac{\partial^2}{\partial r_i \partial r_j}C(\boldsymbol{r}). \tag{B.8}$$

Performing the second partial derivative of C with respect to r_i and r_j,

$$\frac{\partial^2}{\partial r_i \partial r_j}C(\boldsymbol{r}) = \delta_{ij}\frac{1}{r}\frac{\mathrm{d}}{\mathrm{d}r}C(\boldsymbol{r}) - \frac{r_i r_j}{r^3}\frac{\mathrm{d}}{\mathrm{d}r}C(\boldsymbol{r}) + \frac{r_i r_j}{r^2}\frac{\mathrm{d}^2}{\mathrm{d}r^2}C(\boldsymbol{r}). \tag{B.9}$$

Straightforward algebra shows that half the trace of the correlation tensor R_{ij} is given by

$$R(\boldsymbol{r}) = \frac{1}{2}\left[R_{11}(\boldsymbol{r}) + R_{22}(\boldsymbol{r})\right] = -\frac{1}{2}\left[\frac{1}{r}\frac{\mathrm{d}C}{\mathrm{d}r}(\boldsymbol{r}) + \frac{\mathrm{d}^2 C}{\mathrm{d}r^2}(\boldsymbol{r})\right]. \tag{B.10}$$

B.2 Derivation of Eq. (2.40)

By Fourier transform theory, $C(\boldsymbol{r})$ can by defined as

$$C(\boldsymbol{r}) = \frac{1}{4\pi^2}\int_{\mathbb{R}^2}\hat{C}(\boldsymbol{\kappa})\exp(i\boldsymbol{\kappa}\cdot\boldsymbol{r})\mathrm{d}\boldsymbol{\kappa}, \tag{B.11}$$

where $\boldsymbol{\kappa}$ stands for the wavenumber vector and $\hat{C}$ denotes the Fourier transformation of C.

Expressing $\boldsymbol{r}$ and $\boldsymbol{\kappa}$ in polar coordinates as

$$\boldsymbol{r} \equiv (r_x, r_y) = (r\cos\alpha, r\sin\alpha) \tag{B.12}$$

$$\boldsymbol{\kappa} \equiv (\kappa_x, \kappa_y) = (\kappa\cos\theta, \kappa\sin\theta), \tag{B.13}$$

where $\kappa{=}|\boldsymbol{\kappa}|$, $r{=}|\boldsymbol{r}|$ and $\alpha, \theta \in [0, 2\pi)$, Eq. (B.11) is found to be

$$C(r) = \frac{1}{4\pi^2}\int_0^\infty \kappa\hat{C}(\boldsymbol{\kappa})\left[\int_0^{2\pi}\exp(i\kappa r\cos(\theta-\alpha))\mathrm{d}\theta\right]\mathrm{d}\kappa. \tag{B.14}$$

Using the definition of the Bessel function of zeroth order given by

$$\mathrm{J}_0(x) = \frac{1}{2\pi}\int_0^{2\pi} \exp(ix\cos(\theta))\mathrm{d}\theta \tag{B.15}$$

and that in isotropic turbulence α can be chosen equal to zero, we finally recover the desired expression of $C(r)$

$$C(r) = \frac{1}{2\pi}\int_0^{\infty} \kappa\hat{C}(\boldsymbol{\kappa})\mathrm{J}_0(\kappa r)\mathrm{d}\kappa. \tag{B.16}$$

B.3 Derivation of Eq. (2.47)

By definition of the two-point correlation tensor, $R_{ij}(\boldsymbol{r})$, of the velocity field $\boldsymbol{u}'$ expressed in terms of the stream function η we get

$$R_{22}(r\boldsymbol{e}_1) = \langle\frac{\partial\eta}{\partial x}(x,y)\ \frac{\partial\eta}{\partial x}(x+r,y)\rangle, \tag{B.17}$$

where $\boldsymbol{e}_1$ stands for the unit vector in the x-direction.

Taking into account that $R_{22}(r\boldsymbol{e}_1) = g(r)$,

$$g(r) = \langle\frac{\partial\eta}{\partial x}(x,y)\ \frac{\partial\eta}{\partial x}(x+r,y)\rangle, \tag{B.18}$$

and noticing that $[\frac{\partial\eta}{\partial x}(x+r,y) = \frac{\partial\eta}{\partial r}(x+r,y)]$,

$$g(r) = \frac{\partial}{\partial r}\langle\frac{\partial\eta}{\partial x}(x,y)\ \eta(x+r,y)\rangle. \tag{B.19}$$

Since the statistics are homogeneous $\left[\frac{\partial}{\partial x}\langle\eta(x,y)\ \eta(x+r,y)\rangle = 0\right]$,

$$\langle\frac{\partial\eta}{\partial x}(x,y)\ \eta(x+r,y)\rangle = -\langle\eta(x,y)\ \frac{\partial\eta}{\partial x}(x+r,y)\rangle. \tag{B.20}$$

Inserting Eq. (B.20) into Eq. (B.19)

$$g(r) = -\frac{\partial}{\partial r}\langle\eta(x,y)\ \frac{\partial\eta}{\partial x}(x+r,y)\rangle. \tag{B.21}$$

Proceeding as in Eq. (B.19)

$$g(r) = -\frac{\partial^2}{\partial r^2}C(r). \tag{B.22}$$

B.4 Derivation of Eq. (2.57)

The stationary two-point two-time correlation of η is

$$C(\boldsymbol{r},t) = \langle \eta(\boldsymbol{r}_1,t_1)\ \eta(\boldsymbol{r}_2,t_2)\rangle, \tag{B.23}$$

where $\boldsymbol{r} = \boldsymbol{r}_2 - \boldsymbol{r}_1$ and $t = |t_1 - t_2|$. Taking into account the definition of η

$$C(\boldsymbol{r},t) = \langle \int_{\mathbb{R}^2} G(|\boldsymbol{r}_1 - \boldsymbol{r}'|)U(\boldsymbol{r}',t_1)\mathrm{d}\boldsymbol{r}' \int_{\mathbb{R}^2} G(|\boldsymbol{r}_2 - \boldsymbol{s}'|)U(\boldsymbol{s}',t_2)\mathrm{d}\boldsymbol{s}'\rangle, \tag{B.24}$$

straightforward algebra shows that

$$C(\boldsymbol{r},t) = \int_{\mathbb{R}^2}\int_{\mathbb{R}^2} G(|\boldsymbol{r}_1 - \boldsymbol{r}'|)G(|\boldsymbol{r}_2 - \boldsymbol{s}'|)\langle U(\boldsymbol{r}',t_1)\ U(\boldsymbol{s}',t_2)\rangle \mathrm{d}\boldsymbol{r}'\mathrm{d}\boldsymbol{s}'. \tag{B.25}$$

Using the properties of the stochastic field U (see Eq. (2.55))

$$\langle U(\boldsymbol{r}',t_1)\ U(\boldsymbol{s}',t_2)\rangle = \delta(\boldsymbol{s}' - \boldsymbol{r}' - t\boldsymbol{u}_c)R_U(t), \tag{B.26}$$

where δ denotes a 2D Dirac function, which reads $\delta(\boldsymbol{r}) = \delta(\boldsymbol{r}_x)\delta(\boldsymbol{r}_y)$, Eq. (B.25) takes the form

$$C(\boldsymbol{r},t) = \exp(-t/\tau)\int_{\mathbb{R}^2} G(|\boldsymbol{r}_1 - \boldsymbol{r}'|)G(|\boldsymbol{r}_2 - \boldsymbol{r}' - t\boldsymbol{u}_c|)\mathrm{d}\boldsymbol{r}'. \tag{B.27}$$

Using that $\boldsymbol{r}_2 = \boldsymbol{r}_1 + \boldsymbol{r}$

$$C(\boldsymbol{r},t) = \exp(-t/\tau)\int_{\mathbb{R}^2} G(|\boldsymbol{r}_1 - \boldsymbol{r}'|)G(|\boldsymbol{r}_1 + \boldsymbol{r} - \boldsymbol{r}' - t\boldsymbol{u}_c|)\mathrm{d}\boldsymbol{r}'. \tag{B.28}$$

Applying the change of variable $\boldsymbol{\zeta} = \boldsymbol{r}' - \boldsymbol{r}_1$

$$C(\boldsymbol{r},t) = \exp(-t/\tau)\int_{\mathbb{R}^2} G(|-\boldsymbol{\zeta}|)G(|\boldsymbol{r} - t\boldsymbol{u}_c - \boldsymbol{\zeta}|)\mathrm{d}\boldsymbol{\zeta}. \tag{B.29}$$

Therefore, the right hand side of Eq. (B.29) is the self convolution of G,

$$C(\boldsymbol{r},t) = (G * G)(|\boldsymbol{r} - t\boldsymbol{u}_c|)R_U(t). \tag{B.30}$$

Note that the assumption $\boldsymbol{r} = \boldsymbol{r}_2 - \boldsymbol{r}_1$ instead of $\boldsymbol{r} = \boldsymbol{r}_1 - \boldsymbol{r}_2$ does not change the final result since $C(\boldsymbol{r},t) = C(-\boldsymbol{r},t)$.

B.5 Derivation of Eq. (A.4)

The stationary two-point two-time correlation of $\boldsymbol{\eta}$ is given by

$$C_{ij}(\boldsymbol{r},t) = \langle \eta_i(\boldsymbol{r}_1,t_1)\ \eta_j(\boldsymbol{r}_2,t_2)\rangle, \tag{B.31}$$

where $\boldsymbol{r} = \boldsymbol{r}_2 - \boldsymbol{r}_1$ and $t = |t_1 - t_2|$. Taking into account the definition of $\boldsymbol{\eta}$

$$C_{ij}(\boldsymbol{r},t) = \langle \int_{\mathbb{R}^3} G(|\boldsymbol{r}_1 - \boldsymbol{r}'|)U_i(\boldsymbol{r}',t_1)\mathrm{d}\boldsymbol{r}' \int_{\mathbb{R}^3} G(|\boldsymbol{r}_2 - \boldsymbol{s}'|)U_j(\boldsymbol{s}',t_2)\mathrm{d}\boldsymbol{s}'\rangle, \tag{B.32}$$

straightforward algebra shows that

$$C_{ij}(\boldsymbol{r},t) = \int_{\mathbb{R}^3}\int_{\mathbb{R}^3} G(|\boldsymbol{r}_1 - \boldsymbol{r}'|)G(|\boldsymbol{r}_2 - \boldsymbol{s}'|)\langle U_i(\boldsymbol{r}',t_1)\ U_j(\boldsymbol{s}',t_2)\rangle \mathrm{d}\boldsymbol{r}'\mathrm{d}\boldsymbol{s}'. \tag{B.33}$$

U_1, U_2, and U_3 are defined to be three random fields such that

$$\langle U_i(\boldsymbol{r},0)\rangle = 0, \quad \langle U_i(\boldsymbol{r}_1,t_1)U_j(\boldsymbol{r}_2,t_2)\rangle = \delta(\boldsymbol{r} - t\boldsymbol{u}_c)R_{U_i}(t)\delta_{ij}, \tag{B.34}$$

where δ denotes a 3D Dirac function, which reads $\delta(\boldsymbol{r}) = \delta(\boldsymbol{r}_x)\delta(\boldsymbol{r}_y)\delta(\boldsymbol{r}_z)$ and δ_{ij} is the Kronecker symbol. Hence, Eq. (B.33) takes the form

$$C_{ij}(\boldsymbol{r},t) = \delta_{ij}R_{U_i}(t)\int_{\mathbb{R}^3} G(|\boldsymbol{r}_1 - \boldsymbol{r}'|)G(|\boldsymbol{r}_2 - \boldsymbol{r}' - t\boldsymbol{u}_c|)\mathrm{d}\boldsymbol{r}'. \tag{B.35}$$

Using that $\boldsymbol{r}_2 = \boldsymbol{r}_1 + \boldsymbol{r}$

$$C_{ij}(\boldsymbol{r},t) = \delta_{ij}R_{U_i}(t)\int_{\mathbb{R}^3} G(|\boldsymbol{r}_1 - \boldsymbol{r}'|)G(|\boldsymbol{r}_1 + \boldsymbol{r} - \boldsymbol{r}' - t\boldsymbol{u}_c|)\mathrm{d}\boldsymbol{r}'. \tag{B.36}$$

Applying the change of variable $\boldsymbol{\zeta} = \boldsymbol{r}' - \boldsymbol{r}_1$

$$C_{ij}(\boldsymbol{r},t) = \delta_{ij}R_{U_i}(t)\int_{\mathbb{R}^3} G(|-\boldsymbol{\zeta}|)G(|\boldsymbol{r} - t\boldsymbol{u}_c - \boldsymbol{\zeta}|)\mathrm{d}\boldsymbol{\zeta}. \tag{B.37}$$

The right hand side of Eq. (B.37) is the self convolution of the filter G,

$$C_{ij}(\boldsymbol{r},t) = \delta_{ij}R_{U_i}(t)(G * G)(|\boldsymbol{r} - t\boldsymbol{u}_c|). \tag{B.38}$$

Summarising, it has been shown that the stationary correlation of $\boldsymbol{\eta}$ is

$$C_{ij}(\boldsymbol{r},t) = \delta_{ij}R_{U_i}(t)(G * G)(|\boldsymbol{r} - t\boldsymbol{u}_c|). \tag{B.39}$$

Note that the assumption $\boldsymbol{r} = \boldsymbol{r}_2 - \boldsymbol{r}_1$ instead of $\boldsymbol{r} = \boldsymbol{r}_1 - \boldsymbol{r}_2$ does not change the final result since $C_{ij}(\boldsymbol{r}) = C_{ij}(-\boldsymbol{r})$.

B.6 Derivation of Eq. (A.5)

By Fourier transform theory, $C(\boldsymbol{r})$ can by defined as

$$C(\boldsymbol{r}) = \frac{1}{8\pi^3} \int_{\mathbb{R}^3} \hat{C}(\boldsymbol{\kappa}) \exp(i\boldsymbol{\kappa} \cdot \boldsymbol{r}) \mathrm{d}\boldsymbol{\kappa}, \tag{B.40}$$

where $\boldsymbol{\kappa}$ stands for the three-dimensional wavenumber vector and $\hat{C}$ denotes the Fourier transformation of C in three dimensions.

Expressing $\boldsymbol{r}$ and $\boldsymbol{\kappa}$ in spherical coordinates as

$$\boldsymbol{r} \equiv (r_x, r_y, r_z) = (r\cos\varphi\cos\theta, r\cos\varphi\sin\theta, r\sin\varphi), \tag{B.41}$$

$$\boldsymbol{\kappa} \equiv (\kappa_x, \kappa_y, \kappa_z) = (\kappa\cos\alpha\cos\beta, \kappa\cos\alpha\sin\beta, \kappa\sin\alpha), \tag{B.42}$$

where κ=$|\boldsymbol{\kappa}|$, r=$|\boldsymbol{r}|$, φ,$\alpha \in [-\frac{\pi}{2}, \frac{\pi}{2})$, and θ,$\beta \in [0, 2\pi)$, we get:

$$\boldsymbol{\kappa} \cdot \boldsymbol{r} = \kappa r[\cos\varphi\cos\alpha\cos(\beta - \theta) + \sin\varphi\sin\alpha]. \tag{B.43}$$

In isotropic turbulence the directional information depends only on the distance, so we can choose $\varphi = 0$ and $\theta = 0$ yielding

$$\boldsymbol{\kappa} \cdot \boldsymbol{r} = \kappa r\cos\alpha\cos\beta. \tag{B.44}$$

Inserting Eq. (B.44) into Eq. (B.40) and performing the change of variables given by Eqs. (B.41) and (B.42)

$$C(r) = \frac{1}{8\pi^3} \int_0^\infty \hat{C}(\boldsymbol{\kappa}) \int_{-\frac{\pi}{2}}^{\frac{\pi}{2}} \kappa\cos\alpha \int_0^{2\pi} \exp(i\kappa r\cos\alpha\cos\beta)\mathrm{d}\beta\mathrm{d}\alpha\mathrm{d}\kappa. \tag{B.45}$$

Using the definition of the Bessel function of zeroth order given by

$$\mathrm{J}_0(x) = \frac{1}{2\pi} \int_0^{2\pi} \exp(ix\cos\theta)\mathrm{d}\theta, \tag{B.46}$$

$$C(r) = \frac{1}{4\pi^2} \int_0^\infty \hat{C}(\boldsymbol{\kappa}) \int_{-\frac{\pi}{2}}^{\frac{\pi}{2}} \kappa\cos\alpha\mathrm{J}_0(\kappa r\cos\alpha)\mathrm{d}\alpha\mathrm{d}\kappa. \tag{B.47}$$

The integral with respect to α in the above equation

$$\int_{-\frac{\pi}{2}}^{\frac{\pi}{2}} \kappa\cos\alpha\mathrm{J}_0(\kappa r\cos\alpha)\mathrm{d}\alpha = 2\frac{\sin(\kappa r)}{\kappa r}, \tag{B.48}$$

is exactly twice the spherical Bessel function of zeroth order, j_0, evaluated at κr. Hence,

$$C(r) = \frac{1}{2\pi^2}\int_0^\infty \hat{C}(\boldsymbol{\kappa})\mathrm{j}_0(\kappa r)\mathrm{d}\kappa. \tag{B.49}$$

B.7 Derivation of Eq. (A.8)

The stationary two-point correlation of $\boldsymbol{u}'$ is

$$R_{ij}(\boldsymbol{r}) = \langle u_i'(\boldsymbol{x})\ u_j'(\boldsymbol{x}+\boldsymbol{r})\rangle. \tag{B.50}$$

Inserting the definition of $\boldsymbol{u}'$,

$$R_{ij}(\boldsymbol{r}) = \langle \varepsilon_{imn}\frac{\partial}{\partial x_m}\eta_n(\boldsymbol{x})\ \varepsilon_{jpq}\frac{\partial}{\partial x_p}\eta_q(\boldsymbol{x}+\boldsymbol{r})\rangle, \tag{B.51}$$

where ε_{ijk} stands for the alternating symbol

$$\varepsilon_{ijk} = \begin{cases} 1, & \text{if } (i,j,k) \text{ are cyclic ;} \\ -1, & \text{if } (i,j,k) \text{ are anticyclic ;} \\ 0, & \text{otherwise.} \end{cases} \tag{B.52}$$

By properties of the correlation function

$$R_{ij}(\boldsymbol{r}) = \varepsilon_{imn}\varepsilon_{jpq}\langle\frac{\partial}{\partial x_m}\eta_n(\boldsymbol{x})\ \frac{\partial}{\partial x_p}\eta_q(\boldsymbol{x}+\boldsymbol{r})\rangle. \tag{B.53}$$

By properties of partial derivatives

$$R_{ij}(\boldsymbol{r}) = \varepsilon_{imn}\varepsilon_{jpq}\langle\frac{\partial}{\partial x_m}\eta_n(\boldsymbol{x})\ \frac{\partial}{\partial r_p}\eta_q(\boldsymbol{x}+\boldsymbol{r})\rangle, \tag{B.54}$$

which yields

$$R_{ij}(\boldsymbol{r}) = \varepsilon_{imn}\varepsilon_{jpq}\frac{\partial}{\partial r_p}\langle\frac{\partial}{\partial x_m}\eta_n(\boldsymbol{x})\ \eta_q(\boldsymbol{x}+\boldsymbol{r})\rangle. \tag{B.55}$$

Since isotropic flows are been considered, by hypothesis

$$\frac{\partial}{\partial x_m}\langle\eta_n(\boldsymbol{x})\ \eta_q(\boldsymbol{x}+\boldsymbol{r})\rangle = 0. \tag{B.56}$$

Hence, Eq. (B.55) is equivalent to

$$R_{ij}(\boldsymbol{r}) = -\varepsilon_{imn}\varepsilon_{jpq}\frac{\partial}{\partial r_p}\langle\eta_n(\boldsymbol{x})\ \frac{\partial}{\partial x_m}\eta_q(\boldsymbol{x}+\boldsymbol{r})\rangle. \tag{B.57}$$

By the same reasoning as in Eq. (B.54) and Eq. (B.55),

$$R_{ij}(\boldsymbol{r}) = -\varepsilon_{imn}\varepsilon_{jpq}\frac{\partial^2}{\partial r_m \partial r_p}\langle \eta_n(\boldsymbol{x})\ \eta_q(\boldsymbol{x}+\boldsymbol{r})\rangle, \tag{B.58}$$

Using that the two-point correlation tensor of the stream function $\boldsymbol{\eta}$ is given by $C_{ij}(\boldsymbol{r}) = (G * G)(|\boldsymbol{r}|)\delta_{ij}$,

$$R_{ij}(\boldsymbol{r}) = -\varepsilon_{imn}\varepsilon_{jpq}\delta_{nq}\frac{\partial^2}{\partial r_m \partial r_p}C(\boldsymbol{r}), \tag{B.59}$$

where $C(\boldsymbol{r}) = (G * G)(|\boldsymbol{r}|)$.

Performing the second partial derivative of C with respect to r_m and r_p,

$$\frac{\partial^2}{\partial r_m \partial r_p}C(\boldsymbol{r}) = \delta_{pm}\frac{1}{r}\frac{\mathrm{d}}{\mathrm{d}r}C - \frac{r_m r_p}{r^3}\frac{\mathrm{d}}{\mathrm{d}r}C + \frac{r_m r_p}{r^2}\frac{\mathrm{d}^2}{\mathrm{d}r^2}C, \tag{B.60}$$

Eq. (B.59) can be rewritten as

$$R_{ij}(\boldsymbol{r}) = -\varepsilon_{imn}\varepsilon_{jpq}\delta_{nq}\delta_{pm}\frac{1}{r}\frac{\mathrm{d}}{\mathrm{d}r}C - \varepsilon_{imn}\varepsilon_{jpq}\delta_{nq}\left(\frac{\mathrm{d}^2}{\mathrm{d}r^2}C - \frac{1}{r}\frac{\mathrm{d}}{\mathrm{d}r}C\right)\frac{r_m r_p}{r^2}. \tag{B.61}$$

It can be proved that

$$\varepsilon_{imn}\varepsilon_{jpq}\delta_{nq}\delta_{mp} = 2\delta_{ij}, \tag{B.62}$$

$$\varepsilon_{imn}\varepsilon_{jpq}\delta_{nq} = \delta_{mp}\delta_{ij} - \delta_{ip}\delta_{jm}. \tag{B.63}$$

Hence,

$$R_{ij}(\boldsymbol{r}) = -2\frac{1}{r}\frac{\mathrm{d}}{\mathrm{d}r}C\delta_{ij} - \left(\frac{\mathrm{d}^2}{\mathrm{d}r^2}C - \frac{1}{r}\frac{\mathrm{d}}{\mathrm{d}r}C\right)\frac{r_m r_p}{r^2}\delta_{mp}\delta_{ij} + \left(\frac{\mathrm{d}^2}{\mathrm{d}r^2}C - \frac{1}{r}\frac{\mathrm{d}}{\mathrm{d}r}C\right)\frac{r_m r_p}{r^2}\delta_{ip}\delta_{jm}. \tag{B.64}$$

Straightforward algebra shows

$$R_{ij}(\boldsymbol{r}) = \left(\frac{\mathrm{d}^2}{\mathrm{d}r^2}C - \frac{1}{r}\frac{\mathrm{d}}{\mathrm{d}r}C\right)\frac{r_i r_j}{r^2} + \left(-\frac{\mathrm{d}^2}{\mathrm{d}r^2}C - \frac{1}{r}\frac{\mathrm{d}}{\mathrm{d}r}C\right)\delta_{ij}. \tag{B.65}$$

Finally, comparing Eq. (B.65) with the expression of the correlation function in terms of the radial correlations,

$$R_{ij}(\boldsymbol{r}) = [f(r) - g(r)]n_i n_j + g(r)\delta_{ij}, \tag{B.66}$$

it is deduced that

$$f(r) = -\frac{2}{r}\frac{\mathrm{d}}{\mathrm{d}r}C, \quad g(r) = -\frac{\mathrm{d}^2}{\mathrm{d}r^2}C - \frac{1}{r}\frac{\mathrm{d}}{\mathrm{d}r}C. \tag{B.67}$$

It is immediate to show that expressions in Eq. (B.67) verify

$$g(r) = f(r) + \frac{r}{2}\frac{\mathrm{d}f}{\mathrm{d}r}(r). \tag{B.68}$$

Appendix C

Amiet's analytical solution

A modified version of the analytical solution obtained by Amiet [17] is derived in order to validate the numerical results. Amiet's analytical solution provides the pressure jump along the airfoil and the far-field sound generated by the interaction of isotropic, homogeneous, frozen turbulence with a flat plate. It is first modified to account for a fully two-dimensional acoustic field. Then, the analytical solution is extended to include the effects of periodic Gaussian wakes.

C.1 Homogeneous frozen turbulence

Amiet derived a theoretical solution for the sound radiated by a $2b \times 2d$ flat plate in the xy-plane in an isotropic homogeneous subsonic flow. A similar analysis to that in [17] is followed here to obtain the expression for the PSD of pressure but assuming that the turbulent velocity field on the plate is function of its x position only.

The turbulent component of the velocity field normal to the airfoil (upwash velocity) due to a gust excited at the frequency corresponding to the chordwise hydrodynamic wavenumber $\kappa_x = \omega/u_0$ is

$$v(x,t) = \hat{v}(\kappa_x)\exp[i\kappa_x(x-u_0t)], \quad \hat{v}(\kappa_x) = \frac{1}{2\pi}v(x)\exp(-i\kappa_x x), \tag{C.1}$$

where $\hat{v}$ is the Fourier transform[1]of v defined in a frame of reference moving with the mean flow.

[1] The definition of the Fourier transform given here is chosen following Amiet's formulation but differs from the definition used everywhere else in this thesis. Therefore, the corresponding 2π factor must be taking into account when comparing analytical and numerical results.

The pressure jump along the airfoil for a single wave component is given by

$$\Delta P(x,t) = 2\pi\rho_0 u_0 \hat{v}(\kappa_x)\mathsf{g}(x,\kappa_x)\exp(-i\kappa_x u_0 t) \tag{C.2}$$

$$\Delta \hat{P}(x,\omega) = 2\pi\rho_0 \hat{v}(\kappa_x)\mathsf{g}(x,\kappa_x), \tag{C.3}$$

where $\mathsf{g}(x,\kappa_x)$ is the response function along the airfoil.

At high frequencies the response function can be computed iteratively to correct for boundary conditions at the leading and trailing edges [43]. Amiet used the first two iterations to define the response function as the sum of two expressions; one accounting for the scattering of turbulence at the leading edge and another term for corrections due to the presence of the trailing edge [42]. The trailing edge response function used here include the effects of vortex shedding by the addition of an exponential factor of the form $\exp(\epsilon\kappa_x x)$ (see Ref. [54]). Hence, the response function g in Eq. (C.2) is obtained as the sum of the response functions corresponding to the leading edge and trailing edge

$$\mathsf{g}_1(x,\kappa_x) = \frac{\exp\left[-i\left(\mu(1-M)(1+x) - \kappa_x + \pi/4\right)\right]}{\pi\sqrt{\pi(1-M)(1+x)\kappa_x}}, \tag{C.4}$$

$$\mathsf{g}_2(x,\kappa_x) = \exp(\epsilon\kappa_x x)\left\{-1 + (1+i)E^*[-x(\kappa_x + \mu(1+M))]\right\}, \tag{C.5}$$

respectively. Here E^* is defined as

$$E^*(s) = \int_0^s \frac{\exp(-is')}{(2\pi s')^{1/2}}\mathrm{d}s',$$

and ϵ is a parameter that can be fixed by agreement with measurements. In this case we use $\epsilon = 0.75$.

A turbulent flow can be considered as the sum of the contributions from a range of gusts, each with a different frequency. Therefore, the complete turbulent velocity field along the airfoil is of the form

$$v(x,t) = \int_{\mathbb{R}} \hat{v}(\kappa_x)\exp[i\kappa_x(x-u_0 t)]\mathrm{d}\kappa_x, \quad \hat{v}(\kappa_x) = \frac{1}{2\pi}\int_{\mathbb{R}} v(x)\exp(-i\kappa_x x)\mathrm{d}x, \tag{C.6}$$

and the complete pressure jump is given by

$$\Delta P(x,t) = 2\pi\rho_0 u_0 \int_{\mathbb{R}} \hat{v}(\kappa_x)\mathsf{g}(x,\kappa_x)\exp(-i\kappa_x u_0 t)\mathrm{d}\kappa_x, \tag{C.7}$$

$$\Delta \hat{P}(x,\omega) = 2\pi\rho_0 \hat{v}(\kappa_x)\mathsf{g}(x,\kappa_x). \tag{C.8}$$

The sound radiated by the airfoil can be characterised in the far field by the power spectral density of the acoustic pressure p:

$$S_{pp}(x,y,\omega) = \frac{1}{2\pi}\int_{\mathbb{R}} \langle p^*(x,y,t)p(s,y,t+s)\rangle \exp(i\omega s)\mathrm{d}s, \tag{C.9}$$

where the superscript $*$ denotes the complex conjugate. For a two-dimensional acoustic field, the acoustic pressure can be expressed in terms of the pressure jump along the airfoil and the corresponding Green's function $\mathcal{G}$ as

$$p(x,y,t) = -\int_{\mathbb{R}}\int_{\mathbb{R}} \Delta\hat{P}(x,\omega)\frac{\partial}{\partial y}\mathcal{G}(x,y,x_1,\omega)\exp(-i\omega t)\mathrm{d}x_1\mathrm{d}\omega. \tag{C.10}$$

Inserting the complete pressure jump in Eq. (C.7) into Eq. (C.10), the power spectral density of the acoustic pressure is given by

$$S_{pp}(x,y,\omega) = \frac{\rho_0^2 u_0 \kappa_0 y^2 \pi}{2\sigma^3}\phi_{vv}(\kappa_x)|\mathcal{L}(x,\kappa_x)|^2, \tag{C.11}$$

where $\kappa_0 = \omega/c_0$ is the free-field acoustic wavenumber, $\sigma = \sqrt{x^2+\beta^2y^2}$ with $\beta^2 = 1-M^2$, ϕ_{vv} is the streamwise velocity spectrum of v and $\mathcal{L}$. Note that Eq. (C.11) decays as $1/r$ as expected for two-dimensional waves.

In two dimensions the velocity spectrum can be related to the energy spectrum, $E(\kappa)$, by (see Ref. [14])

$$\phi_{jj}(\boldsymbol{\kappa}) = \frac{E(\kappa)}{\pi\kappa}\left(1-\frac{\kappa_j^2}{\kappa^2}\right). \tag{C.12}$$

The lift function in Eq. (C.11) is defined in terms of the pressure jump along the airfoil

$$\mathcal{L}(x,\kappa_x) = \int_{-b}^{b} \mathsf{g}(x_0,\kappa_x)\exp\left[\frac{i\kappa_0}{\beta^2}x_0(M-x/\sigma)\right]\mathrm{d}x_0. \tag{C.13}$$

The lift function is obtained when inserting Eqs. (C.4) and (C.5) into Eq. (C.13) and summing up their contributions.

C.2 Inhomogeneous non-stationary turbulence

Amiet's analytical solution is now extended to accommodate for inhomogeneous non-stationary turbulent flows found downstream of a fan. The turbulent flow downstream a fan rotor can be characterised by a periodic series of Gaussian wakes superimposed over background turbulence. Following Jurdic's [18] approach, the background turbulence is assumed homogeneous and isotropic and the inhomogeneous wake turbulence is obtained by modulating an homogeneous upwash velocity field with a periodic train of Gaussian functions. Therefore, the total sound power levels radiated are given by the sum of the contributions from the background and wake turbulence. The SPL from the background turbulence can be obtained directly from the analytical solution for homogeneous frozen turbulence in Eq. (C.11), so we concentrate on the contribution from the wake turbulence.

The turbulent velocity component normal to the airfoil v_w is expressed in the form of a periodic train of Gaussian functions h that modulates an upwash velocity v:

$$v_w(x,t) = h(x,t)v(x,t). \tag{C.14}$$

The upwash velocity v is assumed homogeneous and it is defined as the sum of contributions from a range of gusts each with a different frequency as in Eq. (C.6). The periodic train of Gaussian functions h describes the evolution of the wake and it is defined as

$$h(x,t) = \sum_{m=-\infty}^{\infty} \exp\left[-\ln(2)\left(\frac{x-u_0t-mu_0T}{L_w}\right)^2\right], \tag{C.15}$$

where L_w is the half-width of the wake, T is the period between adjacent wakes and u_0 is the convection velocity.

In order to relate the upwash velocity field with the pressure jump along the airfoil, the train of Gaussian functions is first rewritten as a Fourier series. Using Poisson's summation formula, the periodic sum in Eq. (C.15) can be related to the Fourier series coefficients yielding

$$h(x,t) = \sum_{n=-\infty}^{\infty} h_n \exp[i\kappa_n(x-u_0t)], \tag{C.16}$$

$$\text{where} \quad h_n = \frac{L_w}{u_0T}\sqrt{\frac{\pi}{\ln(2)}}\exp\left[-\frac{1}{\ln(2)}\left(\frac{\pi L_w n}{u_0T}\right)^2\right] \quad \text{and} \quad \kappa_n = \frac{2\pi}{u_0T}n.$$

Therefore, Eq. (C.14) can be rewritten as

$$v_w(x,t) = \sum_{n=-\infty}^{\infty} h_n \exp[i\kappa_n(x-u_0t)]v(x,t). \tag{C.17}$$

The pressure jump is then given by

$$\Delta P(x,t) = 2\pi\rho_0 u_0 \int_{\mathbb{R}} \sum_{n=-\infty}^{\infty} h_n \hat{v}(\kappa_x-\kappa_n)\mathsf{g}(x,\kappa_x)\exp(-i\kappa_x u_0 t)\mathrm{d}\kappa_x, \tag{C.18}$$

$$\Delta\hat{P}(x,\omega) = 2\pi\rho_0 \sum_{n=-\infty}^{\infty} h_n \hat{v}(\kappa_x-\kappa_n)\mathsf{g}(x,\kappa_x). \tag{C.19}$$

Therefore, in this case the far-field power spectral density of the acoustic pressure defined in Eq. (C.9) is given by

$$S_{pp}(x,y,t,\omega) = \frac{\rho_0^2 u_0 \kappa_0 y^2 \pi}{2\sigma^3} \int_{-b}^{b}\int_{-b}^{b} \sum_{n=-\infty}^{\infty}\sum_{m=-\infty}^{\infty} h_n^* h_m \mathsf{g}^*(x_1, \kappa_x - \kappa_m + \kappa_n) \\ \mathsf{g}(x_2,\kappa_x)\phi_{vv}(\kappa_x-\kappa_m)\exp[iu_0(\kappa_m-\kappa_n)t] \\ \frac{\partial}{\partial y}\mathcal{G}(x,y,x_1,\omega-u_0(\kappa_m-\kappa_n))\frac{\partial}{\partial y}\mathcal{G}(x,y,x_2,\omega)\mathrm{d}x_1\mathrm{d}x_2. \tag{C.20}$$

In order to validate the numerical results, the typical approach used to compared against experimental data of considering the time average of power spectral density is considered here. That is, taking the Fourier mode $m = n$ in Eq. (C.20):

$$S_{pp}(x,y,\omega) = \frac{\rho_0^2 u_0 \kappa_0 y^2 \pi}{2\sigma^3} \sum_{n=-\infty}^{\infty} h_n^2 \phi_{vv}(\kappa_x-\kappa_n)|\mathcal{L}(x,\kappa_x)|^2, \tag{C.21}$$

where the velocity spectrum of the normal component of the turbulent velocity field ϕ_{vv} is defined in Eq. (C.12) and the lift function $\mathcal{L}$ in Eq. (C.13).

Bibliography

[1] Advisory Council for Aeronautics Research in Europe, *Aeronautics and Air Transport: Beyond Vision 2020 (Towards 2050)*, June 2010.

[2] Astley, R. J., Agarwal, A., Holland, K. R., Joseph, P. F., Self, R. H., Smith, M. G., Sugimoto, R., and Tester, B. J., "Predicting and Reducing Aircraft Noise," 14^{th} *International Congress on Sound and Vibration*, Cairns, Australia, July 2007.

[3] Ganz, U. W., Joppa, P. D., Paten, T. J., and Scharpf, D. F., "Boing 18-Inch Fan Rig Broadband Noise Test," Contractor Report 208704, NASA, June 1998.

[4] Omais, M. and Caruelle, B., "Jet Noise Prediction Using RANS CFD Input," 14^{th} *AIAA/CEAS Aeroacoustics Conference*, No. 2938, Vancouver, Canada, May 2008.

[5] Billson, M., Eriksson, L.-E., and Davidson, L., "Jet Noise Prediction Using Stochastic Turbulence Modelling," 9^{th} *AIAA/CEAS Aeroacoustics Conference*, No. 3282, Hilton Head, South California, May 2003.

[6] Kraichnan, R. H., "Diffusion by a Random Velocity Field," *The Physics of Fluids*, Vol. 13, No. 1, 1970, pp. 22–31.

[7] Bailly, C., Lafon, P., and Candel, S. M., "Stochastic Approach to Compute Subsonic Noise Using Linearized Euler's Equations," 5^{th} *AIAA/CEAS Aeroacoustics Conference*, No. 1872, Greater Seatle, Washington, May 1999.

[8] Bechara, W., Bailly, C., and Lafon, P., "Stochastic Approach to Noise Modelling for Free Turbulent Flows," *AIAA Journal*, Vol. 32, No. 3, March 1994, pp. 455–463.

[9] Careta, A., Sagues, F., and Sancho, J., "Stochastic Generation of Homogeneous Isotropic Turbulence with Well-Defined Spectra," *Physical Review E*, Vol. 48, No. 3, 1993, pp. 2279–2287.

[10] Ewert, R. and Emunds, R., "CAA Slat Noise Studies Applying Stochastic Sound Sources Based On Solenoidal Digital Filters," 11^{th} *AIAA/CEAS Aeroacoustics Conference*, No. 2862, Monterey, California, May 2005.

[11] Klein, M., Sadiki, A., and Janicka, J., "A Digital Filter Based Generation of Inflow Data for Spatially Developing Direct Numerical or Large Eddy Simulations," *Journal of Computational Physics*, Vol. 186, 2003, pp. 652–665.

[12] Ewert, R., Dierke, J., Muhlbauer, B., Neifeld, A., Appel, C., Siefert, M., and Kornow, O., "CAA Broadband Noise Prediction for Aeroacoustic Design," *IUTAM Symposium on Computational Aero-Acoustics for Aircraft Noise Prediction*, Southampton, United Kingdom, March 2010, pp. 1–19.

[13] Atassi, H. M. and Logue, M. M., "Effect of Turbulence Structure on Broadband Fan Noise," 14^{th} *AIAA/CEAS Aeroacoustics Conference*, No. 2842, Vancouver, Canada, May 2008.

[14] Pope, S. B., *Turbulent Flows*, Cambridge University Press, 2000.

[15] Siefert, M. and Ewert, R., "Sweeping Sound Generation in Jets Realized with a Random Particle-Mesh Method," 15^{th} *AIAA/CEAS Aeroacoustics Conference*, No. 3369, Miami, USA, May 2009.

[16] Dieste, M., *Generation of Synthetic Turbulent Velocity Fields using Filter Kernels*, MSc. thesis, Facultade de Matemáticas - Universidade de Santiago de Compostela, Santiago de Compostela, Spain, July 2008.

[17] Amiet, R. K., "Acoustic Radiation from an Airfoil in Turbulent Stream," *Journal of Sound and Vibration Research*, Vol. 41, No. 4, 1975, pp. 407–420.

[18] Jurdic, V., *An Investigation into Fan Broadband Noise due to Rotor-Stator Interaction*, Ph.D. thesis, Institute of Sound and Vibration Research - University of Southampton, Southampton, UK, 2009.

[19] Dieste, M. and Gabard, G., "Synthetic Turbulence Applied to Broadband Interaction Noise," 15^{th} *AIAA/CEAS Aeroacoustics Conference*, No. 3267, Miami, Florida, May 2009.

[20] Dieste, M. and Gabard, G., "Random-Vortex-Particle Methods for Broadband Fan Interaction Noise," 16^{th} *AIAA/CEAS Aeroacoustics Conference*, No. 3885, Stockholm, Sweden, June 2010.

[21] Dieste, M. and Gabard, G., "Broadband Fan Interaction Noise using Synthetic Inhomogeneous Non-stationary Turbulence," 17^{th} *AIAA/CEAS Aeroacoustics Conference*, No. 2708, Portland, Oregon, June 2011.

[22] Dieste, M. and Gabard, G., "Broadband Interaction Noise Simulations using Synthetic Turbulence," 16^{th} *International Conference in Sound and Vibration*, No. 451, Krakow, Poland, July 2009.

[23] Dieste, M. and Gabard, G., "Investigations of Broadband Fan Interaction Noise using Synthetic Turbulence," 17^{th} *International Conference in Sound and Vibration*, No. 738, Cairo, Egypt, July 2010.

[24] Dieste, M. and Gabard, G., "Predicting Broadband Fan Interaction Noise using a Random-Vortex-Particle Method," 20^{th} *International Congress on Acoustics*, No. 615, Sydney, Australia, August 2010.

[25] Billson, M., Eriksson, L.-E., and Davidson, L., "Jet Noise Modelling Using Synthetic Anisotropic Turbulence," 10^{th} *AIAA/CEAS Aeroacoustics Conference*, No. 3028, Manchester, United Kingdom, May 2004.

[26] di Mare, L., Klein, M., Jones, W. P., and Janicka, J., "Synthetic Turbulence Inflow Conditions for Large Eddy Simulation," *Physics of Fluids*, Vol. 18, No. 025107, 2006.

[27] Ewert, R., "Broadband Slat Noise Prediction Based on CAA and Stochastic Sound Sources from a Fast Random Particle-Mesh (RPM) Method," *Computers and Fluids*, Vol. 37, 2008, pp. 369–387.

[28] Ewert, R., Kornow, O., Tester, B. J., Powles, C. J., Delfs, J. W., and Rose, M., "Spectral Broadening of Jet Engine Turbine Tones," 14^{th} *AIAA/CEAS Aeroacoustics Conference*, No. 2940, Vancouver, Canada, May 2008.

[29] Ewert, R., "Slat Noise Trend Predictions Using CAA with Stochastic Sound Sources from a Random Particle Mesh Method (RPM)," 12^{th} *AIAA/CEAS Aeroacoustics Conference*, No. 2667, Cambridge, Massachusetts, May 2006.

[30] Ewert, R., "RPM - The Fast Random Particle-Mesh Method to Realize Unsteady Turbulent Sound sources and Velocity Fields for CAA Applications," 13^{th} *AIAA/CEAS Aeroacoustics Conference*, No. 3506, Rome, Italy, May 2007.

[31] Lund, T. S., Wu, X., and Squires, K. D., "Generation of Turbulent Inflow Data for Spatially-Developing Boundary Layer Simulations," *Journal of Computational Physics*, , No. 140, 1998, pp. 233–258.

[32] Smirnov, A., Shi, S., and Celik, I., "Random Flow Generation Technique for Large Eddy Simulations and Particle-Dynamics Modelling," *Journal of Fluids Engineering*, Vol. 123, 2001, pp. 359–371.

[33] Billson, M., Eriksson, L.-E., and Davidson, L., "Modelling of Synthetic Anisotropic Turbulence and its Sound Emission," 10^{th} *AIAA/CEAS Aeroacoustics Conference*, No. 2857, Manchester, United Kingdom, May 2004.

[34] Arfken, G. B. and Weber, H. J., *Mathematical Methods for Physicists*, Elsevier Academic Press, 2005.

[35] Kreyszig, E., *Advanced Engineering Mathematics*, John Wiley and Sons, Inc., ninth ed., 2006.

[36] Bracewell, R. N., *The Fourier Transform and its Applications*, McGraw-Hill, 2000.

[37] Hixon, R., Sescu, A., Nallasamy, M., and Sawyer, S., "Prediction Noise from Realistic Rotor-Wake/Stator-Row Interaction Using Computational Aeroacoustics," 15^{th} *AIAA/CEAS Aeroacoustics Conference*, No. 3339, Miami, USA, May 2009.

[38] Roger, M. and Moreau, S., "Broadband Self-Noise from Loaded Fan Blades," *AIAA Journal*, Vol. 42, No. 3, March 2004, pp. 536–544.

[39] Paterson, R. W. and Amiet, R. K., "Acoustic Radiation and Surface Pressure Characteristics of an Airfoil due to Incident Turbulence," Contractor Report NASA CR-2733, NASA, September 1976.

[40] Mish, P. F. and Devenport, F., "An Experimental Investigation of Unsteady Surface Pressure on an Airfoil in Turbulence - Part 1: Effects of Mean Loading," *Journal of Sound and Vibration*, Vol. 271, 2006, pp. 417–446.

[41] Adamezyk, J. J., "Passage of a Swept Airfoil Through an Oblique Gust," *J. Aircraft*, Vol. 11, No. 5, May 1974, pp. 281–287.

[42] Amiet, R. K., "High Frequency Thin-Airfoil Theory for Subsonic Flow," *AIAA Journal*, Vol. 14, No. 18, August 1976, pp. 1076–1082.

[43] Martinez, R. and Widnall, S. E., "Unfied Aerodynamic-Acoustic Theory for a Thin Rectangular Wing Encountering a Gust," *AIAA Journal*, Vol. 18, No. 6, June 1980, pp. 636–645.

[44] Amiet, R. K., "Noise Produced by Turbulent Flow into a Rotor: Theory Manual for Noise Calculation," Contractor Report 181788, NASA, June 1989.

[45] Roger, M. and Moreau, S., "Extensions and Limitations of Analytical Airfoil Broadband Noise Models," *International Journal of Aeroacoustics*, Vol. 9, No. 3, May 2010, pp. 273–306.

[46] Glegg, S. A. L., "The Response of a Swept Blade Row to a Three-dimensional Gust," *Journal of Sound and Vibration*, Vol. 1, No. 2327, 1999, pp. 29–64.

[47] Peake, N. and Evers, I., "On Sound Generation by the Interaction Between Turbulence and a Cascade of Airfoils with Non-uniform Mean Flow," *J. Fluid Mech.*, Vol. 463, 2002, pp. 25—52.

[48] Roger, M. and Carazo, A., "Blade Geometry Considerations in Analytical Gust-Airfoil Interaction Noise Models," 16^{th} *AIAA/CEAS Aeroacoustics Conference*, No. 3799, Stockholm, Sweden, June 2010.

[49] Sandberg, R. D. and Sandham, N. D., "Direct Numerical Simulation of Turbulent Flow Past a Trailing Edge and the Associated Noise Generation," *J. Fluid Mech.*, Vol. 596, 2008, pp. 353–385.

[50] Colonius, T. and Lele, S. K., "Comupational Aeroacoustics: Progress on Nonlinear Problems of Sound Generation," *Progress in Aerospace Sciences*, Vol. 40, 2008, pp. 345–416.

[51] Fang, J. and Atassi, H. M., "Numerical Solutions for Unsteady Subsonic Vortical Flows Around Loaded Cascades," *Journal of Turbomachinery*, Vol. 115, October 1993, pp. 810–816.

[52] Atassi, H. M., Ali, A. A., Atassi, O. V., and Vinogradov, I. V., "Scattering of Incident Disturbances by an Annular Cascade in a Swirling Flow," *J. Fluid Mech.*, Vol. 499, 2004, pp. 111–138.

[53] Casper, J. and Farassat, F., "A Time Domain Formulation for Broadband Noise Predictions," *Aeroacoustics*, Vol. 1, No. 3, 2002, pp. 207–240.

[54] Casper, J. and Farassat, F., "Broadband Trailing Edge Noise Predictions in the Time Domain," *Journal of Sound and Vibration*, Vol. 271, 2004, pp. 159–176.

[55] Ewert, R., Appel, C., Dierke, J., and Herr, H., "RANS/CAA based Prediction of NACA 0012 Broadband Trailing Edge Noise and Experimental Validation," 15^{th} *AIAA/CEAS Aeroacoustics Conference*, No. 3269, Miami, Florida, May 2009.

[56] Goldstein, M. E., *Aeroacoustics*, McGraw-Hill, 1976.

[57] Tam, C. and Webb, J., "Dispersion-relation-preserving finite difference schemes for computational acoustics," *Journal of Computational Physics*, Vol. 107, No. 2, 1993, pp. 262–281.

[58] Bogey, C. and Bailly, C., "A Family of Low Dispersive and Low Dissipative Explicit Schemes for Flow and Noise Computations," *Journal of Computational Physics*, Vol. 194, 2004, pp. 194–214.

[59] Kim, J. and Lee, D., "Generalized Characteristics Boundary Conditions for Computational Aeroacoustics," *AIAA Journal*, Vol. 38, No. 11, 2000, pp. 2040.

[60] Colonius, T., "Modeling Artificial Boundary Conditions for Compressible Flow," *Annu. Rev. Fluid Mech.*, Vol. 36, 2004, pp. 315–345.

[61] Percival, D. and Walden, A., *Spectral Analysis for Physical Applications: Multitaper and Conventional Univariate Techniques*, Cambridge University Press, 1993.

[62] Blandeau, V. P., Joseph, J. F., and Gabard, G., "Sound Power Radiation Due to an Isolated Airfoil in a Turbulent Stream," 20^{th} *International Congress on Acoustics*, Sydney, Australia, August 2010.

[63] Kloeden, P. E. and Platen, E., *Numerical Solution of Stochastic Differential Equations*, No. 23 in Applications of mathematics, Springer-Verlag, 1992.

[64] van Kampen, N. G., *Stochastic Processes in Physics and Chemistry*, Elsevier, 3rd ed., 2007.

[65] Favre, A., Gaviglio, J., and Dumas, R., "Some Measurements of Time and Space Correlation in Wind Tunnel," Technical Memorandum 1370, National Advisory Committee for Aeronautics, February 1955.

[66] Townsend, A. A., *The Structure of Turbulent Shear Flow*, Cambridge University Press, 2nd ed., 1976.

[67] Krasnoff, E. and Peskin, R., "The Langevin Model for Turbulent Diffusion," *Geophysical Fluid Dynamics*, Vol. 2, 1971, pp. 123–146.

[68] Ventres, C. S., Theobald, M. A., and Mark, W. D., "Turbofan Noise Generation Volume 1: Analysis," Contractor Report NASA CR-167952, NASA, July 1982.

[69] Sawyer, S., Nallasamy, M., and Hixon, R., "Computation of Rotor Wake Turbulence Noise," 9^{th} *AIAA/CEAS Aeroacoustics Conference*, No. 3268, California, USA, May 2005.

[70] Cheong, C., Joseph, P., and Lee, S., "High Frequency Formulation for the Acoustic Power Spectrum due to Cascade-Turbulence Interaction," *J. Acoust. Soc. Am.*, Vol. 119, No. 1, January 2006, pp. 108–122.

[71] Gruber, M., Joseph, P. F., and Chong, T. P., "Experimental Investigation of Airfoil Self Noise and Turbulent Wake Reduction by the use of Trailing Edge Serrations," 16^{th} *AIAA/CEAS Aeroacoustics Conference*, No. 3803, Stockholm, Sweden, June 2010.

[72] Chong, C., Joseph, P., and Davies, P., "A Parametric Study of Passive Flow Control for a Short, High Area Ratio 90 deg Curved Diffuser," *Applied Acoustics*, Vol. 70, No. 4, 2009, pp. 605–614.

[73] Amiet, R. K., "Refraction of Sound by a Shear Layer," *Journal of Sound and Vibration*, Vol. 54, No. 4, 1978, pp. 467–482.